Design Options for Low Cost, Low Power Microsatellite Based SAR

Naveed Ahmed

Thesis Submitted for the Degree of Doctor of Philosophy

6 December 2012

UNIVERSITY OF SURREY

Abstract

This research aims at providing a system design that reduces the mass and cost of spaceborne Synthetic Aperture Radar (SAR) missions by a factor of two compared to current (TecSAR – 300 kg, ~ £ 127 M) or planned (NovaSAR-S – ~ 400 kg, ~ £ 50 M) mission. This would enable the cost of a SAR constellation to approach that of the current optical constellation such as Disaster Monitoring Constellation (DMC).

This research has identified that the mission cost can be reduced significantly by: focusing on a narrow range of applications (forestry and disasters monitoring); ensuring the final design has a compact stowage volume, which facilitates a shared launch; and building the payload around available platforms, rather than the platform around the payload. The central idea of the research has been to operate the SAR at a low instantaneous power level—a practical proposition for a micro-satellite based SAR. The use of a simple parabolic reflector with a single horn at L-band means that a single, reliable and efficient Solid State Power Amplifier (SSPA) can be used to lower the overall system cost, and to minimise the impact on the spacecraft power system.

A detailed analysis of basic pulsed (~ 5 – 10 % duty cycle) and Continuous Wave (CW) SAR (100 % duty cycle) payloads has shown their inability to fit directly into existing microsatellite buses without involving major changes, or employing more than one platform. To circumvent the problems of pulsed and CW techniques, two approaches have been formulated.

The first shows that a CW SAR can be implemented in a mono-static way with a single antenna on a single platform. In this technique, the SAR works in an Interrupted CW (ICW) mode, but these interruptions introduce periodic gaps in the raw data. On processing, these gapped data result in artefacts in the reconstructed images. By applying data based statistical estimation techniques to "fill in the gaps" in the simulated raw SAR data, this research has shown the possibility of minimising the effects of these artefacts. However, once the same techniques are applied to the real SAR data (in this case derived from RADARSAT-1), the artefacts are shown to be problematic. Because of this the ICW SAR design technique it is—set aside.

The second shows that an extended chirp mode pulsed (ECMP) SAR (~ 20 – 54 % duty cycle) can be designed with a lowered peak power level which enables a single SSPA to feed a parabolic Cassegrain antenna. The detailed analysis shows the feasibility of developing a microsatellite based SAR design at a comparable price to those of optical missions.

Acknowledgements

First of all, I am thankful to Allah Almighty for providing me opportunity to carry out this research at this prestigious university. He provided me the sustenance and guidance to successfully complete the research and pass the PhD.

I am also grateful to my supervisor, Prof. Craig I. Underwood for his continued guidance and support. His always cheerful conversations, a friendly behaviour, his unique way to make his students realize their hidden research talents and then leaving the initiative with the students to follow a research methodology and produce the desired results, are extraordinary.

My sincere thanks to Karen Collar whose friendly behaviour and ever ready administrative support has turned space centre a home like place where we can peacefully concentrate on the research issues.

I am forever grateful to my mother Assia Bibi for her untiring prayers that had always been source of eternal help and guidance throughout my research. I am obliged to my wife Riffat and my kids Ahmed, Maria and Javeria to spare me for such long periods of involved research and I always found them accommodating. I also extend my sincere thanks to friends here and back home, who always encouraged and helped me to do well.

Finally, I owe my loving thanks and gratitude to my country Pakistan which has provided me with this opportunity. I gratefully acknowledge the financial support of the National University of Sciences and Technology, Higher Education Commission of Pakistan and Surrey Space Centre that has made this work possible.

Supervised by: Prof. Craig I. Underwood

Examiners:

Prof. Shaun Quegan, University of Sheffield

Dr. Raffaella Guida, University of Surrey

Table of Contents

List of Figures

List of Tables

List of Abbreviations

ADC	Analogue to Digital Converter
ACF	Autocorrelation Function
AOCE	Attitude and Orbit Control Electronics
APAA	Active Phase Array Antenna
BCR	Battery Charge Regulator
BOL	Beginning of Life
BPF	Band Pass Filter
CO_2	Carbon dioxide
CVA	Canonical Variate Algorithm
CPA	Closest Point Approach
CS	Compressed Sensing
DOD	Depth of Discharge
DEM	Digital Elevation Model
DMC	Disaster Monitoring Constellation
EOL	End of Life
EO	Earth Observation
ECMP	Extended Chirp Mode Pulsed
FFT	Fast Fourier Transforms
FPGA	Field Programmable Gate Array
FBS	Fine Beam Single
FBD	Fine Beam Dual
FPE	Final Prediction Error
FIR	Finite Impulse Response Filter
FAO of UNO	Food and Agriculture Organization of United Nations Organization
GaAs	Gallium Arsenide
GaN	Gallium Nitride
GPS	Global Positioning System
GOES	Geostationary Operational Environmental Satellites
HPA	High Power Amplifier
HPF	High Pass Filter
ICW SAR	Interrupted CW SAR
IIR	Infinite Impulse Response Filter
InP	Indium Phosphide
IFFT	Inverse Fast Fourier Transforms
LFM CW	Linear Frequency Modulated Continuous Wave
LoS	Line of Sight
Li-ion	Lithium-ion

LO	Local Oscillator
LNA	Low Noise Amplifier
LPF	Low Pass Filter
LEO	Low Earth Orbit
MO	Master Oscillator
MEO	Medium Earth Orbit
Mbps	Mega bits per second
MAPSAR	Multi-Application Purpose SAR
MIMO	Multiple Input Multiple Output
NASA	National Aeronautics and Space Administration
NESZ	Noise Equivalent Sigma Zero
NaN	Not a Number
N4SID	Numerical Algorithms for Sub-Space State Space System Identification
NiCd	Nickel-Cadmium
NiH_2	Nickel-Hydrogen
NOAA	National Oceanic and Atmospheric Administration
PCA	Principle Component Algorithm
PA	Power Amplifier
PAE	Power Added Efficiency
PEM	Prediction Error Model
PDF	Probability Density Function
PRF	Pulse Repetition Frequency
PRI	Pulse Repetition Interval
Pol-InSAR	Polarimetric – interferometric SAR
POES	Polar Operational Environmental Satellites
PPAA	Passive phase array antenna
Rect	Rectangular Function (Time Limited)
RAR	Real Aperture Radar
RDA	Range Doppler Algorithm
RF	Radio Frequency
SAR	Synthetic Aperture Radar
SD	Standard Deviation
SDT	Statistical Distribution Tables
SID	System Identification
SiC	Silicon Carbide
SISO	Single Input Single Output
SSTL	Surrey Space Technology Limited
SSC	Surrey Space Centre
SSPA	Solid State Power Amplifier
SNR	Signal to Noise Ratio

SiGe	Silicon Germanium
SLC	Single Look Complex
SPDT	Single Pole Double Throw switch
SVD	Singular Value Decomposition
SS	Sun Synchronous
TWT	Travelling Wave Tube
TWTA	Travelling Wave Tube Amplifier
T/R	Transmit/Receive
VIR	Visible and Infrared
VoIP	Voice over Internet Protocols
UAV	Unmanned Aerial Vehicle
UHF	Ultra High Frequency
UPC	Un-weighted PCA
UTJ	Ultra Triple Junction

List of Acronyms

ΔA	Azimuth resolution
A_{min}	Minimum area of the antenna
α_{az}	Azimuth FM rate (Hz/s)
α	Rate of change of the frequency in the chirp
B	Bandwidth
β	Incidence angle
β_i	Instantaneous incidence angle
$BW_{3\,dB}$	Half Power Beamwidth
γ	Angle subtended by an arc of length (ground range) at the centre of Earth
c	Speed of light in the free space, ($3\times10^8 m/s$)
D	Diameter of the parabolic dish antenna
d	Depth of curvature of the parabolic dish antenna
D_{min}	Minimum diameter of the Parabolic Antenna
D_S	Synthetic length which is the azimuth distance illuminated by R_o
F_a	Azimuth footprint
$PRF_{\min}$	Minimum PRF
$PRF_{\max}$	Maximum PRF

R_e	Mean local radius of the Earth
ΔR_s	Slant range resolution
ΔR_g	Ground range resolution
R_g	Ground range to the target
$R_{g,C}$	Ground range to the centre of the ground Swath
$R_{g,N}$	Ground range to the near edge of the ground Swath
$R_{g,F}$	Ground range to the far edge of the ground Swath
R_S	Slant range to target
$R_{S,C}$	Slant range at the centre of the swath (slant range)
$R_{S,N}$	Slant range at the near edge of the swath (slant range)
$R_{S,F}$	Slant range at the far edge of the swath (Slant Range)
R_o	Slant range to the target at closest point approach
ℓ	Antenna length in the direction of flight (azimuth direction)
W	Width of the antenna
θ_a	Azimuth Angle/Azimuth Half Power Beamwidth
θ_r	Range Angle/ Range Half Power Beamwidth
$\theta_{\mathrm{i,N}}$	Local incidence angle at the near edge of the swath
θ_{i}	Local incidence angle
S	Ground range swath
λ	Wavelength of operating frequency
ψ_a	A small angle within antenna 3 dB beam width – θ_a
ψ_r	A small angle within antenna 3 dB beam width – θ_r
τ	Pulse width
τ'	Chirp length
ξ	Compression Ratio(τ'/τ)
E	Energy of the received pulse
t_d	Delay/transmission time
h	Mean height of the platform carrying the payload
IF	Intermediate Frequency
t_{off}	Time during which transmitter remains off (for the ICW SAR)

t_{on}	Time during which transmitter remains on (for the ICW SAR)
T_{sys}	Operating Temperature in, Kelvin
T	LFM CW Waveform Time Period
T_i	Observation/Integration/Aperture Synthesis Time
t_{FT}	Time at which the feed through signal is received at the receiving antenna
t_{Nn}	Time at which the nadir returns reach the receiving antenna
T_{RW}	Slant range swath imaging time/slant range receive window time
f	Focal length of the parabolic antenna
f_c	Carrier frequency
f_b	Beat frequency
f_i	Instantaneous frequency of the chirp
f_d	Rate of change of phase with respect to time in azimuth direction
f_r	Pulse Repetition Frequency
$\phi(t)$	Phase term in the chirp expression
n	Number of Pulses that are needed to synthesize the antenna
NF	Receiver Noise Figure
$n_{p,td}$	number of pulses transmitted in time interval = t_d
P_N	Noise Power
σ	The radar cross section (RCS) of the target
σ^0	Normalized Back Scattering Coefficient / unit area
σ^0_{HH}	σ^0 for the horizontally received and horizontally transmitted signal
σ^0_{VH}	σ^0 for the vertically received and horizontally transmitted signal
σ_n	Thermal Noise Equivalent Back Scattering Coefficient (for SNR=1)
K	Boltzmann Constant = 1.6×10^{-23} $WK^{-1}Hz^{-1}$
v_s	Platform/Satellite velocity
v_g	The ground velocity, with which the radiation interact with the ground
v_e	Effective or relative velocity
P_{av}	Average RF Power spread over the entire PRI

P_t	Peak Power generated by the RF PA and fed to the antenna
P_R	Received Signal Power from the main lobe
$P_{R,N}$	Received Power from the Nadir Echo
P_{DC}	DC Power
P_{RFout}	Output RF Power
P_{RFin}	Input RF Power
P_D	Power Density
S_q^i	Scattered power density
G_t	Gain of the Transmitter Antenna
G_r	Gain of the Receiver Antenna
ω_0	Carrier frequency (radians/s)
Wdc	Watts direct current
$h_r(t)$	Range match filter
$h_s(t)$	Azimuth match filter

Applicable to Chapter 5 only

b	Raleigh distribution parameter
$u(t)$	Input vector to a system
$y(t)$	Observation/output vector from a system
A	The State Matrix
B	The Input Matrix
C	The Output Matrix
D	The "feed through" or "feed forward" matrix
K	The Kalman Gain
$e(t)$	The Error or Residual
$x(t)$	State vector
$\hat{y}(t)$	Estimated value of y(t)
w_k	Zero mean, white vector noise sequences
v_k	Zero mean, white vector noise sequences
δ_{pq}	Kronecker delta

Q, S and R	Covariance matrices of w_k and v_k
G	Covariance matrix between the state x(t) and the output y(t)
P	State covariance matrix
H	Block Hankel matrix
$\phi[A,B]$	Covariance matrix between matrices A and B
$\sum^s$	State covariance matrix
Λ_0	Output covariance matrix
Γ_i	The extended Observability matrix
Δ_i^c	Reversed Extended Stochastic Controllability Matrix
C_i and L_i	The block Toeplitz matices of output covariance matrices
W_1 and W_2	Weighting Matrices
Y_p	Block Hankel matrix containing the past outputs
Y_f	Block Hankel Matrix of the future outputs
O_i	The orthogonal projection matrix
$\hat{X}_i$	The state sequence
μ	Mean of the data
σ	Standard deviation
T	Transformation matrix
I & Q	In phase and Quadrature phase components of the complex data format

1 INTRODUCTION

1.1 Aims

The aims of this research are:

- To provide a system design that reduces the mass and cost of spaceborne Synthetic Aperture Radar (SAR) mission by a factor of two as compared with current or planned missions.
- To focus the research on a SAR payload that is suitable for forestry and disaster monitoring applications.

The limitations imposed on these aims are:

- The proposed system design should maximize the benefits of already designed, developed, time tested and space proven buses available from Surrey Space Technology Limited (SSTL). The SAR payload design should propose minimal essential changes to the existing buses.
- The mission life should be at least 5 years.
- The design should yield a compact stowage volume that facilitates injecting multiple payloads from a single launch.
- Initially, as a standalone mission, it should complement the existing optical imaging Disaster Monitoring Constellation (DMC), but eventually, should provide a baseline design for a future low cost SAR constellation.

1.2 Motivation

This research is inspired by the long term benefits that would be achieved by combining a SAR payload with a microsatellite platform.

Spaceborne Earth observation (EO) missions employ either passive or active sensors. Passive (optical) sensors, operate in the ultraviolet, visible, near-infrared and long wave infrared regions of the electromagnetic spectrum, and derive their name from the fact that the area being imaged is not illuminated by sensor radiation—rather, it is illuminated by some natural phenomenon such as sunlight or the thermal heat of the Earth. These sensors only capture the reflected, scattered or emitted radiations, thus from a design point of view, these have the advantage of being low cost,

consume less power and are light in weight. But their performance is degraded by environmental factors such as the presence of clouds, fog, haze, rain etc. in the imaging area. [1]

In the case of active sensors, the area being imaged is illuminated by the sensor itself and then the returned radiations are processed for image reconstruction. Most often this radiation is in the form of microwaves which have the ability to penetrate clouds, rain, tree canopies, and even dry soil surfaces depending on their operating frequency. Thus, it is the only technique which allows continuous, day or night imaging, regardless of prevailing environmental conditions. [1]

In the last ten years, programs such as DMC and RapidEye have demonstrated that low cost (~ £ 10 – 20 M) small satellites (100 – 300 kg) can provide solutions for medium to high resolution EO applications [2]. However, these have all been passive optical missions and there have been many occasions when useful imagery has not been acquired due to clouds or low light conditions. For an all-weather, day/night imaging capability, an active payload such as a SAR becomes necessary. But SAR missions have not yet made the same evolutionary step as those of the optical low cost missions, mainly because of the perception that SAR, being an active payload, is considered to be a power hungry system, thus needs larger and more powerful platforms.

In order to exploit the individual benefits offered by EO satellites (whether passive or active), often it is desirable to have quick revisits—which can be achieved by combining multiple satellites together in a constellation. SAR-Lupe (constellation of 5 identical satellites) and Cosmo-Skymed (constellation of 4 identical satellites) are recent examples [3], [4]. The Cosmo-Skymed SAR constellation cost is ~ £ 775 M, with a unitary cost of ~ £ 190 M [5].

The RapidEye constellation of 5 identical passive optical satellites—each ~ 150 kg, cost was ~ £ 135 M with a unitary cost of ~ £ 18 M [6]. Thus, it would appear that the cost of a single active satellite is more than the cost of entire passive optical RapidEye constellation.

Recent missions, such as TecSAR/TecSAR-2 (2008/9, ~300 kg) have demonstrated that a SAR payload can be flown on smaller platforms, but the unitary cost of only the space segment without launch or insurance was still high ~ £ 127 M [7]. These individual costs of the active payloads are affordable for rich governmental sponsored agencies but are beyond the reach of developing countries or customers with low financial budgets.

In order to fill this wide gap in the unitary costs of passive and active spacecrafts, recently SSTL, in close collaboration with Astrium UK, has begun designing and developing an affordable SAR mission that would cost ~ £ 50 M [8]. Although this would be a low cost SAR mission that would provide a basis for building a SAR constellation, the individual price, as compared with that of a typical (~300 kg, ~ £ 20 M) EO DMC passive optical mission, is more than double.

Given the rapid technological advancements taking place in radio frequency (RF) system design, it is envisaged that it should be possible to decrease the cost of a SAR mission further. The aim of this research is to reduce it to a point—comparable to that of a typical DMC class passive optical mission.

1.3 Objectives

Research at Surrey Space Centre (SSC), recently concluded, has shown the feasibility of employing a low cost and low power consumption linear frequency modulated (LFM) continuous wave (CW) SAR payload on microsatellite (~ 150 kg) platforms. However, due to high antenna isolation requirements of this SAR technique, a solution based on employing the transmitter and receiver on two spatially separated platforms, was proposed. By splitting the payload onto two platforms reduces the mass and cost of individual space segments. Nonetheless, overall mission mass and cost is similar to SSTL SAR mission, and this solution remains a two platforms based mission. [9]

The objective of this PhD research is to propose and analyse a SAR payload design that can be operated from a single microsatellite (~ 150 kg) at very low cost.

1.4 Scope

For a spaceborne SAR payload, the logical design and development cycle follows the route of crystallizing the applications first, and then deriving the application-specific requirements such as power, navigation and control system, stability, data handling, storage, downlink bandwidths etc. that would be required by the payload from the platform. Then, a platform that fulfils these requirements is designed. This application-specific platform development approach has historically been adopted for missions such as Seasat, ERS-1 & 2, Envisat, RADARSAT-1 & 2, ALOS and many others. But this approach is very expensive and time consuming. Due to these reasons, the time taken for developing the mission concept, working out the mission requirements, developing the payload and the platform accordingly, system integration, testing and finally launching, can often spread to a decade or so.

Space technology and philosophy have evolved and refined especially in last two decades and it has been learned that if general purpose platforms with certain baseline capabilities are designed, developed and space qualified, then a lot of time and cost may be saved. Nowadays, the payloads are often built around these available platforms instead of redesigning/reengineering the platforms from *ab initio*. Only minor modifications are carried out that are necessarily required for each payload design.

Pursuing this philosophy, SSTL has designed, developed and spaceflight proven platforms (buses) in a variety of categories which offer different baseline capabilities. The relevant information about these capabilities is publicly available. The SSTL platforms in the "micro-/mini-satellite" category that concerns this research, were examined, particularly the SSTL-100, SSTL-150 and larger SSTL-300 buses. The numbers (100, 150 and 300) indicate the approximate mass of the spacecraft (platform + payload), hence the SSTL-150 corresponds to a ~ 100 kg platform supporting a ~ 50 kg payload. Thus, on one hand these buses save time and money, but on the other hand put constraints on the payload mass; power supplied; limits on data storage and transmission bandwidths; mission life; type of attitude determination, knowledge and control; stability; position knowledge etc. Thus performance requirements of any payload have to conform to these constraints.

The SAR payload design may be performance or application driven. In the case of performance driven missions, the payload is first designed to provide certain baseline capabilities such as frequency band, spatial resolution, sensitivity, swath, revisits, polarimetric and interferometeric modes of operations etc., and then—keeping these capabilities in mind—what could be achieved/imaged with this sensor is analysed (i.e., what is the broader spectrum of the applications where this sensor can be used). RADARSAT-2 is one of the examples of this development philosophy [10]. This approach yields the type of missions which are usually institutionally supported and take a long development time, although the result provides very high performance capabilities. Whereas the applications driven approach, starts the design by deriving the intended application-specific payload parameters such as frequency, spatial resolution, the incidence angles, the swath, revisits, the polarization and interferometeric requirements etc., and then the sensor is designed accordingly. By keeping a narrow spectrum of intended applications, a light-weight mission may be designed although the payload flexibility (capability) is reduced. The planned MAPSAR mission is an example of this kind [11].

Weighing these two design approaches, the application driven approach looks attractive for a light-weight mission if a narrow set of applications is considered. However, once mass, the available power and the cost limitations are considered in the framework of microsatellite buses, a *'compromised approach'*—where the design begins with deriving application-specific sensor parameters and then trading off certain aspects of these parameters with respect to the baseline capabilities of the buses—eventually leads to a design solution that may not be purely termed as an application driven design.

To pursue this design approach, the intended applications are analysed with a view to find out the sensor parameters that help in servicing these applications. The more pronounced ones are the

frequency to be used, the spatial resolution, the range of incidence angles, the swath, sensitivity, polarization and the interferometric requirements.

Figure 1 - 1 has been drawn to summarize/clarify this multidimensional environment that the intended design has to deal with, while achieving the objectives of this research.

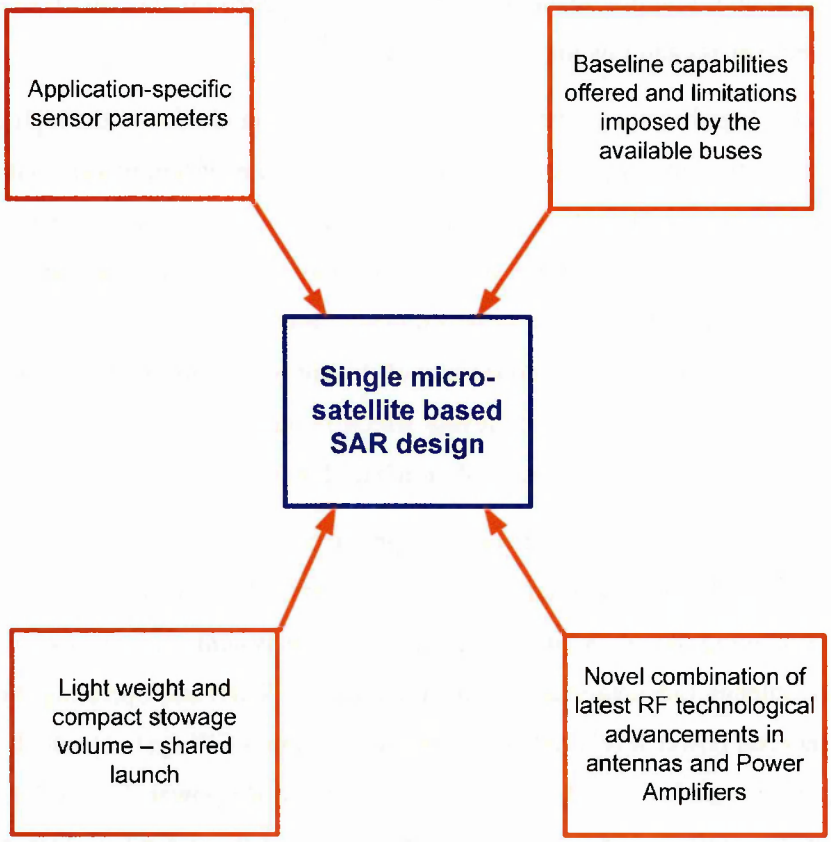

Figure 1 - 1: A pictorial representation of the multidimensional design philosophy

In this backdrop, different light-weight (both operational and planned) SAR missions are analyzed to determine whether any of these SAR design approaches can directly be applied to build a payload that conforms to all the constraints imposed on this research without introducing any major changes to the available buses, or there is a need to look for some new technique—or modify existing techniques—to meet the desired objectives.

A typical spaceborne SAR payload transmits narrow (~ 5 – 10 % of the duty cycle) but high powered RF pulses (~ 1 – 2 KW) through an antenna [12]. The same antenna is used to collect the backscattered radiation. This operation results in a well synchronized mono-static design. However, generating narrow and high peak powered pulses usually involves heavy and expensive RF power amplifiers and the antenna. Inplementation of pulsed SAR design technique from the SSTL platforms necessarily requires major changes in the power subsystem and the overall mass

and cost would increase.

In contrast, the last decade has seen the successful development of extremely light-weight (~ 1 kg) and low cost (~ USD 0.2 M [13]) SAR payloads for small airborne platforms such as Unmanned Aerial Vehicles (UAVs). This technique mainly focuses on continuous wave (CW) instead of transmission of narrow pulses. This yields significant advantages like operating the entire system at low instantaneous power levels, reduced circuit complexity, efficient duty cycle, cost effectiveness and low mass and volume. [14]

This technology has not yet been employed in space mainly due to the high isolation requirements between the transmitter and the receiver antennas as the system works continuously. This eventually necessitates a bi-static configuration where the transmitter and receiver are spatially separated by using two satellites and two antennas (one each for the transmitter and the receiver) [9]. This bi-static configuration in return needs careful synchronization across spatially separated platforms for maintaining the coherency of the entire system. In short it offers operating the system at low instantaneous power levels which require a light-weight bus (thereby reducing the cost), but nonetheless it remains a solution based on using a minimum of two satellites.

Analysing these two basic SAR design approaches, it appears that none of these in its original form fits directly to a single microsatellite platform. Thus, this research investigated the possibility of combining the major advantages of both these systems, i.e., the use of a single platform and a single antenna (advantage achieved from a pulsed SAR) and operating the entire system at low instantaneous power levels (advantage achieved from a CW system) which enables a single solid state power amplifier (SSPA) to provide the required RF power. This investigation yields two design options: interrupted CW SAR (ICW SAR) and the extended chirp mode pulsed (ECMP) SAR.

In the ICW SAR mode, the transmitter is switched on for just enough time for the signal to be scattered off the ground and return to the spacecraft. The transmitter is then turned off until all the signal returns have been collected by the receiver. But this process of switching on and off the transmitter leaves gaps in the synthetic aperture (known as the sparse aperture). Processing the sparse aperture data, without filling these gaps, introduces false targets (artefacts) in the image. Thus it can be ascertained that the ICW SAR technique provides a design solution to an engineering problem but gives birth to a signal processing problem.

To address the problem of sparse aperture filling, in the recent past different researchers claimed success in filling gaps of varying sizes. They have adopted various models to tackle this problem. During the course of this research, the system identification (SID) approach was adopted. This is based on numerically manipulating the available data to estimate different matrices and vectors of a state space model. The inferred state space model is assumed to represent the available data.

Once this model is estimated, the same model is then used to predict the missing data. This SID gap filling algorithm was applied to simulated point targets, and the initial results were encouraging. To evaluate the efficacy of this approach, it has also been applied to a dataset acquired by RADARSAT-1. The input data was arranged according to the scenario of ICW SAR operation, which introduces the periodic gaps. However, the performance of this gap filling approach appears to be unsatisfactory according to the requirements which need to suppress the artefacts that appear due to the gaps in the input data. Nonetheless, this is ongoing research in other fields of science and engineering, and in future new gap filling techniques may be developed that meet these requirements. Due to the unavailability of having a suitable gap filling technique in hand to necessarily demonstrate the fidelity of ICW SAR design technique it is—set aside.

The ECMP SAR design ensures that the benefits of both pulsed and CW SAR basic techniques are retained while associated problems are evaded. This technique is based on reducing the peak RF power by extending the pulse (~ 20 – 54 %) to a point which enables a single SSPA to feed a parabolic antenna. This technique yields a continuous aperture, thus, the problems faced due to the interrupted aperture synthesized during ICW technique, are circumvented.

The cost of launchers which are often used for injecting small satellites (< 1000 kg) into a low earth orbit varies from £ 16 – 21 M (~ £ 20,000/kg) [8]. Thus, keeping the mass of the spacecraft low, the launching cost can be reduced significantly. This formula works well for most of the EO passive optical missions, as the mass and density of these spacecrafts are almost the same. For a SAR payload, it is not the mass rather combination of mass and stowage volume that determines the launching cost. For a SAR payload such as SSTL NovaSAR-S, launching cost appears to be ~ 50 % of the total mission cost. It is because of the stowage volume at the time of launch, which dictates a dedicated launch. This launch cost may be reduced significantly if the payload is designed that facilitates a shared launch—thus sharing the launch cost with other payloads being injected into space by the same launcher.

In order to ensure a shared launch, the antenna configuration and its deployment mechanism, during and after the launch, plays a critical role. To this effect, different antenna illumination configurations (Newtonian and Cassegrain) and deployment techniques (mechanically deployable or inflatable) are analysed. It has been concluded that the dual reflector Cassegrain configuration with inflatable technology is the most suitable combination to design a 5 m reflector antenna with ~ 25 kg mass while keeping the stowage volume compact—almost similar to that of the bus itself.

The proposed ECMP SAR design offers a compromised solution between the purely application-driven sensor requirements, the mass and cost limitations imposed on the mission and the technical limitations imposed by the available buses. Detailed analysis of the design under the given limitations shows that a wide range of detection capabilities can serve a broader range of applica-

tions than initially anticipated, at a unitary mission cost of ~ £ 20 M.

1.5 Novel Contributions

This research has shown that operating a SAR at a low instantaneous power level is a practical proposition for a single microsatellite based SAR mission. The use of a simple parabolic mesh reflector with a single feed horn and dual receive channels (HH and HV polarized), at L-band , means that a reliable and efficient SSPA can be used to lower the overall system cost and to minimise the impact on the spacecraft power system.

The main novelty of this thesis has been to show that the ECMP SAR design, orchestrated around a highly constrained SSTL-150 bus, would yield a light-weight mission (which would be half the mass of the nearest operational mission TecSAR, or less than half of the planned NovaSAR-S mission) at a comparable cost to that of an optical mission.

Also, this research has shown that ICW SAR concept is not yet viable because of the unavailability of a suitable gap filling technique.

1.6 Thesis Structure

The thesis is organised in the following order:

Chapter 2 – The Literature Review: Different pulsed SAR missions in the light-weight category (~ 500 kg) are analysed to identify how various subsystems, particularly the antenna and RF power amplifier (PA) play their role in reducing overall mission mass. In addition, the latest developments taking place in the field of low cost and light-weight CW SAR techniques are also evaluated so that the necessary inferences may be drawn from this research. Moreover, the latest trends in PA and antenna designs, as potential cost, power and weight savers, have been included. The cost impacts of the spaceborne SAR missions (as a complete system), launching systems, antennas and PA have been kept in mind throughout the different stages of this research. Considering different antenna and RF PA combinations and how these combinations have been historically used—and what the cost effects are of these on the overall design—a low cost, light-weight and novel combination of a "*reflector antenna with a single SSPA*" was identified and built upon for this research.

Chapter 3 – User Requirements: To pursue an application driven development approach, a narrow set of applications that mainly focus on environmental hazards related to forestry (clear cut/deforestation monitoring and forest fire monitoring and mapping) and disaster monitoring (which encompasses flood delineation and monitoring, oil spill detection, geological hazards and hurricanes) are analysed with the intent of deducing the sensor parameters. From the user point of view, in order to reduce the development time and cost, available SSTL buses and their baseline

capabilities are considered, so that the payload should be designed around these buses. This chapter thus sets the application-specific sensor requirements, and also what the available platform resources/capabilities and their limitations are.

Chapter 4 – Design Options for SAR Based Microsatellite: Given the application-specific sensor requirements and the available baseline capabilities offered by the buses, certain tradeoffs are necessarily required while selecting factors such as the frequency, polarization, spatial resolution, range of incidence angles and swath, mode of operations, orbital altitude and inclination, and the antenna type and size, etc. Given these choices, two basic SAR operational techniques, i.e., pulsed and CW, are analysed with the intent of determining their impacts if they are implemented on the microsatellite platform and what changes would thereby be required. It appears that these two techniques in their basic form would either need significant changes in the bus or need two platforms, respectively. In order to work out suitable design approaches which combine the advantages of these two basic techniques and avoid the disadvantages, ICW and ECMP SAR techniques are evolved in the framework of their implementation on a microsatellite platform. These are analysed and problem areas are identified. In the light of these design options, the available SSTL-100 , SSTL-150 and SSTL-300 buses are evaluated in order to support the intended design approach—either ICW or ECMP SAR. After analysis of the design options, the available buses are re-examined to select the most suitable one out of the available three. SSTL-150 is considered sufficient to meet most of the requirements, thus it is selected for further design analysis.

Chapter 5 – Signal Processing Aspects of ICW SAR: This chapter deals with the issues related to the signal processing problems associated with the ICW SAR. In order to highlight these problems, a real SAR dataset which was acquired by the RADARSAT-1 is used. The initial part of the chapter deals with the detailed analysis of both continuous and interrupted apertures and compares the corresponding results at different signal processing stages. The latter part deals with the adopted sparse aperture filling technique. To evaluate and validate the performance of the gap filling algorithm, it is applied to the same dataset of RADARSAT-1. The results are analysed and a way forward is suggested.

Chapter 6 – Detailed Design Aspects of ECMP SAR: This chapter deals with the implementation issues of ECMP SAR on the SSTL-150 platform, within the confines of requirements and limitations imposed by the intended applications, the platform and the launching system (particularly the stowage volume during launch phase). In this context, different antenna design options (Newtonian/Cassegrain and deployable/inflatable) are analysed to suggest an antenna that yields a compact stowage volume, and is also easy to fit and operate from the SSTL-150 bus. This antenna in combination with the selected SSPA and the available power subsystem are used to work out the ambiguities, flexibilities and limitations imposed on the SAR operation. Under the given con-

ditions, the imaging time, expected data rates, onboard storage and data downlink bandwidth requirements are analysed with a view to highlight the perceived problems and suggest the solutions. The SAR requires very stable platform during imaging. The affects of attitude determination and control capabilities of the SSTL-150 and the stability requirements are discussed. In this perspective the role of position knowledge and how it affects the intended applications is also highlighted. In addition, the estimated mass budget and the estimated price in comparison with the NovaSAR-S are also worked out. Finally the detection potentials are determined and how these can be exploited to enhance the scope of applications, are also evaluated.

Chapter 7 - Conclusions and Future Work: This chapter summarizes the work presented in this thesis and highlights the key contributions of the current research. In order to improve the applicability of the ECMP SAR technique, several suggestions are proposed for further research.

1.6 Publications

During this research, following have been published:

- Naveed Ahmed, Craig I. Underwood, "*Software Defined LFM CW SAR Receiver Design for Microsatellites*", paper presented at 7th IAA Symposium on Small Satellites for Earth Observation, May 4-8, 2009, Berlin. This paper was published as a chapter in the book titled "Small Satellite Missions for Earth Observation - New Developments and Trends", Publishers Springer Verlag, Germany, ISBN 978-3-642-03500-5, 2010.
- Naveed Ahmed, Craig I. Underwood, "*Monostatic CW SAR Concept For Micro-Satellites*", Conference proceedings, 8th European Conference on SAR, Jun 8-10, 2010, Aachen, Germany.
- Naveed Ahmed, Craig I. Underwood, "*Switched CW SAR – A Novel and Low Cost SAR Solution for Microsatellites*", Paper presented at 8th IAA Symposium on Small Satellites for Earth Observation, April 4 - 8, 2011, Berlin, Germany.

2 LITERATURE REVIEW

A literature review has been conducted to evaluate design aspects of different SAR systems (either operational or planned) with a view to exploring the trend towards low cost and light-weight technologies that may be considered suitable for use on a microsatellite. Against this backdrop state of the art, the mini-satellite based TecSAR, NovaSAR and MAPSAR are analysed [7], [15], [16]. In addition, the latest technological developments taking place for extremely low cost LFM CW SAR for UAVs are also discussed as an alternative technique for use on microsatellites.

Detailed cost analysis helps in decision making at subsequent stages. Due to the confidential nature of spaceborne SAR missions, it is hard to find a publicly available complete cost analysis for these missions. However, scattered information has been gathered to provide a broad view about the cost impacts of different systems and subsystems, so that a low cost spaceborne SAR mission can be built accordingly. To quote an example, for a £ 150 M mission, the individual £ 2 M price of a Travelling Wave Tube (TWT) PA may look petty but for a £ 20 M mission—it is comparatively significant. To design a low cost mission, suitable alternative technologies—mainly RF PA and the antennas, are therefore analysed, too, as these are considered to be critical sub-systems which have direct impact on the mission's cost, mass and performance.

2.1 Characteristics of Spaceborne SAR Missions

Traditionally all the known spaceborne SAR missions use pulsed technology, where a single antenna is time shared between transmitter and receiver. In these designs, a narrow but high powered, modulated pulse is transmitted. Then the transmitter remains off and allows the receiver to receive, process and record the backscattered echo signal. Figure 2 - 1 pictorially shows this concept. Alternate switching between transmitter (pulse) and receiver (echo) allows sharing the most crucial onboard resource—the antenna. This arrangement makes it possible to operate the SAR from a mono-static (same) location.

If the SAR is designed to operate from an airborne platform, then due to the short slant ranges between the sensor and the target, the timing, as shown in Figure 2 - 1 is so adjusted that it also allows receiving the returns before the next pulse is transmitted. For a satellite case, the principle remains the same, but due to the long distance involved between the sensor and the targets, there

would be a certain number of pulses (depending upon the distance involved and the set pulse repetition frequency (PRF)) present in the transmission channel between the SAR and the target area. So the PRF is selected so as to maintain the separation between transmit pulse and the echo returns.

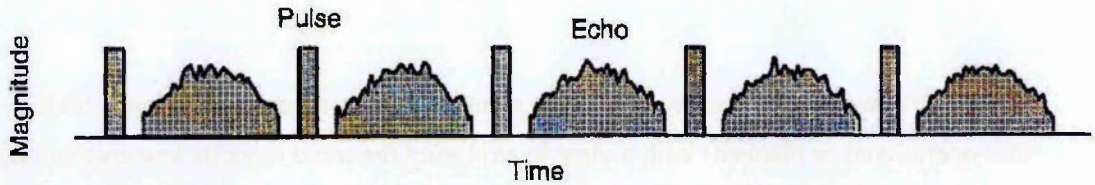

Figure 2 - 1: Pulsed SAR - time sharing concept with the same antenna

Source: Adapted from [12]

For sharing a single antenna between the transmitter and the receiver, a switching mechanism (duplexer) has to be inserted in the system to ensure the corresponding paths, from the transmitter to the antenna (during time of transmission) and from antenna to the receiver (during time of reception), remain isolated from one another.

The use of a duplexer ensures the protection of the highly sensitive receiver from any leakage signals that may flow from the transmitter to the receiver during the time of transmission. Duplexers are constructed in many forms, such as: [17]

- Ferrite Circulators (hybrid-ring duplexer) – heavy and expensive, suitable for high isolation requirements in the range of 40 – 50 dB.
- Resonant cavity coaxial or waveguide systems – involve complex mechanical structures and these are heavy, too.
- Transmit Receive (T/R) Switch – solid state technology based.

Each has its own characteristics and choosing the appropriate one for a specific radar configuration is a complicated process. However it is the net isolation requirement between transmitter and receiver which determines the type of duplexer to be used. For the low isolation requirements (~ 30 dB or so) such as envisaged within the Active Phase Array Antennas (APAA), T/R switches provide a suitable solution.

The first documented SAR payload in space was Seasat SAR launched in 1978. The main objective of this mission was to acquire data in geo-scientific research, particularly oceanography and polar ice studies [18]. Since then, spaceborne SAR missions have been launched by all the major space powers of the world.

The mass of a spaceborne SAR mission is determined by many mutually dependent factors such as: the intended applications which dictate the operating frequency band, swath and the resolution requirements, polarimetric and interferometric requirements; the type of the PA and the type of the antenna used etc. Table 2 - 1 has been organized to present an overview of salient SAR missions according to the frequency band, the antenna size, mass and type, and the overall mission mass.

Mission	Band	Antenna (m x m)	Antenna Mass (kg)	Antenna Type	Mission Mass (kg)
SEASAT [19]	L	2.14 x 10.74	250	PA with corporate feed antenna	2300
JERS-1/LSAR [20]	L	2.4 x11.9	278	PA with corporate feed antenna	1340
ALOS-1/ PALSAR [21]	L	3.1 x 8.9	250	APAA	4000
ENVISAT/ASAR [22]	C	1.3 x 10	608	APAA	8140
ERS-1 [23]	C	1 x 10	325	APAA	2157
ERS-2 [24]	C	1 x 10	325	APAA	2516
RADARSAT-1 [25]	C	1.5 x 15	679	APAA	2713
RADARSAT-2 [26]	C	1.4 x15	800	APAA	2200
TerraSAR-X [27]	X	0.75 x 4.8	–	APAA	1230
COSMO-Skymed [4]	X	1.4 x 5.6	–	APAA	1700
SAR-Lupe [3]	X	2.7 x 3.3	–	Elliptical Reflector	770
TecSAR [7]	X	3 m diameter	21	Deployable parabolic Reflector	300
RISAT-2 (TecSAR-2) [28]	X	4.5 m diameter	21	Deployable Parabolic Reflector	300
NovaSAR-S (planned) [15]	S	1 x 3	70	APAA	400
MAPSAR (planned) [16]	L	5 x 7.5	74	Deployable Elliptical Reflector	532

Table 2 - 1: Examples of prominent SAR missions, showing the frequency band used, the size, mass and type of the antenna used and overall mass of the mission

These examples particularly highlight the relationship between the overall mass of the mission and the mass of the antenna. With the technological developments taking place in deployable and lightweight antenna designs, it is becoming possible to launch antennas that have much larger projected areas with a much reduced mass; such as on TecSAR - 2 (projected antenna area of 15.90 m^2, 21 kg antenna mass) and the planned MAPSAR (projected antenna area of ~ 30 m^2, 74 kg antenna mass) [28], [16]. These reduced antenna masses, as a result, lead to lighter weight SAR missions.

Historically spaceborne SAR missions had been employed on large satellites, mainly due to the fact that these require large antennas (to address the range and azimuth ambiguities) and the high power demands required during imaging (thus necessitating large solar panels). These large platforms then needed powerful launchers, thus giving birth to very high mission costs. As a result, there were very few SAR missions launched into space during 1980s and 90s.

Pulsed SARs with phased array front ends incorporating T/R modules (APAA) have been termed as "RF Dinosaurs" [29] as these need a large number of T/R modules and RF cables to switch narrow and coherent pulses. Although APAA technology provides flexibility in terms of beam steering, it comes at the cost of expensive, heavy, complex and less efficient antennas.

As seen in Table 2 - 1, the antenna size, type and mass contribute significantly towards overall mission mass. APAAs particularly require large platforms. One of the reasons which resulted in a high space segment mass for the previous missions such as SEASAT, ALOS, ENVISAT, ERS 1 &2 etc. was the fact that these were multi-sensor missions incorporating scatterometers, altimeters as well as SARs . As the experience matures in this field, there is a growing interest to use single sensors on the platforms. The missions such as RADARSAT-1 & 2, TerraSAR-X, SAR-Lupe, TecSAR-1 & 2, NovaSAR-S and MAPSAR are examples of this class of missions. Focusing on a single sensor reduces cost and mass of an individual spacecraft.

The launch of SAR-Lupe (770 kg – 2006) and TecSAR (300 kg – 2008) has shown that spaceborne SAR missions can be flown on smaller satellites (< 1000 kg) by using appropriate technologies (such as reflector antennas instead of APAA). The combination of light-weight SAR and platform would then, as a result, need less powerful launchers, thus yielding, overall, a lower cost mission. In addition, more satellites (NovaSAR-S and MAPSAR) in the mass category of ~ 500 kg are planned in the near future [15], [16].

Since this research aims at even a lighter weight and low cost SAR design suitable for a microsatellite platform *circa* 150 kg, these lightest weight SAR missions (either operational (TecSAR) or planned in near future (NovaSAR and MAPSAR)) are analysed in detail with a view to draw necessary inferences from design point of view. The next three sections provide a representative overview of specific systems in the category of ~ 500 kg small satellites. The purpose is to focus on different baseline technologies/techniques that are instrumental in reducing the mass of these missions.

2.2 TecSAR – Lightest Weight Operational SAR Mission

TecSAR is a trend setter in the light-weight category of spaceborne SAR missions. TecSAR is primarily a military satellite—where primary objective is to detect the potential targets not the measurement of backscattering properties of the distributed targets. The relevant information is summarized in Table 2 - 2. [7], [30] , [31]

Parameter	Given Values
Operating Band	X (8.5 – 10.6 GHz)
Bandwidth	> 200 MHz
Antenna Diameter	3 m
Antenna Mass	21 kg
No of Transmission Beams	8
Polarization	VV
Online data compression	From 8 to 3 bits
A/D Sampling Rates	240, 360,720 MHz
Onboard Memory	256 GB
Max Data Transmission Rate	600 Mbps
Orbital Height	450 to 580 km
Orbital Inclination	41°
Weight of the Mission	300 kg (200 kg Bus and 100 kg SAR)
Operational Modes (Wide Coverage, Strip, Super Strip (Mosaic) and Spot modes)	Corresponding Resolution (8,3,1.8,1 m)

Table 2 - 2: TecSAR Parameters

Given that TecSAR operates at X-band with a 3 m diameter parabolic antenna, if incidence angle of 25^0 is assumed, then the ground swath is expected to be very narrow (~ 8 km). This single beam narrow swath is not particularly useful compared with the much wider swaths of other SAR systems. This problem has been offset by using eight beams instead of one. This needed eight PAs. For this purpose, 10 Travelling Wave Tube (TWT) amplifiers (8 are used for 8 beams and 2 kept cold redundant) are used in the transmitter. To transmit and receive corresponding beams, it requires a multi-feed (8 feed) arrangement, as shown in Figure 2 - 2 (a).

The system needs 1.6 kW of RF power during imaging. To sustain this power, the bus is designed to deploy two large solar panels that are capable of providing 750 Wdc EOL (end of life). Figure 2 - 2 (b) shows these deployable solar panels.

For TecSAR use, the TWTs were specially designed to give more than 50 % efficiency. These TWTs need high potential difference between anode and cathode, which is provided by High Voltage Power Supply. Each TWT is provided with 6 kV for its operation.

As reported by [28] and [32], India has acquired an improved version of TecSAR from Israel in

2009 at a cost of ~ £ 127 M. It is not known whether this cost includes that of the launcher or not. This version has a 4.5 m diameter parabolic dish antenna with a gold platted mesh and the ribs made of composite materials. Despite 1.5 times increase in the antenna diameter, the overall mission mass is maintained at 300 kg.

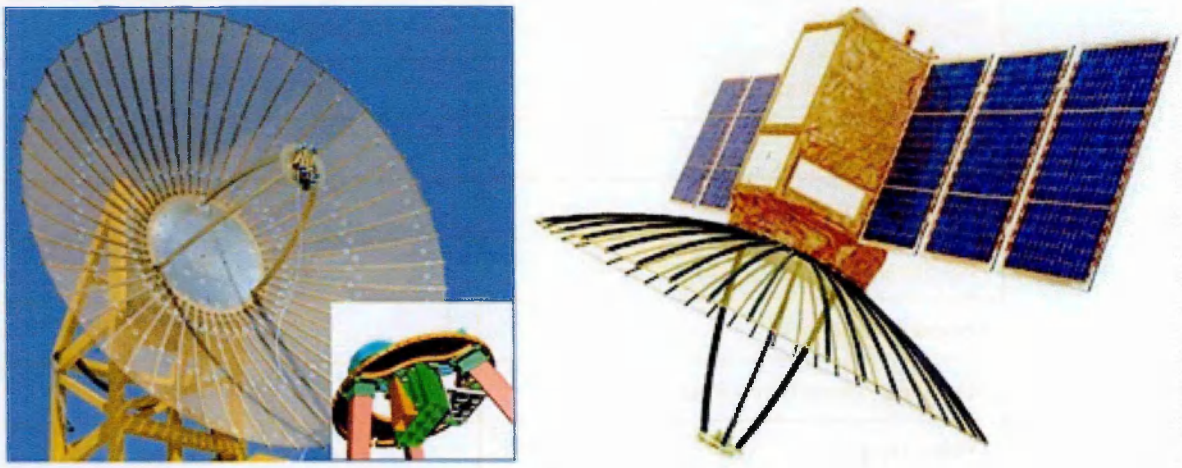

(a) (b)

Figure 2 - 2: (a) – The antenna and the multi feed system (b) – TecSAR bus, deployed solar panels, payload and the parabolic dish antenna

Sources: Adapted from [7] and [30]

2.2.1 Applicability of TecSAR Design to this Research

TecSAR utilized the already operational and time tested bus that was being used with other optical satellites. This reduced the development cost and time for the mission.

For parabolic antennas, the antenna gain is degraded by the errors introduced due to reflecting surface (shape/figure) inaccuracies. For a given deformation, these errors are more pronounced at higher frequency bands (e.g. X-band) as compared with low frequency band (L-bands). Acceptable surface inaccuracies should be within the limits of ±1/8 of the wavelength. If the surface inaccuracy is more than this limit, then the errors introduced to the net antenna gain would typically be higher than 1 dB [33]. This limit requires a rigid antenna structure – to help achieve highly accurate surfaces within ± 3.7 mm or so at X-band (whereas for L-band, this limit is relaxed to ± 4 cm, which implies less rigid antenna structures are required).

To offset the effects of narrow ground swath achieved from a single beam—needed complex RF front end requiring 8 TWTs, 8 coaxial cables and the multi-feed arrangement. If similar parabolic reflector antenna is used at low frequency band such as L-band, then a wider swath may be achieved from a single beam, thus evading the complex RF front end arrangement.

TecSAR, although light in weight, had to use a mission dedicated launch mainly due to the large stowage volume of the antenna. The antenna was stowed like a single folded umbrella during the launch. For a low cost SAR payload to be specifically designed to facilitate a shared launch, the antenna deployment techniques should be such that these yield a compact stowage volume.

2.3 NovaSAR-S (SSTL Planned SAR)

Since late 2009, SSTL in collaboration with Astrium UK has planned to design and develop a low cost and light-weight SAR mission, for potential customers with low budgets. The mission is expected to be launched by 2014. Some of the design features are: [15], [34], [35], [36]

- It is based on conventional pulsed technology at S-band (3.1 – 3.3 GHz).
- It transmits 1.8 kW of RF power through a 1 m x 3 m APAA.
- Likely mission mass is ~ 400 kg, with the payload mass of 100 kg and the antenna mass of 70 kg.
- The mission design is based on already developed and time tested SSTL-300 bus which is currently being used with NigeriaSat-2 (with optical payloads).
- The single beam strip map mode swath is approximately 20 km with 6 m resolution. Swath is extendable by electronically steering the beam to achieve approximately 100 km at 20 m or 150 km at 30 m resolution.
- It supports the strip map and scanning modes of operation (spot mode is not supported).
- Although not yet confirmed, the likely mission cost would be in the range of £ 40 – 50 M.
- The payload is designed to operate for ~ 2 minutes per orbit.
- NovaSAR-S aims to provide polarimetric medium resolution (6 – 30 m) imagery that is considered suitable for applications such as:
    - Flood monitoring.
    - Agricultural crop assessment.
    - Forest monitoring (temperate and rain forest).
    - Land use mapping.
    - Disaster management.
    - Maritime applications (e.g. ship detection and oil spill monitoring).
- The design enjoys the benefits of the availability of suitable T/R module at S-band that provides more than 100 W RF output. Thus by using only 18 T/R modules in the APAA, 1.8 kW of RF power would be generated. This is in contrast to other spaceborne SAR missions that use large number of comparatively less capable T/R modules e.g. RADARSAT-2 uses 512 T/R modules [26]. Using fewer T/R modules, saves a lot of complexity, weight, power and thus cost.

- Designers have selected a 40 % efficient (Power Added Efficiency (PAE)) Gallium Nitride (GaN) based SSPA within the T/R module [36]. It is considerably more efficient than other commonly used 25 – 30 % [29] modules. To generate 1.8 kW RF power at 40 % efficiency actually needs 4.5 kW of DC power. 60 % DC power is dissipated during the process. Due to these reasons, the mission would afford limited imaging time of ~ 2 minutes per orbit only.
- Overall it would be a lightest weight SAR mission (in the public domain) for measuring distributed targets, at reduced cost and a very quick development time (~ 24 months).
- SSTL estimated the cost of NovaSAR-S to be around £ 40 – 50 M. Recently UK government has granted funding of £ 21 M for manufacturing the space segment (payload and the bus). The launching cost would be arranged separately in future. [8]

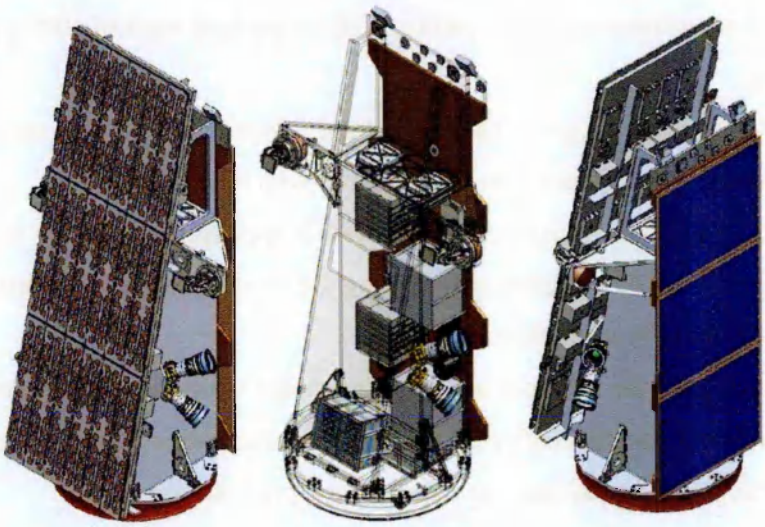

Figure 2 - 3: The NovaSAR-S

Source: Adapted from [36]

Figure 2 – 3 shows the NovaSAR-S design. The left part of the figure depicts the APAA with 18 radiating elements. This antenna is un-foldable thus, maintains the same condition during launch and subsequent orbital operations. The middle figure displays the layout of subsystems. The right most part of the figure shows the solar panels. It is evident that there are no deployable parts involved—which increases the overall reliability of the mission during launch and subsequent operational phases.

2.3.1 Applicability of NovaSAR-S Design to this Research

SSTL-300 bus operates at 28 V. To generate the pulse of 1.8 kW (RF power), 4.5 kW of DC power is required, which needs ~ 160 A (dc) from the onboard power sub-system. The power systems

are not designed for providing this type of current. To sustain this high current demand, bulk capacitors are required with the T/R module—adding additional weight and complexity to the antenna and the system [36]. This aspect highlights the importance of operating the payload at low instantaneous power levels. Insertion of bulk capacitors—either with the T/R modules (upfront with the antenna) or using these inside the power system—these are major mass contributors, thus should be avoided.

For the NovaSAR-S design, the main cost savers are: the availability of already designed, developed and operational bus; and, the availability of Astrium UK modular SAR design (except the antenna). Only the antenna required design and development. The antenna design is based on an S-band T/R module which is already a designed, developed and space qualified product. This aspect highlights the importance of using maximum available commercially off the shelf resources.

This design also highlights the importance of individual capabilities (mainly the RF output power of ~ 100 W and the PAE of ~ 40 %) of the S-band SSPA being used within the T/R module. These individual capabilities contribute significantly in deciding the number of modules in the APAA. Higher output power needs fewer PAs. However, the choice is strongly frequency dependent, as more capable SSPAs are available at low frequency bands (S- and L-band) as compared with the higher frequency bands (C- and X-bands).

This design also suffers from the problems of stowage volume during launch phase, which necessitates a dedicated launch, mainly due to the antenna design. Because of dedicated launch, the proportionate launching cost would be ~ 50 % of the mission cost.

2.4 MAPSAR (Multi-Application Purpose SAR)

MAPSAR is a joint Brazilian and German venture. The SAR is being designed to operate at L-band. The mission is based on the Brazil's Multi-Mission Platform (500 kg class spacecraft)—an already designed and developed platform. The mission objectives are the assessment, management and monitoring of natural resources especially forests. [11]

The main envisaged problem for the L-band SAR is the large antenna size required compared to other higher frequency bands. For this purpose, the designers have selected a light-weight Cassegrain reflector configuration with an elliptical parabolic main reflector, 7.5 m in azimuth and 5 m in elevation, as shown in Figure 2 - 4. [16]

The second design issue is the implementation of the high power amplifier (HPA) for generation of the radar pulses. In order to generate 1 kW of peak RF power, 4 space qualified TWT PAs, each with 250 W output power, are used. The output from these individual TWTs is combined in the waveguides [16]. The combined mass of RF PAs, the mechanical assemblies (waveguides),

the harness, backend sensor electronics etc. is ~160 kg [11].

Single, dual and quad polarization modes would be available. The satellite altitude is selected at 620 km. The incidence angle varies from 20 – 45° with instantaneous swaths of 32 – 55 km and resolutions of 4 – 20 m. [11]

It would only support the strip map mode of operation. Within this mode, pre-programmed flexible look angles, on both sides of the nadir (left/right looking) allows achieving wider imaging area.

The anticipated mission mass would be 532 kg. Although there have been considerable delays in the design and development stages, the MAPSAR is scheduled for launch by the end 2012 or early in 2013. [37]

The MAPSAR is an application-specific design which provides single, dual and quad polarimetric modes with varying resolutions and swath. These sensor requirements are particularly helpful to serve the applications such as forestry, agriculture, hydrology, urban mapping, disaster monitoring (oil slicks, ship monitoring etc.) and many other public and commercial applications. The longer wavelengths at L-band penetrate deeply through the canopy and help in monitoring the surface conditions in forests and agricultural lands [11].

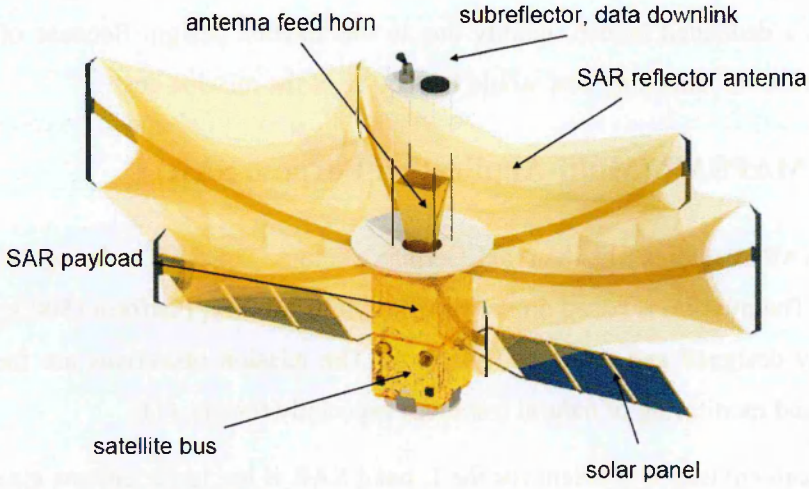

Figure 2 - 4: The MAPSAR

Source: Adapted from [11]

2.4.1 Applicability of MAPSAR Design to this Research

The MAPSAR's innovative reflector antenna design using Cassegrain configuration suggests another reflector illumination technique that has many advantages over the Newtonian technique

used with the TecSAR. Cassegrain configuration is particularly useful for large size antennas. The size of the horn (feed mechanism) is large for the L-band as compared with the X-band (TecSAR). For the Newtonian design, the horn is kept away from the main reflector at a focal point. It means a large and heavy horn hanging away from the main body, besides other issues, would start acting as a gravity boom—a situation which should always be avoided from the astro-dynamic point of view. The Cassegrain configuration keeps the horn at the vertex, thus evading these problems faced with the Newtonian configuration.

To generate 1 kW RF power, 4 TWTs are used in this design. RF PA is a critical component in the SAR payload design. It needs at least 2 TWTs to be kept in cold redundancy. The mass of each TWT at L-band is ~ 6 kg. In total six TWTs would require ~ 36 kg mass budget for RF PA. This research aims at proposing a microsatellite based design which should have mass of ~ 150 kg. Allocating ~ 36 kg only for the RF PA, may not be a feasible solution. This problem can be circumvented by keeping the instantaneous RF power levels low so that a single SSPA or TWT could be used.

2.5 LFM CW SAR – A Nano-SAR Design for Aerial Platforms

During recent years the demand to provide battlefield imagery in all environmental conditions has increased. Being flexible, low cost and low risk, Unmanned Aerial Vehicles (UAVs) are considered a suitable platform for this purpose. Besides these advantages, these platforms have constraints that restrict them to support limited payload mass, volume and power. Any payload considered suitable for use with these platforms, needs to conform to these constraints. Since SAR can provide imagery in all environmental conditions, however, the conventional SARs based on pulsed technology are neither low cost nor light-weight.

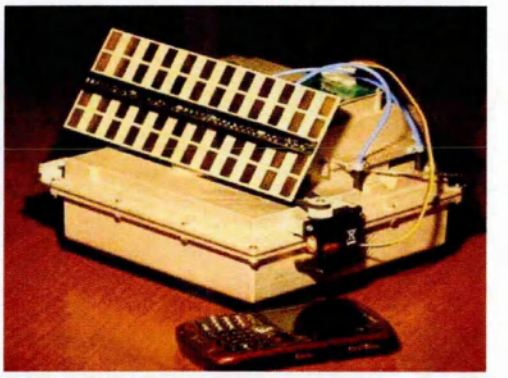

Figure 2 - 5: A 2 lb Nano-SAR based on LFM CW technique

Source: Adapted from [38]

This scenario motivated SAR designers to develop an alternative technology in the form of LFM

CW SAR in early 2002. Technology demonstrators have proved to be successful and now qualified products are being provided to end users. [39] Figure 2 - 5 shows one of these finished products. The manufacturers named it a 2 lb (~ 1 kg) Nano-SAR. [38]

2.5.1 Working Principle

To achieve adequate antenna isolation (through a duplexer network) for a spaceborne pulsed SAR, high powered (~ 1 – 2 kW or so) and narrow (~ 5 – 10 % duty cycle [12]) pulses as shown in Figure 2 - 6, are transmitted. After transmitting this narrow chirp (Appendix A), the transmitter remains silent and the system waits for the echo to be received, processed and recorded. But in the case of CW, the same chirp is extended over the complete cycle (100 % duty cycle) and is transmitted continuously. In the first case the pulse has to be high powered so that the average transmitted RF power (on time + off time) over the entire cycle remains high enough to achieve adequate Signal to Noise Ratio (SNR). The process of generating this high peak powered pulse necessarily needs a very high instantaneous power. But for the CW case, the equivalent average power over the complete cycle is maintained such that requirement of high instantaneous power is avoided.

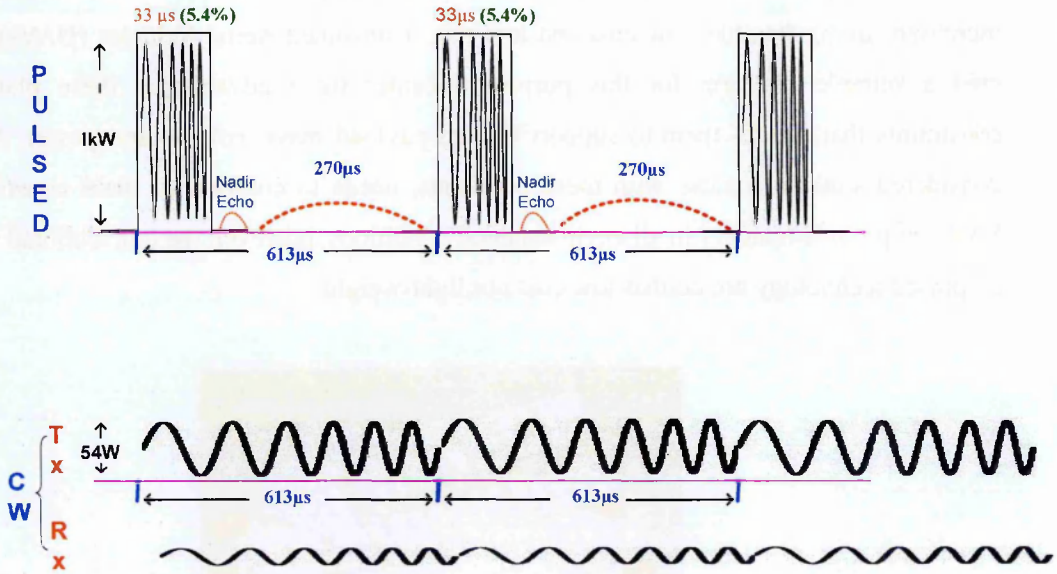

Figure 2 - 6: Comparison of Pulsed (Seasat SAR) and LFM CW SAR (Time vs. Power)

The Average RF Power 'P_{av}' over the entire cycle (pulse on time+ off time = PRI) may be related to the Peak RF Power 'P_t' by:

$$P_{av} = P_t \times f_r \times \tau' = \frac{P_t \times \tau'}{PRI} \text{ (W)} \quad \ldots\ldots\ldots\ldots \quad (2 - 1) \qquad \textbf{[40]}$$

where f_r is the PRF (Hz), τ'(s) is the chirp length, and PRI (s) is Pulse Repetition Interval (reciprocal of PRF). Thus by using this relationship, as an example, the Seasat SAR mission (timing diagram shown in Figure 2 - 6) that had P_t = 1 kW, $f_r = 1630$ Hz and $\tau' = 33\ \mu s$ (5.4 % duty cycle). [18], actually required average RF power of $P_{av} = 54$ W only.

Now if the pulse is fully extended (over entire PRI) keeping $P_{av} = 54$ W , an equivalent SNR may be achieved. Figure 2 - 6 shows the comparison for both pulsed and CW SAR cases. It shows that the average RF power in both the cases remains the same, but the instantaneous power levels vary significantly. Generation and handling of low instantaneous power levels in the case of CW is easier as compared with the very high instantaneous power levels (1 – 2 kW) typical of spaceborne pulsed SAR missions.

Similar to the pulsed SAR, CW SAR also uses a chirp signal where the carrier frequency is linearly increased according to the modulating (saw tooth waveform in this case) signal. While continuously transmitting, the frequency of the transmit signal increases and decreases repeatedly. The time interval it takes for the frequency oscillation to ramp up and down is considered the pulse repetition interval (PRI) and the number of up/down cycles per second is the PRF. [14]

For a CW SAR the transmission is continuous in nature, therefore a dedicated transmitter antenna is required. The radar returns are also continuous in nature, thus in order to receive the returns, a dedicated receiver antenna is necessarily required. Depending upon the antenna isolation requirements, the transmitter and the receiver antennas may be co-located—having a very short inter antenna distance, that virtually yields a mono-static configuration (from platform point of view). Consequently an airborne CW SAR design may be characterized as a two antenna solution from a single (mono-static) platform.

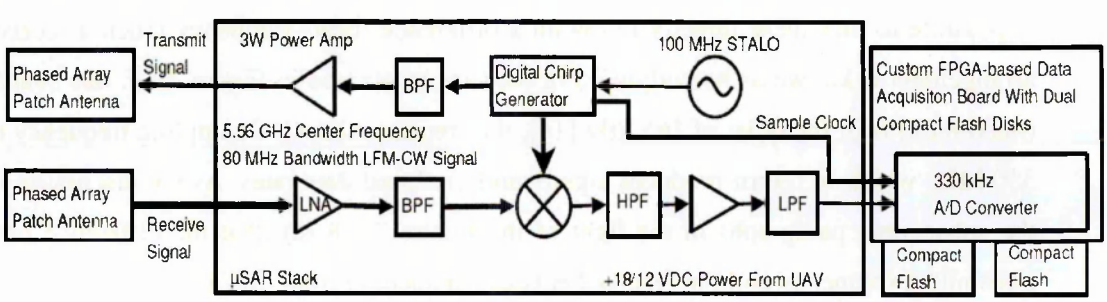

Figure 2 - 7: Simplified block diagram of a UAV based LFM CW SAR

Source: Adapted from [14]

Figure 2 - 7 shows the block diagram of an initially developed LFM CW SAR (for an airborne

platform) [14]. The upper portion of the block diagram represents the transmitter and the lower, the receiver. The right hand portion is a customized Field Programmable Gate Array (FPGA) based data acquisition board. In the transmitter portion, the digital chirp generator operates on two inputs. One is the carrier frequency (5.56 GHz) that is derived from a 100 MHz stable oscillator and the other is the saw-tooth waveform that repeats itself according to the set PRF. The saw-tooth waveform varies the carrier frequency from 5.56 GHz to 5.64 GHz (i.e., 80 MHz is the required bandwidth). During this process, additional frequencies (harmonics) are also produced. At the output of the Digital Chirp Generator, the Band Pass Filter (BPF) allows only the band of frequencies (5.56 – 5.64 GHz) to be passed to the RF PA, which are required for SAR operation. Since the sensor electronics generates the LFM CW signal at very low power levels, a 3 W SSPA is used to amplify this low power signal before transmission through a dedicated transmitter antenna. A copy of this transmitted signal (LFM CW) is also fed to the receiver for demodulation.

Note: This copy should be the same that is being transmitted (before amplification), whereas in this published block diagram, apparently the authors are showing it as the unfiltered copy from the digital chirp generator (thus having harmonic frequencies). In reality the signal is fed back to the receiver after passing through BPF.

The amplified signal is then transmitted through a micro strip patch antenna. The echo is then received by the receiver antenna; it is amplified by the Low Noise Amplifier (LNA) that is centred at the carrier frequency. The output of the LNA is filtered using a BPF. This output is then fed to the mixer that is also provided with the copy of the transmitted signal. This direct mixing of the two signals results into a difference/beat frequency that is then digitized by the Analogue to Digital Converter (ADC). Thus, range (i.e., time delay) is directly translated to frequency.

Figure 2 - 8 (a) shows the transmitted and the received signals. For airborne platforms the distance to the target is short, the received signal returns before the chirp period finishes, therefore it is possible to mix these directly to obtain a difference (beat) frequency (such a receiver design arrangement is known as homodyne). For the case mentioned in Figure 2 - 7, this beat frequency (maximum) is of the order of 165 kHz [14], thus requires the ADC sampling frequency to be only 330 kHz, which in return produces significantly reduced data rates. As the discussion follows in the subsequent paragraphs in the light of the Figure 2 - 8 (a), that the difference between the transmitted frequency and the received echoes (frequency) from the farthest distance (time delays translated into the frequency) would be 165 kHz.

Note: The pulsed SAR receivers usually employ baseband conversions (these receivers are also known as the heterodyne receiver design [41]). Through a stepwise down conversion, the original baseband bandwidth 'B' is recovered. This particular case needs a bandwidth of 80 MHz to achieve a slant range resolution of 1.87 m. The equivalent pulsed heterodyne receiver needs to

sample it at 160 MHz to satisfy the Nyquist criterion, thus producing very high data rates (pulsed: 160 MHz; CW: 330 kHz).

Despite using separate transmitter and receiver antennas, the LFM CW SAR designs encounter major problems from two types of interfering signals: the feed through and the nadir echo signal.

The feed through signal is the leakage signal that flows from the transmitter antenna to the receiver antenna. Since SAR is used from a mono-static aerial platform where both antennas are separated over a very short (few cm) distance, this results in a distinct feed through signal. This signal needs to be filtered out in the processing before digitizing the beat frequencies (that are representative of different targets).

Similar to feed through signal, the nadir returns are also strong and continuous in nature. The effect of nadir returns in the case of pulsed SAR is mitigated by adjusting the PRF but in the case of CW SAR, due to continuous nature of the transmission, nadir returns also appear continuously and thus need to be filtered out before digitizing the beat frequencies.

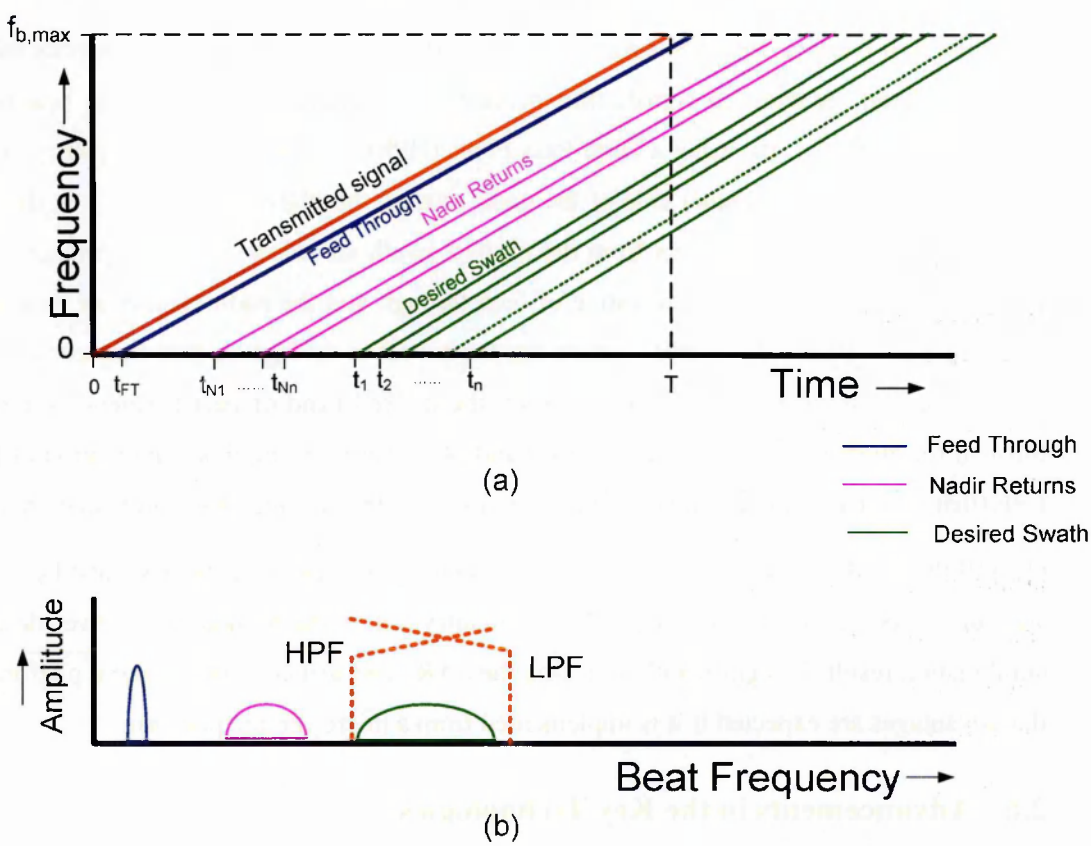

Figure 2 - 8: (a): Time vs. Frequency relationship of a chirp signal in LFM CW SAR. (b): Beat frequencies corresponding to feed through, nadir returns and radar returns

For the homodyne receiver design, the beat frequency f_b (Hz) may be calculated as:

$$f_b = \frac{2 \times R_S}{c} \times f_r \times B \quad \text{(Hz)} \quad \ldots\ldots \quad (2 - 2) \quad [42]$$

where R_S is the slant range to the target (m), c is the speed of light (m/s), f_r is the PRF (Hz) and B is the bandwidth (Hz).

Figure 2 - 8 (a) shows the time vs. frequency relationship amongst the transmitted signal (that spans from 0 to T seconds, where T is the PRI) and the feed through signal (received at t_{FT}), the nadir returns (represented by $t_{N1}, \ldots\ldots, t_{Nn}$) and the radar returns from the desired swath (represented by $t_1, \ldots\ldots, t_n$). The transmitted signal varies from the carrier frequency f_c to ($f_c + B$) Hz (according to the set bandwidth, B). By using Eq. 2 - 2, due to very short inter-antenna distance, the resultant feed through beat frequency would be very distinct among the band of beat frequencies, as shown towards the lower part of the beat frequency spectrum in Figure 2 - 8 (b). After this feed through beat frequency appears the beat frequencies for nadir returns, which are followed by the returns from desired swath. The time related term $2R_S/c$ in the Eq. 2 - 2 translates into corresponding beat frequencies in the spectrum. As shown in the Figure 2 - 7, after directly mixing the transmitted and the received signals (this process is also called de-chirping), the beat frequency spectrum is achieved. By using a High Pass Filter (HPF) that has a cut off frequency at the beat frequencies towards the higher side of the nadir returns, the higher frequencies i.e., the beat frequencies representing the targets from the desired swath are allowed to pass through and lower beat frequencies, that are representative of feed through and the nadir returns are stopped. Then by using a Low Pass Filter (LPF)—which has the cut off at the highest beat frequency that is representative of the farthest target in the swath, the desired band of beat frequencies are allowed through for digitization. As claimed by [43] and [44], that by using this combination of HPF and LPF (that is actually implemented a BPF), the effects of feed through and nadir echo are reduced.

Overall the LFM CW SAR design yields the advantages of operating the SAR and bus at low instantaneous power levels and with reduced circuitry due to the homodyne receiver design. This combination results in significantly reducing the SAR mass and cost for the aerial platforms. Similar advantages are expected if it is implemented from a microsatellite platform.

2.6 Advancements in the Key Technologies

In the preceding sections complete SAR systems were discussed with a view to identifying the contributions of different design aspects on the overall mission mass, volume and the cost. Here a brief discussion follows to focus on some individual sub-systems that are considered critical and potential cost, mass and power savers, for microsatellite SAR payload design.

2.6.1 RF PA

The choice of RF PA and the antenna is largely dependent on the frequency of the radar. Before discussing the antennas, let us focus on the PA first. While selecting the PA one has to look at the trade-off factors such as peak and average power, stability and low noise. The PA has to operate with high efficiency, wide bandwidth, high reliability, long life, minimum maintenance, and ideally comparable cost to that of the antenna, reasonable weight and size etc. [41]

During subsequent discussions, the term power efficiency will be used. It means Power Added Efficiency (PAE) that may be defined as a measure of how much DC power (P_{DC}) is converted to output RF power ($P_{RF\,out}$) keeping into consideration the input RF power ($P_{RF\,in}$).

$$PAE = 100 \times \frac{(P_{RFout} - P_{RFin})}{P_{DC}} = 100 \times \frac{(P_{RFout} - P_{RFin})}{V_{DC} \times I_{DC}} \quad \ldots\ldots \quad (2-3) \qquad [45]$$

A RF PA may be an electron beam amplifier (e.g. Klystron, TWT etc.) or transistor based (i.e., SSPA). Each of these technologies has its own pros and cons. Electron beam amplifiers are considered 50 – 65 % power efficient and can provide high power outputs in the ranges from a few hundred watts to a MW. These are designed for almost the entire RF spectrum with varying output performances [46]. Since Radar inception, these have dominated the radar transmitters because a single electron beam amplifier may be sufficient to provide the required amplification. The major concerning issues with these devices are:

- In order to operate the electron beam amplifier, it needs a very high potential difference between the cathode and anodes (e.g. 6 kV for the X-band TWT used with TecSAR [30]). For this purpose, a switch mode DC to DC power supply is used, which adds weight and complexity to the transmitter and also introduces additional power losses in the form of heat during this DC up conversion.
- Overall the mass and size of an electron beam amplifier is inversely related to the operating frequency. The higher frequency bands would get a light-weight and small sized tubes. As an example, X-band TWT used with TecSAR weighs 720 g [30] whereas S-band TWT weighs more than 5 kg [46]. The 150 W L-band TWT weighs ~ 6 kg, with dimensions of 634 x 66 x 77 mm^3 [47].
- The choice of the type of the tube amplifier is also driven by the bandwidth it can support. For example, a single Klystron tube provides much higher output powers but these are heavy (~ 25 – 35 kg), expensive, less efficient and support only narrow bandwidths. On the other hand, the TWT are more efficient and support wide bandwidths but as the power output increases, the supported bandwidth reduces. These are considered more suitable for large duty cycles and at low output powers. [41]

- The transmitter is a critical subsystem of the SAR design thus needs to be kept redundant to increase system reliability. If only one tube is used, then to keep one in reserve (cold redundant) means a complete tube assembly—thus adds additional weight and cost to the mission.

Electron beam amplifiers are best suited for transmitter designs where central amplification is required such as for the passive corporate fed patch antennas (e.g. as on Seasat SAR) or reflector antennas (e.g. TecSAR, MAPSAR etc.).

SSPAs offer many inherent advantages over the electron beam tube amplifiers. The factors which help in making a suitable choice are:

- These do not need any high voltage power supplies which are otherwise required with electron beam amplifiers.
- As was previously mentioned that at S-band, the TWT weighs ~ 5 kg but the equivalent SSPA weighs ~1.2 kg. In addition, the footprint volume is also very important. The same S-band SSPA's footprint is about 1/5 the volume of equivalent electron beam amplifier. [46]
- SSPA intrinsically supports wider bandwidths as compared with the electron beam amplifiers. For example, the electron beam amplifiers generally support bandwidths in the range of 10 – 20 % whereas SSPA support up to ~30 % bandwidths. [41]
- A single SSPA remains limited in providing the large output power as compared with a single tube amplifier. This limitation is offset by using a large number of low power individual SSPAs in distributed (in parallel) arrangement within the APAA. This arrangement provides space amplification that yields equivalent output power as achieved through a single electron beam amplifier. But this arrangement increases complexity and gives rise to high antenna weight and cost.
- Once used in parallel within the APAA, then inherent redundancy is also ensured. Failure of a few individual amplifiers is gracefully compensated by others.
- The SSPA have demonstrated good performance at low frequency bands such as L- and S-bands. But SSPA individual output power and the efficiency drops as the frequency increases. Thus applicability of SSPA is more appropriate at low frequency bands where suitable individual output power coupled with high efficiency may be utilized in different PA/antenna configurations.

The SSPA technology relies on semiconductor materials that are generally based on various compound semiconductors such as Gallium Arsenide (GaAs), Indium Phosphide (InP), Silicon Carbide (SiC), Gallium Nitride (GaN), or Silicon Germanium (SiGe). Each has its own advantages and disadvantages once compared on frequency vs. amplification matrix but GaN, SiC

and GaAs are referred to as wide band gap semiconductors that yield high output power levels at most of the low radar frequency bands. [41]

Different researchers have claimed achieving equivalent or better performance than the electron beam amplifiers. As claimed by [48] it has been possible to achieve 37 % efficiency for the 50 W, L-band for a space qualified SSPA by using GaAs. Whereas [46] claims that space systems of Mitsubishi have achieved space hardened 150 W outputs at S-band by using GaN with 53.8 % efficiency, which is comparable to those of the TWT. In addition, [49] claims to have achieved 63 % PAE at L-band with 75 W output power by using GaN technology. They also claim to have achieved 56 % PAE at L-band with 204 W. Their products are radar specific.

This discussion may be summarised on this note that although higher power amplifications may be achieved with other semiconductor compounds such as SiC or GaAs at low frequency bands with moderate efficiencies in the range of 30 – 40 % but higher efficiencies are becoming possible by using GaN. The on-going research in GaN is expanding the frontiers of the efficiency, power output and frequency. [50]

2.6.2 Spaceborne SAR Antennas

To address the range and azimuth ambiguities, the antenna has to conform to a minimum area limitation. This requires a large size antenna for a spaceborne SAR mission. On one hand, designing, developing and launching a large size antenna poses serious technological challenges but on the other hand, it yields a high antenna gain that is necessarily required to obtain adequate SNR with limited onboard power resources. Two types of SAR antennas are used for spaceborne SAR missions. These are the planar and reflector antennas.

The Planar Antennas

The planar antennas may further be classified as passive phase array antenna (PPAA) and APAA.

PPAA (also called passive corporate feed patch antennas or constrained type) use micro strip patches or slotted waveguide to transmit and receive RF power. In most of the cases, the RF power amplification is done centrally. After amplification, the RF power is transported to these patches through RF coaxial cables/wave guides. In order to maintain phase centre, phase shifters are used at the front ends. SEASAT, JERS – 1/LSAR used this type of antenna. The major advantage comes from the fact that design is based on a central RF power amplification that may be achieved from a single or combination of few electron beam amplifiers.

APAA is based on distributed RF power amplification. In this design a large number of SSPA based T/R modules are attached to the micro strip patches. This design provides inherent redundancy to the RF PA as these are used in large numbers, a failure of a few may be compensated by

others. ALOS-1/ PALSAR, COSMO-Skymed, ENVISAT/ASAR, ERS-1 & 2, RADARSAT-1 & 2 etc. have used this type of antenna. As the gain of individual SSPA increases, the number of T/R modules needed in the antenna correspondingly reduces e.g. only 18 T/R modules each with 100 W output, are being used with NovaSAR-S APAA antenna to produce a net output RF power of 1.8 kW. As the SSPA technology develops in future, giving rise to higher output powers from individual amplifiers, the number of these modules would be further reduced. Due to complex design involved in the development of these antennas, the mass of these antennas varies for each mission generally from 70 – 800 kg.

Reflector Antennas

Reflector antennas provide a suitable low cost and light-weight alternative to the planar antennas as was discussed while analysing TecSAR and MAPSAR missions [30], [16]. In addition, to accrue the similar benefits, reflector antennas are also becoming popular with communication satellites as well. For example, a 9 m diameter AstroMesh reflector antenna has been used with Inmarsat-4 satellites and now another 11 m diameter is being used with Alphasat I-XL communication satellite [51], [52].

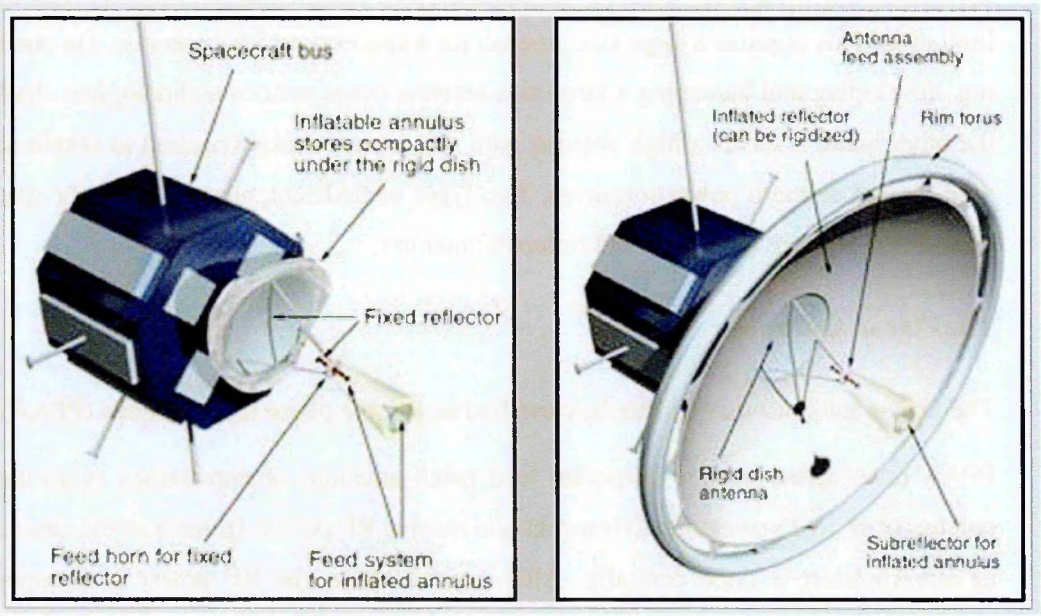

(a) (b)

Figure 2 - 9: Depicts the inflatable antenna system concept. (a) shows that inflatable annulus is stored completely under the feed system during launch phase (b) shows once inflated in the space

Source: Adapted from [53]

However, these antennas are based on the deployable techniques (similar to folding an umbrella).

Since early 1960's, the research has been directed to develop alternative technologies for launching large size antennas with compact stowage volume. National Aeronautics and Space Administration (NASA), under the Earth Science Technology Program, is currently developing a novel instrument concept with associated antenna technologies for a space-based 35 m diameter, Ka-band (35 GHz) radar for monitoring hurricanes, cyclones and severe storms from a geostationary orbit. [54]

This technique utilizes inflatable technology instead of deployable ones. This concept is shown in Figure 2 - 9. Part (a) shows that during the launch phase, the reflector surface remains un-inflated under a small and rigid dish. The feed horn may be kept fixed or may also be rolled back (like a telescopic arm) during launch phase. The compact stowage volume is almost same as that of the bus itself. After launch, the reflector is inflated and maintained using gases. Part (b) shows how the space segment looks like after the reflector is inflated.

Proof of concept experiments of this inflatable technology were conducted in space in 1996 by NASA. A 14 m diameter antenna was successfully deployed within 5 minutes by using Nitrogen gas. The demonstration proved to be very successful especially achieving very high surface accuracies in the order of 0.1 – 0.2 mm in the true thermal and microgravity environment. These demonstrated accuracies satisfy the requirements of all L – X bands. This antenna was developed at a cost of $ 1 M (in 1996). [55]

Inflatable technology would be instrumental in providing light-weight and compact stowage volumes for space missions with large antenna sizes.

2.7 Cost Analysis

For most spaceborne SAR missions, the cost effects are publicly not released due to confidential nature of these projects. Often, these missions are institutionally funded and considered a source of national power projection.

Envisat (space segment mass of 8140 kg, launched in 2002) is considered as an extreme case where many Earth observation and scientific sensors were put together on a large satellite and launched as a single mission. The overall cost of the mission was £ 2 Billions. This included the design, development, manufacturing, launch and 5 years operations. [56]

While considering the overall mission costs, the major portion of this goes to the launching system. For injecting small satellites (< 1000 kg) into the orbit, less powerful launchers are needed. If Russian launcher such as Naper is arranged, then the dedicated launch cost is ~ £ 12 – 16 M, and if European (Vega) or American (Falcon) launchers are considered then the price would be ~ £ 21 M. [8]

Within SAR payload, the antenna and the type of the PA have significant imprints on the mission mass and the cost. If an APAA is used, then ~ 60 % payload cost goes to design and development of this antenna and rest is shared among other electronic subsystems. Recently, UK government has funded £ 21 M for the payload and the platform development of NovaSAR-S [8]. Due to commercially confidential nature of the NovaSAR-S, the further breakdown of £ 21 M (between payload and the bus) is not known but previously released information about SSTL-300 bus price is ~ £ 9.5 M [57]. It may be inferred that ~ £ 11.5 M is allocated to payload development.

While considering the prices for the RF PA, the unit price of an off the shelf space qualified L-band 50 W TWT amplifier varies from £ 0.5 – 1 M [8]. On the other hand, the unitary prices of different T/R modules vary from £ 100 – 1000. [58] If the PA is separately used, the price will be further reduced. For radar specific (commercial off the shelf) SSPA of 150 – 200 W RF output at L-band, the exaggerated cost may be £ 5,000 – 10,000 per unit [8].

2.8 Conclusions and Research Potential

The examples of light-weight spaceborne SAR missions discussed in this chapter indicate a shift from heavy planar antennas to light-weight and low cost reflector antennas as demonstrated by TecSAR (3 m and 4.5 m) and MAPSAR (7.5 m x 5 m). These examples take the advantage of already designed and developed, time tested existing buses. This aspect contributes significantly in reducing the overall mission cost and development time.

CW SAR offers two major advantages: it operates at reduced RF instantaneous power levels hence are more power efficient, and simple system (especially receiver) design. A major disadvantage comes from achieving higher antenna isolations that necessitates using two antennas. Use of this technique with microsatellites has the potential of employing a single SSPA.

The PA and the antenna play significant roles in designing light-weight and cost effective SAR missions. The analysis of TecSAR and MAPSAR designs shows the use of deployable reflector antennas with TWTs. But these required mission dedicated launches due to large stowage volume. There is a research potential to explore the benefits of using a novel combination of *"reflector antenna with a single SSPA"*, such that the planned mission yields a compact stowage volume which is suitable for a shared launch.

3 USER REQUIREMENTS

By pursuing an application-driven development approach and focusing on a narrow range of applications, a low cost and light-weight mission may be designed. Since this research aims at complementing the existing optical DMC resources, applications mainly related to environmental hazards such as forestry and disaster monitoring are analysed with a view to deducing the relevant SAR parameters. The forestry applications include clear cut/deforestation monitoring and forest fire monitoring and mapping. The disaster monitoring applications encompass flood delineation and monitoring; oil spill detection; hurricanes; geological hazards such as earthquakes, landslides and volcanic disasters.

A detailed analysing of different facets of these applications and finding out the relevant spatial, radiometric and platform's attitude, orbit and control parameters, it reveals that these are closely related to the recently retired phase array L-band (PAL) ALOS SAR system. ALOS has been a source of providing continuous L-band imagery during its mission life from Jan 2006 up till May 2011. If the spatial, radiometric and platform parameters of the proposed design can be matched to those of the ALOS, it would then imply that the wide range of applications which were served with fine beam dual polarized ALOS can also be served by the proposed mission.

Nowadays, a widely accepted and practiced approach is to build the payload around the available satellite buses. This approach saves significant time and labour cost because the bus does not need to be engineered according to the payload rather the payload can be built around the capabilities/limitations these busses offer/impose. Keeping this in mind, the baseline capabilities of already designed, developed, time tested and space qualified SSTL buses are also included.

This chapter thus sets the application-specific sensor requirements, and also what the available platform resources/capabilities and their limitations are. Subsequent mission (payload and platform) design would emerge as a trade-off between them.

3.1 Radar Clutter Statistics

When a radar (air, ground, ship or shore based) is used to detect/track a target, the energy backscattered from the terrain clutters the fidelity of the desired signal. During World War II the term radar clutter was introduced to denote unwanted radar echoes from extended targets such as

rain, land, water etc., that interfered with the intended signals (echoes from the actual targets). In this context the radar terrain clutter encompassed all aspects of scattering from terrain surfaces. The advent of imaging radar in early 1950s changed the outlook of the clutter from an interfering (problematic) source to an information source. It was mainly due to the fact that imaging radar acquires the information that is derived from the knowledge of how the electromagnetic waves scatter from rough surfaces and inhomogeneous media. This information takes into account theoretical models for electromagnetic interactions with surfaces and volumes, experimental measurements of the backscattering cross section per unit area 'σ^0' for various types of the terrain, and the statistics associated with the scattering process. Because of this wider scope of the intended applications of the radar scattering, in today's literature the generic term "Radar Scattering from Distributed Targets", has become a norm (instead of terrain clutter) to refer to the topics previously classified as radar clutter. [59]

Historically radars have predominantly been used in the military domain, thus many terms and concepts associated with it have strong association with its military inheritance. From the detection and tracking applications, terrain scattering is viewed in statistical terms because the objective is to determine the degradation in the false alarm probability that may result from terrain background. Consequently the term radar clutter has evolved into the more specific term "Radar Clutter Statistics" denoted by Probability Density Functions (PDF) characterising σ^0. [59]

σ^0 of the terrain varies as a function of two sets of parameters: [1] , [59]

- The sensor parameters that include the wavelength, the polarization configurations and the viewing geometry.
- The terrain parameters that include its dielectric properties, surface roughness and geometrical characteristics.

In this backdrop, it may be said that in general, the PDF is both sensor and terrain type specific. In some cases, more precisely, it may be termed as terrain condition specific e.g. a forest exhibit changes in both its dielectric properties and geometry as a function of time; the backscattering properties vary significantly from a calm or rough sea. [59]

A distributed target usually consists of several randomly distributed scatterers. On illumination by a coherent electromagnetic signal, the magnitude of the scattered signal is equal to the phasor sum of the returns from all the scatterers illuminated by the incident beam. The backscattered signal is a random variable because the dielectric and geometric properties of the terrain surfaces are also random variables. [59]

3.2 SAR Applications

During early development stages (1950s) of SAR, the technology remained mainly restricted for military applications. In the subsequent years (1960 – 70s) the access to this technology was made open for civilian use as well. As the sensor technology developed, in return, it enhanced the capabilities of the SAR. These have diversified the scope of practical applications of SAR. Salient applications relevant to this research are discussed in the following sections. [1], [60], [61], [62]

3.3 Land Cover and Land Use Applications

Land cover refers to the surface cover on the ground, whether vegetation, urban infrastructure, water, bare soil or others. It involves identifying, delineating and mapping the land cover. Land cover information is important for global monitoring studies, resource management and planning activities. Identification of land cover establishes the baseline from which monitoring activities (change detection) can be performed, and provides the ground cover information for baseline thematic maps. [1]

Land use refers to the purpose the land serves, for example, recreation, wildlife habitat, forests, agriculture, urban etc. It involves both baseline mapping and subsequent monitoring. Timely information is required to know what current quantity of land is in what type of use and to identify the land use changes with respect to time. [1]

The difference between land cover and land use is instrumental in exploiting the information obtained during data acquisition process. The properties measured with remote sensing techniques relate to land cover from which land use can be inferred, particularly with ancillary data or *a priori* knowledge. [1]

SAR plays important role in diversified land specific applications such as: [1], [60], [62], [63], [64]

- Agriculture classification and management
- Aquaculture mapping
- Digital Elevation Model (DEM) and mapping
- Disaster monitoring (forest fires, floods, earthquakes and volcanic eruptions etc.)
- Forest mapping
- Monitoring of land subsidence
- Rice mapping
- Snow and ice mapping

- Hydrology and water resource management
- Land use monitoring and land cover classification
- Geological surveying and mineral resource exploration
- Terrestrial ecosystem and forestry management
- Surveying of archaeological sites
- and many other new areas of research being explored.

The list of SAR land applications is long and ever expanding. To remain focused in this research, forestry and disaster monitoring are analysed in detail in the subsequent sections.

3.3.1 Forestry

Figure 3 - 1 represents the distribution of the world's forests according to the areas (tropical, temperate) and type of wood (hard, soft and mixed wood). According to the statistics released by the Food and Agriculture Organization (FAO) of United Nations (UN) Global Forest Resources Assessment 2000, forests cover almost one-third of the world's land area or 3869 million hectares, of which 95 % is natural forest and 5 % is planted forest. Forests are distributed unevenly across the globe with 17 % in Africa, 14 % in Asia, 27 % in Europe, 14 % in North and Central America, 23 % in South America and 5% in Oceania. [65]

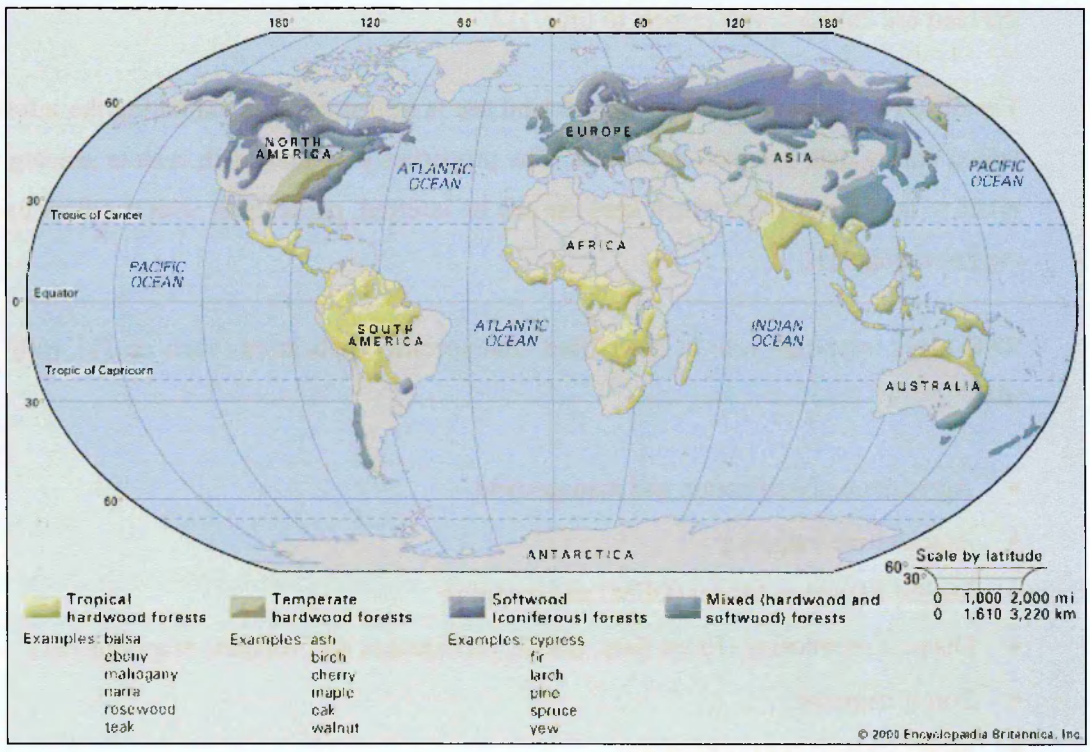

Figure 3 - 1: Distribution of the world's forests

Source: Adapted from [66]

Looking at the world's forests distribution, two distinct regions may be identified: tropical and boreal. Both these regions have characteristic environmental conditions that strongly support the use of SAR. The ability of the SAR to provide high resolution imagery independent of weather or sunlight is particularly important for regions of the planet that present restrictions to the use of optical sensors due to the presence of rain, perennial clouds, haze etc. (e.g. tropical regions such as Amazon) or where solar illumination is insufficient (boreal regions). Besides this, SAR also has the ability to penetrate the vegetation canopy, which is not possible using optical sensors. Thus the data acquired by SAR serves to map and monitor the use of the land, forestry and agriculture particularly in these regions. [11], [60], [65]

Forests are a valuable resource providing wildlife habitat, food, shelter, and daily supplies such as medicinal ingredients and paper. Forests play an important role in balancing the Earth's CO_2 supply and exchange, acting as a key link between the atmosphere, geo-sphere, and hydrosphere.

Major issues concerning forest management are depletion due to natural causes (fires and infestations) or human activity (clear-cutting, burning, land conversion) and monitoring of health and growth for effective commercial exploitation and conservation. [1]

The forest related applications may be sub-categorized as: [10]

- Forest resource assessment applications which include the inversion of dendrometric or structural parameters at the stand level such as biomass, forest species, and stand structural organization.
- Forest resource monitoring that includes the routine mapping of deforestation, clear-cuts, fire (scars) and flooding.

3.3.1.1 Forest Resource Assessment

Forests play important role in maintaining the global carbon balance. Carbon cycle as it relates to CO_2 (Carbon dioxide) which is a greenhouse gas, is fundamental to the study of the Earth's climate. The deforestation and afforestation are believed to have the highest effect on the net flux of greenhouse gases. Carbon is stored in the form of biomass in forests. This biomass is interdependent with factors such as nutrient fluxes, water availability, forest age, and temperature. Critical piece of information gathered by monitoring the changes in biomass helps in better understanding the global carbon cycle. [64]

Among remote sensing instruments, SAR has shown to have unique capabilities to respond to biomass over a usable range and give reliable temporal information [64]. In order to quantify the biomass, the sensor requires, in most cases, measurements from the complete structure of the forest canopy or tree depending upon the spatial resolution of the sensor [10]. The shorter wavelengths (such as C- or X-band etc.) do not penetrate deep through the canopy, thus for this

type of measurements, low frequencies such as L- or P- bands are preferred [64], [10]. If it is desired to discriminate the forest type and estimate the biomass, a single polarization offers little potential [10].

Previous research and experiments conducted by polarimetric L-band spaceborne imaging radar (SIR-C) mission has demonstrated the potential of monitoring patterns of forest re-growth following disturbance in many different forest ecosystems. However, the use of SAR for biomass mapping is often complicated by factors that include the non-homogeneity of forest stands and relief induced backscatter variations [10]. For high biomass heterogeneous forest with trees of different types, height and structure, classification based on polarimetric SAR data alone does not provide sufficient sensitivity for the separation of representative forest classes. To extend the classification observation space is to introduce interferometric observations. However, the sensitivity of the interferometric coherence to the spatial variability of vegetation height and density makes the classification of forest structural parameters a challenge. Even small variations of the vegetation layer characteristics (height and density) and variation of the underlying ground scattering mechanism (on the order of few percent) affect the position of the effective scattering centre and are reflected with different coherence values. [67]

More recent research based on utilizing polarimetric-interferometric SAR (Pol-InSAR) has shown that reliable forest classification may be attainable that eventually helps forest monitoring and forest management. Jointly with forest height estimation, forest classification improves biomass estimation and forest mapping. [67]

One such study by using Pol-InSAR was demonstrated using DLR airborne E-SAR L-band Pol-InSAR datasets acquired in 2003 in a fully polarimetric repeat pass interferometric mode with a small spatial baseline (5 m), spatial resolution of less than 3 m and a temporal baseline (10 minutes) over the Traunstein test site. The forest classification results were validated against the available ground measurements. The Traunstein test site is located in SE-Germany and is a managed high biomass forest test site (biomass up to 450 t/ha) on relatively flat terrain. The site is composed of various agricultural areas, forests, and some urban zones. [67]

This research focuses on the forest resource monitoring (clear cuts/deforestation and forest fire monitoring/mapping). Against this backdrop, the proposed SAR design should primarily cater for the spatial and radiometric specifications relating to the resource monitoring. If it could also partially serve the resource assessment specifications, it would be an added advantage.

3.3.1.2 Forest Resource Monitoring

3.3.1.2.1 Clear Cuts and Deforestation

Wood extraction from forests is an ever increasing demand. Depletion of forest resources has long

term implications for climate, soil conservation, biodiversity and hydrological regimes, and is therefore a vital concern of environmental monitoring activities. Commercial forestry is an important industry throughout the world. Forests are cropped and re-harvested, and the search for potential new areas continues. In order to conserve native and virgin forest areas, and curb the unsustainable forestry practices in the remaining areas of potential cutting, the companies involved in extracting wood need to be more efficient, economical, and aware of sustainable forestry practices. In the areas where forest are extracted, a healthy regeneration of trees ensures: good future prospects for the commercial forestry firms, adequate wood supplies to meet the demands of a growing population, and most importantly it is essentially required for the conservation of forests. [1], [68]

Non-commercial sources of forest depletion include removal for agricultural (pastures and crops), urban development, droughts, desert encroachment, loss of ground water, insect damage, fire and other natural phenomena (disease, typhoons). In some parts of the world, predominantly in the tropics, forests are covering prime agricultural land. Forests are burned or clear cut to facilitate access to, and use of, the land. This short term undesired practice has associated long term concerns for species-rich forests, local and regional hydrological system, polluting the atmosphere etc. Thus, the rate and extent of clear cut and deforestation, as well as monitoring regeneration, are key parameters to be measured by the remote sensing instruments. [1]

To this effect, optical (VIR) sensors produce satisfactory results but persistent local environmental conditions (such as clouds or low light conditions) restrict their use from the satellite altitudes. SAR plays its complementary role in this scenario especially if global coverage is envisaged. Comparative studies conducted indicate that longer wavelengths result in a higher contrast between forest and non-forest such as clear cuts. [68]

One of these studies was conducted for mapping of the clear cuts in Swedish forest using satellite images acquired by the radar sensor ALOS PALSAR. ALOS operated at L-band (24 cm). It had combinations of different imaging and polarimetric modes (total 72 combinations). The selected combinations were Fine Beam Single (FBS) polarization (could operate either HH or VV with a bandwidth of 28 MHz in a look angle range of 9.9 – 50.8^0), Fine Beam Dual (FBD) polarization (HH/HV or VV/VH (HH/VV not supported) with 14 MHz bandwidth). Within these combinations, the FBS (HH) and FBD (HH/HV) were selected with a look angle of 34.3^0, 70 km of the swath could be achieved in these modes with a ground range resolution of 20 x 20 m respectively. Multi temporal results show that a 3 dB difference in the backscatter value between forest and non-forest were consistently observed. [68]

In addition, similar experiments were reported for tropical and temperate forests. The results also indicated a 1.5 to 3 dB difference in the backscatter for the forest and clear cut existed. [68]

Similar experiments for L-band cross polarized data show a large backscattering difference between clear-felled and mature forest because of much weaker surface scattering component. For a test site in Brazil, HH and HV backscatter difference of 8 dB was observed between forest and clear-cut. [68]

These experiments demonstrated that to discriminate between forest and clear-cut, a single polarization may not be beneficial—rather, a combination of co- and cross-polarized channels provide the dynamic range, which is instrumental in polarimetric image processing.

Note: while mentioning the polarization directions such as HV, the first letter refers to the incident and the second to the scattered radiations, respectively. Also, the extensive field experiments conducted for measuring the backscattering properties of the distributed targets have shown the scattering process in the backscattering direction is reciprocal in character, which leads to the equality: $\sigma_{HV} = \sigma_{VH}$ [59]

3.3.1.2.2 Forest Fire Monitoring and Mapping

Fire is part of the natural reproductive cycle of many forests. It revitalizes growth by opening seeds and releasing nutrients from the soil. However, some times it may endanger the settlements and human lives, thus needs to be controlled. [1]

Forest fire may be distinguished into two stages as:

- Fire detection/monitoring: during burning, it is treated as disaster monitoring.
- Post fire assessment: at subsequent stages it is the stage that deals with the damage assessment, the forest monitoring and assessment with a view to analyse how well the forest is recovering. It is known as burn mapping.

During fire monitoring, the sensors are required to survey the wider swaths to detect fire especially in remote and inaccessible areas, alert the relevant agencies and facilitate the fire fighting etc. To achieve this requirement, wider swaths and quick turnaround (within a day or so) response is envisaged. To this effect, passive sensor data from NOAA (National Oceanic and Atmospheric Administration) satellites which mainly utilize the AVHRR (Advanced Very High Resolution Radiometer) is considered sufficient. These sensors provide an effective spatial resolution of 4 km with a swath of 2600 km while operating from 830 to 870 km altitude. These provide once to twice a day revisits depending upon the latitude of the imaging area. [69] In order to reduce the revisit time and to establish an early fire alert system, ESA driven FUEGO project was launched. This constellation of 12 polar satellites in three orbital planes, work jointly and provide approximately a 15-minute temporal resolution. [70]

SAR plays its role in the post fire assessment stage because it provides high spatial resolution da-

ta as compared to the passive sensors (radiometers) mentioned above which have very poor spatial resolution. For post fire assessment, a narrow swath (50 – 100 km), high resolution (10 – 25 m), moderate turnaround (few months to a year) and multi-polarimetric sensor is envisaged. [1], [62]

3.3.1.3 Forestry Related ALOS Images

The previous discussion relating to different forestry applications can best be explained with the help of L-band ALOS images. Figure 3 - 2 presents HH, HV and VV polarimetric images and RGB colour composite images of Tomakomai, Japan, acquired by PALSAR using H/V polarization on August 19, 2006. This area consists of cultivated land (upper area), forest areas (middle area) and the Pacific Ocean (lower area). Although it is difficult to recognize the difference among HH, HV, and VV from the three single polarimetric images on the left, the RGB colour composite image represents the scattering properties of each area as colour differences. [71]

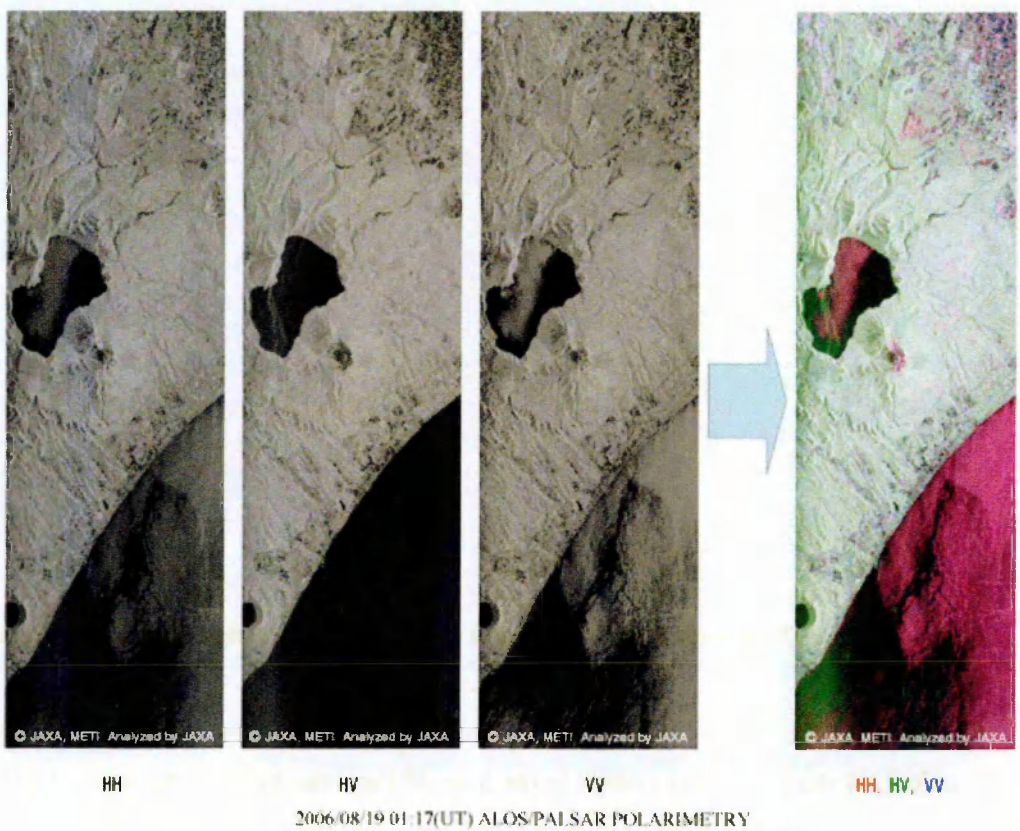

Figure 3 - 2: ALOS polarimetric (HH, HV,VV and HH+HV+VV)

Source: Adapted from [71]

Figure 3 - 3 depicts the cultivated area, residential area, and forest area extracted from the RGB

colour composite images in Figure 3 - 2. The green region, where the cross-polarized component occurs, shifts with the change of polarization. Cross-polarized component generation is related to volume scattering from H/V polarized signals whereas double-bounce scattering and surface scattering from linearly polarized signals. This information is used for terrain and land-use classification. [71]

Figure 3 - 3: Zoomed in/ classification of the Polarimetric data presented in Figure 3 - 2

Source: Adapted from [71]

Figure 3 - 4 shows forestry change in the State of Para, the Amazon, between 1993 and 2010. Deforestation (blackened areas in images) was not very common in the 1990s, but was much more frequent after 2006, as can be seen in the images. The images of the 1990s were taken by the radar JERS-1. By comparing acquired images in time order, one can understand the progress of deforestation and forest deterioration on a global scale. [71]

The Figure 3 - 5 shows the false colour composite where the co-polarisation (HH) band is displayed in the red channel, the cross-polarisation band (HV) in the green and the (HH-HV)

difference in the blue channel. With the HH band sensitive to direct and specular backscatter and the HV band to volume scattering, the forest appears green, clear cut areas dark purple, open water black, and flooded vegetation light violet in this image. [71] From this example, it can also be ascertained that polarization diversity (HH and HV) helps in distinguishing the clear cuts from rest of the forest.

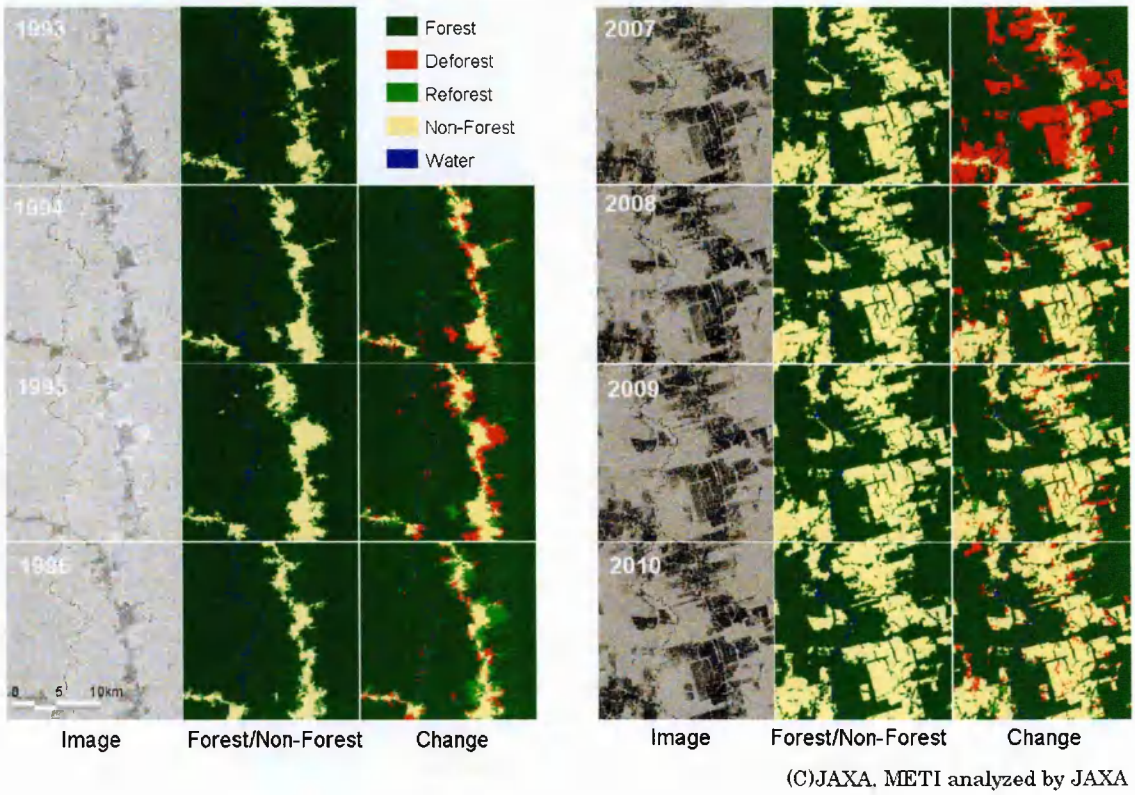

Figure 3 - 4: Forestry change over time in the State of Para, Amazon between 1993 and 2010. From the image, Forest/Non-forest, forest change. Red indicates forest reduction and light green shows forest recovery. The location is at a south latitude around 8 degrees and west longitude around 55 degrees.

Source: Adapted from [71]

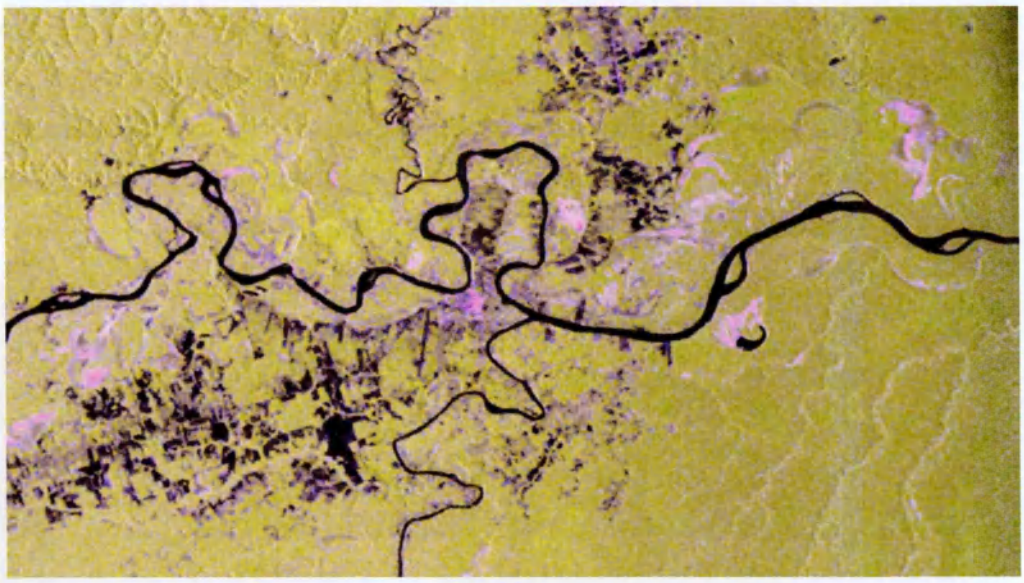

Figure 3 - 5: ALOS PALSAR dual-polarization image (Western Amazon, 21 August 2006)

Source: Adapted from [71]

Forgoing in view, it can be ascertained that different polarizations can be combined to provide additional information about the imaging area. However different polarisations have different detection capability depending on the area observed. For instance, the cross-polarized HV or VH data are better for detecting clear cuts, tropical forest, and temperate forest as well as post flood inventory in the forested areas. For inundation and extended flood, HH is better. [72], [73]

3.3.1.4 Summary of Forestry Related Applications

This research is focused on environmental hazards such as forestry and disaster monitoring. The forestry applications include clear cut/deforestation monitoring and forest fire monitoring and mapping. Since these are also linked to forest resource assessment, thus the aspects of periodic growth of the forest (not to be mixed with the detailed tree classification based on tree types, tree height, age etc.) should also be taken care off. As can be seen in the ALOS images discussed in Figures 3 – 2 through 3 – 5 that if the proposed SAR sensor is designed that matches the spatial and radiometric capabilities of the ALOS, then that sensor should be able to serve these applications as well.

Against this backdrop, the ALOS sensor parameters, spatial and radiometric specifications are mentioned in Table 3 – 1 [74]. From the radiometric performance point of view, the 2 kW of RF peak power yields high sensitivity (i.e., what value of σ^0 can be detected) in comparison with that of JERS-1, which exhibited limited sensitivity to low backscatter targets (NESZ: noise equivalent sigma zero ~ – 18 dB). The JERS-1 SAR had to be operated with a reduced (25%) transmission power (325 W), during its entire mission following problems with antenna deployment.

ALOS - Sensor/Platform Parameters	
Frequency	1270 MHz / 23.6 cm
Bandwidth	28 MHz (single polarisation) 14 MHz (dual, quad-pol., ScanSAR)
Transmission power	2 kW (peak power)
Image modes and Polarizations	Single polarization (HH or VV) Dual pol. (HH+HV or VV+VH) Quad-pol. (HH+HV+VH+VV) ScanSAR (HH or VV)
Incidence Angle	Strip map: 9.9 – 50.8 deg. ScanSAR: 20.1-36.5 (inc. 18.0-43.3)
Ground resolution Rg (1 look) x Az (2 looks)	~ 9 m x 10 m (single pol.@41.5°) ~ 19 m x 10 m (dual pol.@41.5°) ~ 30 x 10 m (quad-pol.@21.5°) ~ 71-157m (4 look) x 100m (2 look) - (ScanSAR 5-beam)
Swath	Swath width 70 km (single/dual pol.@41.5°) 30 km (quad-pol.@21.5°) 350 km (ScanSAR 5-beam)
Data rates	240 Mbps (single/dual/quad-pol) 120 or 240 Mbps (ScanSAR)
Orbit Inclination	98.16 deg. Sun Synchronous (SS)
Revisit	46 days
Platform's Attitude, Orbit and Control System	
Attitude determination/ knowledge	$\pm 0.0003^0$ (3 SD) all 3 axis
Attitude Control	R, P, Y: ± 0.095°(3 SD)
Position Knowledge	± 1m
Pointing Control	30 arcsec (3 SD)
Pointing stability (Jitter)	1 arcsec/sec (3 SD)
Radiometric Specifications	
Noise Equivalent Sigma Zero (NESZ)	-24 ~ -27 dB (single pol.@41.5°) -27 ~ -30 dB (dual pol.@41.5°) -30 ~ -31 dB (quad-pol.@21.5°) -23 ~ -32 dB (ScanSAR 5-beam)
Ambiguities – Range	9 - 26 dB (single/dual pol. @41.5°) 39 - 46 dB (quad-pol.@21.5°; co-pol) 20 - 27 dB (quad-pol.@21.5°; X-pol) 24 - 60 dB (ScanSAR 5-beam)
Ambiguities – Azimuth	21 dB (single/dual pol.@41.5°) 21 dB (quad-pol.@21.5°) 19 - 32 dB (ScanSAR 5-beam)
Radiometric accuracy	< 1 dB relative (within scene)

Table 3 - 1: Comparison of ALOS and proposed ECMP SAR Spatial, Radiometric and Platform Specifications

Source: Adapted [74] and [121] for ALOS

While discussing the radiometric performance, it is necessary to highlight that civilian SAR systems concentrate on achieving high radiometric accuracy (not the fine spatial resolution) necessarily required for investigation of natural targets, whereas the military systems focus on detection and recognition of manmade targets (such as vehicles) which require fine spatial resolution instead of high radiometric accuracy. [75]

3.4 Disaster Monitoring

3.4.1 Flood Delineation and Mapping

Flooding is a major hydrological hazard that occurs quite frequently. During 1990 – 99, floods affected approximately 1.5 billion people – more than 75 % of the total number of people reported as affected by natural disasters world-wide. [62] However, flooding is sometimes necessary to replenish soil fertility by periodically adding nutrients and fine grained sediments [1]. In order to measure and monitor the aerial extent of the flooded areas, to efficiently target rescue efforts and to provide quantifiable estimates of the amount of land and infrastructure affected, remote sensing techniques are necessarily employed. Floods are a short lived phenomenon and mostly occur during inclement weather. For efficient crisis management, the flood information requires almost a "near real time turnaround". [1]

As spaceborne optical sensors cover wider swaths (such as DMC optical sensors having a moderate resolution of about 30 m cover a swath of ~ 600 km – thus providing an opportunity to daily cover the entire globe with few satellites operating in the constellation), these may be considered the first choice. But over a period of time, it has been observed that flooded areas mostly remain under cloud cover (e.g. the dominant source of flooding in India, Pakistan, Bangladesh, Thailand etc. is the Monsoon season which is characterized by almost continuous cloud cover during this season). This prevailing environmental condition affects the performance of optical sensors. Likewise, if a flooded area is highly vegetated or thickly forested, then the performance of optical sensors is furthered hindered. SAR has the potential to offset the effects of such environmental conditions. In addition, by carefully selecting the operating frequency, the soil conditions under forests and cropped/vegetated areas may also be ascertained, thus facilitates assessing the extent of damage caused by the floods.

The land/water interface is easily discriminated with SAR data, thus allowing the flood extent to be delineated and mapped. SAR data are most useful when integrated with a pre-flood image [1].

The difference in roughness of the land (diffuse scattering), water (specular scattering – which appears dark in the image) and flooded vegetation and build up areas (double bounce) is quite evident on radar imagery which allows easy interpretation of the flooding extent. [10]

Extensive research has been conducted by using different airborne and spaceborne SAR platforms to determine the best configurations for flood mapping. It has been established that HH polarization and large incidence angles (> 45^0) provide the optimal configuration. [10]

Detecting flooding underneath a substantial vegetation or forest cover remains mainly the function of operating frequency as longer wavelengths (L-or P-band) have the potential to penetrate deep through the canopy and tree trunks and get reflected from underneath the surface. For flooded forests, it was shown that differences in backscatter returns between flooded and non-flooded areas are greatest at HH and lowest at HV or VV. [10]

The key requirement for this application is "near-real time turnaround" as the information is needed during (or immediately after) an incident has happened. But this requirement can be relaxed in hydrologic modelling, calibration/validation studies, damage assessment and the planning of flood mitigation. [1]

After the serious rain falls in Pakistan by the end of July 2010, the ALOS observed the Indus River basin and the related flooded region to detect the temporal changes. In order to effectively detect the flooded extents under the possible rainy and cloudy conditions, PALSAR-ScanSAR, which serves 100 m resolution and 350 km imaging swath with quick revisit time, was used to provide the required imagery. The same image is used here – as an example to highlight the benefits a SAR can provide in this situation. [71]

Figure 3 - 6 shows the colour composite of the ScanSAR mosaic data which are acquired between Aug. 5, 2010 and Aug. 29, 2010 in six times and mosaicked to 1500 km geographical scale in east-west and north-south directions as after the rain fall event and another six-ScanSAR-data mosaic acquired between June 27, 2010 and July 19, 2010 as the before the event. Colour assignments are red for before the event and green/blue for after the event so that the red colour represents the flooded flat region with no- or less radar backscatter and blue colour represents the increase of the radar backscatter due to the rain events. The ScanSAR data are terrain-corrected using the USGS 90 meter topography data and slope corrected for eliminating the radar backscatter modulation due to the terrain height variation. Indus river basin was widely inundated by these recorded heavy rain events. [71]

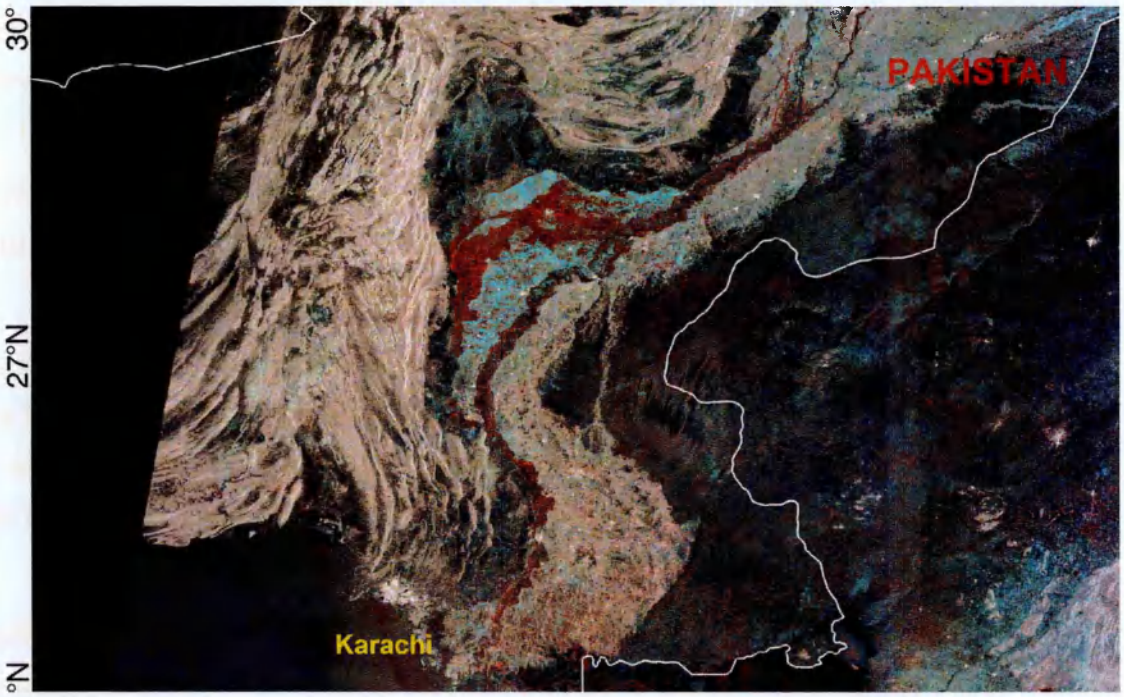

Figure 3 - 6: Colour composite of the PALSAR ScanSAR mosaic: Red for before the disaster, Green and Blue for after the disaster.

Source: Adapted from [71]

These images helped the Pakistan' Disaster Management Authority to provid the early warnings to the residents in the effected areas. It was also instrumental to the aid agencies to direct the post disaster relief efforts. Due to persistent cloud cover in the effected areas, the optical imagery could not furnish the necessary information during this worst hit disaster.

In the light of these discussions it may be ascertained that for the flood delineation and mapping, the sensor should have 100 m resolution, wide swath of 350 – 500 km, quick revisit time and HH polarization.

3.4.2 Oil Spill Detection

Oil spills can destroy marine life as well as damage habitat for animals and humans. Minor but frequently occurring marine oil spills result from ships emptying bilge tanks before or after entering port. Major oil spills result from oil tanker accidents [1]. These oil spills have severe environmental effects and are thus media eye catchers. Recent oil spillages from a deep sea oil well situated in the Gulf of Mexico is one of the biggest oil spills in the world that has left long term environmental hazards.

Following a spill, the shipping operator or the oil company involved is responsible for setting up emergency evaluation and response teams, and carryout the containment and cleanup efforts.

During this process, there are number of factors that need to be considered, such as: spill location, size and extent of the spill; direction and magnitude of the oil movement; and, wind, current and wave information for predicting future oil movements. [1], [10]

The remote sensing information regarding oil spills is required by coast guards, national environmental protection agencies and departments, oil companies, shipping industry, insurance industry, fishing industry, national departments of fishing and oceans and departments of defence etc. [1], [10]

The key operational requirements are fast turnaround time and frequent imaging of the site to monitor the dynamics of the spill. For spill identification, high resolution sensors are generally required although wide area coverage is very important for initial monitoring and detection. Airborne sensors offer advantages of frequent revisits but these are expensive to operate and provide limited swaths when compared with spaceborne sensors. A combination of VIR (laser fluorosensors) and SAR sensors are used for detection and subsequent operations to offset the effects of ocean oil spills. SAR sensors have an advantage over sensors as these provide data under poor weather conditions. [1]

The detection of oil spills by radar systems is based on the dampening effect oil has on the capillary surface waves. At incidence angles ($20 - 55^0$) these waves govern the backscattering of radar waves of comparable wavelengths (Bragg scattering mechanism). Hence, wave dampening in the presence of oil results in a localised reduction of the measured radar backscatter. In SAR images, the darker oil covered areas are often clearly visible among the rougher, and hence brighter, oil free water surfaces. [10]

The detection of an oil spill in the SAR image is strongly dependent upon the wind speed. Winds ranging from 3 – 10 m/s may be considered optimal since these generate a good oil-water backscatter contrast. At lower wind speeds, the return signal of oil-free water will approach that of oil-covered water while at higher wind speeds the backscattering of both oil-covered and oil-free water will be governed by large scale wind induced waves. At wind speeds greater than 10 m/s the slick will be broken up and dispersed, making it difficult to detect. Oil, which floats on the top of the water, suppresses the ocean's capillary waves, creating a surface smoother than the surrounding water. This smoother surface appears dark in the SAR image. [1], [10]

Eventually, to detect oil spills in radar images is a function of the observed backscattering contrast. Research has proved that oil-water backscatter contrast decreases with an increase in radar wavelength. But there is varied opinion among the researchers about finding the detection potentials of different polarizations. Results show a slightly higher contrast achieved from VV polarized images than either HH or HV polarized images. [10]

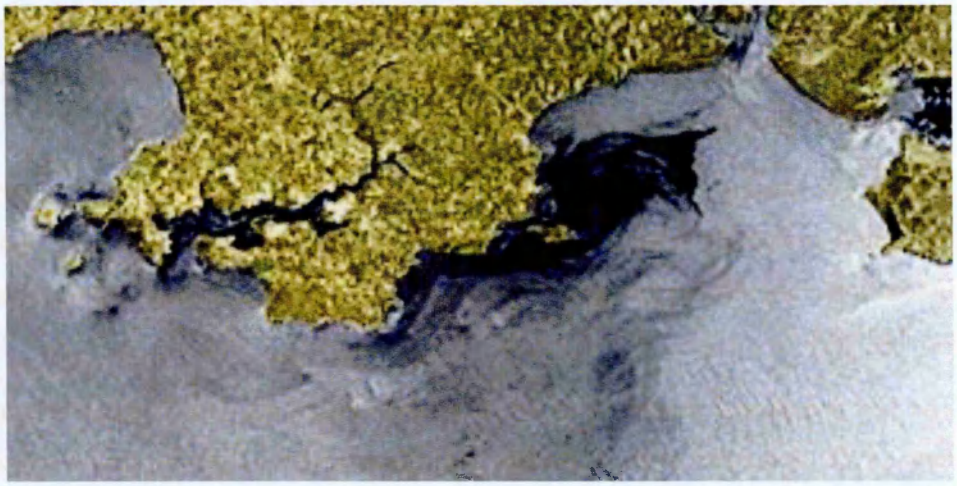

Figure 3 - 7: RADARSAT-1 Image of Super tanker, The Sea Empress accident on 15th Feb 1996

Source: Adapted from [1]

On 15th February, 1996, near the town of Milford Haven, Wales, a super-tanker, the Sea Empress, hit the rocks and the outer hull was breached and approximately 70,000 tonnes of light grade crude oil was dispersed southward under stormy conditions. After a week, RADARSAT-1 took the image of the area which is shown in Figure 3 - 7. This image was acquired with a view to detect the extent of the oil spill. The darker areas off the coast, are the ones where the oil is floating on the surface. This floating oil suppresses the ocean's capillary wave, thus creating a surface smoother than the surrounding water. This smoother surface appears dark in the radar image, thus providing the opportunity to effectively discriminate the oil from the water.

3.4.3 Hurricanes

Hurricanes are tropical cyclones which have winds that reach sustained speeds of 64 knots (33 m/s) or more. Hurricane winds blow in a spiral pattern around a relatively calm "eye". The "eye" may be 30 to 50 km in diameter and the storm may extend outward from the "eye" for more than 500 km. As hurricanes move towards land, their trajectories can be difficult to predict and they can bring torrential rains, high winds and storm surges. A Hurricane's development is a short lived phenomenon (few days) but its effects may be devastating and can last several weeks. [10]

It would be pertinent to make a distinction between routine surveillance (to spot the development of the "eye") versus tracking (the approximate location of the "eye" has been detected and now it is matter of following the direction of its movement). For surveillance applications, wide area coverage through the scanSAR mode (with a worsened spatial resolution) is envisaged. For tracking applications a narrow swath with a fine spatial resolution is required. Thus it involves a trade-off between wide area coverage (scanSAR) and high spatial resolution. [10]

SAR images of the ocean surface often show the imprint of atmospheric phenomena that modu-

lates the ocean surface roughness (such as surface winds). These SAR images may be used to estimate the corresponding wind fields. Rougher areas corresponding to higher wind speeds appear bright in the radar images, whereas smoother areas corresponding to lower wind speeds appear relatively dark. [10]

SAR can penetrate clouds to provide images that can be used to infer the wind speed and storm structure at the ocean's surface with fine resolution (as compared with spectrometer). Traditional visible and infrared weather sensors such as those on the National Oceanic and Atmospheric Administration (NOAA) Geostationary and Polar Operational Environmental Satellites, (GOES and POES, respectively), are limited to providing information on the topmost level of the storm clouds. Other sensors, such as scatterometers (a microwave radar sensor that is used to measure wind speed and direction over the ocean surface) can also penetrate clouds, but are limited in their ability to observe localized wind events near the coast by their 15 km to 25 km resolution cell size [76]. In addition, shore based weather radars have a limited operating range to detect and track a hurricane developing deep in the ocean. To cover large coastal areas, terrestrial weather radars are required in large numbers. Airborne weather radars provide a suitable solution but these are associated with very high operational costs and limited swaths. Spaceborne SAR provides a suitable alternative and complementary information for hurricane surveillance and tracking.

The results published by [76], [77], [78], [79] and many others, using images acquired from different spaceborne SAR systems have shown that hurricanes may be detected and tracked. But the major problem of these SAR sensors is the temporal resolution/revisit time. They need to be programmed or assigned to the designated areas well in advance. Individual spaceborne SAR sensors have equatorial revisits of 13 – 25 days or so. In order to reduce this revisit time, these are needed more in numbers to form a constellation or there may be a mechanism to take benefits from other spaceborne radars available over a specific area at the time of requirement.

The research has proven that for detection of the hurricanes, C-band sensors operating at HH polarization are considered sufficient (e.g. RADARSAT-1), provided wide area coverage through the scanSAR mode of operation is available. ScanSAR provides the added advantage of imaging the entire diameter of the hurricane in a single or couple of passes. A daily revisit is essential to update the situation with global access. [10], [76]

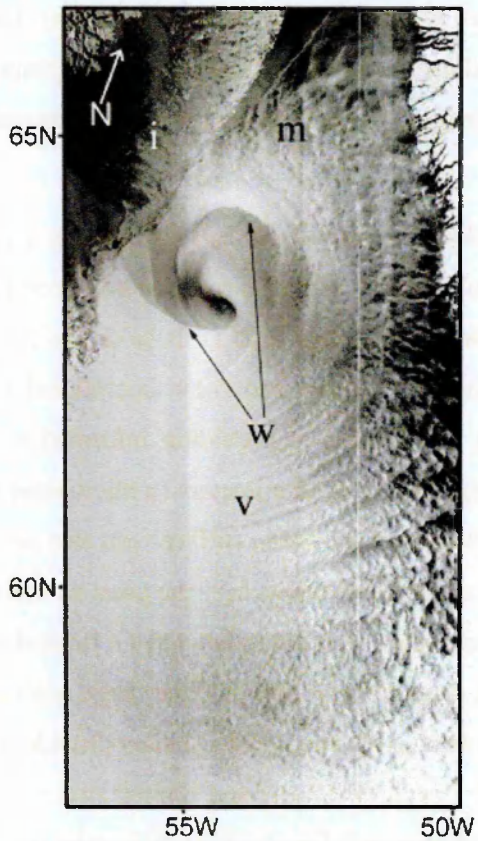

Figure 3 - 8: RADARSAT-1 ScanSAR Wide image of a spiral-like Hurricane in the Labrador Sea. The imaged area is 500 km wide.

Source: Adapted from [76]

Figure 3 – 8 shows the spiral-like hurricane developed near Baffin Island (labelled 'i') was taken on 29th December 1997 at 2120 UTC by RADARSAT-1 The core 'eye' of this well-developed hurricane is near 'i'. The SAR image shows in detail the spiral-form structure of the surface wind field around the eye (the dark ellipsoid-shaped pattern) of the hurricane. The convergence zone of the surface winds in the core is characterized by several sharp wind field gradients that are revealed by the fine spatial resolution of the ScanSAR image (labelled 'w'). Similarly different wind behaviour is observed at other parts of the image—which helps in retrieval of important information. [76]

Foregoing above discussion, it may be inferred that for hurricane detection and subsequent tracking, the sensor needs wide swath ~ 500 km, spatial resolution of ~100 m and quick turnaround of ~ a day or so.

3.4.4 Geological Hazards/Disasters

Geology involves the study of landforms, structures, and subsurface, to understand physical pro-

cesses creating and modifying the Earth's crust. Geology also encompasses structural mapping that deals with the identification and characterization of structural expression. Structures include faults, folds, synclines and anticlines and lineaments. Understanding structures is the key to interpreting crustal movements that have shaped the present terrain. Structures can indicate potential locations of oil, gas and other minerals. Structures are also examined for clues to crustal movement and potential hazards such as landslides, earthquakes and volcanic activity. Identification of fault lines can facilitate land use planning by limiting construction over potentially dangerous zones of seismic activity. [1], [10]

From the user point of view, the role of the SAR related to geological disasters (landslides, earthquakes and volcanic activity) may be classified into the following two distinct phases.

- Pre-disaster Phase: this is related to detecting, collecting and analysing the data concerning that hazard, before its activation and becoming a disaster. Long term monitoring and detection of seismic activity and crustal movements may provide necessary inputs to risk assessment models that are developed for disaster mitigation purposes.

  Mapping slow Earth deformations is considered a challenging goal for spaceborne SAR missions. [64] The temporal separation in a repeat pass interferometry of days, months or even years, can be used to advantage for the long term monitoring of geodynamic phenomena, in which the target has changed position at a relatively slow pace, as in the case of glacial or lava flow movements. However, it is also useful for analysing the results of single events, such as earthquakes. If two acquisitions are made at different times from the same position, so there is no across-track baseline, then the phase of the interferogram depends only on the change in topography between the acquisition times. In general, a difference in across track (range) position of the acquisitions also exists. In this case, multiple acquisitions can be made to measure the topography, and measure the change in topography (differential effects) over time. [62]
- Post-Disaster Phase: this relates to the activities that are kicked off once the hazard has become the disaster. These may include identifying the extent of the damage, response and recovery efforts. SAR plays its complementary role in identifying the extent of the damage particularly in inclement weather conditions that restrict the utility of the optical sensors.

  To this effect, the focus is on change detection in the terrain relief before and after the occurrence of the disaster. For the post-disaster phase, the temporal analysis of SAR images that are acquired before and after the disaster helps in identifying the extent of the damage and directing the response and recovery efforts.

The following sections provide an insight on the role SAR plays during the pre-disaster phase of geological hazards.

3.4.4.1 Landslides

Landslides pose serious threats to settlements and structures that support transportation, natural resource management and tourism. They do considerable damage to highways, railways, waterways and pipelines. They commonly occur with other natural disasters such as earthquakes, volcanic activity and floods caused by heavy rainfalls [10]. Recent scientific publications [80] show a partial success in addressing the application of SAR to the morphological characterization of landslides and the measurement of slow slope movements.

For detecting slow motions, a repeat pass interferometric technique is used. The data acquired through this technique is exploited to produce interferometric DEMs, that are useful for wide-area preliminary assessments of susceptibility of slopes to failure, and to detect and quantify slow landslide movements. However, use of this technique for detecting landslide motion is difficult because mass movements are small in size and typically occur on steep slopes in high relief vegetated terrain. SAR has its inherent limitations (foreshortening, layover and shadowing) when dealing with slopes. The presence of vegetation (especially in areas where rainfall is frequent) also requires very quick revisits (a week or so) of the sensor to ascertain the change. Moreover, it would also need longer wavelengths (L- or P-bands) to penetrate through and get the reflections from the surface for clear assessment and detection of surface deformation/movements. [10]

To improve the detection capability—for susceptible areas that are under thick vegetation cover—another technique that relies on the presence of Permanent Scatterers (such as houses, roads or other prominent landmarks like bare exposures) helps in detecting movements. [80] In site specific or single landslide investigations show that Permanent Scattering data can represent a very useful complementary data source with respect to information acquired through ground based observations and in situ surveying. [81]

German space agency, DLR is currently studying a space borne mission to map Earth surface deformation and vegetation structure from space. In this study the scientific requirements for deformation measurements are collected, traded off versus technical feasibility and a mission concept is investigated that provides a global monitoring capability of geo-tectonic threats. [82] The findings of this research group pertaining to the landslides are mentioned in Table 3 – 2.

Product Characteristics	Value
Area	Mountainous areas
Accuracy	1 cm
Resolution	5 – 20 m (5 m in emergency)
Update frequency	Every revisit/as quickly as feasible
Swath width	> 20 km
Derived product	1/2/3 D - displacement vector map

Table 3 - 2: Summary of parameters – Tectonic/landslides

Source: Adapted from [82]

3.4.4.2 Volcanic Hazards

The population and infrastructure near erupting volcanoes is seriously threatened due to hazards such as lava flows, mudflows and ash falls. The eruption of Iceland's famous volcanic ash in 2010 had global environmental hazards as most of the international flights passing over Iceland were cancelled which caused huge financial losses to all concerned.

Many volcanic phenomena are detected and partly quantifiable using remote sensing information. This includes the monitoring of deformation, thermal and gas emissions, and processes during eruptions. The high resolution mapping of topographic and geomorphic changes is important since they influence the direction of lava and pyroclastic flows and lahars. [10]

Effective volcanic hazard monitoring and mitigation requires access to high quality geomorphic and topographic data to predict the direction of lava or pyroclastic flows and lahars. In addition mapping of young volcanic deposits is essential to the evaluation of volcanic hazards. [83], [84]

Geological structures related to volcanic edifices such as cones and calderas have a morphological expression which stands out in relief. These topographic changes are easily mapped with SAR due to changes in average local slope. [85] Active volcanoes are difficult to monitor due to the extreme hazard and remote sensing with optical imaging systems is typically impeded due to clouds of smoke and ash during eruptive cycles. SAR is able to detect the changing morphology of the eruptive centre. [10]

To quantify the tectonic deformation, the findings of DLR research group [82] pertaining to the tectonic/volcanoes are mentioned in Table 3 - 3.

Mode	Product Characteristics	Value
Global volcano surveillance	Area	All volcanoes (~540,000 km^2)
	Accuracy	2 cm
	Resolution	50 – 100 m
	Update frequency	Weekly
	Swath width	50 – 100 km
	Derived product	3 D - displacement vector map
Emergency	Area	Active volcanoes and vicinity
	Accuracy	1 cm
	Resolution	10 m
	Update frequency	Twice per Week
	Swath width	50 – 100 km
	Derived product	1/2/3 D displacement vector map

Table 3 - 3: Summary of parameters – volcanoes

Source: Adapted from [82]

3.4.4.3 Earthquakes

Remote sensing systems are usually used for geological base mapping (lithology and faults) and earthquake damage assessment [86], [10]. Repeat pass interferometric techniques have been used to observe the motion related to earthquakes. The regional tectonic setting of an area forms the basis for assessing its vulnerability to earthquakes. The structural maps developed using SAR data can further be improved if these results are fused with other optical, topographic and geophysical images. [10]

Active faulting, differential erosion along ancient faults or along lithological boundaries exhibit some topographic expression which can be recognized in SAR images of almost any polarization provided the resolution is comparable to the features. [10]

For most of the land applications like polarized data (HH or VV) have similar information content due to a similar backscatter response from rough surfaces or through volume scattering. Cross polarized data (HV or HV) are more sensitive to the larger scale (larger than the radar wavelength) geometry of the surface or volume scatters. The cross polarized data are therefore sensitive to areas of extreme surface roughness or where abrupt changes in relief occur (escarpments) to cause depolarization of the radar return. The bedrock fracture zones and fault scarps are typically highlighted by a much stronger contrast in backscatter returns relative to the surroundings in cross polarized data than in the like polarized. [10]

In arid environment, the experimental results show at C-band, the imaging depths are expected go

up to 0.5 m, thus permitting the recognition of bedrock structures beneath sand sheets. [10] This imaging depth further increases as longer wavelengths (L- or P-bands) are used. Using longer wavelengths are particularly important for detecting movements of the seismic faults beneath vegetation/forest cover.

Most researchers conclude that at a minimum, dual-polarization at a single frequency is a requirement for geological applications. Experimental results (basing on multi-frequency and multi-polarization SIR-C/X SAR data) have shown that cross polarized L-band has the greatest information content and provide a strong contrast especially in a vegetated terrain. [87]

To derive the scientific requirements, the findings of the research group [82] pertaining to earthquakes are mentioned in Table 3 - 4 .

Mode	Product Characteristics	Value
Global	Area	Whole earth surface
	Accuracy	1 cm
	Resolution	200 m
	Update frequency	4 times per year
	Swath width	400 km
	Derived product	2 D - displacement vector map
Risk Areas	Area	All active areas
	Accuracy	5 mm/month
	Resolution	100 m
	Update frequency	monthly
	Swath width	200 – 400 km
	Derived product	3 D displacement vector map
Emergency	Area	50 km across fault
	Accuracy	1 cm
	Resolution	5 - 20 m
	Update frequency	Weekly (2 months after the event)
	Swath width	100 km
	Derived product	1/2/3 D displacement vector map

Table 3 - 4: Summary of parameters – Tectonics/earthquakes

Source: Adapted from [82]

3.5 Summary of Application-Specific Sensor Requirements

The foregoing discussions on various intended applications outline different sensor requirements. If it is desired to define a SAR sensor that could be used to serve these applications, then the

baseline capabilities of that sensor should conform to these requirements. Keeping this in mind, in addition to mentioning the sensor requirements against each application, these are summarized in Table 3 - 5.

Forestry and Disaster Monitoring—application specific sensor requirements

Frequency	P,L,S
Polarization	HH, VV and HV
Incidence Angle	20 – 50^0
Spatial Resolution	5– 200 m
Swath	50 – 500 km
Orbit Inclination	SS/Global
Revisit	Variable from real time turnaround /twice a day to once a year
Access to Data	Near real time on occurrence/once a day
Additional Requirements	minimum acceptable polarizations: HH & HV InSAR ScanSAR

Table 3 - 5: Preliminary user requirements for forestry and disaster monitoring applications

3.6 Available Buses

At the start of space age, initially small satellites were built and launched. As time went on, the satellites that were flown were developed to serve several different projects and they became larger and more expensive and took a longer time to develop, build and launch. Envisat (8140 kg) may be quoted as one of the extreme examples of such large and multi sensor mission. For a large, expensive and multi-sensor mission, failure of one subsystem (e.g. short circuiting in Seasat SAR) may leads to complete/partial failure of entire mission. [88]

As space experience grew especially in the field of Earth observation and space science, a corresponding realization also developed to distribute the mission objectives to small satellites. But still sensor-specific customized buses had to be developed for each mission (up till late 70s). This required longer design and building time that had large associated labour costs. [88]

The MagSat (launched in Oct 1979) was the first technology demonstrator that exhibited the usefulness of a general-purpose bus for science applications. The bus could support a variety of sensors and anticipated range of missions. This open architecture bus design concept reduced the

mission cost significantly because each satellite did not need to be designed from the scratch. [88]

SSC at University of Surrey and its spin-off (and now a private company) Surrey Satellite Technology Limited (SSTL), also contributed to fostering this concept in 80s and 90s. Taking advantage of this inheritance, different missions are planned keeping the baseline capabilities of available buses, so that minimum alterations are required in the bus. This concept significantly reduces the lead time for development of the mission. The three examples quoted in the previous chapter for light-weight spaceborne SAR missions (i.e., TecSAR, NovaSAR and MAPSAR) all have taken advantage of already developed, space qualified and time tested existing buses.

To this effect, SSTL platforms provide a robust and flexible solution. The most notable buses that are considered for this research are SSTL-100, SSTL-150 and SSTL-300. The detailed baseline characteristics of these are presented in Table 3 - 6.

Some of these terminologies need further explanation at this stage. These capabilities have a direct impact on the SAR mission design that will be analysed in chapter 6.

- Pointing knowledge: How accurately can the bus measure (know) any directional vector? If it is assumed that directional vector (say the SAR antenna pointing/incidence angle) is at 30^0 then the SSTL-150 bus can know the direction vector within the bounds of a $30^0 \pm 25$ arcsec (for 1 SD if normal distribution is considered).
- Pointing Control: Knowing the inaccuracy in the desired direction, how accurately can it be corrected? For the SSTL-150 it is 36 arcsec. Thus for the worst case scenario it would be: $30^0 \pm 25$ arcsec ± 36 arcsec .
- Pointing Stability (Jitter): This is an uncontrolled zone that may not be corrected by the attitude control system. It may be caused by onboard vibrations etc.
- Position Knowledge: How accurately is the position known? For these buses it is ± 10 m
- Slew Rate: This is the rate at which the attitude determination and control system can rotate the satellite from one known direction to another desired direction. For example, the SSTL-150 bus has the capability to change the direction of SAR antenna at $1^0 s^{-1}$.

		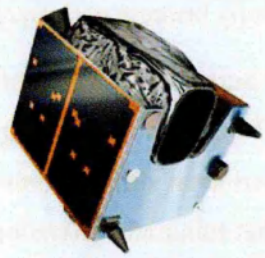	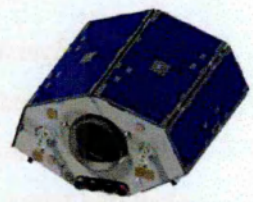
	SSTL-100	**SSTL-150**	**SSTL-300**
Total Mass (platform dry mass / maximum payload)	(83/15) kg	(103/50) kg	(218/ 150) kg
Payload power (average/peak)	(24 – 33/48 – 67) W EOL	(80/100) W EOL	(140/180) W EOL
Payload data downlink	80 Mbps, X-band	105 Mbps, X-band	105 Mbps, X-band
Data storage	16 GB capacity, dual-redundant mass memory	16 GB capacity, dual-redundant mass memory	16 GB capacity, dual-redundant mass memory
Pointing knowledge	2520 arcsec (1 Standard Deviation (SD)) all 3 axes	25 arcsec (1 SD) all 3 axes	72 arcsec(1 SD) all 3 axes
Pointing control	2880 arcsec (1 SD) all 3 axes	36 arcsec(1 SD) all 3 axes	36 arcsec (1 SD) all 3 axes
Pointing stability (Jitter)	15 arcsec/sec	1.5 arcsec/sec	2 arcsec/sec
Slew rate	Nadir pointing mode only	$1^0 S^{-1}$	$0.75^0 S^{-1}$
Position knowledge	10 m	10 m	10 m
Propulsion	Liquefied Butane gas	Hot gas Xenon resistojet	Hot gas Xenon resistojet
Attitude Control System	Sun sensors and 3-axis control with reaction wheels and magnetorquers	Sun sensors and 3-axis control with reaction wheels and magnetorquers	Sun sensors and 3-axis control with reaction wheels and magnetorquers
Delta V	20 m/s	36 m/s	15 m/s
Mission Lifetime	5 years	7 years	7 years
Batteries	Li-ion cells providing 15 Ah capacity	Li-ion cells providing 15 Ah capacity	Li-ion cells providing 15 Ah capacity
Solar Cells	3 body mounted solar arrays with single junction GaAs cells, total area 1.08 m^2. 1 deployable solar array with triple Junction GaAs cells, total area 0.36m^2.	Early designs (Rapideye) used single junction GaAS cells, now more efficient triple-junction GaAs cells, with a total area of 1.81 m^2 are being used.	Triple-junction GaAs cells, total area 2.44m^2
Cost	-	USD 10 M	USD 15 M
Heritage Missions	UK-DMC-1 & 2, Deimos-1, AlSat-1,	RapidEye, DMC-4, TopSat	NigeriaSat-2

Table 3 - 6: Baseline capabilities of SSTL-100, SSTL-150 and SSTL-300 Buses

Sources: Adapted from [57], [89], [90]

3.7 Summary and Conclusions

Radar clutter statistics, characterized by a PDF, are both sensor (wavelength, polarization configuration and viewing geometry) and terrain type (dielectric properties, surface roughness and geometrical characteristics) specific. Designing a new SAR sensor for measuring distributed targets has to encompass both these aspects.

The horizon of SAR applications is wide and ever expanding but in order to complement the optical DMC resources, these are focused on a narrow range that includes forestry related environmental hazards (clear cut and fire scar monitoring) and disaster monitoring.

The dictates of these applications lead to preliminary SAR parameters to build upon the corresponding mission. Most pronounced ones are L-band with moderate resolution of 10 – 50 m over a swath of approximately 50 km, with HH and HV polarizations.

After going through the intricacies of the intended applications and deducing relevant sensor parameters which can serve these applications, it has been found that these specific requirements closely resemble the specifications offered by the fine beam dual (FBD) polarization (HH/HV) ALOS sensor. Thus, FBD ALOS is considered as a reference—to be matched in terms of spatial and radiometric characteristics—by the proposed SAR design.

In addition, baseline capabilities of different available buses are also included here. The underlying consideration is that if the SAR mission is built around already developed and time tested buses, then there would be significant saving in cost and time. The concept of using available platforms also poses constraints over the design in terms of payload mass, power and volume.

Thus, the microsatellite based SAR mission design—to emerge as an outcome of this research—would be a suitable compromise between: what is required from the applications point of view, what these platforms are offering, and what constraints these are imposing.

4 DESIGN OPTIONS FOR MICROSATELLITE BASED SAR

The application-specific requirements dictate the capabilities a SAR design should ideally possess. Once these dictates are analysed according to the baseline capabilities of available buses, certain tradeoffs need to be incorporated in the design.

This chapter is built upon discussing these tradeoffs that lead to the selection of suitable frequency, polarization, operational modes, orbit and inclination, antenna design etc. These choices then lead to the derivation of SAR parameters to be used within different design options such as Pulsed, CW, ICW and ECMP SAR techniques. The associated problems of each technique are highlighted with intent to quantify the effects these would have on the onboard subsystems. These options are then utilized in selecting the suitable bus out of three available busses.

4.1 Design Tradeoffs

While designing a microsatellite based SAR, a wide range of issues are required to be considered, particularly the frequency, polarization, orbit and the most pronounced one being the antenna design. In each case, the various options that are available have different pros and cons that affect the performance of the system and need to be evaluated in the light of limitations posed by the microsatellites. The forthcoming sections deal with this selection process.

4.1.1 Choice of Frequency

While considering different forestry related applications, L- and P-bands offer greater canopy penetration. Implementation of P-band spaceborne SAR has issues such as:

- Limited allocated bandwidth (only 6 MHz around 435 MHz [91]) by the ITU (international telecommunication union). This bandwidth governs the maximum attainable range resolution, which would remain poor in this case.
- A spaceborne mission requires considerably a large antenna to address the range and azimuth ambiguities. Recent research focused on implementing a P-band SAR satellite for biomass

mission [92] suggest minimum of 10 m diameter and 100 kg antenna mass. Besides mass and volume, antenna gain—which is non-linearly related to the wavelength, remains low, thus needs higher RF power output from the PA to achieve adequate SNR.

Because of these issues, so far, none of the known spaceborne SAR missions uses P-band. The other frequency choice is L-band. Due to the retirement of ALOS on 12th May 2011, there is no other operational mission in space that can provide remote sensing imagery at L-band. The planned MAPSAR mission has been facing delays and early 2013 launch is not confirmed yet.

For the flood related disaster applications especially making a distinction between flooded/non-flooded areas, higher frequency bands (S-, C- and X-bands) may be used. But if the flooded area has a thick vegetation cover (such as the Indian sub-continent and other tropical regions etc.) then SAR radiations are required to penetrate through the vegetation cover and get scattered from the surface underneath to make this distinction. For this purpose, L-band is considered a better choice than other higher frequency bands.

For the geological hazard detection (pre-disaster) stages, where the crustal movements are to be detected, different researchers recommend using L-band over other high frequency bands because it offers longer coherence length [64], [82]. To carryout the damage assessment and coordinate the recovery and rescue efforts (during post-disaster stage), higher frequency bands may be used but for the areas that are under vegetation cover, L-band offers a suitable choice.

Thus, for these intended applications, L-band is selected.

4.1.2 Choice of Polarization

As it has been elaborated in the previous chapter by giving examples of ALOS images that in order to make clear distinction between forest and non-forest; preparing the forest fire scars maps; and subsequent resource assessment of the forest re-growth, it is necessary to have at least HH and HV polarizations. If VV channel is available, it will be of an added advantage. But adding a VV channel means including a complete PA, the RF cables up to the antenna, complex feed assembly and an additional receive channel. These increase engineering complexities, weight and power consumption etc., thus may not be feasible to support from a microsatellite platform. Keeping these requirements and limitations in mind, from the forestry applications point of view, a dual channel HH & HV polarization is considered sufficient.

Similarly it was also discussed that differences in backscatter returns between flooded and non-flooded areas are greatest at HH and lowest at HV or VV, particularly in the forested areas [10] . Therefore, HH channel in combination with HV channel would cater for this requirement. For the oil spill detection and monitoring where experiments show a slightly higher oil-water backscatter

contrast from VV polarized images than either HH or HV polarized images. But for this application, the predominant factor remains the wind speed (with 3–10 m/s providing optimal detectability) and the wind direction (up-wind, down-wind or cross-wind [91]) not the polarization. To support this argument, an oil spill detection image which was taken by RADARSAT-1 (that had only HH polarization) has been discussed in the previous discussion with a view to highlight that oil spill can be detected with a single HH channel. Therefore, from the oil spill detection point of view, HH should be sufficient. Similarly it was also shown that detection of hurricanes (that is basically looking at the sea state) can also be achieved with the help of a single HH polarized channel. In the same way, geological hazard detection (pre-disaster phase) is mainly dependent upon the periodic repeat pass interferometric data acquisition not the polarization diversity.

Foregoing above in view, to serve the intended applications, a dual polarization (HH &HV) is selected.

4.1.3 Choice of Spatial Resolution, Incidence Angles and Swath

As discussed in the previous chapter, each application requires a different spatial resolution and swath. For most of these applications, the researchers have recommended flexible limits of 5 – 100 m for range and azimuth resolutions. Fine spatial resolution (~ 5 m) requires higher bandwidth which needs a larger onboard memory to store the data produced during imaging. Correspondingly it would need high speed data downlink to transfer the stored data to ground stations. The available memory onboard SSTL buses provides a limited capability. The detailed aspects pertaining to these issues will be discussed in chapter 6, but for the purpose of developing different design options, at this stage, a moderate resolution of 30 m is considered.

During establishing different application-specific requirements, it was observed that a large incidence angle interval that spans over 20 – 50° is preferable. Large incidence angles yield longer slant ranges and need comparatively high RF power to achieve adequate SNR. More so, these result in larger swaths that produce correspondingly larger amounts of data for the same resolution cells as compared to narrow swaths. The detailed impacts of these incidence angles will be dealt in chapter 6; at this stage, it is considered to be 30°.

Similarly the swath requirements for these applications are also flexible in the range of 30 – 500 km. Wider swaths are desirable but net effect has to be analysed keeping the baseline capabilities (particularly the available power, safety limits of the batteries, the PA capabilities, memory storage and data downlink) of the SSTL buses. Considering these aspects, at this stage of the research, the swath is set at 50 km for the incidence angle of 30°.

4.1.4 Choice of Imaging Modes

Swath is the antenna's radiation (half power point beamwidth) footprint on the surface being imaged [12]. There are three commonly used SAR imaging modes which are shown in Figure 4 - 1. Once the background for a new design is being established, it is necessary to analyze these in the framework of the capabilities offered by the microsatellite buses.

Strip Map

Strip map SAR is the most commonly used imaging mode of operation. In this mode, the radar beam is pointed in a fixed direction (usually) perpendicular to the velocity vector of the radar platform. The beam sweeps a long strip of terrain, collects the returns and after processing, a long image or strip map is generated. The antenna does not need to change its orientation during imaging. [93]

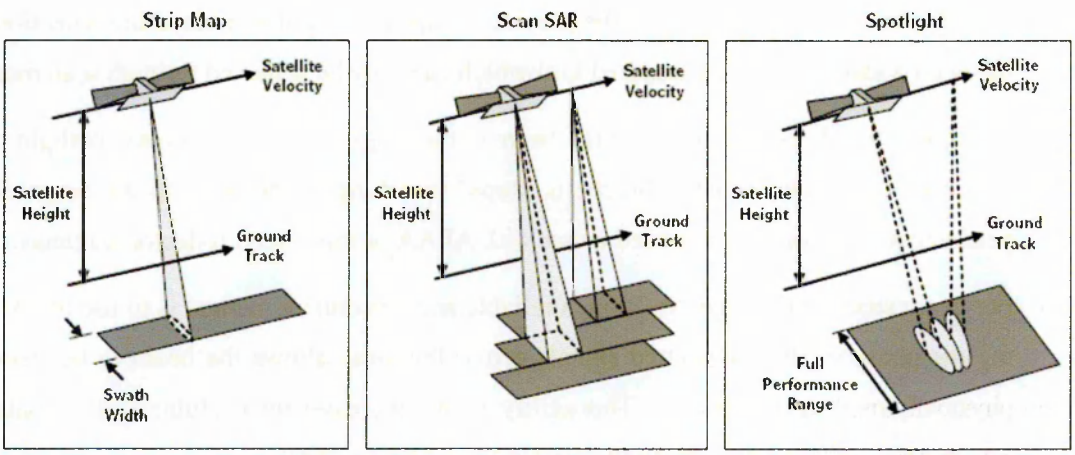

Figure 4 - 1: Typical SAR imaging modes

Source: Adapted from [94]

The antenna footprint on the ground defines the swath in the range direction. Since a strip is continuously imaged, the length of the strip is almost the same as that of the distance the SAR travels during the antenna synthesis time.

ScanSAR

In scanSAR mode, the beam is slewed to produce images of adjacent strips of terrain. Images from scanSAR generally have coarser resolution than strip map images because there is less time spent imaging each strip. [94]

ScanSAR yields a much wider swath than what is achieved from the strip map. Here in this case, the antenna is scanned between several incidence angles to obtain a wider swath, which is com-

posed of several sub-swaths. Azimuth resolution decreases as the synthetic aperture is shared (sub-sampled) between the sub-apertures.

Spotlight

Contrary to the previous modes, in spotlight mode the SAR beam keeps on steering at one single patch of the ground while the satellite passes over that area. The entire integration time (during which the aperture is synthesized) is thus utilized on imaging one scene only. This yields the highest azimuth resolution imagery. However, this mode is complex for radar control and signal processing because the beam must constantly be repositioned during imaging. It also does not provide continuous imaging in the azimuth direction, thus is often used to map small specific areas. [93], [94]

Analysis

The necessity to have a single or multiple imaging modes stems from the intended applications of the mission. As was discussed in the previous chapter, oil spill and hurricane detection and tracking need wider swaths (few hundred km) which can only be achieved through scan mode.

Scan mode needs rapid steering of the beam in the range direction, whereas spotlight mode needs it in both range and azimuth directions. Rapid switching of the beam in the range direction depends upon electronic means used either with APAA or multi-feed reflector antennas.

For beam steering in range direction, a reliable and convenient method is to use the APAA. Varying the phase of the transmitted signals across the array allows the beam to be steered without physically moving the aperture. This agility greatly increases the usefulness of the radar, allowing it to produce images of multiple sites in rapid succession. [94]

Recently TecSAR has demonstrated the implementation of scanSAR mode by simultaneously using multiple beams and controlling these from a multiple feed array (arrangement shown in Figure 2 - 2). If similar multiple feed array arrangement is adopted at L-band then each beam needs a dedicated PA. If TWTA are used, these are heavier (> 5 kg each) and more expensive (> £ 1 M each) for the L-band than for the X-band tubes (< 1 kg), thus these would add a lot of extra weight to the payload.

Foregoing this discussion, it appears that APAA provides the required agility needed for the scanSAR mode but is a heavy and expensive choice. So far the lightest weight APAA planned with the NovaSAR-S is 70 kg whereas the TecSAR reflector antenna is only 21 kg. Supporting such a heavy (70 kg) is not feasible for a microsatellite.

Keeping these system design aspects and constraints in mind, for the applications such as oil spill detection and hurricane detection, it is envisaged that SAR would play a complementary role to other DMC optical sensors, thus the initial monitoring and detection information would be pro-

vided from other sources. More so, for hurricane detection and monitoring, it is required to have daily revisits, which is out of the capabilities of a single SAR. Thus, due to these constraints, only the strip map imaging mode is selected.

4.1.5 Spacecraft's Altitude and Inclination

The selection of the orbit altitude and the inclination are governed by many factors such as: the intended applications; availability of the suitable launching sites particularly if a shared launch is envisaged, then, inclination should be such which suites and facilitates sharing payload parties from their perspective; variety and availability of the launchers; the nature of the space environment in which the satellite would operate from; the availability of sunlight and the Earth's shadowing effects on the charging the batteries; etc.

The environment depends on the altitude. Below 500 km, the atmosphere is still dense, thus drags the satellite more and to compensate the effects of this drag, the satellite needs to use more propellants, which shortens its operational life. [94]

At higher altitudes, radiation poses problems. The Earth's magnetic field captures charged particles from the cosmic and solar radiation and traps them in bands, called Van Allen belts. Considering these effects, the satellites are deployed in one of three altitude ranges: [94]

- 500 – 1000 km called low Earth orbit (LEO)
- 5000 – 15000 km called medium Earth orbit (MEO)
- 20000 km and higher, most commonly around 36000 km known as geosynchronous orbit.

Orbit's selection involves certain tradeoffs. On one hand, higher altitudes offer better coverage or more viewing at any one time than a satellite operating with a lower altitude. These would reduce the Earth's shadowing effects, thus generate more electric power through solar panels. To achieve a given level of global coverage, if a constellation is to be formed, then high altitude (within LEO say 900 km) requires fewer (but more capable) satellites as compared with lower altitudes. [94]

Another prominent aspect related to the selection of the altitude for the SAR is "power aperture product" (radar's RF power fed at the input of the antenna multiplied by its aperture size). The transmitted signal must travel to the Earth, be scattered, and then travel back to the satellite for detection. As the range to the surface increases, the strength of the radar echo received at the satellite diminishes rapidly. For the SAR, detection is proportional to the "power aperture product" and is inversely proportional to the 4th power of the slant range to the target. These requirements necessitate a larger and more expensive satellite with a bigger solar array, battery and antenna, for

a SAR mission at higher altitudes as compared with low altitudes. Keeping these aspects in mind, almost all the known SAR missions operate in the LEO. [94]

Apart from altitude, the inclination of a satellite's orbit (the angle between the plane of the orbit and the plane of the equator) is also important. Orbital inclination primarily affects the area of the globe that the satellite can observe. By choosing a particular inclination, the satellite can spend more time over specific (latitudes) areas of interest. [94]

In order to provide global coverage, traditionally Earth observation satellites have been launched into sun-synchronous (SS) polar i.e.; high inclination orbits (~ 90 – 100^0). This does provides global access but the revisit rates at the equator are reduced considerably. Whereas injection into low inclination orbits provides maximum access and revisits to the equatorial and tropical regions. It thus remains a competing choice between how wide areas are to be accessed and how frequent are the revisits required, and these are primarily dictated by the selection of the suitable inclination angle.

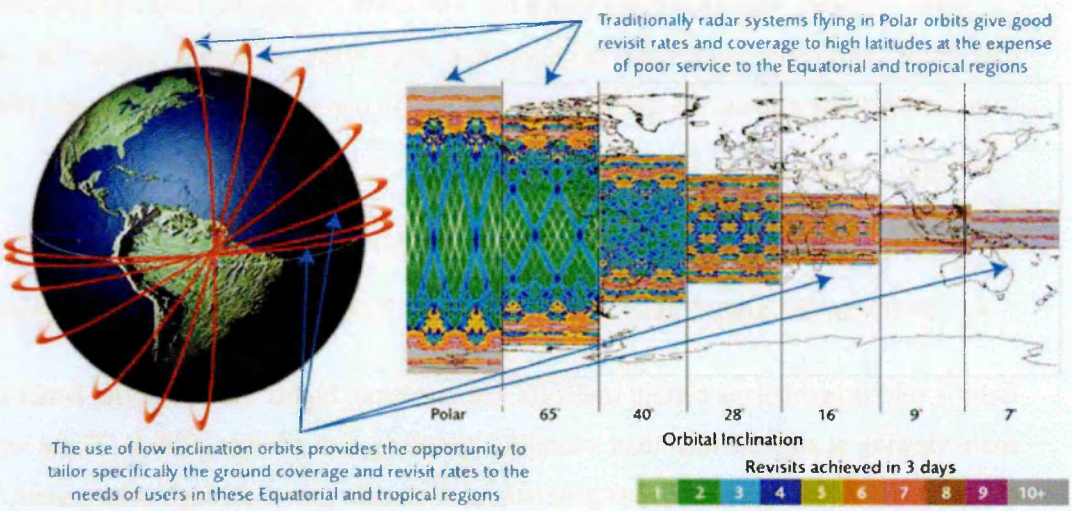

Figure 4 - 2: Effects of orbit inclination on the access

Source: Adapted from [95]

Figure 4 - 2 makes it obvious how the orbit inclination affects the revisit rate at any latitude from the equatorial through to the polar. If a specific application requires near real time imaging closer to equator or tropical regions, then using a very low inclination such as 7^0 would provide up to 13 revisits per day with a minimum revisit interval of only 90 minutes. And a constellation of 3 reduces this to 30 minutes. [95] As the inclination increases, the access to wider areas also increases. By selecting a near polar (90 – 100^0) inclination, global access can be achieved by a single satellite but at much reduced equatorial revisits. Besides access, inclination also affects the

time a satellite spends in the Earth's shadow. Low inclination increases this time compared with high inclination satellites. Shadowing affects the power generation capability through solar panels.

Since most of the intended applications discussed in the previous chapter need global coverage, a SS, polar inclination in the range of 97 – 99° is selected. A major advantage of this inclination is that most of the optical sensors operate in this polar and SS range, thus suitable launching sites and low cost launching systems are already in place. This would also facilitate in arranging a shared launch in conjunction with variety of other missions, thus reducing launch cost. This inclination would yield a poor equatorial accessibility that can be improved by deploying more than one satellites either in the same or different orbital planes.

By using the Earth satellite orbital parameters (i.e., the set of standard equations given by [96]) Table 4 - 1 has been organized to show the effects of variations in the altitude over other parameters in the LEO.

Altitude (km)	Velocity (km s^{-1})	Period (minutes)	Max. eclipse duration (minutes)	Daylight duration (minutes)	Eclipse/ year	Rev/day	SS inclination (deg)
500	7.613	94.62	35.75	58.86	5540	15.18	97.40
550	7.585	95.65	35.61	60.04	5480	15.01	97.59
600	**7.558**	**96.69**	**35.49**	**61.20**	**5421**	**14.85**	**97.79**
650	7.531	97.73	35.38	62.35	5364	14.69	97.99
700	7.504	98.77	35.29	63.49	5307	14.54	98.19
750	7.478	99.82	35.20	64.62	5251	14.39	98.39
800	7.452	100.87	35.13	65.74	5196	14.24	98.60
850	7.426	101.93	35.07	66.86	5142	14.09	98.82
1000	7.350	105.12	34.94	70.18	4986	13.66	99.48

Table 4 - 1: SS orbital parameters

SS circular Earth orbits with varying altitude show that the eclipse duration remains similar for altitudes from 500 – 1000 km, but the time the satellite remains in the sunlight increases from 58.86 – 70.18 minutes. This maximises the use of solar energy for the power subsystem. If this aspect is considered alone, then it appears that higher altitudes are better but the power-aperture product advocates using lower altitudes.

Besides these aspects, the selection of orbit altitude and inclination has to be weighed against the availability of low cost launchers and suitable launching sites. The purpose of this research is to

propose a SAR design that complements the optical DMC sensors, which are often deployed in SS circular Earth orbits in the altitude range of 575 – 625 km. Placing the microsatellite based SAR in the same orbit as those of DMC would provide a constellation having both optical and SAR sensors. For these reasons, the same SS orbit as that of the DMC is considered for this research, with average altitude at 600 km and inclination of 97.79^{o}.

By considering an altitude of 600 km and inclination of 97.79^{0}, Satellite Tool Kit (STK) software has been utilized to visualize the global coverage achieved from a single SAR satellite that has 50 km ground swath. During this simulation, a ground station near the equator is assumed. The results are presented in Figure 4 - 3.

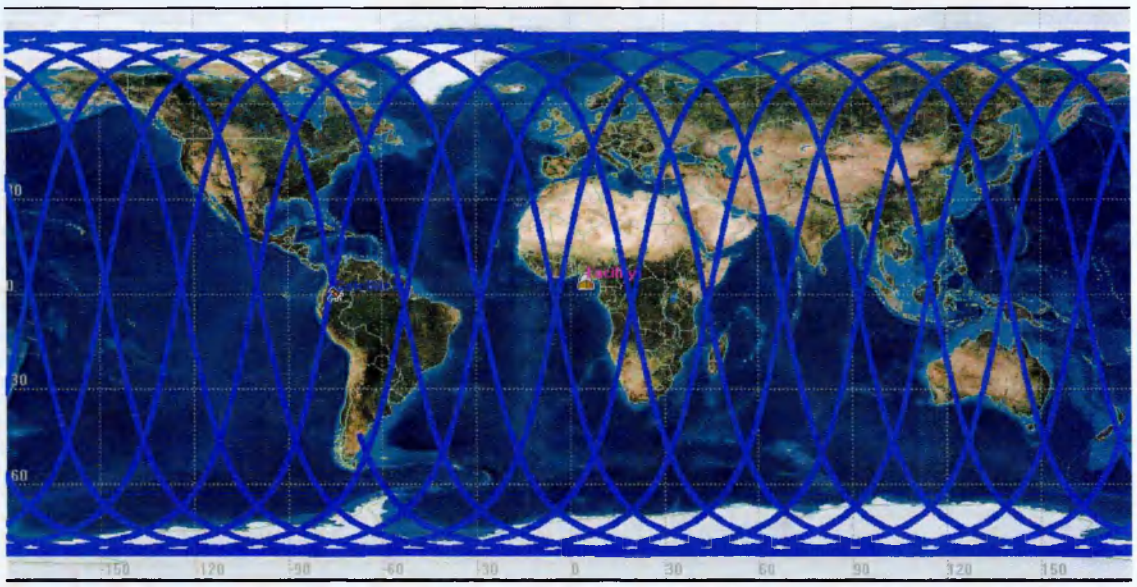

Figure 4 - 3: STK simulated results – ground tracks per day from a satellite at SS orbit, 600 km altitude

Table 4 – 1 also shows that the satellite would have 14.85 equatorial crossings per day at an altitude of 600 km. From this information, the revisit time is determined as:

- The Earth equatorial circumference = 40,075.16 km
- Thus the inter-ground track distance between two successive revolutions (at the equator) = 40,075.16/14.85 = 2698.66 km
- If the ground swath is 50 km, then the revisit time = 2698.66/50 = 53.97 days ~ 54 days.

It is pertinent to mention that RADARSAT 1 & 2, with 100 km swath had 24 days whereas ALOS had 48 days revisit time. [20], [25], [26]

Note: SAR design planning is done through an iterative process and is governed by a set of dif-

ferent equations. These equations have been derived by different authors and are available in relevant text books. To avoid cluttering up this part of the thesis, detailed derivation of the required expressions is done separately and attached as Appendix A.

4.1.6 Selection of the Antenna Design

The antenna is the most critical component of the SAR system design. As has been discussed at length in the literature review and in section 4.1.4, that a reflector antenna is lighter, less expensive and simpler than APAA. These reasons make it the most suitable contender to be used with microsatellites at L-band. Thus, for a baseline design, a single horn, parabolic mesh is considered for the dual-polarisation (HH and HV).

Within reflector antennas, there are different design configurations such as deployable or inflatable, Newtonian or Cassegrain etc. Each has its own pros and cons, but these yield similar far field radiation patterns—the main interest for the SAR—from the same size of the antenna. The decision to opt for the best configuration within the reflector antennas needs to evaluate a few other factors such as overall stowage volume, ease in construction, maintenance during launch and deployment in the space, cost, expected mass etc. These aspects will be discussed in chapter 6.

After selecting the reflector antenna, in order to deal with range and azimuth ambiguities, the minimum antenna area is to be determined. For a reflector circular dish antenna of diameter D,

the projected area: $\frac{\pi D^2}{4}$ ..... (4 - 1) [97]

and the minimum antenna area A_{min}:

$$\Rightarrow \quad A_{min} = \frac{\pi D_{min}^2}{4} = \frac{4\lambda v_s}{c}\left[\frac{h}{\cos\beta}\right]\tan\beta \quad \text{.....} \quad (4 - 2) \qquad [18]$$

$$\Rightarrow \quad D_{min}^2 = \frac{16\lambda v_s}{\pi c}\left[\frac{h}{\cos\beta}\right]\tan\beta \quad \text{.....} \quad (4 - 3)$$

where v_s is the satellite velocity = 7.558 km/s as given in Table 4 – 1

h = mean satellite altitude = 600 km

β = the incidence angle = 30^0

λ = operating wavelength = 23.5 cm

c = speed of the light in free space, 3×10^8 m/s

D_{min} = minimum diameter of the dish (m)

$$\Rightarrow \quad D_{min} = 3.47 \text{ m}$$

Therefore, to adequately address the ambiguities, the minimum antenna diameter should be greater than 3.47 m. In practical dish/circular antenna systems, a beam broadening factor is also taken into account. This factor varies from ~ > 1 – 1.22 [97]. To be realistic and to cater for this aspect, an antenna with a slightly larger diameter should be selected. Hence D = 3.66 m is considered for subsequent discussions.

When considering the antenna design for the spaceborne SAR mission, there are two mutually dependent aspects that need to be analysed at this stage. Firstly the effects of antenna radiations on the nadir returns and secondly the desire to have minimum depth/curvature of the parabola. Minimum depth yields a comparatively flat dish that is easy to construct and maintain.

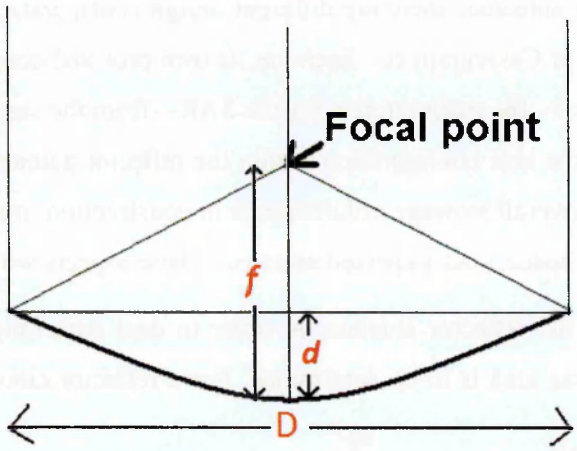

Figure 4 - 4: Diagram showing the Focal Length (*f*), Diameter of the dish (D) and the Depth (d) of the parabolic antenna

The antenna radiation pattern depends on how the reflector is illuminated by the feed. The variation in electric field across the antenna diameter is called the antenna taper [97]. By varying the position of the feed (i.e., the focal length (*f*)), not only the radiation pattern but the depth/curvature of the dish can also be controlled. Figure 4 - 4 pictorially shows how focal length (*f*), the depth of curvature (*d*) and the diameter of the parabolic dish antenna (*D*) look like in the context of the parabolic antenna. These are mathematically related by:

$$f = \frac{D^2}{16\,d} \qquad \text{.....} \qquad (4 - 4) \qquad [98]$$

The tapering is commonly known as focal length to diameter (*f/D*) ratio and for large size parabolic dish antennas, it is commonly set in the range of 0.45 – 0.65 [97]. The values higher than 0.65 introduce spill-over losses (i.e., the incident radiations going outside the dish), and to control

these, a larger horn (feed) is required. Thus to achieve a suitable balance among different parameters, the *f/D* ratios are chosen within this range.

CADFEKO is an antenna design and simulation software tool that has been utilized for carrying out simulations of the proposed antenna, encompassing the above mentioned aspects. During these simulations, diameter of 3.66 m and surface inaccuracies of ± 4 cm are considered. The *f/D* ratio is varied from 0.45 – 0.65 and the combined results are shown in Figure 4 – 5 and Figure 4 – 6.

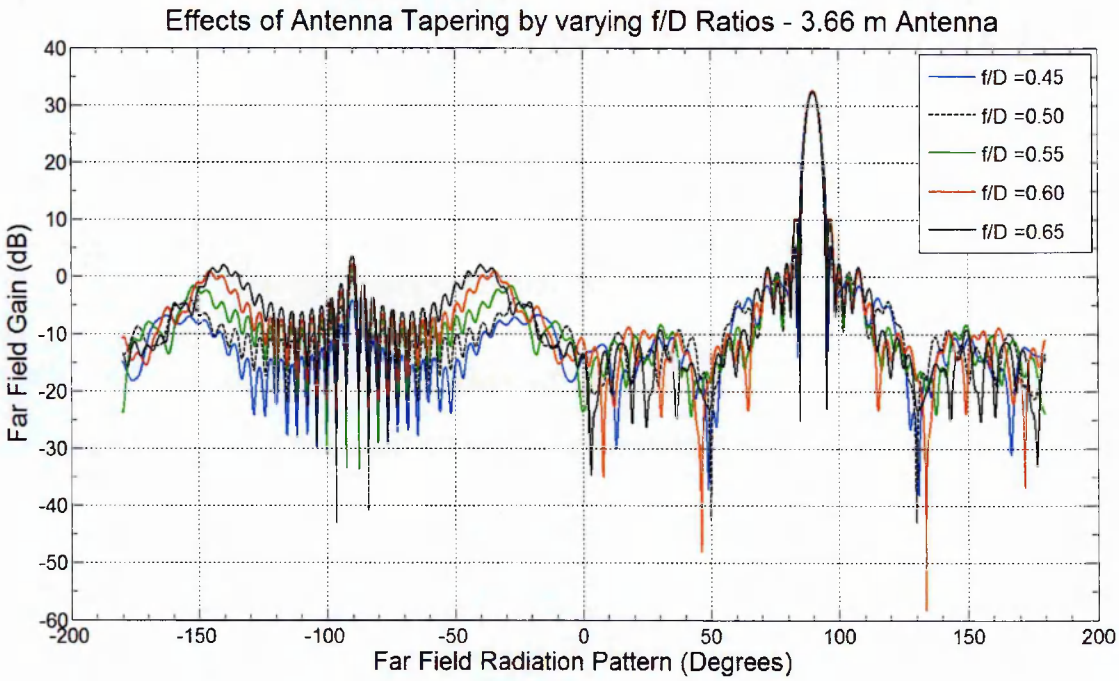

Figure 4 - 5: Comparison of 3.66 m antenna radiation patterns by varying *f/D* Ratios

Analysing these results, it appears the radiation pattern achieved from *f/D* ratio of 0.60 is slightly narrow and higher over the main lobe, although yields the highest first sidelobe but towards the lower angles (from 80° towards 45° : Figure 4 – 6) it performs better than others. More so it is within safe limits, where the losses caused by the spill-over radiation are low. It strikes a suitable balance between reduced sidelobe radiations (nadir oriented) and a low depth parabolic structure. Therefore a *f/D* ratio of 0.6 is selected for further use. The angular distribution of the far field radiation pattern is shown in Figure 4 - 7. Figure 4 - 8 shows the 3D radiation pattern whereas Figure 4 - 9 displays the polar radiation plot.

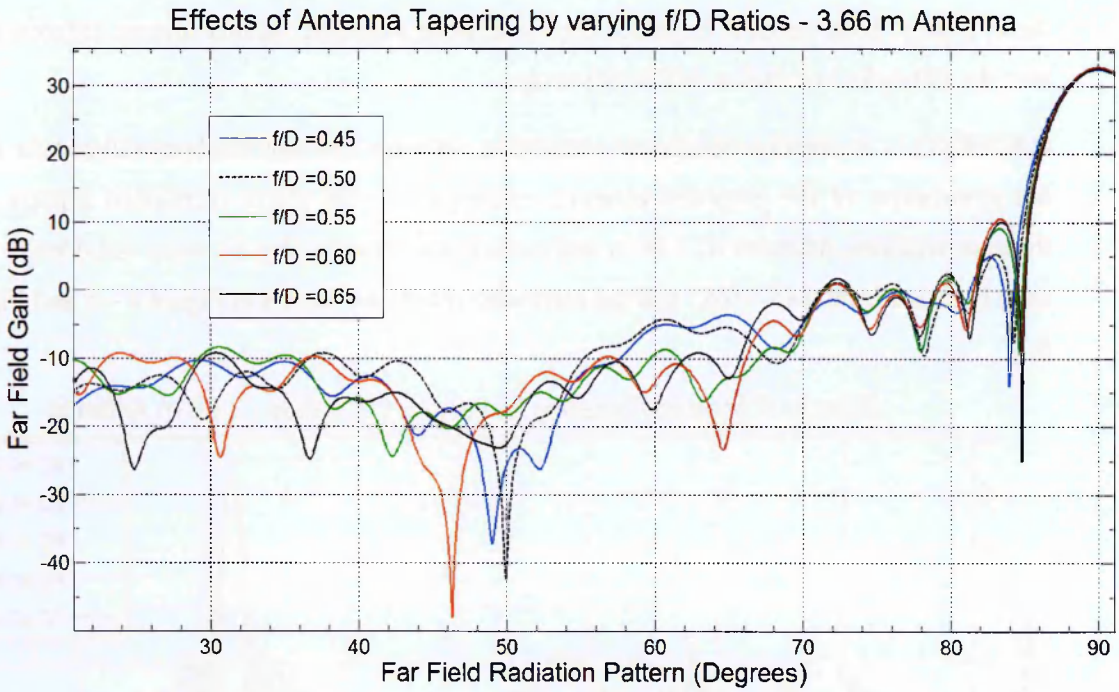

Figure 4 - 6: Zoomed in part of Figure 4 - 5

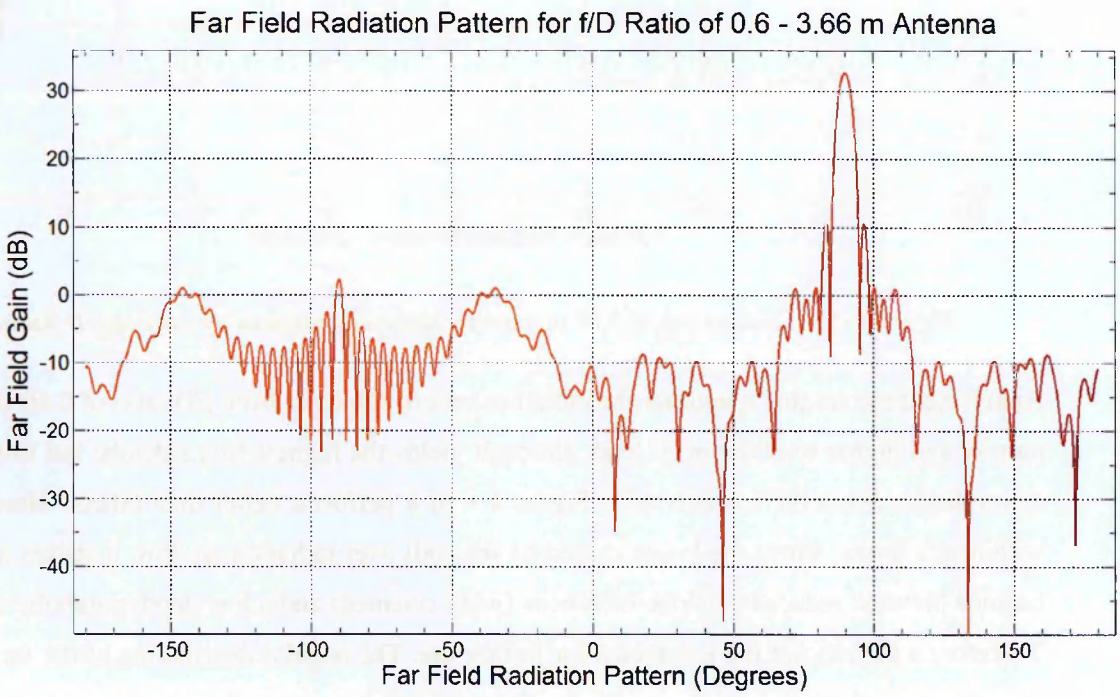

Figure 4 - 7: Far field radiation pattern for the selected *f/D* ratio of 0.6 m

These simulations show that the main lobe gain is 32.67 dB. The half power point beam width (BW_{3dB}) is 4°, this determines the 3 dB swath in range/azimuth directions. The first sidelobe level is 10.50 dB at $\pm 6.65°$ off the main lobe. This yields sidelobe to peak ratio of – 22.17 dB. This ratio has a direct bearing on the returns from the first sidelobe.

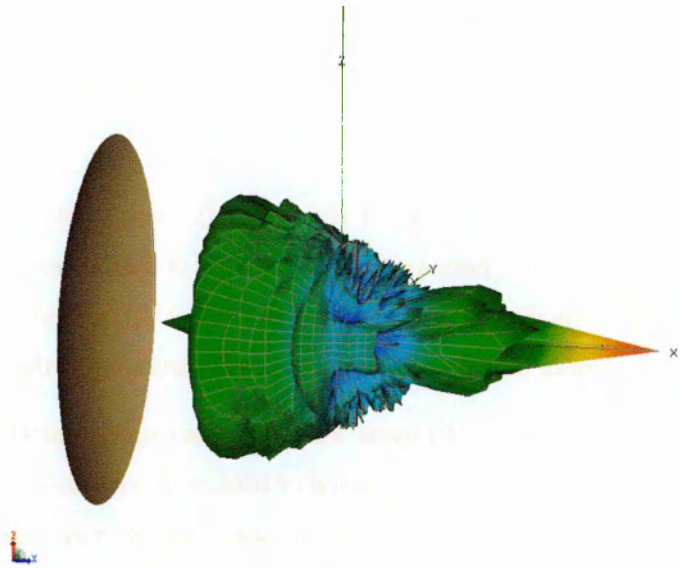

Figure 4 - 8: 3 Dimensional view of the radiation pattern for the selected *f/D* ratio of 0.6

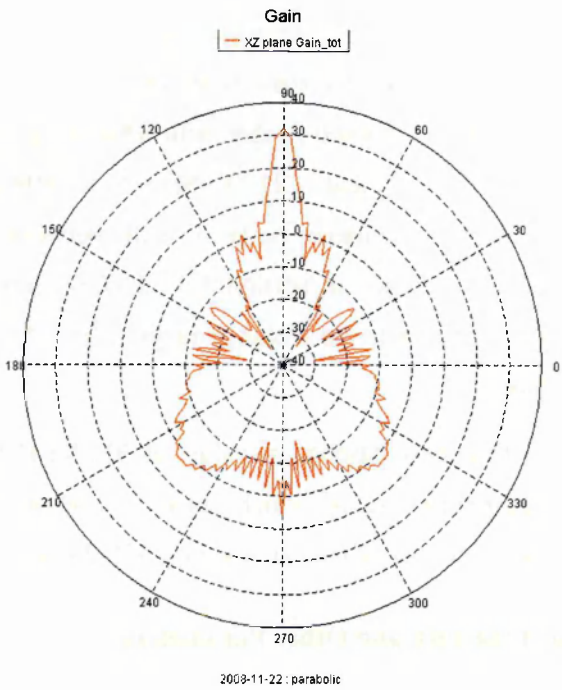

Figure 4 - 9: Polar radiation pattern at *f/D* ratio of 0.6

Associated with the first sidelobe is the region of the radiation pattern that contributes to the nadir returns (depending upon the incidence angle). As was previously mentioned that the intended applications need to look at the target area over a range of incidence angles (20 – 50^0), thus the corresponding average gain in this region is ~ – 15 dB.

The radiation pattern in the direction of $\pm$ 90^0 (off the main beam) is about – 10 dB. The back blast is narrow and a low gain of 2.2 dB.

4.1.7 Sensitivity

As different sensor specific parameters (frequency (L-band), polarization (HH and HV), range of incidence angles (20 – 50^0, nominal 25 – 35^0), range of spatial resolution (10 – 50 m, nominal 30 m) etc.) relating to the design have been worked out, it is pertinent to figure out the range of different sensitivity values (target specific parameters) pertaining to the intended applications.

Measuring σ^0 over a variety of targets with calibrated spectrometers is an expensive, time consuming and difficult process. Over a period of time, different projects were initiated to measure σ^0 from calibrated sensors. A combined master dataset had been prepared by [59], the PDFs for different types of terrains, vegetation and trees were organized and information was publicly released. The lookup tables and the corresponding PDFs that are relevant to the intended applications of this research are selected and separately included in the Appendix B.

Considering different PDFs and the mean values presented in the Appendix B for trees, shrubs and the short vegetation, at 30^0 incidence angle, the σ^0 = – 14.6 to – 16.2 dB (SD = 4 to 6.6) and – 18.7 to – 24.9 dB (SD = 4 to 6) variations are observed for HH and HV polarizations respectively, at L-band. In order to proceed further with SAR design options, at 30^0 inclination, let us consider σ^0 = – 15 dB (SD = 5) and – 21 dB (SD = 5) for HH and HV polarizations, respectively. This would also ensure a dynamic range of 6 dB between HH and HV polarizations. This satisfies the conditions discussed in section 3.3.1.1 (forest resource assessment) and 3.3.1.2.1 (forest resource monitoring) where a dynamic range from 1.5 – 8 dB depending upon changing scenarios, is recommended.

The purpose of selecting these baseline σ^0 values at 30^0, for HH and HV polarizations at L-band is to work out the approximate values which can serve a set of applications. Indeed, σ^0 is strongly incidence angle dependent, thus while calculating SNR, this aspect will be taken into account.

4.1.8 Selection of the PRF and Other Parameters

Since a parabolic reflector antenna has been selected, it yields the same half power beamwidth '$BW_{3\,dB}$' in both range and azimuth directions. By using antenna simulation results given in

Figure 4 - 7, $\Rightarrow$ Azimuth '$BW_{3\,dB}$' (θ_a) = Range '$BW_{3\,dB}$' (θ_r) = 4^0

Basing on this beamwidth, different slant ranges (R_S) would be:

- The slant range at the centre of the swath '$R_{S,C}$', at 600 km altitude and 30^0 incidence angle:

$$R_{S,C} = h/\cos\beta = 600/\cos 30^0 = 693 \text{ km} \qquad \ldots\ldots\ldots \qquad (4-5)$$

- The slant range at the near edge of the swath '$R_{S,N}$' would be:

$$R_{S,N} = h/\cos(\beta - \theta_r/2) = 600/\cos 28^0 = 679 \text{ km} \qquad \ldots\ldots \qquad (4-6)$$

- The slant range at the far edge of the swath '$R_{S,F}$' would be :

$$R_{S,F} = h/\cos(\beta + \theta_r/2) = 600/\cos 32^0 = 707 \text{ km} \qquad \ldots\ldots \qquad (4-7)$$

For the spaceborne SAR, the curvature of Earth effects are pronounced and need to be incorporated while calculating the ground ranges, ground swath and ground range resolution. The detailed discussion and derivation of expressions are included in Appendix A. By using these expressions, the corresponding ground ranges have been shown in Figure 4 - 10. It shows that ground swath (S) in range would be = 58 km.

- The SAR's azimuth resolution 'ΔA' is related to physical length (diameter) 'D' of the antenna in the azimuth direction by $\Delta A = D/2$. By incorporating the curvature of Earth effects, it improves by: $\Rightarrow$

$$\Delta A = \left(\frac{R_e}{R_e + h}\right) \times \frac{D}{2} = 1.67 \text{ m} \qquad \ldots\ldots\ldots\ldots \qquad (4-8) \qquad [75]$$

where R_e is the mean local radius of the Earth.

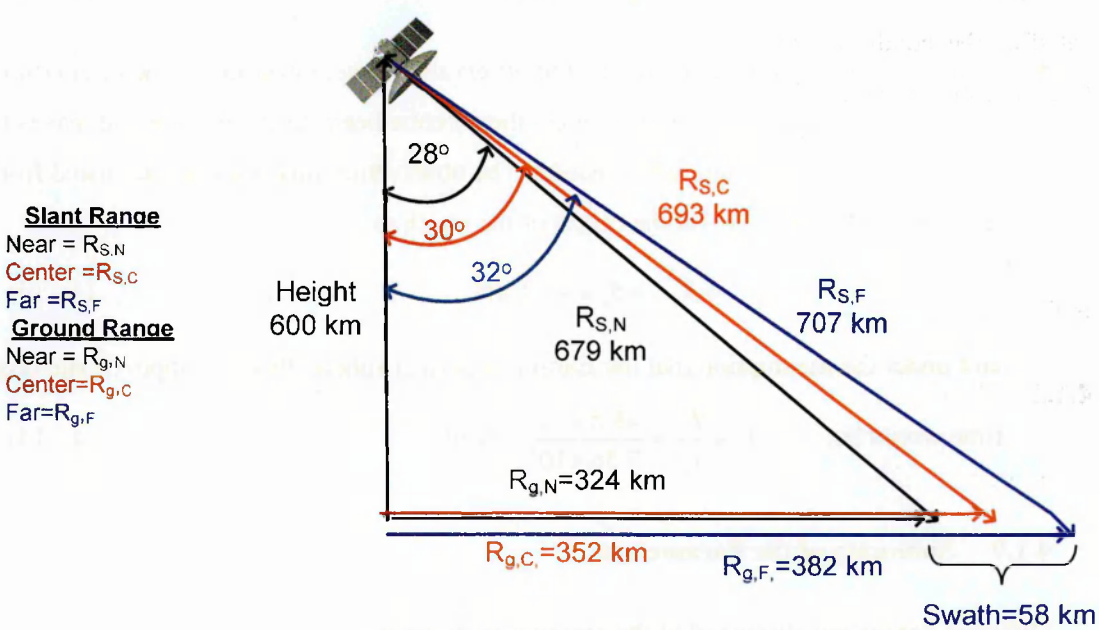

Figure 4 - 10: Ground and Slant Ranges due to 4^0 beamwidth

- In order to set a 30 m ground range resolution, the system bandwidth 'B' is calculated at the

near edge of the swath. The off nadir/incidence angle that defines the near edge of the swath is $(\beta - \theta_r / 2) = 28^0$. Since it would be an orbital mission, thus the effect of curvature of Earth needs to be taken into account by calculating the local incidence angle, '$\theta_{i,N}$', that is given by:

$$\theta_{i,N} = \sin^{-1}\left[\left\{\frac{R_e + h}{R_e}\right\}\sin 28^0\right] = 30.91^0$$

- The required system bandwidth needs to be calculated according to this local incidence angle and it would be: $B = \dfrac{c}{2 \times \Delta R_g \times \sin(\theta_{i,N})} = 9.74$ MHz ..... (4 - 9)

- In order to adequately sample the Doppler frequency, the minimum PRF should be:

$$PRF_{\min} \geq \frac{2v_e}{D} = 3950 \text{ Hz} \qquad \text{.....} \qquad (4 - 10)$$

where v_e is the effective/relative velocity.

- Similarly to ensure that at any instance of time, only one pulse is impinging in the target area, the maximum PRF = $PRF_{\max} \leq \dfrac{c}{2(R_{S,F} - R_{S,N})} = 5236$ Hz ..... (4 - 11)

- By ensuring that the minimum PRF is over sampled and also to be in the mid range, for time being, the PRF may be set at 4500 Hz.

$$\Rightarrow \qquad PRI = 1/PRF = 222\ \mu s \qquad \text{.....} \qquad (4 - 12)$$

- Under the strip map imaging mode, the observation time, integration time or aperture synthesis time, is the time once a target enters the antenna beam from one side and leaves the beam from the other side in azimuth direction. The observation time may be calculated from that of the azimuth footprint (F_a) at the centre of the swath as:

$$F_a = R_{S,C} \times \theta_a \cong 48.5 \text{ km} \qquad \text{.....} \qquad (4 - 13)$$

and under the assumption that the Earth is a perfect sphere, then the approximate observation time would be: $T_i \cong \dfrac{F_a}{v_s} = \dfrac{48.5 \times 10^3}{7.56 \times 10^3} = 6.39\ s$ ..... (4 - 14)

4.1.9 Summary of the Parameters

Different parameters discussed in the previous sections are summarised in Table 4 - 2.

Symbol	Description	Values
f_c	Carrier frequency	1.28 GHz
ΔA	Azimuth resolution (single look)	1.67 m
ΔR_g	Ground range resolution	30 m
B	Bandwidth to get 30 m range resolution at the near edge of the swath	9.74 MHz
f_r	Selected PRF (within the range of 3950 – 5350 Hz)	4500 Hz
Duty Cycle	Pulsed CW Extended Chirp (with 3.66 m diameter antenna)	6 % 100 % 14 %
P_t P_{av}	Peak RF transmitter power (at the input of the antenna) Average RF power	1 kW 60 W
PRI	Pulse repetition interval (reciprocal of selected PRF)	222 μs
S	Ground swath achieved from strip map imaging mode	58 km
h	Satellite altitude (SS, 97.7^0 inclination)	600 km
β	Incidence Angle (design should cater for 20 – 50^0)	30°
D	Diameter of the parabolic reflector antenna	3.66 m
BW_{3dB}	Half power beamwidth	4°
G	Gain of the antenna	32.67 dB
NF	Receiver noise figure	3 dB
Loss	Additional loss budget	3 dB
Polarization	Dual polarization (HH & HV)	
σ^0_{HH} σ^0_{HV}	Sensitivity (at 30^0 incidence)	– 15 dB – 21 dB
$(SNR)_{min}$	Minimum SNR at the centre of the main lobe - for the HH polarization - for the HV polarization	 12 dB 6 dB
σ_n	Thermal noise equivalent back scattering coefficient (for SNR=1)	– 27 dB

Table 4 - 2: Summary of the SAR parameters to be used in the design options

4.2 SAR Design Options

In order to arrive at the practically suitable design that fits in the stringent constraints imposed by available microsatellite buses, different SAR design options are analysed in the forthcoming sec-

tions. The SAR parameters mentioned in Table 4 - 2 would be used to calculate the SNR.

4.2.1 Option 1: Pulsed SAR

Almost all the known spaceborne SAR missions are based on pulsed technology. A pulsed system is characterised by transmitting a narrow (5 – 10 % of the PRI) but high powered modulated pulse. This pulse is scattered off the target and received, demodulated and recorded by the receiver. The system is designed such that both transmitter and receiver share same antenna.

If it is assumed that a power amplifier with 1 kW output is used and to achieve a $SNR > 12$ dB for $\sigma^0_{HH} = -15$ dB, then the required pulse width would be $\tau' = 13.33$ µs (which is a typical 5 – 10% duty cycle for a spaceborne pulsed SAR design [12]).

In order to image the swath (slant range), without overlapping the pulses, a minimum imaging time/receive window time is required, that may be calculated as:

$$T_{RW} = \frac{2\left(R_{S,F} - R_{S,N}\right)}{c} = 187\ \mu s\ . \qquad \ldots\ldots \qquad (4 - 15)$$

As previously calculated the PRI =222 µs, then 187 µs needs to be reserved for receiving the echoes from corresponding target area. These aspects are shown in Figure 4 - 11.

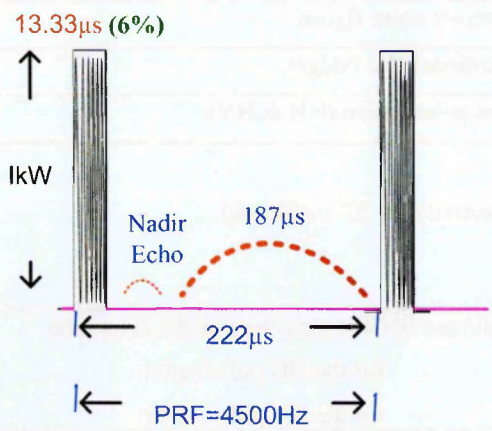

Figure 4 - 11: Pulsed SAR timing arrangement

SAR Equation for computing SNR

The radar equation links the physical dependences of the radar parameters from the transmitter, to the target and back to the receiver. It is a basic and important equation and could be derived in different forms. Detailed derivation is included in the Appendix A, whilst the form to be used is discussed here as:

The SNR for n coherently integrated pulses is:

$$(SNR)_n = \left[\frac{(P_t \times f_r \times \tau') \times G^2 \times \lambda^3 \times \sigma^0 \times \Delta R_g}{(4\pi)^3 \times R_S^3 \times 2 \times v_s \times K \times T_{sys} \times NF \times Loss} \right] [\mathrm{W}] \qquad \text{.....(4 - 16)}$$

where:

P_t = Peak RF power – the output of the PA (which is fed at the input of the antenna) [W]

G= Gain of the antenna (it is not a fixed value but incident angle dependent).

λ = Wavelength of the radar centre frequency. [m]

σ^0 = Normalized backscattering coefficient per unit area (incident angle dependent).

ΔR_g= The ground range resolution (varies non-linearly and is local incident angle dependent). [m]

f_r = The pulse repetition frequency. [Hz]

R_S= Slant range to the target (incident angle dependent). [m]

v_s = Satellite velocity. [m/s]

K= Boltzmann's constant = 1.6 x 10^{-23} $WK^{-1}Hz^{-1}$

T_{sys} = Operating Temperature in, Kelvin (290 K).

NF=Receiver noise figure (3 dB).

$Loss$= Lumped losses (scanning, beam shape, collapsing, integration, cable etc.) in the system (3 dB).

τ' = The time period of the chirped signal. [s]

The term $(P_t \times f_r \times \tau')$ used here in this equation sets the average RF power that the transmitter feeds to the antenna. If τ' is extended up to 100 % of the PRI, it becomes the CW case, where $\tau' = PRI = 1/f_r$, which yields $P_t = P_{av}$.

While looking at the SNR equation, there are four terms that have the angular dependencies. These are: the antenna gain, ground range resolution, σ^0, and slant range. In order to find out the SNR distribution according to the angular variations of the incidence angle, these factors need to be evaluated from nadir (0^0) to the set incidence angle (30^0) and beyond.

Figure 4 - 12 shows the antenna gain distribution over a range of ± 30^0 off the main lobe.

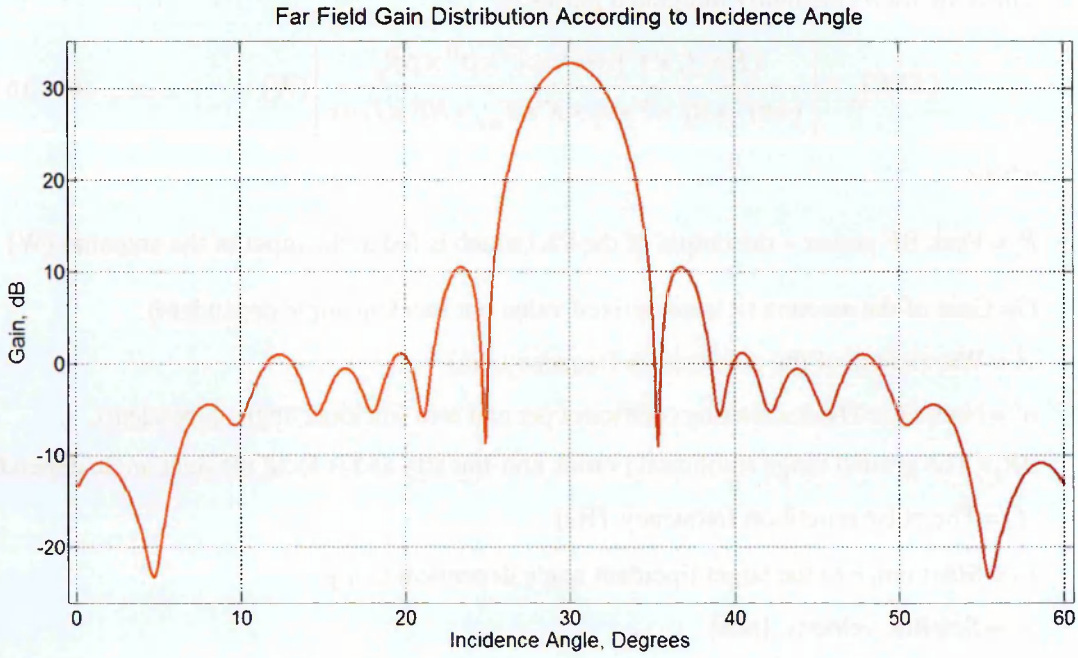

Figure 4 - 12: Antenna gain distribution around the ±30^0

Let us define an instantaneous incidence angle vector centred at 30^0 as $\beta_i = 0.01, 0.06, 0.11, \ldots\ldots\ldots\ldots\ldots\ldots, 60^0$, and map it over to calculate the instantaneous slant ranges according to: $R_S = h / \cos\beta_i$

Thus yields slant ranges from 600 km (nadir point) to 1201.8 km (at 60^0).

For calculating the instantaneous values of ground range resolution 'ΔR_g', additional effects of the curvature of Earth need to be incorporated. The instantaneous local incidence angle '$\theta_{i,N}$' may be calculated as:

$$\theta_{i,N} = \sin^{-1}\left[\left\{\frac{R_e + h}{R_e}\right\}\sin\beta_i\right] \quad \ldots\ldots\ldots \quad (4 - 17) \qquad [75]$$

By using this instantaneous local incidence angle, the ΔR_g is calculated by:

$$\Delta R_g = \frac{c}{2B\sin\theta_{i,N}} \quad \ldots\ldots \quad (4 - 18)$$

that varies non-linearly from 80.64 km (at nadir) to 16.25 m (at slant range of 1201 km).

The next factor which has the angular dependency is the σ^0. For calculating the SNR, standard profile of radar signatures are used [59], [91] which show the σ^0 variations according to the incidence angle. These angular plots are developed and published by [59] and are based on the data acquired from the field experiments. Appendix B shows the details of σ^0 characteristics at the L-band according to different terrain classifications. After analysing the available information, espe-

cially from the nadir returns point of view, the L-band, HH polarized, angular plot for Shrubs is selected, as it provides higher values at low incidence angles (near nadir). The plot is shown in Figure 4 - 13. This plot shows the mean values and the 5 % and the 95 % occurrence levels.

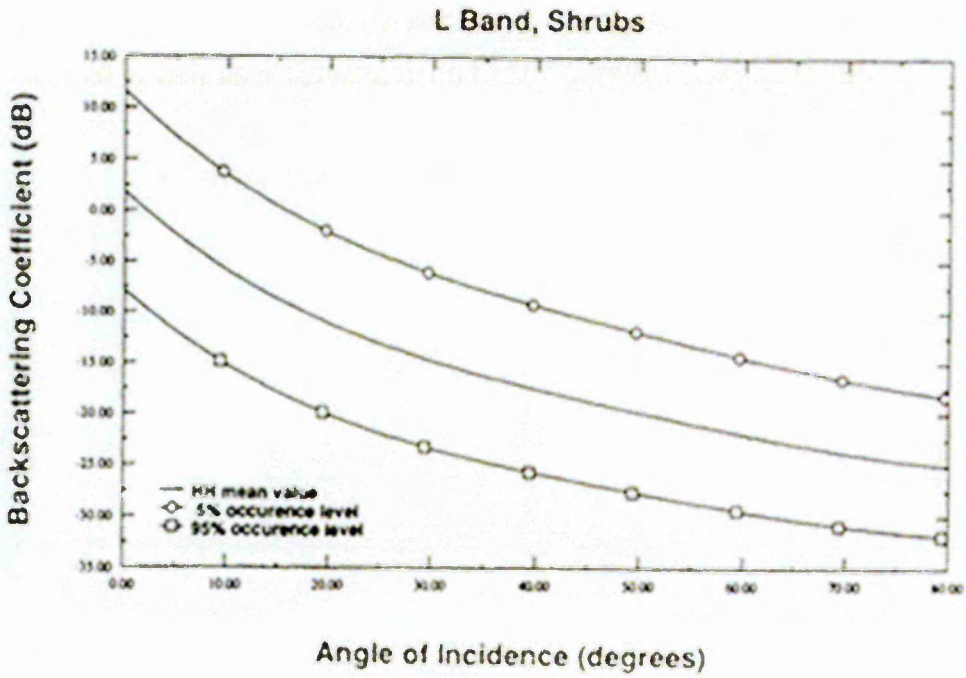

Figure 4 - 13: Relationship between incidence angle and backscattering coefficient

Source: Adapted from [59]

Considering this plot, the σ^0 variations are grouped into short intervals of incidence angle, and these are assumed to be constant during these intervals. These variations are shown in Table 4 - 3.

Range of incidence angles (degrees)	Mean value of σ^0 (dB)
0 – 5	2.5
6 – 15	– 7.5
16 – 25	– 12.5
26 – 35	– 15
36 – 45	– 17.5
46 – 60	– 20

Table 4 - 3: Mean values of σ^0 according to variations in the incidence angle

By incorporating the angular dependent instantaneous values of the antenna gain, ground range

resolution, slant range and σ^0 (from Table 4 - 3) into SNR equations, the achieved results are presented in Figure 4 - 14. It shows that the returns closer to the nadir angle produce a spike that has a value of ~ – 26 dB. This is because of the fact that ground range resolution is very large (~ 81 km). As the incidence angle increases, the ground range resolution size decreases, so does the SNR, as it drops to an average of – 45 dB. The returns from the first sidelobe (towards nadir) are ~ – 28 dB. The highest $(SNR)_{HH} = 12.01$ dB is achieved at the peak of the main lobe.

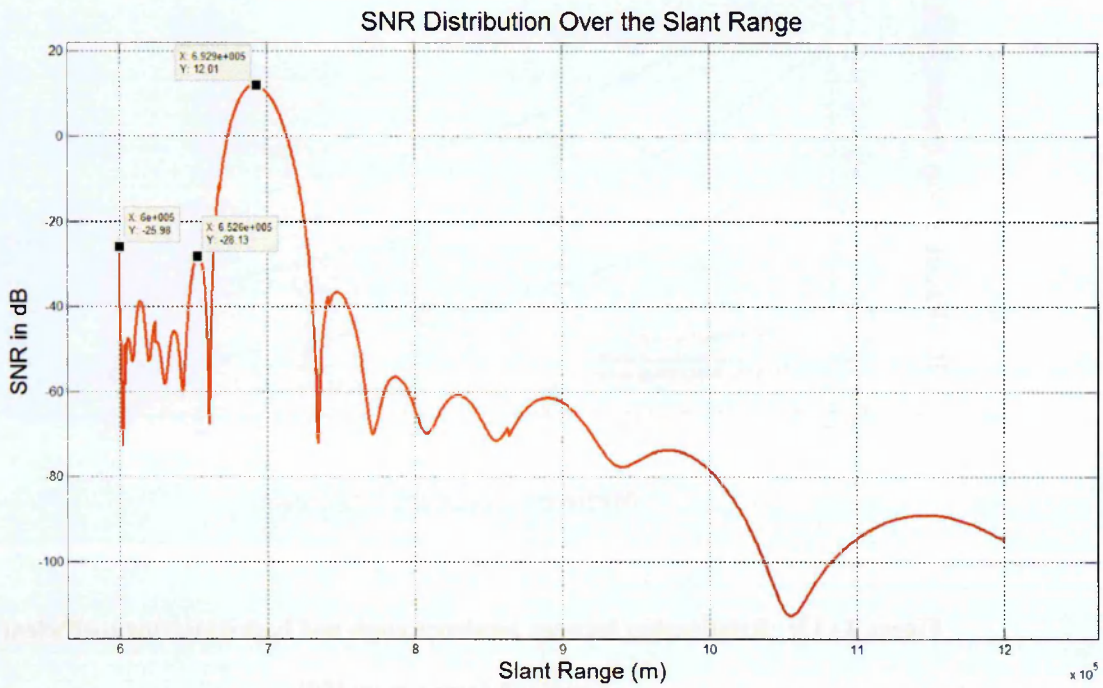

Figure 4 - 14: SNR distribution incorporating the angular dependencies and curvature of Earth

The role of each factor that contributes to the SNR is important but looking at this plot, it appears that the antenna radiation pattern has most dominating impact on the outcome of these results. Let us consider the different scenarios for the nadir returns. Although at nadir, the range resolution of 81 km (≡ 49 dB) is fed to the equation, which yields SNR = ~ – 26 dB, for $\sigma^0 = 2.5$ dB. If it is hypothetically assumed that range resolution size becomes 1000 km (≡ 60 dB), it would still yield the SNR = ~ – 15 dB at the nadir incidence, which would be far below the SNR achieved at the main lobe. In addition, if $\sigma^0 = 12.5$ dB is considered at 5 % occurrence level (shown in the Figure 4 -13), the corresponding SNR = ~ – 5 dB would be achieved for the ground range resolution of 1000 km.

Let us assume a special case scenario and assume that the flat earth at nadir is un-vegetated and acting as an mirror for the radar radiations. If it is assumed that all the parameters are kept same while analysing the impact of σ^0 under this scenario. Consider only the impact of the peak power

(1 kW); the gain of the antenna at nadir (- 13 dB) and at the main lobe (32 dB); and, the range resolution (81,000 at nadir and 30 m at the main lobe).

The received power from the nadir will be: Peak power x twice the antenna gain x range resolution and in terms of dB it would be 30 – 13 – 13 + 49 = 53 dB. Similarly for the main lobe, it would be 30 + 32 + 32 + 15 = 109 dB.

This simple calculation shows that there is a very wide gaps between the returns from the nadir and from the main lobe.

Considering all these worst case scenarios, it can be established that the effect of nadir returns onto the SNR may be ignored.

There are few glitches observed in Figure 4 - 14. These are because of abruptly changing the σ^0 values in the Table 4 – 3.

The relationship between instantaneous power, P_t (i.e., the peak RF output power from the PA and fed to the antenna at the time of transmission) and the average RF power P_{av} was established in Eq. 2 – 1. Here in this case, it yields the average RF power: $\Rightarrow$ $P_{av} = 60$ W

Analysis of Pulsed SAR Option

The design utilizes time tested and space proven concepts. The major advantage offered by this technique is the use of a single satellite and a single antenna. This mono-static design provides well synchronized transmitter and receiver operations.

In order to lessen the impact on mass and cost of the mission, a parabolic reflector antenna would be used. Reflector antennas need centralized RF power amplification. Generation and transportation of high instantaneous RF power (1 kW) remains a key technological challenge in the context of the microsatellite environment.

If a highly efficient (60 %) L-band PA is assumed, then to get 1 kW RF power, it needs 1.66 kW dc (direct current) power. The onboard power bus is designed to operate at 30 V. 1.66 kW dc would need 55 A current at the time of generating this pulse. The power sub-systems onboard the available buses are not designed to provide this type of power. There may be two approaches to handle this problem: either use 4 TWTAs as used with the MAPSAR, or use 5 parallel SSPAs, each with 200 W RF power output [49].

The TWTA approach is not only expensive (~ £ 6 M for only the TWTAs) but also heavy (~ 36 kg), thus may not be feasible in this situation. The SSPAs approach is cost effective, however, to compensate the peak power demands, it needs to use bulk capacitors—which are also large and heavy.

Although both transmit and receive cycles are separated in different time slots yet isolation is needed to prevent leakage signal flowing through the receiver. The RF output from the PA would be 1 kW (30 dB) and in the absence of any receive signal at that instant of time, it is only this 30 dB isolation which is to be achieved. Commercially available duplexers provide ~ 40 – 50 dB isolation; therefore, these may serve the purpose.

Due to handling high instantaneous powers, overall power losses (heat dissipation) would be higher once compared with a system that operates at low instantaneous power levels. Against this backdrop, irrespective of whether TWTs or SSPAs are used, the existing SSTL buses need to be significantly modified or redesigned to withstand corresponding changes. The combined effect of these changes may lead to somewhere closer to TecSAR (200 kg bus+100 kg SAR) or NovaSAR-S (300 kg bus +100 kg SAR). Therefore, using traditional pulsed SAR technology in the current form may bode ill for use with microsatellites.

4.2.2 Option 2: LFM CW SAR

The major concern of pulsed SAR technology is to sustain a high rate of change of current. Contrary to a pulsed system where the duty cycle is typically 5 – 10 %, a CW SAR is based on continuously transmitting and receiving the modulated signal (i.e., 100 % duty cycle) – usually through separate dedicated transmit and receive antennas as was discussed in section 2.5.

An attraction of a CW system for microsatellite use is to operate the SAR and the bus at reduced instantaneous RF power levels. For example, considering the pulsed case just discussed, with chirp period $\tau' = 13.33$ µs at $P_t = 1$ kW yields a $(SNR)_{HH} \sim 12.01$dB; has an average RF power of $P_{av} =$ 60 W. Approximately the same $(SNR)_{HH}$ may be achieved by increasing the chirp period to 0.222 ms (reciprocal of the PRF, thereby making it a CW case) and keeping all other parameters the same, with 60 W of continuous RF power.

The main inspiration for considering CW SAR as a suitable technology for the use with microsatellites stems from the fact that it is successfully being used from small aerial platforms and many concerning issues related to the conceptual design and subsequent developments have been tackled amicably. But once an extension of this technology to microsatellites is considered, many new challenges need to be addressed. These will be discussed in the forthcoming sections.

Antenna Isolation

In a CW system, the transmitter and receiver work simultaneously. High transmitter power suppresses the receiver if it is co-located. Isolation can be achieved through a duplexer with a common antenna, but commercially available duplexers can only provide isolation in the order of 50 dB or so. The spaceborne case under investigation has much higher requirements. Figure 4 - 15 has been drawn to illustrate the net isolation requirements. It is assumed that both transmitter

and receiver antennas are placed at the same location and both are pointing towards the same target area. It shows that the effective isotropic radiated power for the transmitter is 49.7 dBW. Due to the continuous nature of operation, at the same instant of time, the echoes would also be received, and the receive signal strength behind the receiver antenna would be -116.2 dBW. The echo signals have to compete with the signals continuously being transmitted from the co-located transmitter antenna. Thus, at any instant of time, the net required isolation would be ~ 166 dBW. This may not be achievable with duplexers alone.

Recently concluded PhD research at SSC has shown that physically separating the antennas i.e., operating transmitter from one satellite and the receiver from the other satellite—a typical bi-static (dual satellite) configuration—helps to achieve the required antenna isolation. In order for the echo signal to be interference free from the leakage signals flowing from the sidelobes of the transmitting antenna, the receiving satellite should be at least 20 km apart from the transmitter satellite. [99]

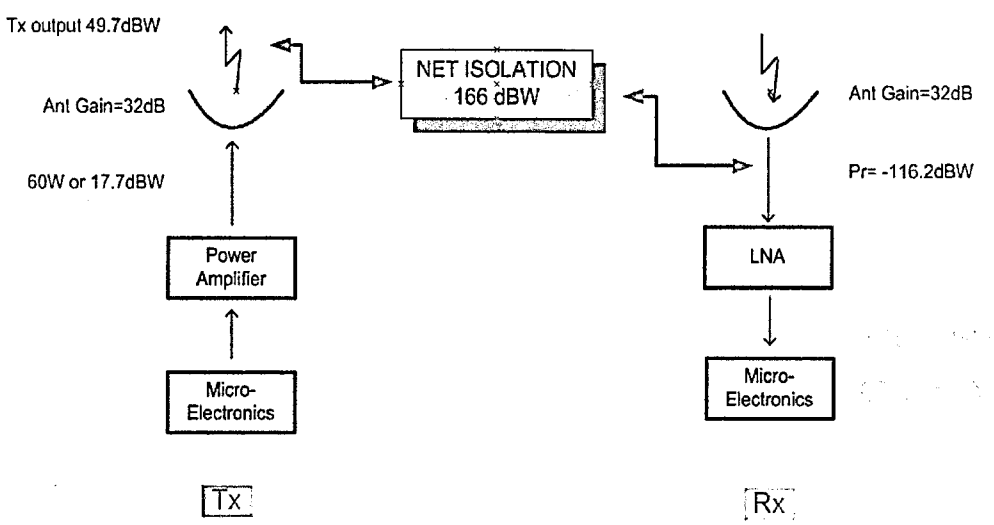

Figure 4 - 15: Antenna isolation requirements for a microsatellite based CW SAR

Synchronization between Bi-static Transmitter and Receiver

SAR is a coherent system, thus requires a very stable, well synchronized master oscillator/clock to perform modulation and demodulation. In the case of a mono-static pulsed system or an aerial CW SAR system (where two antennas are used from the same platform), the same master oscillator is used, thus synchronization does not become an issue. But it remains a major challenge to synchronize spatially separated transmitter and receiver platforms (in a situation where both are apart over a minimum of 20 km or so).

Establishing an inter-satellite link for this purpose seems to be a viable solution but it would incur

additional cost, weight and a continuous drain on already meagre power resources. Since both satellites would be spatially separated, both would have relative velocities due to natural orbital dynamics. Any information sent over an inter-satellite link would also suffer from additional Doppler shift due to this relative motion. Any synchronization scheme based on an inter-satellite link needs to incorporate this additional Doppler shift.

Analysis of the Bi-static CW SAR

Generating this low RF power (60 W) in continuous form is much easier then generating narrow and high powered pulses (1 kW) through a PA technology. It also certainly enables the use of single SSPA at these low RF power levels. Now the bus may not need any additional capacitor network or high power cathode voltage supply as 60 W at 30 V (60 % SSPA efficiency) would only need about 3.3 A of current that can be either drawn directly from the solar panels or through batteries. Thus, operating the system at low instantaneous power remains a major advantage that contributes to significantly reducing the weight of the entire system. In addition, continuous transmit and receive operations without involving any switching would get rid of T/R modules/switches, hence it would need a comparatively simple RF design.

However, to achieve adequate antenna isolation for the space applications, a spatially separated bi-static configuration becomes the necessity. A Bi-static configuration needs very accurate synchronization scheme to maintain coherency. By establishing an inter-satellite link for synchronization purpose would add cost and additional power consumption on both the satellites.

Besides many advantages, overall a full CW SAR implementation remains a two satellite based solution. This would increase the mission cost in terms of employing two satellites, their launch, insurance etc. This option therefore, does not fulfil the aims set for this research.

4.2.3 Option 3: ICW SAR – A Mono-static CW SAR Design Approach

It has been analyzed in the previous sections that the major advantage achieved from the pulsed system is in the form of a mono-static operation sharing a common antenna whereas from that of CW SAR is to operate the SAR and the bus at low instantaneous power levels. Major disadvantages that emerge from these techniques are: the pulsed system needs to operate with high instantaneous power levels thus requires a compatible power supply chain, increasing the complexity, weight and cost of the system; and from that of CW SAR is the need to use two satellites each for transmitter and receiver so that the required antenna isolation is achieved. There is a possibility of combining the advantages of pulsed and CW techniques while avoiding the disadvantages embedded in each type. This section will focus on this design concept and highlight the perceived problems.

ICW SAR Concept

For a spaceborne SAR (may it be pulsed or CW), there is a long travelling/delay time involved at the satellite altitudes. By exploiting this long delay time, a CW SAR can be designed that would only need a single platform while sharing the common antenna with the transmitter and the receiver (a peculiarity of a pulsed SAR).

This delay time t_d may be defined as the time taken by the transmitted chirp to travel from the satellite down to the Earth, reflected/scattered and travel back to the receiving antenna. Mathematically it may be linked with the near edge of the swath (i.e., Slant Range Near '$R_{S,N}$') as:

$$t_d = \frac{2 \times R_{S,N}}{c} = 4.52 \text{ ms} \qquad \ldots\ldots\ldots \qquad (4 - 19)$$

During this time interval 't_d' the number of pulses 'n_{p,t_d}' transmitted may be calculated as the product of the delay time and the PRF (f_r):

$$n_{p,t_d} = t_d \times f_r \qquad \ldots\ldots\ldots\ldots\ldots\ldots\ldots\ldots \qquad (4 - 20)$$

and by incorporating values, it would be: $n_{p,td} \sim 20$ pulses

The proposed SAR in this technique would work in an ICW mode, where the transmitter is switched ON for just enough time, t_{on} (= t_d) for the signal to be transmitted to the ground, scattered/reflected and returned to the spacecraft. The transmitter is then turned OFF, t_{off} (for the same length of time = t_d) until all the signal returns have been collected by the receiver. This process of switching ON and OFF is then repeated until the strip map image of desired length is acquired.

This arrangement is principally different from the pulsed system in which transmitter is switched ON and OFF according to a set PRF i.e., every time a pulse is sent, transmitter switches on and off once. Here, the transmitter remains continuously ON for a comparatively long time = t_{on} and keeps on transmitting chirps in CW form (in this ON time, '$n_{p,td}$'number of CW chirps would be transmitted) and then remains OFF for time = t_{off} (= t_d) of virtually the same period – achieving mark-space ratios approaching 50 %. Thus the switching ON and OFF the transmitter is set according to the delay time (t_d) and not the PRF. This arrangement thus yields a synthesized aperture that would have gaps for the off time – and this has consequences for the image reconstruction during signal processing.

The timing diagram presented in Figure 4 - 16 has been drawn with a view to show the summary of the design options discussed in this chapter.

The necessary comparison with a pulsed, extended chirp (a variant of the pulsed SAR but with higher duty cycle using same sized antenna), a full CW system and proposed ICW options in the light of parameters shown in Table 4 – 2 has been drawn to clarify these concepts in detail. The main aspect that needs to be kept in mind here is the relationship between the set PRF = 4500 Hz and the delay time, $t_d = 4.52$ ms.

First of all let us look at the pulsed system, it shows that once the transmission starts at $t = 0$ s, the first high powered but narrow pulse (chirp) is transmitted and then the receiver is switched on before the next pulse is transmitted. This defines one cycle of switching on and off. These cycles would be repeated according to set PRF. That means in one second, transmitter and receiver would be alternatively switched on and off 4500 times.

Although the switching ON and OFF between the transmitter and receiver would start at t = 0 s, but due to the long distance that the chirps have to traverse at space altitudes, the first reflected echo would be received after time = $t_d = 4.52$ ms. To achieve adequate SNR, the power needs to be amplified to 1 kW.

The second system shown here is a variant of the pulsed system in which the chirp duty cycle is increased to 14 % (30 μs). This extension in the chirp reduces the peak power from 1 kW to 445 W. The chirp can not be further increased as PRI = 222 μs and imaging the required swath needs 187 μs, thus 30 μs is the space where chirp may be extended, leaving 5 μs for safety margins.

The extended chirp with reduced peak RF power, yields the equivalent SNR – as achieved from pulsed system with 6 % duty cycle. Although this arrangement reduces the peak power by more than half however, generating 445 W RF power suffers from similar problems as seen with the pulsed system.

The third system shown is the bi-static CW. It shows that once the transmission starts, the corresponding echo starts receiving after 20 chirps but since a separate receiver antenna is used on the second satellite, this transmission and reception is done continuously for the required time period without any gap.

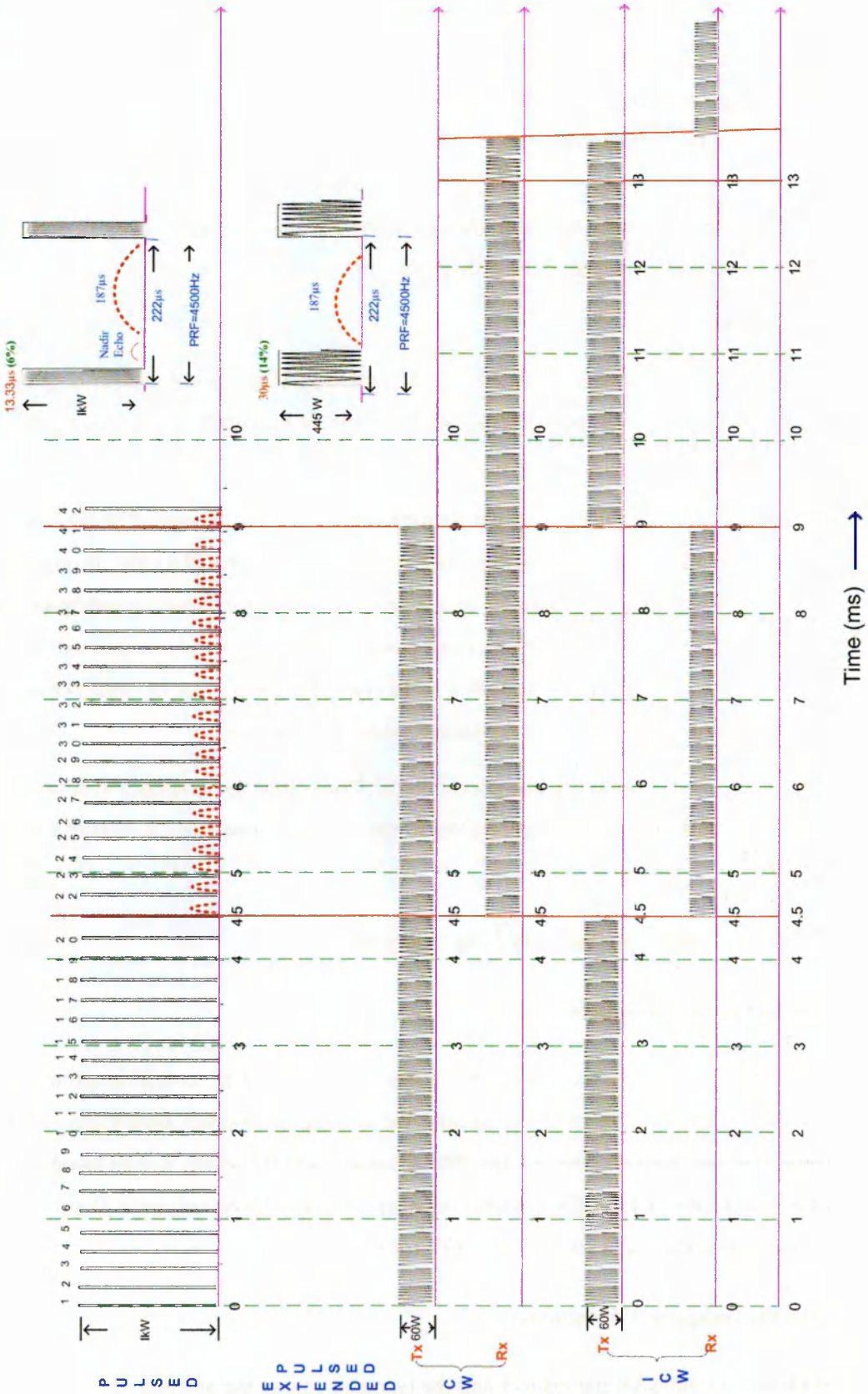

Figure 4 - 16: Timing diagram for the different SAR options

For the ICW case, the PA is cut off after transmitting 20 CW chirps and then lets the receiver to receive these 20 echoes. Antenna isolation between transmitter and receiver paths would be achieved by switching on/off the PA and LNA alternatively. This will make it possible to use only one antenna for both the transmitter and receiver (like that of a pulsed system). The mono-static configuration achieved with this ICW arrangement would facilitate in maintaining coherency by using the same Master Oscillator (MO) for the transmitter and receiver operations (somewhat similar arrangement to that of the pulsed system).

Advantages

ICW design would have advantages over the pulsed system in terms of operating the SAR and the bus at low instantaneous power levels which would be instrumental in reducing the overall power consumption, weight and thus cost.

It will have an overriding advantage once compared with the bi-static CW SAR as that would require two platforms whereas in this case it will use only one platform. In vogue airborne CW SARs yield two major advantages once compared with their pulsed counterparts and these are; operating the system at low instantaneous power levels and homodyne receiver design. Both these advantages can be achieved from this technique whereas in case of spaceborne CW SAR discussed previously, only the first advantage could be achieved.

Now since the transmitter is being used for 50 % less time as compared with pulsed or CW SAR operations, this provides the opportunity to use the same available DC power for longer imaging durations.

Problems Concerning the ICW SAR Concept

Sub-sampling the Doppler

It appears that leaving the gaps in the aperture are equivalent to sub-sampling the Doppler frequency. In essence, in order to sample the estimated Doppler bandwidth (3950 Hz)—while respecting the Nyquist criteria—the PRF is set at 4500 Hz which is over sampling the minimum PRF by a factor of 1.14. This ensures adequately sampling the estimated Doppler bandwidth during each time the transmitter remains ON for 4.52 ms.

Will the Image be Contiguous?

With the current SAR parameters and the type and size of the antenna selected, whenever a chirp is transmitted through the antenna, it impinges a footprint on the surface of the Earth that is approximately 50 km in azimuth (at the centre of the swath) and a 58 km in range. During one ON or OFF period, the along track (azimuth) distance that would be traversed:

$$t_d \times v_s = 4.52\times10^{-3} \times 7.56\times10^{3} = 34 \text{ m}$$

And during this ON/OFF time, 20 chirps would be transmitted /received. For the strip map mode of operation, the aperture synthesis time to image the whole of the scene (~ 50 × 58 km) requires ~ 6.39 s (Eq. 4 - 14) and 4.52 ms is a small fraction of this time. Once SAR moves 34 m in the azimuth direction, approximately for the same distance, the scene also moves out of the beam footprint in the opposite direction. But overall the scene remains under SAR illumination for the ~ 6.39 s. These corresponding movements of the sensor and the scene in opposite directions introduce gaps in the data being synthesized, for the periods the transmitter remains off, but the scene as a whole remains contiguous.

Affects of Gapped Synthesized Aperture on Image Reconstruction

For an ICW SAR the transmitter is cut off periodically as a design feature, thereby introducing gaps in the synthesized aperture. In Radar and SAR literature this gapped aperture is known as sparse aperture. Sparse aperture gives birth to known and pronounced signal processing problems. To obtain a fully compressed image, the synthesized data are processed by separately convolving, first of all with range and then with azimuth reference chirps. If both (the reference chirp and the data) are continuous, the fully compressed data produce representative target area image. But if the same operation is performed with the sparse data, image artefacts are produced due to appearance of gaps in the data. To illustrate this problem, the RADARSAT-1 data are processed for both continuous and interrupted modes of operations. The results are presented in the Figure 4 - 17.

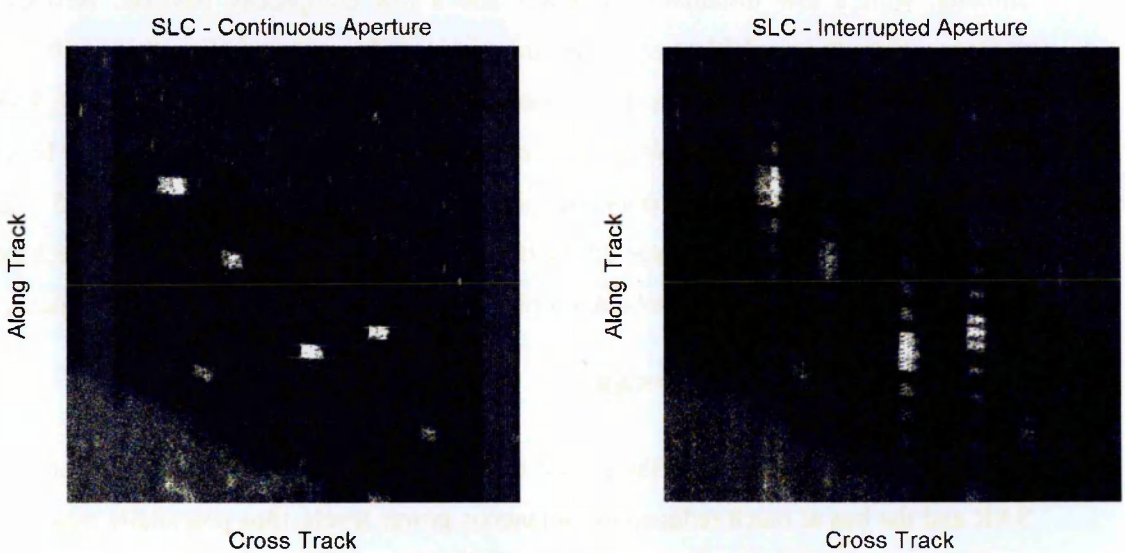

Figure 4 - 17: Comparison of continuous and interrupted aperture data and corresponding images

Part (a) represents an amplitude image of the range and azimuth compressed data—also called single look complex (SLC). The ships, sea and the built up areas etc. can be distinguished.

To generate sparse data, the gaps along the azimuth direction are introduced according to the settings of ICW SAR case under investigation (i.e., 20 time samples ON and 20 OFF) in the raw data. Now once this sparse data are processed by the same signal processing algorithm, artefacts are produced, as shown in the part (b).

These artefacts blur the image and reduce the signal levels by half as compared to those of the continuous aperture. In reality, these image artefacts mask the weak neighbouring targets, thus making it hard to distinguish the real targets from those of the artefacts.

To achieve full benefits offered by ICW SAR concept, this signal processing problem needs to be tackled efficiently so that an artefact free image can be obtained.

Note: Appendix C has been arranged with a view to define the radiometric artefacts in the context of SAR images and what are different contributing factors for these artefacts? To develop discussions during thesis, only the gaps in the data are considered as the concerning factor, thus, where so ever "artefacts" are discussed, it is discussed in the context of these gaps in the synthesized data.

Summary of ICW SAR Option

The ICW SAR technique provides a solution to the problems confronted once pulsed or CW SAR techniques are applied to the microsatellites. It allows a mono-static solution, employing a single antenna, with a low instantaneous power and a low complexity payload. Besides these advantages, from the available power onboard microsatellite point of view, it uses 50 % less power as compared to any other option. This saving is particularly useful for operating the SAR from the same available power for doubling the imaging time, or compensating the power loss due to reduction in the performance of onboard solar cells which typically degrade at 0.5 – 2.75 % per year. [100]. The problem of image artefacts (due to the sparse aperture) that this technique necessarily endangers needs to be resolved in order to establish the efficacy of this technique.

4.2.4 Option 4: ECMP SAR

LFMCW once compared with the pulsed technique offers the major advantage of operating the SAR and the bus at much reduced instantaneous power levels, thus potentially making it possible to use a single SSPA with the reflector antenna. This advantage makes it more attractive for use from the microsatellite bus that has a highly constrained power budget. But using LFMCW SAR technique from a single platform necessitates ICW technique to achieve the required antenna isolation.

To offset the problems associated with the ICW technique, if the swath is compromised then it may be possible to fit an ECMP SAR within the power limits of the microsatellites. This would yield benefits similar to those achieved from using FMCW SAR from microsatellites.

With the current SAR parameters under consideration (i.e., with 3.66 m diameter antenna), the PRI is 222 μs. As shown in Figure 4 - 11 that for a swath of 58 km, the required slant range imaging time T_{RW}=187 μs, thus the chirp may be extended up to 30 μs. This extension reduces the instantaneous power level from 1 kW (for the pulsed SAR) to 445 W to achieve same SNR. By considering 60 % efficiency of the power amplifier, this power level would still need hardware somewhat similar to that of a pulsed system discussed earlier.

If it is desired to bring down this 445 W RF power level closer to LFM CW case (60 W) then both the swath and the minimum PRF have to be manipulated. As we know from A – 37 that $PRF_{\min} = {2v_e}/{\ell}$, where v_e is the relative velocity, which almost remains fixed at 7.22 km/s; and ℓ is the antenna length along azimuth direction. By incrementally increasing ℓ, correspondingly $PRF_{\min}$ value decreases. If the SNR is simultaneously calculated by incrementally lowering the PRF and increasing the pulse width, a situation comes which brings the peak RF equal to 60 W. At that instance, the ℓ is found to be 5 m. This size of the antenna thus creates the required "space" where chirp may be extended to a safe limit which enables a single SSPA to be used directly with the available buses.

With the similar reasoning used while selecting a suitable *f/D* ratio for 3.66 m antenna, the simulations were run for the 5 m antenna as well. The comparative results are shown in Figure 4 - 18. Basing on these results, a *f/D* ratio of 0.6 is selected and accordingly the far field radiation pattern is shown in Figure 4 - 19. These results show that the main lobe gain is 35.31 dB and the half power beamwidth, $BW_{3dB} = 3.1^o$. Using this information, different ranges are calculated.

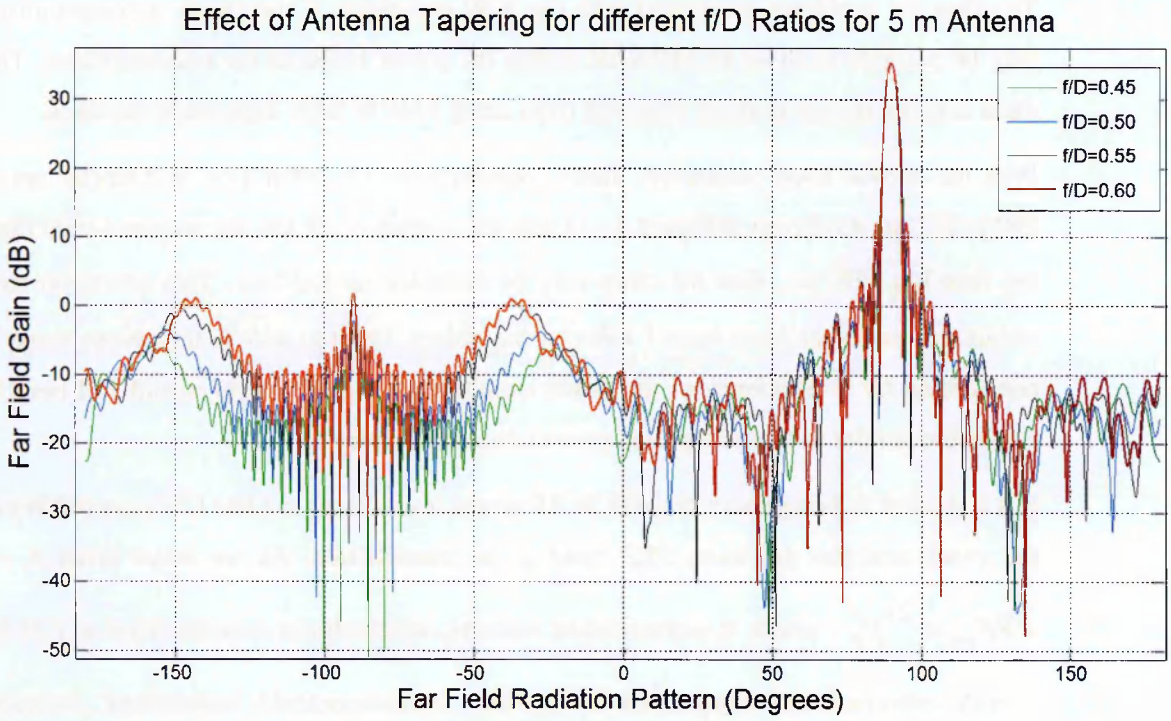

Figure 4 - 18: Comparison of 5 m antenna radiation patterns by varying *f/D* ratios

Given h=600 km, incidence angle, β = 30^0 and $\theta_r = 3.1^0$,

- The Centre slant range would be: $R_{S,C} = 692.82$ km
- The Near slant range would be: $R_{S,N} = 682.41$ km
- The Far slant range would be: $R_{S,F} = 704.07$ km
- The incidence angles at the near and far slant ranges, due to the half power beamwidth are: $\beta - \theta_r/2 = 28.45^0$ and $\beta + \theta_r/2 = 31.55^0$, respectively. By incorporating the curvature of Earth effects, the local incidence angles at the near and far slant range would be: 31.40^0, and 34.91^0, respectively. These local incidence angles yield the corresponding ground ranges of 330 km and 375 km (off nadir point), thus a ground swath of approximately 45 km is achieved.
- By using the 31.40^0 (local incidence angle $\theta_{i,N}$ at the near edge of the swath), a ground range resolution of 30 m requires the system bandwidth of 9.6 MHz.
- The minimum PRF = $PRF_{\min} \geq \frac{2v_e}{D} = 2890\ Hz$

- The maximum PRF should be: $PRF_{\max} \leq \dfrac{c}{2\left(R_{S,F} - R_{S,N}\right)} = 6923 \text{ Hz}$

- By over sampling the minimum PRF by ~ 1.25 times, the PRF may be set at 3600 Hz.

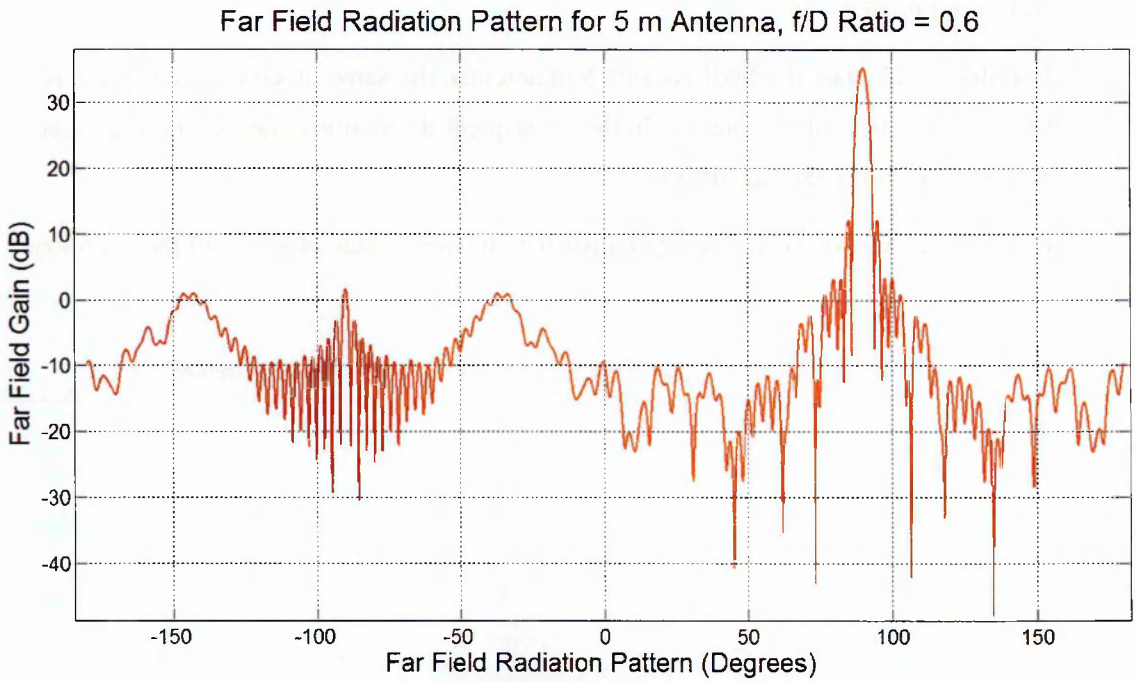

Figure 4 - 19: Far field radiation pattern for the selected *f/D* ratio of 0.6 m

Then, the $\text{PRI} = 277\ \mu\text{s}$. The receive window time (to image the swath in slant range) would be:

$$T_{RW} = \frac{2\left(R_{S,F} - R_{S,N}\right)}{c} \cong 145\ \mu\text{s}$$

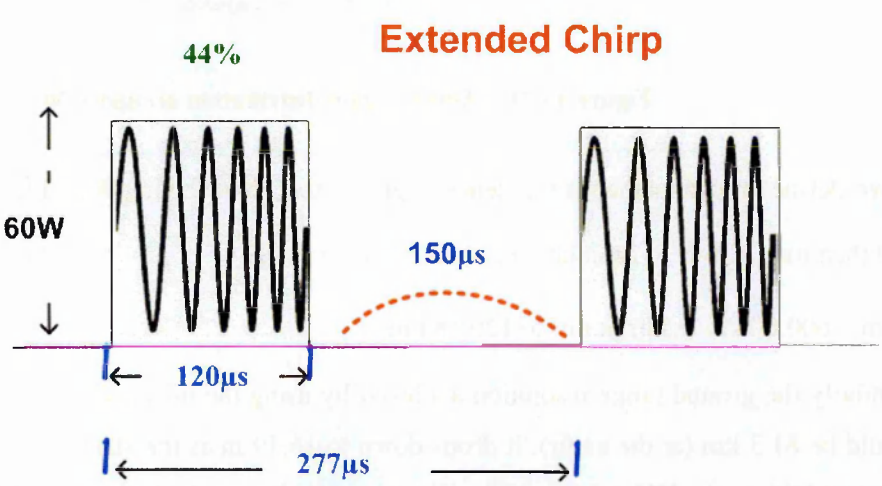

Figure 4 - 20: Timing arrangement for ECMP SAR

In order to keep safety margins, this may be slightly extended to ~ 150 μs. If the effect of the nadir return is neglected, then 277 – 150 = 127 μs is the usable space to adjust the chirp. Additionally if 7 μs are kept for pulse rising/falling and switching over times etc., then 120 μs would be available for the chirp to be extended. This yields a 44 % duty cycle. These setting are shown in Figure 4 - 20.

In order to calculate the SNR for this 5 m antenna, the same procedure is adopted here that was followed for the 3.66 m antenna. In the subsequent discussions, the effects of curvature of Earth are incorporated in the calculations.

Figure 4 - 21 shows the antenna gain distribution over a range of ± 30^0 off the main lobe.

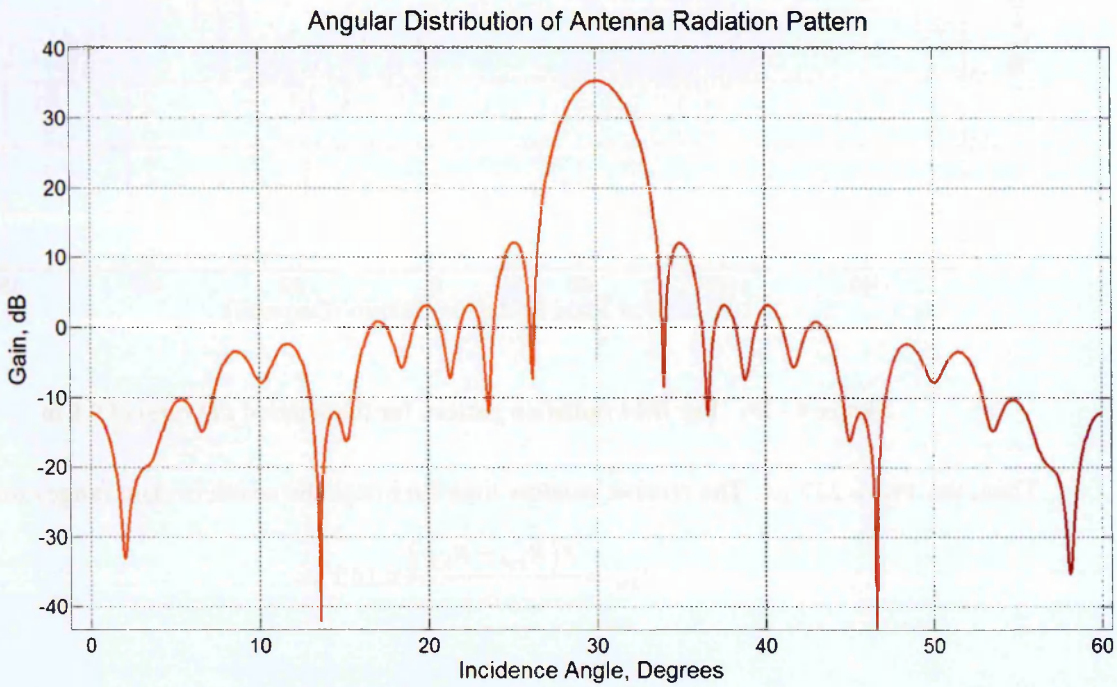

Figure 4 - 21: Antenna gain distribution around ± 30^0

If we define an instantaneous incidence angle vector: $\beta_i = 0.01, 0.06, 0.11, \ldots\ldots\ldots\ldots, 60^0$ and then map it over to calculate the slant range by $R_S = h/\cos\beta_i$; it would yield the slant ranges from ~ 600.00 km (nadir point) to 1201.8 km.

Similarly the ground range resolution achieved by using the instantaneous local incidence angle, would be 81.3 km (at the nadir). It drops down to 16.49 m as the slant range increases to 1201.8 km. In addition, the HH polarized σ^0 variations according to the incidence angle mentioned in Table 4 - 3 are used here.

By incorporating the angular dependent instantaneous values of the antenna gain, ground range resolution (after taking into the curvature of Earth effects), slant range and σ^0 into SNR equation, the results so achieved are shown in Figure 4 - 22.

It shows that the returns closer to the nadir angles are ~ – 35 dB because of a very large ground range resolution (~ 81km) size. As the incidence angle increases, the resolution cell size decreases, so does the SNR, which drops to an average of – 60 dB. The returns from the first sidelobe (towards nadir) are ~ – 30 dB. The highest $(SNR)_{HH} = 12.72$ dB is achieved at the centre of main lobe. Likewise for the HV polarization, if $\sigma^0 = -21$ dB is considered for 25 – 35^0 then the main lobe SNR would be ~ 6.57 dB in the centre.

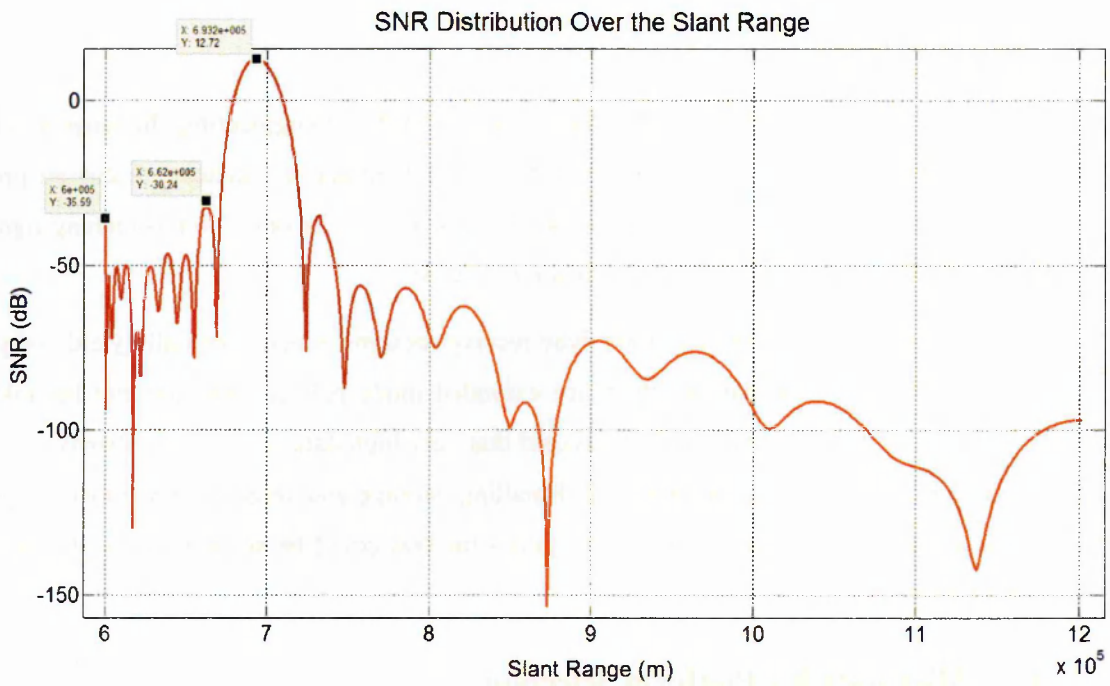

Figure 4 - 22: SNR distribution over the slant range

Advantages

This design option is based on operating the pulsed SAR in extended chirp mode. This design approach is orchestrated around using a 5 m parabolic antenna. This antenna provides two fold design benefits: one reducing the 3 dB beamwidth that yields comparatively smaller ground swath thus reducing the receive window timing; and secondly lowers the minimum PRF limit.

By using the pulsed SAR in this extended chirp mode under these design arrangements, the advantages of operating at low instantaneous power levels that are equal to those of the CW SAR would be achieved. This would enable the transmitter to operate a single SSPA with the low cost

and light-weight reflector antenna, thus reducing much of the complexity and additional arrangements required with the narrow but high peak powered pulse. 60 W peak power operating at 30 V would need (with 60 % SSPA efficiency) 3.3 A of the current, which may directly be drawn from the batteries/solar panels without involving any capacitive network or high voltage power supplies required for the electron beam amplifiers.

Being a pulsed SAR the synthesized aperture would be continuous in nature in comparison to the aperture achieved from the ICW SAR technique, which yields a sparse aperture (hence it needs sparse aperture filling algorithms).

Achieving a 45 km swath by operating a single beam at L-band, makes the overall design simple as compared with TecSAR (X-band) where multi-beams are required to achieve adequate swath.

Concerning Issues

Launching 5 m antenna with a microsatellite poses a difficult engineering challenge and needs an out of the box solution. The advances in the field of inflatable antennas, discussed previously, look promising and they are strong competitors for deployable ones—for launching light-weight and large size antennas with compact stowage volume.

The CW SAR benefits from the homodyne receiver designs which eventually yields very low data rates from the same bandwidth. Since extended mode pulsed SAR may not be able to take benefits of reduced data rates, it is envisaged that very high data rates—a peculiarity of the spaceborne pulsed SAR, would be produced. Handling, storage and subsequently transferring the data to the ground stations, for the given imaging time that could be achieved from this design, is a concerning issue.

4.3 Microsatellite Platform Selection

SSTL-100 , SSTL-150 and SSTL-300 buses and their baseline capabilities were discussed in the previous chapter with a view to keep the capabilities and limitations of the platforms in mind while analysing the SAR design options. After analysing different design options, let us select one out of these buses to proceed with further design analysis.

Considering the mass these platforms offer to the payload, the possibility of fitting an APAA is remote as the minimum sized APAA that is planned with the NovaSAR-S weighs ~ 70 kg at S-band and it may be envisaged that this mass would increase significantly if a similar design is adopted at L-band. Thus we are left with the choice of a passive reflector antenna. Inference may be drawn directly from the L-band, 6 m AstroMesh antenna that weights 14.5 kg (less feed assembly). If ~ 25 kg mass budget is allocated for the antenna (reflector and the feed), then besides other constraints, the SSTL-100 bus is limited to supporting only 15 kg of payload. Thus we need

to rule out the SSTL-100 bus on these grounds.

Although the average RF power remains the same in both pulsed and CW techniques generating narrow, high powered pulses through TWTAs or SSPAs would need considerable changes in the bus design, specially the power sub-system. Considering these aspects, the Pulse SAR option—from the point of view of using it from the SSTL-150 or SSTL-300 bus without incorporating major changes is also remote.

Now we are left with CW SAR (both bi-static and mono-static options) and ECMP SAR options. The instantaneous RF average power of 60 W at 30 V with a SSPA having 60 % efficiency would need a DC power of 100 W that is within the capabilities of existing batteries and the solar cells onboard SSTL-150 bus.

From the RF transmission point of view, the major mass contributing subsystems are the complete antenna assembly and the PA. As stated earlier, a mass budget of ~ 25 kg may be allocated for the reflector antenna and the feed assembly. A mass needs to be allocated for the PA and the sensor electronics. Since both the design options (ICW and ECMP SAR) utilize a single SSPA that is considerably light in weight as compared to TWTs, by allocating ~ 30 kg mass budget (similar to that of NovaSAR-S) for the PA and sensor electronics, a total of ~ 55 kg mass is achievable for the payload. Thus from the payload mass point of view, the SSTL-150 seems to be sufficient to support the SAR payload. SSTL-300 bus would be an over kill.

The attitude determination and control system onboard SSTL-150 and SSTL-300 buses provide almost similar capabilities. Likewise onboard data storage and the download links also come with equivalent capacities. The detailed impact of these on the SAR design will be dealt with in chapter 6.

This discussion may be summarized that SSTL-150 bus is considered suitable for accommodating any of the ICW or ECMP SAR options presented in this chapter.

4.4 Summary and Conclusions

This chapter dealt with a number of key issues that encompass the SAR design in the framework of microsatellites. Initially different application-specific requirements were analysed in the light of baseline capabilities offered by the available buses and necessary tradeoffs were discussed. This led to derivation of SAR parameters that are subsequently used with the different design options.

Pulsed technology is a time tested and widely used from aerial and spaceborne platforms. It offers the major advantage of completing transmit and receive cycles from a single platform. But overall, the design is complex, requiring high instantaneous operating power, hence the spacecraft bus

needs to be tailored/redesigned to withstand such requirements. All this gives birth to high weight and costs, thus limiting its suitability for a 150 kg class of micro-satellites.

The CW technique is a catching up technology for airborne SAR and is being successfully used from UAVs which share many of the constraints of micro-satellites. It may therefore be a suitable contender for use from micro-satellites. However, due to simultaneously transmitting and receiving the chirped signals, satellites need a much greater isolation between the transmitter and receiver as compared to aircraft. Thus, in order to achieve adequate antenna isolation, two satellites are essentially required, one each for the transmitter and the receiver. This doubles the overall mission cost.

The ICW SAR concept combines the advantages of pulsed and CW techniques and avoids the disadvantages of both. It provides a solution for completing the transmit and receive cycles from a single platform but the signal processing needs additional stages to address the problems from the sparse aperture.

It was discussed in the specific scenario of ECMP SAR where the chirp is extended to a limit that peak power is reduced to a level somewhat equal to CW cases. It would then enable a single SSPA with reflector antenna and by operating a single beam at L-band, the swath of 45 km may be achieved. Reduced swath eventually gives the benefits of synthesising a continuous aperture as opposed to ICW where a sparse aperture is synthesized, which requires a gap filling algorithm to obtain artefact free images.

5 SIGNAL PROCESSING ASPECTS OF ICW SAR

The concept of ICW SAR was introduced in the previous chapter and it was also highlighted that this technique inherently gives birth to sparse apertures that have pronounced signal processing problems. This chapter deals with the detailed analysis of these signal processing aspects of the ICW SAR concept and presents the gap filling technique to address these problems. For this purpose, a real SAR dataset which was acquired by the RADARSAT-1 is utilized. The gap filling algorithm's effectiveness is evaluated by comparing the results with those of the available dataset, as if there were no gaps.

5.1 The RADARSAT-1 Dataset

The efficacy of the sparse aperture filling algorithm can be established by applying it to real SAR data. For this purpose, both raw data (unprocessed data taken from the sensor, also known as SAR signal data) and the signal processing algorithms are required. Since none of the existing operational spaceborne SAR mission utilizes LFM CW SAR technique, for the purpose of demonstrating the signal processing problems of the ICW SAR and validating the gap filling algorithm's efficiency, spaceborne pulsed SAR data are used instead, under an assumption, that both pulsed and CW systems adhere to the same SAR principles to measure the target backscattering properties, and the difference is only in the RF front end/technique.

The raw dataset that is utilized for this purpose was acquired by RADARSAT-1on 16th June, 2002 of the Vancouver area, Canada, at 02:03:50 and 02:04:50 hours, by using Fine Beam 2 (Near). In this mode, the radar could achieve ~ 8 m ground resolution (nominal) with 45 km ground swath. It was only capable of providing single polarized (HH) data. This raw data has been provided by [12] for academic research purposes. To process this data, the relevant signal processing algorithms have been acquired from the Microwave Earth Remote Sensing laboratory, Brigham Young University. During the signal processing of this dataset, different values of the parameters are utilized which are mentioned in Table 5 - 1 [12].

Figure 5 - 1 shows map of the Vancouver area acquired by optical sensors. The area of interest (approximately 40 x 40 km) which corresponds to the SAR data is marked with the black square.

Parameter	Symbol	Value	Units
Pulse Width	τ'	41.74	μs
Pulse Bandwidth	B	32.317	MHz
Radar Frequency	f_c	5.30	GHz
PRF	f_r	1256.98	Hz
Effective Radar Velocity	v_e	7062	m/s
Ground Velocity	v_g	6613	m/s
Azimuth FM Rate		1733	Hz/s
Slant range sample spacing	ΔR_S	4.635	m
Ground range sample spacing	ΔR_g	~ 7.2	m
Spacecraft heading		344.49	degrees
Platform Latitude		48.36	degrees
Platform Longitude		229.29	degrees
Satellite orbit radius	(R_e+h)	7,189,029	m
Local Earth sphere radius	R_e	6,390,524	m
Incidence angle at near range		38.64	degrees
Incidence angle at the mid range		40.15	degrees
Incidence angle at the far range		41.61	degrees
Nominal slant range	$R_{S,C}$	1000	km

Table 5 - 1: RADARSAT-1 parameters used during the signal processing

Source: Adapted from [12]

A detailed description has been included in the Appendix A, which shows how the one dimensional data (the echo) are stored in the signal memory—so that at the subsequent stages, it could be processed to obtain a two dimensional map like image. For this dataset, the memory was arranged that stored the each received chirp along the rows of the matrix and range samples are along the columns. The rows are also called range lines whereas the columns are known as range cells. The direction of the radar forward movement is upward and from the left side of the image. A portion (6104 rows and 6098 columns) of the available raw dataset is selected for the subsequent signal processing analysis. Figure 5 - 2 represents the amplitude of the range and azimuth compressed data. The range and azimuth processed data are also known as the single look complex (SLC) image. The images produced by the SLC data are in the slant range whereas the optical image shown in the Figure 5 – 1 is in ground range.

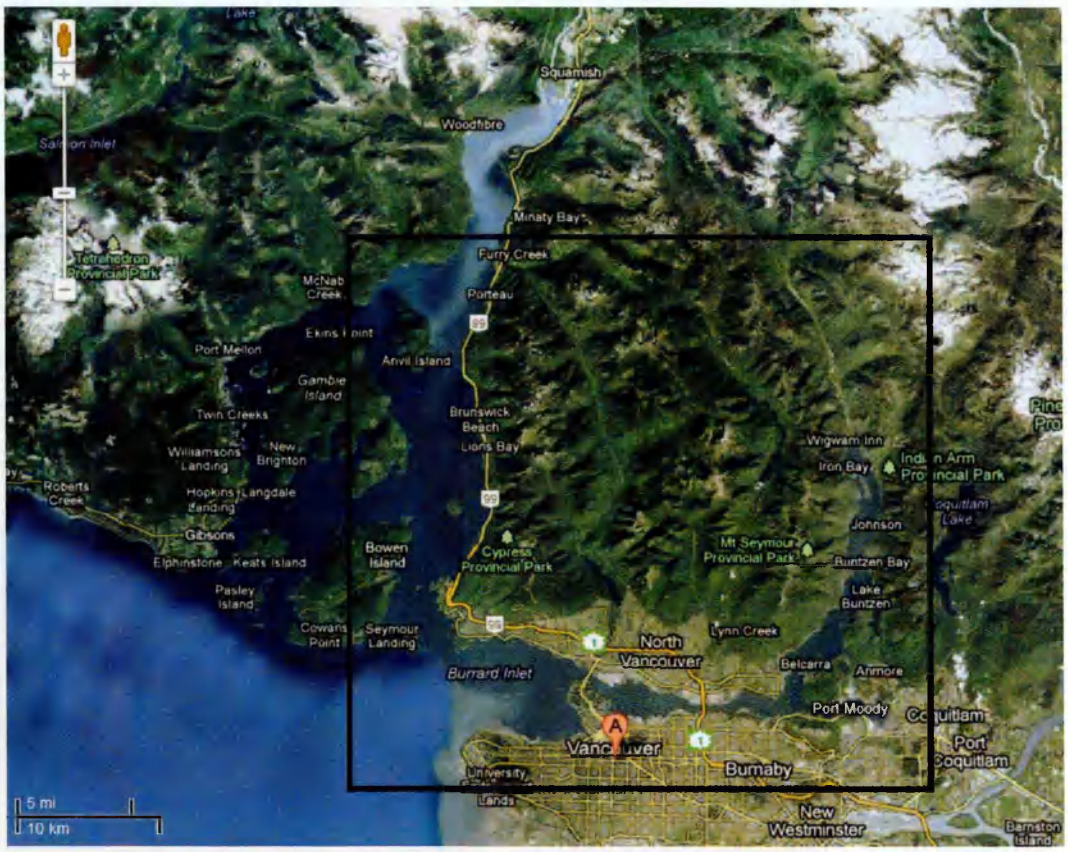

Figure 5 - 1: Map of the Vancouver (Canada) area, acquired by optical sensors

Source: Adapted from Google Maps (Grid Reference: 49.399356, – 123.021126)

The received echoes are down converted to the baseband signal and are recorded as complex data that have real and imaginary parts, which are called in-phase (I) and quadrature (Q) channels. The phase of a single channel (HH polarized in this case) is uniformly distributed over the range $-\pi$ to $+\pi$. In essence, the single channel SAR system phase provides no valuable information, while the amplitude (or intensity/power) conveys the useful information. [62]

The SLC amplitude image shows a wide range of landscape features in the area. These encompass: homogenous and inhomogeneous, natural and manmade, shorelines and off shore areas, part of Vancouver city area (towards middle lower part of the image), sea, ships, mountains etc.

The classic SAR image distortions can be clearly observed. The layover of the mountains suggests that the data was acquired from the left hand side of the image. The manmade features, especially in the urban areas, look much brighter in the image. The image also shows a calm sea, as a result of specular or mirror like reflection – where the reflecting surface directs incident energy in the direction away from the sensor. Had it been a rough sea, the predominant radiation interaction would have been due to diffuse reflection and the sea would have looked much brighter. As a result of the calm sea, the presence of ships in the dark background can be easily

identified. As a whole, these features make the data and the image a good test case for analysing the effects of the interrupted SAR mode of operation and validating the efficacy of the gap filling algorithm.

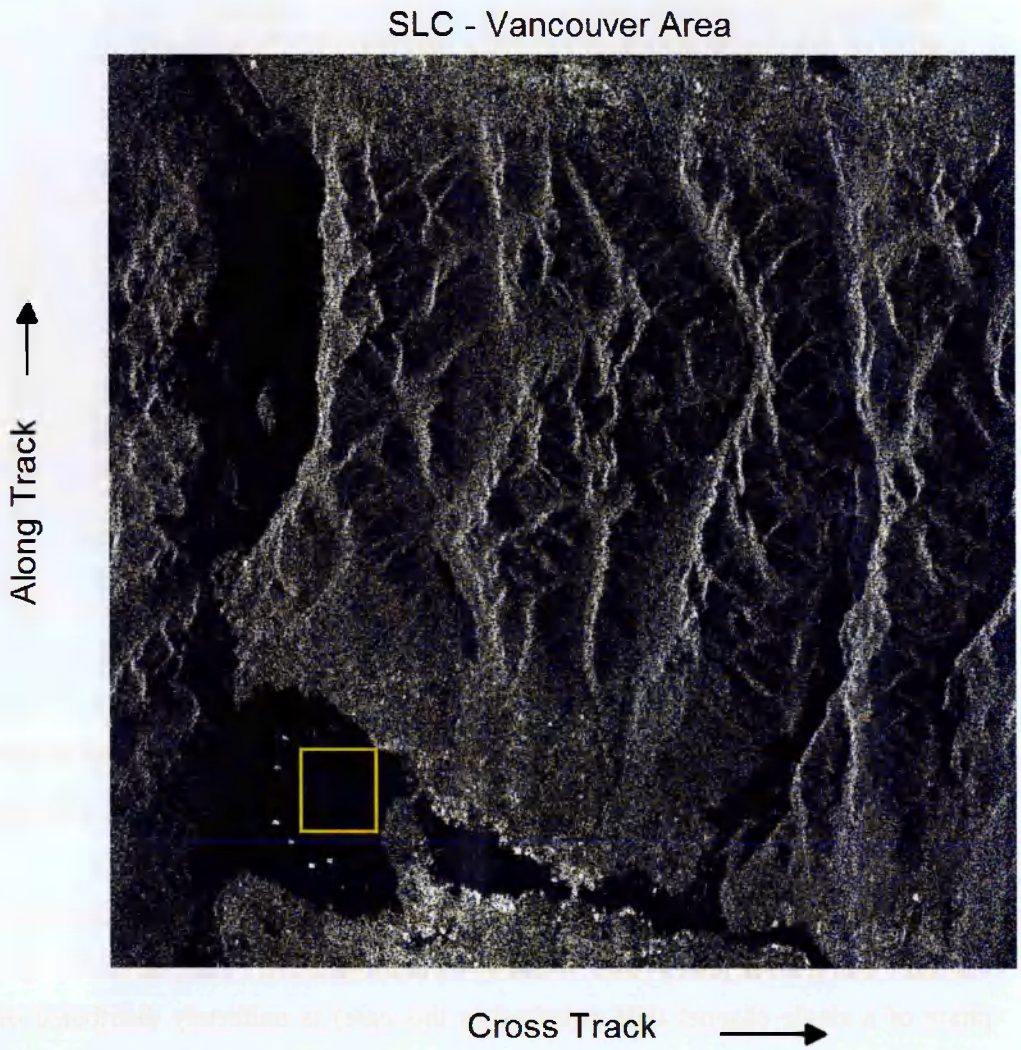

Figure 5 - 2: The SLC amplitude image of the Vancouver area

For a homogeneous area, the SLC data statistics adhere to established distributions [67]. The SLC amplitude, given by $A=\sqrt{I^2+Q^2}$, displays the Rayleigh distribution; whereas the intensity/power $= A^2$, follows a negative exponential distribution; and the real and imaginary parts follow zero mean Gaussian distribution [62].

To demonstrate/validate these data statistics, a small portion of the SLC image, as shown by a yellow box towards the lower left part of the Figure 5 - 2 is selected. This selected area encompasses 500 azimuth and 500 range bins. By analyzing these SLC data samples for amplitude, intensity, real and imaginary parts, the corresponding histograms are obtained, as shown in the subsequent figures.

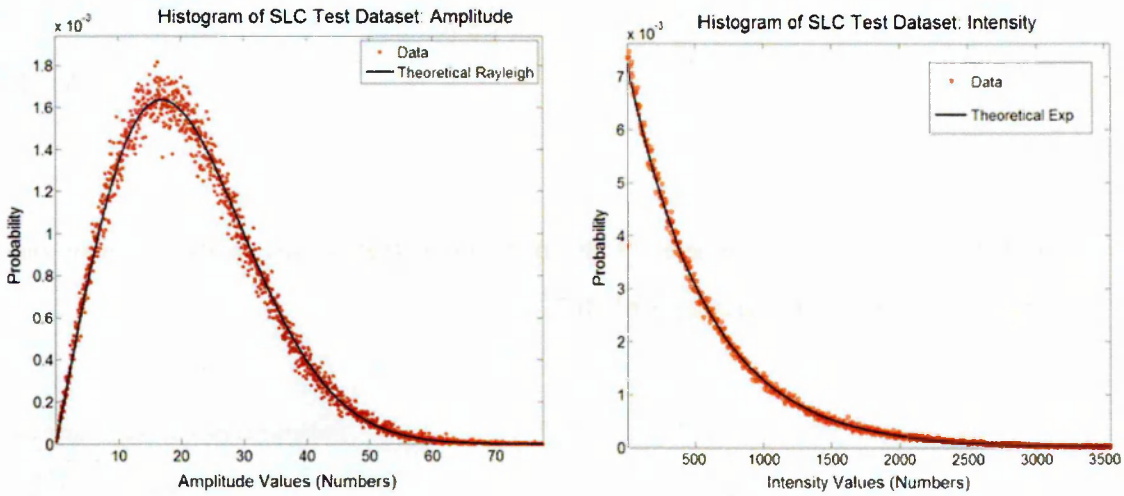

(a) (b)

Figure 5 - 3: (a) – The fitting of Rayleigh PDF to the amplitude histogram of SLC test dataset

(b) – The fitting of Negative Exponential PDF to the intensity histogram of SLC test dataset

The SLC amplitude dataset under consideration has mean = 21.2032, variance = 126.7578 and the SD = 11.2587, thus it yields a ratio of the SD to the mean = 0.5310 (that is close to the single look theoretical value of 0.5227 of the Rayleigh distribution [67]).

Figure 5 - 3 (a) shows the histogram of the amplitude SLC test dataset. This histogram matches the theoretical Rayleigh PDF that is defined by:

$$f(A,b) = \frac{A}{b^2}\exp\left(-\frac{A^2}{2b^2}\right) \qquad \text{.....} \qquad (5 - 1)$$

where 'A' is the amplitude of the dataset and 'b' is the Rayleigh distribution parameter that relates to the mean of the data by: mean = b $\sqrt{\pi/2}$; and for the given dataset, b = 16.9754. The probability is maximum at 'b' as shown here in this plot.

For the Intensity/Power = p = I^2+Q^2 = A^2 of the SLC dataset under consideration, have mean = 576.3344, variance = 351980 and the SD = 593.2795, thus it yields a ratio of the SD to the mean = 1.0294 (that is close to the single look theoretical value of 1.0 of the negative exponential distribution [67]). This ratio indicates that the speckle noise would appear more pronounced in the intensity images than in the amplitude images that have this ratio of 0.5227.

Figure 5 - 3 (b) shows the histogram of the intensity/power SLC test dataset. This histogram data are consistent with the theoretical negative exponential PDF that is defined by:

$$f(p,b)=\begin{cases}\dfrac{p}{b^2}\exp\left(-\dfrac{p}{b^2}\right) & \text{for } p \geq 0 \\ 0 & \text{for } p < 0\end{cases} \qquad \ldots\ldots\ldots \qquad (5-2)$$

where 'b' is the rate parameter of the distribution that relates to the mean of the data by: mean = b^2, and to the variance = b^4. [67]

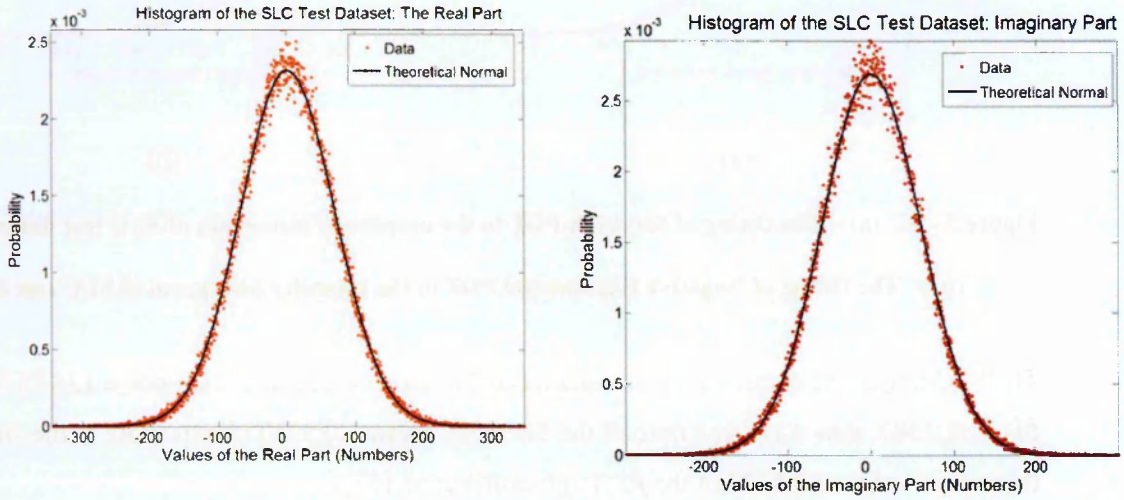

(a) (b)

Figure 5 - 4: Fitting of Gaussian PDF to the histogram of (a) – the real part (b) – the imaginary part of the SLC test dataset

Similarly the real and imaginary parts of the data adhere to the Gaussian distribution, given by:

$$f(\mu,\sigma)=\frac{1}{\sigma\sqrt{2\pi}}\exp\left(-\frac{(x-\mu)^2}{2\sigma^2}\right) \qquad \ldots\ldots\ldots \qquad (5-3)$$

where μ is the mean of the data and σ is the SD. The histogram of the real and imaginary parts of the SLC test dataset are plotted in Figure 5 – 4 (a) and (b) respectively. The real part have mean = – 0.2461, variance = 287.7514 and the SD = 16.9632. And the imaginary part have mean = – 0.2864, variance = 288.4318 and the SD = 16.9833. These histograms are consistent with the Gaussian distribution.

Since this chapter is organized in the framework of ICW with a view to highlight the signal processing problems and suggest/validate the gap filling algorithm, and for this purpose, the analysis of the raw data is also considered helpful for subsequent discussions.

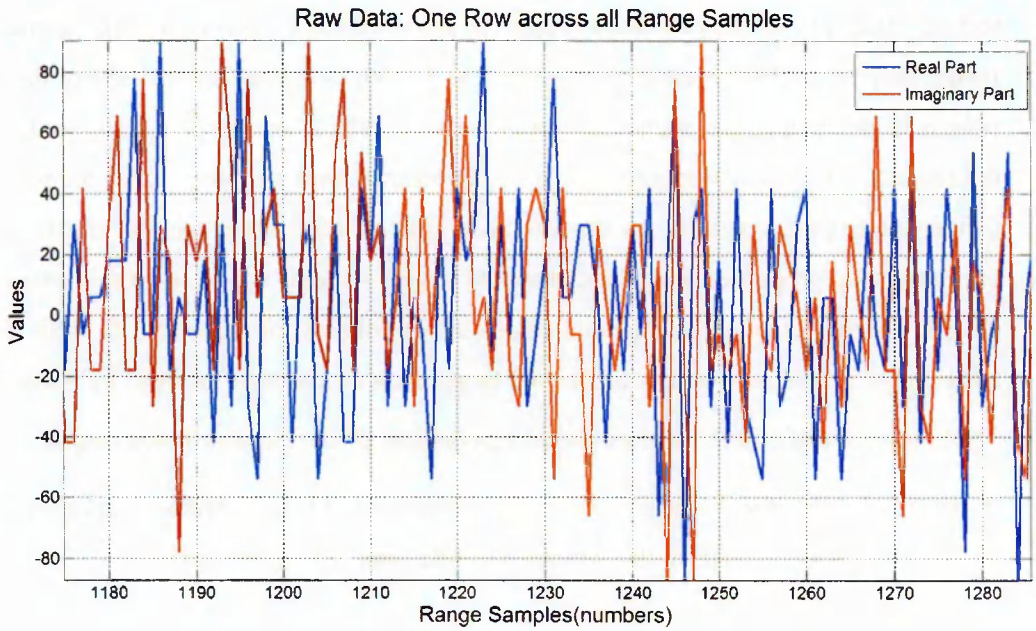

Figure 5 - 5: The real and imaginary parts of the received signal (one row across all the columns)

By considering the raw dataset that was used to produce the SLC image of Vancouver area, if only a single row across all columns (i.e., one range line) is selected, then the real part have the mean = – 0.4838, variance = 2280.8 and SD = 47.7582 and the imaginary part mean = 0.6091, variance = 2295.5 and SD = 47.9114. These statistics show a wide spread of the data about the mean values.

The time vs. signal values for the real and imaginary parts are shown in the Figure 5 - 5. The plot shows a rapidly changing and highly excursive signal that has values ranging from ~ ± 85.

5.1.1 The Effects of Continuous and Interrupted Apertures on the SLC Amplitude Image

To compare the effects of an interrupted aperture with that of a continuous aperture, the same raw dataset that was used to produce Figure 5 – 2 is now introduced with the required gaps (i.e., 20 time samples ON and 20 time samples OFF) along the track direction. To draw comparison between continuous and interrupted apertures, both the SLC amplitude images are shown together in Figure 5 – 6. The upper image represents the continuous aperture whereas the bottom one is for the interrupted image.

By comparing the images, it can be determined that the interrupted image has become blurred and grainy looking. However, features such as mountains, lakes, sea, presence of ships in the sea, build up areas etc., are detectable/distinguishable.

Having a synoptic view of both the images, it may be ascertained that at the image level, the de-

tection capability of the processed image for the interrupted aperture is still maintained, and the image may be useful for some users—such as for military applications, where the primary purpose is to detect a target, such as the presence of a vehicle or a tank in a forested area, a ship in the sea etc., which means targets with a strong contrast with the surrounding areas, as can be seen in this interrupted aperture. As this research aims at application-specific measurements of the backscattering properties from the distributed targets—it may not be helpful in extracting the fine details. For this situation, as the detailed discussion follows subsequently, the SNR drops for each target (may it be distributed or individual target such as a vehicle or ship) by 3 dB. This reduced SNR makes it difficult to measure the corresponding σ^0 for the distributed targets.

In order to restore the imagery to be comparable to that of the continuous aperture, the problems introduced due to the gaps in the synthesized data need to be addressed.

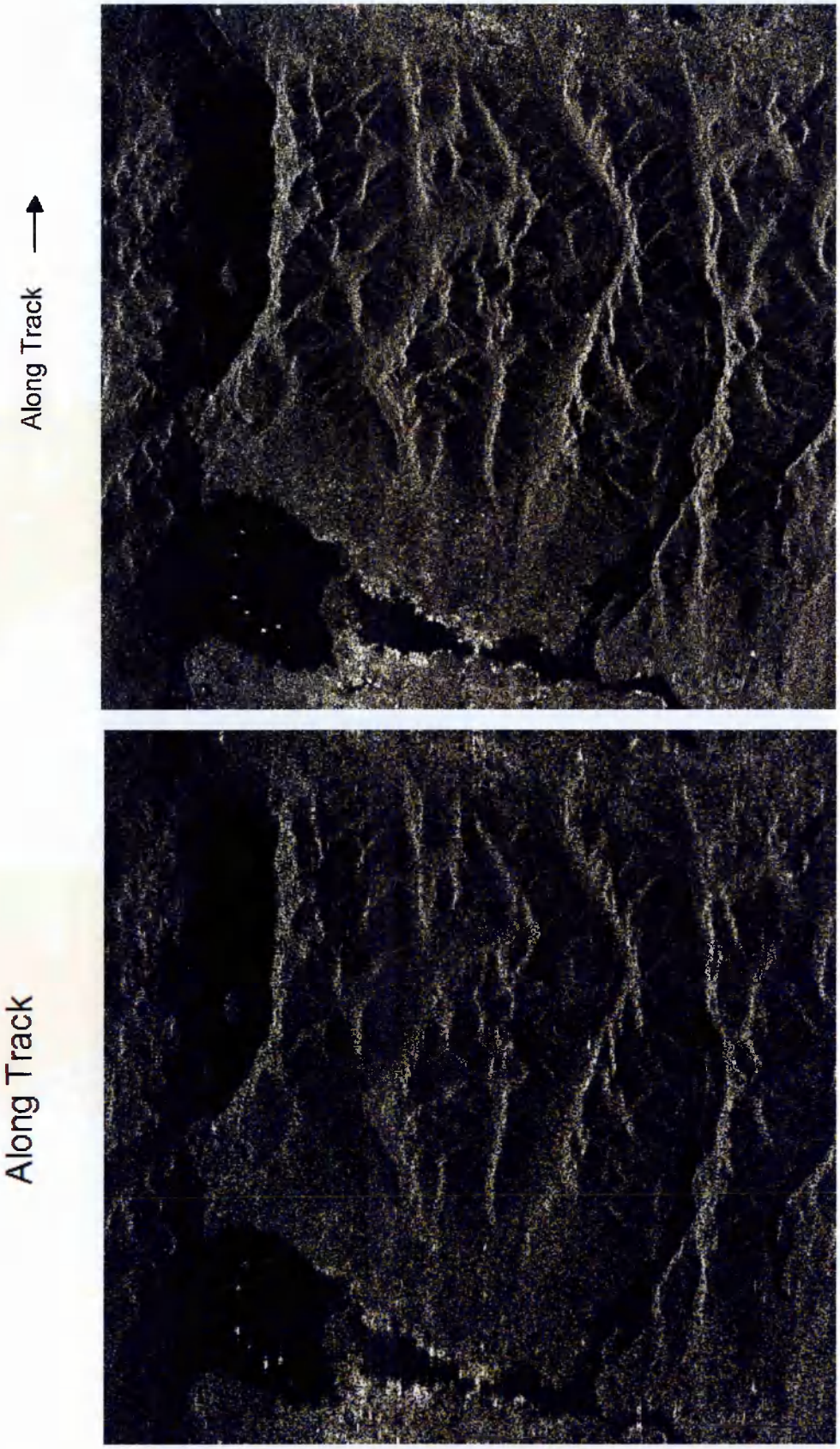

Figure 5 - 6: The SLC amplitude image of the Vancouver area for the interrupted aperture

The gaps have more severe impact once the image is zoomed to, to find the fine details. Thus a portion of this figure (ships in the sea), is selected for comparative analysis. Figure 5 - 7 shows the stepwise signal processing implementation for both continuous and interrupted apertures. Parts (a), (b), (c) correspond to continuous aperture whereas (d), (e), and (f) relate to the corresponding interrupted aperture stages.

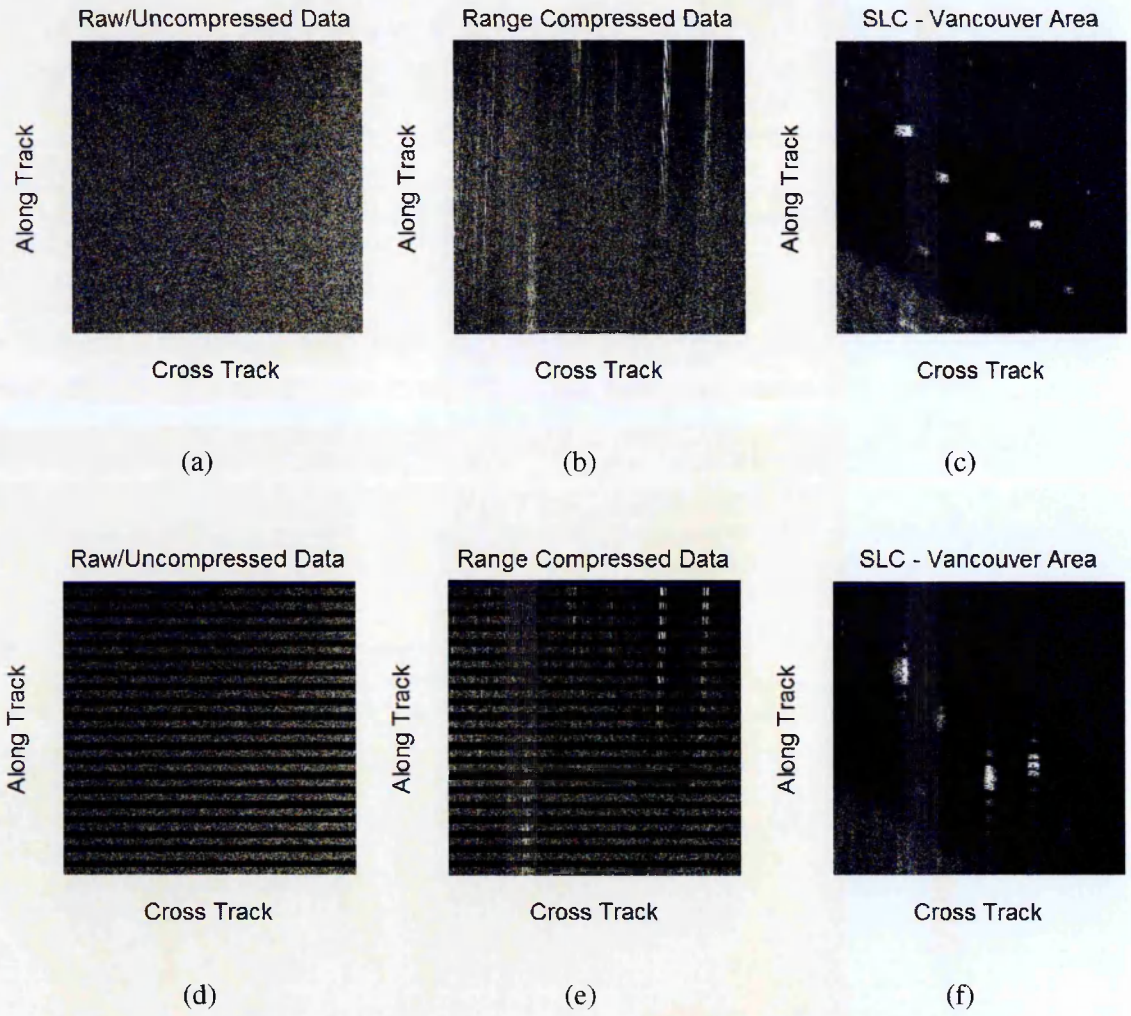

Figure 5 - 7: Stepwise comparison between continuous and interrupted apertures

It is discussed at length in the Appendix A that in order to achieve fine range resolution and higher SNR, a chirped signal is transmitted instead of a narrow and high power pulse. The energy in the echo signal is spread all along range and azimuth directions. Signal processing is therefore required to compress the signal in a way that energy corresponding to each target in range and azimuth is put into corresponding energy bins that help in finally making the map-like image of

the target area. For this purpose, the received signals need to be compressed separately in both range and azimuth directions.

Figure 5 - 7 part (a) displays the grey scale image of the raw data matrix for the continuous aperture. At this stage, since the received energy is spread all along the range and azimuth directions it is difficult to discriminate the targets in either direction. To obtain a meaningful image, first of all the received data are range compressed by matched filtering the cross track data with the copy of the transmitted signal (chirp) – which is also known as the range reference chirp. This operation compresses the data along the cross track direction, as shown in part (b) of this figure. Next step is for the azimuth processing which needs the azimuth reference chirp. This reference chirp is convolved with the range compressed data along the azimuth direction. The output is range and azimuth compressed (SLC) data, the amplitude of which is shown in the part (c) of this figure. The ships in the background of calm sea can be easily discriminated.

For the interrupted aperture, periodic gaps are introduced along the track direction, as can be observed in part (d). Similar to the continuous aperture, the first step is the range compression and the corresponding results are shown in part (e). When comparing part (e) with part (b), it is evident that the gaps which were present in the raw data are still visible in the range compressed data. It is because the range compression is performed along each range line and those range lines where data are missing yield empty data locations. This is not the case for the azimuth compression as now the gaps occur along rows (range lines) and data are processed for each column (range cell). As a result of this matched filtering operation between a continuous signal (azimuth reference chirp) and the other signal that has periodic gaps, the outcome is to fill up the gaps with artefacts that can be seen in SLC amplitude image of part (f). The individual ships—easily identified in the part (c)—are now looking three and more in part (f).

In addition to the above description, let us have a look at these processing steps (in the framework of Range Doppler Algorithm (RDA)) at discrete level for both continuous and interrupted apertures.

- The raw data are in the time domain.
- The first step is to perform the range compression through convolution. It involves a range Fast Fourier Transform (FFT), followed by reference signal (range filter multiply) and then a range Inverse FFT (IFFT). The reference signal is the copy of the chirp that was transmitted.
- Figure 5 – 8 shows the stepwise implementation of the range compression operation. Part (a) shows the real part of one of the rows (range lines) across all the columns (range cells). For achieving higher processing efficiency, the range data are converted to the frequency domain, where the range reference chirp (real part of which is shown in part (b)) is multiplied by the frequency domain data and then converted back to the time domain by taking the IFFT. The

result of this convolution is the range compressed data. The real part of the range compressed signal (same row across all columns) is shown in the part (c).

- From the range compression point of view, there is no difference in the results achieved from continuous and interrupted apertures except the gaps along the track direction would remain visible, as has been discussed previously and shown in Figure 5 – 7 (e).
- The azimuth FFT transforms the data into Range Doppler domain for further processing.
- Range cell migration correction that is range time and azimuth frequency dependent is then performed here.
- Azimuth matched filtering is performed as a frequency domain matched filter multiplied at each range bin. Finally the complete data are again converted to time domain by taking IFFT.
- This range and azimuth compressed data are called SLC.

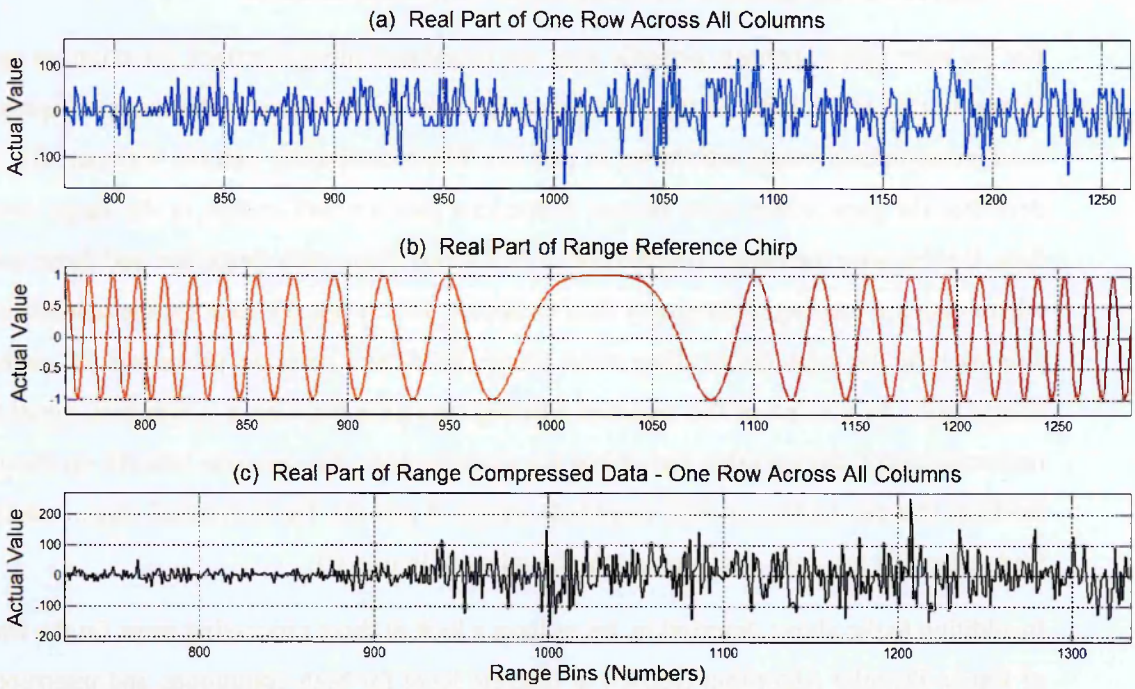

Figure 5 - 8: Stepwise discrete level implementation of the range compression

Figure 5 - 9 has been arranged to highlight the azimuth processing differences between the continuous and interrupted apertures. Parts (a) and (b) show one column (range bin) across all the rows (azimuth bins) for the continuous and interrupted apertures, respectively (for the range compressed data). For each range bin, a separate azimuth chirp is generated because the estimated Doppler is range dependent, as discussed in the Appendix A. For clarity, the azimuth chirp that is generated for one range bin is shown in part (c). This azimuth reference chirp—separately generated for each range bin—is multiplied by the azimuth data that is converted to the frequency domain.

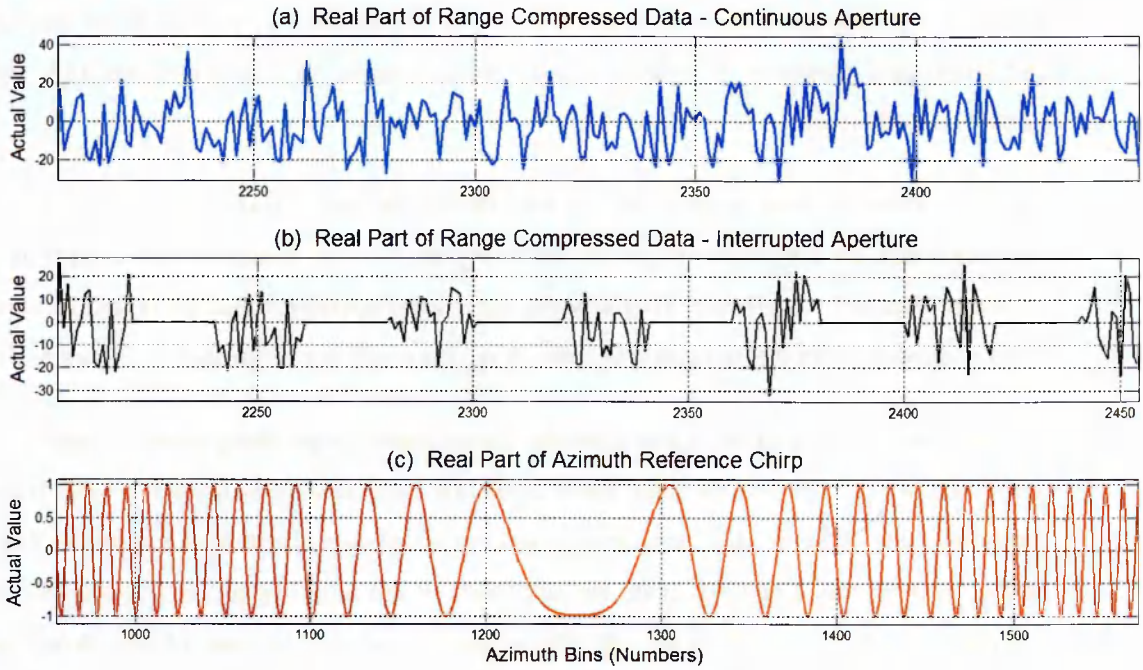

Figure 5 - 9: Azimuth compression for continuous and interrupted apertures

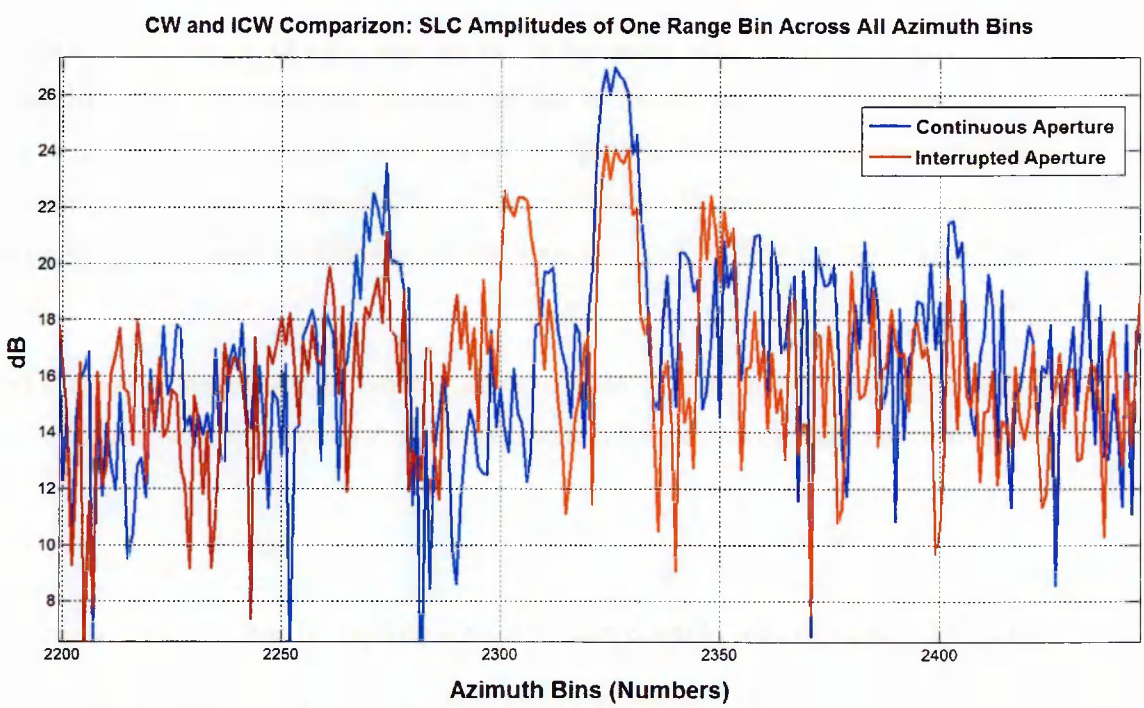

Figure 5 - 10: Comparison of SLC amplitude of one range bin across all azimuth bins for continuous and interrupted apertures

For the interrupted aperture scenario, the actual problem arises during azimuth compression. Here the matched filtering is performed between one signal that has periodic gaps and the other that is continuous in nature.

Figure 5 - 10 illustrates the comparative results of the azimuth compression for the continuous and interrupted apertures. In order to clarify the difference, SLC discrete amplitude signals are plotted on a dB scale.

Having a combined look at these two figures clarifies the problem associated with the interrupted aperture. Once the continuous signal shown in Figure 5 – 9 (a) is azimuth processed, the result is shown in Figure 5 – 10 (blue). Similarly the interrupted aperture signal presented in Figure 5 – 9 (b) is convolved with the azimuth reference chirp, the result is over plotted in Figure 5 – 10 (red).

For the continuous aperture, let us consider the strongest target along these azimuth bins, it has amplitude of ~ 27 dB. For the interrupted mode, the same amplitude drops by 3 dB. It also introduces artefacts in the neighbouring areas, masking actual targets with low amplitude. The severity of the masking effect depends upon the amplitude of the actual target itself. As is the case here, the main target has 27 dB amplitude, the artefacts produced because of this strong target are masking the nearby low amplitude targets.

5.1.2 Analysis of the Image Artefacts

Figure 5 – 9 (b) represents one range cell across all range lines for an interrupted aperture scenario (only the real part of the signal). It can be observed that the periodically switching ON and OFF the transmitter makes the data appear like a train of Rect functions. In order to analyse the phenomenon of appearance of the artefacts in the SLC image, it would be helpful to discretely analyse the data as a train of Rect functions and then extend the same analogy to complete data matrix.

Before analysing the train of Rect functions through computer experiment, it needs to be analysed mathematically. This periodic signal is shown in Figure 5-11 and may be written as:

$$x(t) = \sum_{n=-\infty}^{\infty} \Pi\left(\frac{t - nT_0}{\tau}\right) \qquad \ldots\ldots\ldots \qquad (5 - 4) \qquad [101]$$

Where 'τ' is the ON time of this signal, 'T_0' is the time period and 'n' is an arbitrary number. To get the Fourier series of this signal, let us first find out the Fourier series coefficients 'x_n' that is given by:

$$x_n = \frac{1}{T_0} \int_{-\frac{T_0}{2}}^{\frac{T_0}{2}} x(t) e^{-jn\frac{2\pi t}{T_0}} dt \qquad \ldots\ldots \qquad (5 - 5)$$

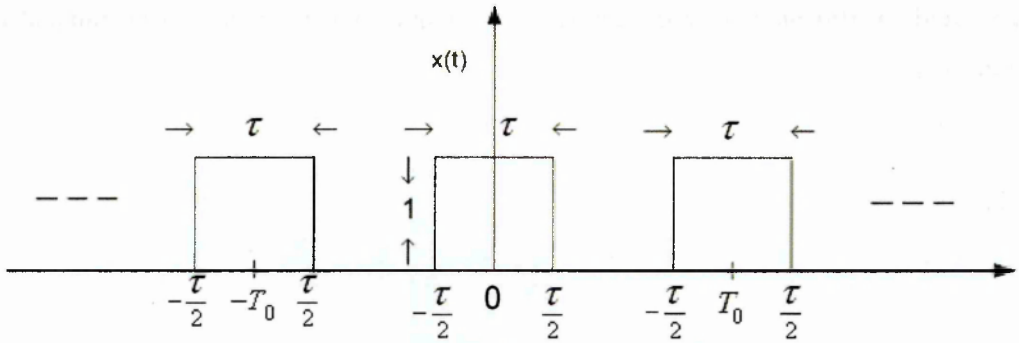

Figure 5 - 11: Periodic Signal x(t)—Train of Rect Functions

Since x(t)=1 within given boundaries, thus

$$\Rightarrow \qquad x_n = \frac{1}{T_0}\int_{-\frac{\tau}{2}}^{\frac{\tau}{2}} e^{-jn\frac{2\pi t}{T_0}}\,dt$$

$$\Rightarrow \qquad x_n = \frac{1}{T_0}\frac{T_0}{-jn2\pi}\left[e^{-jn\frac{2\pi\tau}{T_0}} - e^{jn\frac{2\pi\tau}{T_0}}\right]$$

$$\Rightarrow \qquad x_n = \frac{1}{n\pi}\sin\left(\frac{n\pi\tau}{T_0}\right)$$

$$\Rightarrow \qquad x_n = \frac{\tau}{T_0}\sin c\left(\frac{n\pi\tau}{T_0}\right) \qquad \ldots\ldots\ldots\ldots\ldots\ldots \qquad (5 - 6)$$

Now by using these coefficients, the Fourier series would be given by:

$$x(t) = \sum_{n=-\infty}^{\infty} x_n e^{jn\frac{2\pi}{T_0}t} \qquad \ldots\ldots\ldots\ldots\ldots\ldots \qquad (5 - 7)$$

$$x(t) = \sum_{n=-\infty}^{\infty} \frac{\tau}{T_0}\sin c\left(\frac{n\pi\tau}{T_0}\right) e^{jn\frac{2\pi}{T_0}t} \qquad \ldots\ldots\ldots\ldots\ldots\ldots \qquad (5 - 8)$$

Evaluating this function for different values of *n* over time axis yields summation of sinc functions with decaying amplitudes as amplitude remains inversely proportional to '*n*'.

For the purpose of time evaluation of this function, it would be discussed under three different cases, as follows:

- A Rect function (with 20 time samples only) is represented here in the Figure 5 - 12 (a). While plotting this function, the horizontal (time) axis is centred at zero and there are ± 500 time samples, out of which the Rect function has values from ± 10 time samples only. Part (b) of this figure shows the corresponding frequency response. It yields a sinc function with ampli-

tude of 100 and first zero crossing at 50th frequency bin, second at 100th bin and so on.

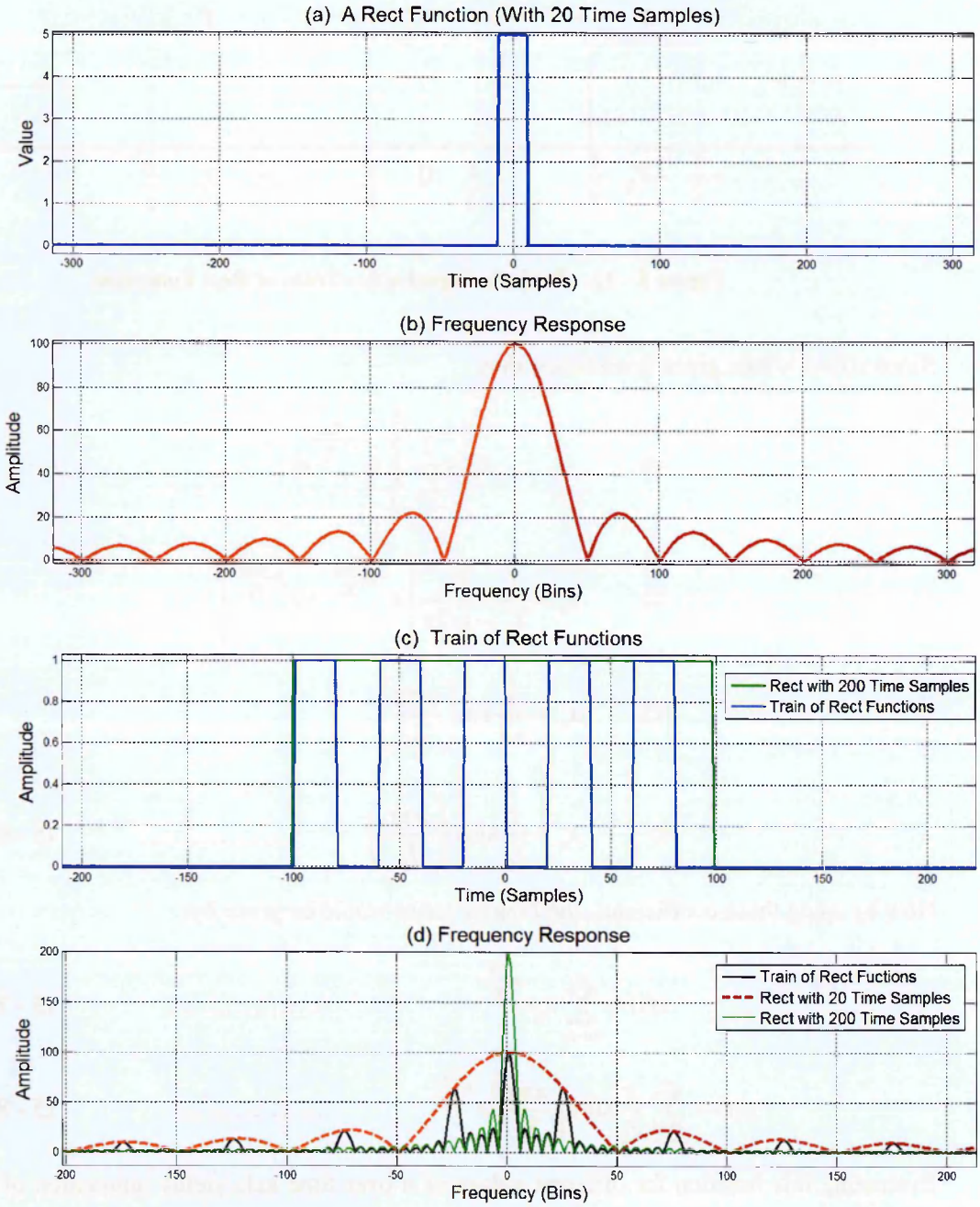

Figure 5 - 12: Frequency response of a single/train of Rect functions

- Similar to this Rect function with 20 time samples, another Rect function with 200 time samples (± 100, centred at zero time axis) is considered. It is represented in part (c) of the figure. Its corresponding frequency response is shown in part (d) of the figure. It yields a sinc function with amplitude of 200 and first crossing at ± 5th frequency bins.
- This Rect function with 200 time samples is further divided into a train of Rect functions, each with 20 time samples, with a gap of 20 time samples. Its time vs. amplitude signal is shown in

part (c) of this figure. It has been over plotted with a blue colour to distinguish it from the Rect of 200 time samples (plotted in green colour). Its frequency response is represented in the part (d), by over plotting it with the other frequency responses. It yields amplitude of 100.

The frequency response of the train of Rect function has the effect of replicating the sinc function along the frequency axis. By over plotting the response of Rect function (dashed red lines) of the 20 time samples, represents the envelope – over the underneath replicating sinc functions. It appears that the impulse response due to a train of Rect functions would indeed, be enveloped by the impulse response of a single Rect function—with only 20 time samples).

If there were no gaps (for a Rect with 200 time samples), then the impulse response, as represented by green colour, would have been one main spike with amplitude 200. The introduction of the gaps in this function – that makes it a train of Rect functions, has two immediate effects on the impulse response: one being reduction of the amplitude to half, and other, worsening the resolution (which is measured at the point once the main lobe amplitude drops to half), the phenomenon observed and discussed for Figure 5 – 10. The reduction of the amplitude to half may also be interpreted as reduction of the SNR to half i.e., 3 dB down as compared to continuous aperture.

By extending the same analogy to the real SAR data, as shown in Figure 5 - 13 yields almost similar results. For this purpose, only one column (range cell) across all rows (range lines) is considered. Out of this data, only 200 time samples are selected, and then gaps are introduced to make it a train of Rect functions.

These results, as presented in part (d) of Figure 5 - 13 are similar to those achieved previously (Figure 5 – 12 (d)). However, the amplitude and location of the sidelobes are different presumably due to varying frequencies present in the data, and the wide amplitude variations in the time domain data which may be attributed to a high contrast ratio (such as observed between a calm sea and ships)—which appears in the real SAR data due to coherent nature of the electromagnetic radiations during acquiring this data.

Having seen the impulse response of these few bursts of data samples in the form of train of Rect functions, it is observed that by considering a large number of bursts, the overall behaviour remains similar. It yields different widths and heights of the main and sidelobes according to the length and number of input Rect functions considered at that instance of time. Due to this phenomenon taking place at the discrete level, the significant spurious energy flowing out from the main spikes of the targets is clearly visible, at discrete level in Figure 5 – 10 and at the image level in the Figure 5 – 7 (f).

The same analogy may be extended to the azimuth compression of the complete dataset. As the

data with the gaps are converted to the frequency domain for implementing the matched filtering, it yields replicating the sinc function. The azimuth compression is accomplished by multiplying the azimuth reference chirp with this data, in the frequency domain. The product is then converted to the time domain to be used as SLC. The gaps, as a result of this matched filtering operation, would be filled and the result would be same as shown previously in Figure 5 – 7 (f).

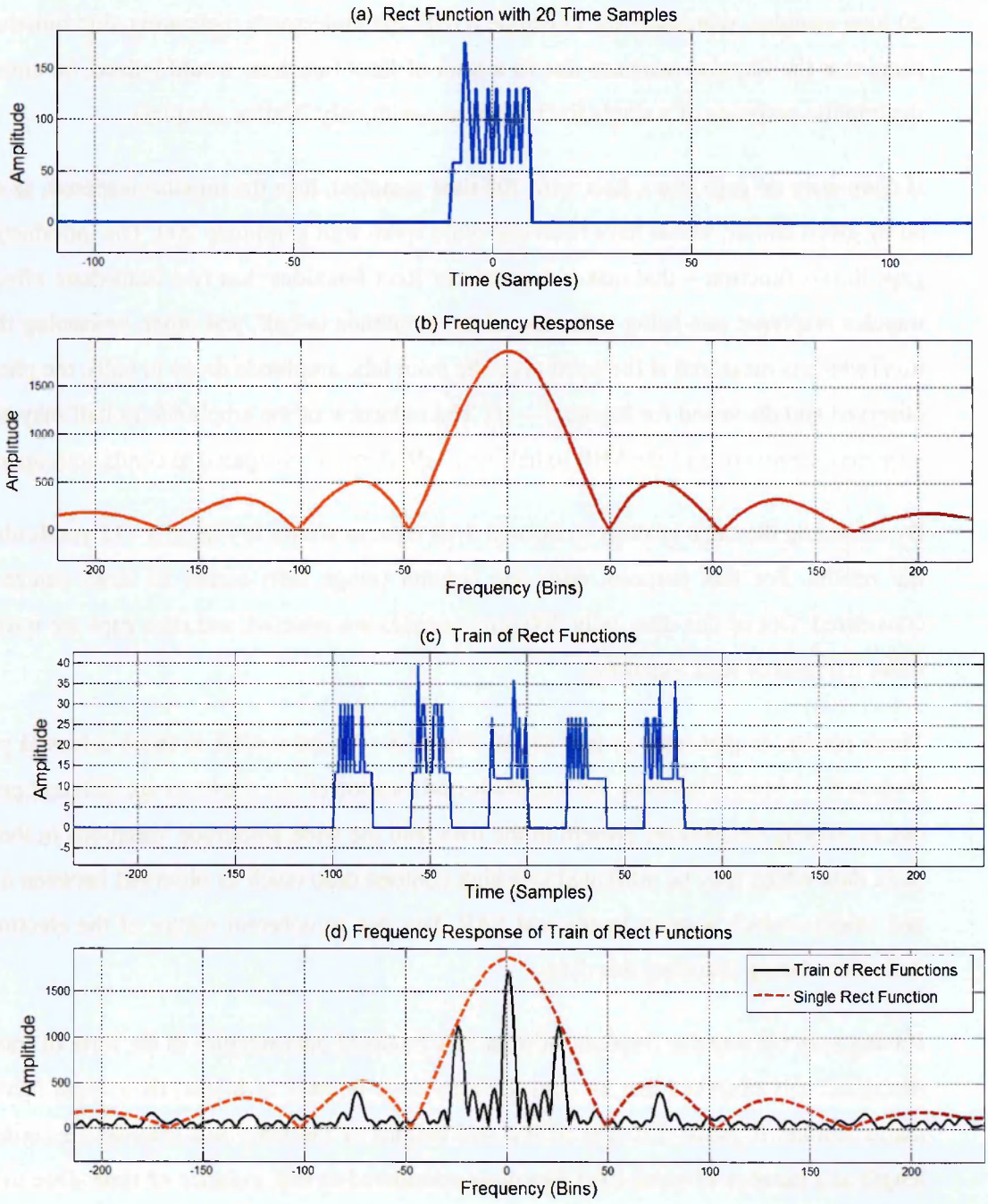

Figure 5 - 13: Frequency response of a single/train of Rect functions – real SAR data

The discussion may be concluded on this note that the main reason of appearance of artefacts in the processed data, is due to the gaps. The gaps need to be filled in the raw data, in order to obtain

the artefacts free image.

5.2 Sparse Aperture Filling Algorithm

A literature survey on sparse apertures reveals that it is not a unique problem for SARs or radars. Gaps in the coherent SAR/radar signal data may occur intentionally or unintentionally. In the recent past, different researchers have claimed success in coherently filling these gaps in varying scenarios using different techniques.

5.2.1 Literature Survey on Sparse Aperture Filling Techniques

Sparse apertures may result from malfunctioning of hardware or software; the result of purposely removing segments of the signal data corrupted by some interfering source [102]; sharing the onboard resources (like antenna, PA, processors etc) with other systems (Electronic Warfare or communication equipment) [103]; enhancing the resolution by combining the resources operating in different frequency bands to achieve ultra wide bandwidths [104], or as a design feature, here with the ICW SAR concept.

As established in the previous sections, the source of image artefacts is due to appearance of gaps in the raw data. The raw data may be characterized by a mathematical model. A mathematical model is then defined by its representative parameters e.g. the coefficients of a filter define that filter operation, the coefficients of a polynomial define that polynomial function, the state space model is defined by the model matrices and vectors etc.

Data driven mathematical models are being widely used in diversified fields such as communications, control system engineering, industrial processes, learning algorithms for voice, facial image or video recognition etc. For these models, the foremost issue remains how to estimate the model parameters. If this is achieved, then using these model parameters, the missing data may be predicted. A few examples are discussed to show how these are used in sparse aperture filling algorithms.

Similarly the paper on "Reconstruction of Sparse Bandwidth by Regularization Method in SAR Imagery" has used similar method by estimating the parameters from the available data and then using those to regenerate data in the missing areas. [105]

In addition, the paper "Interrupted SAR" has highlighted the associated problems due to sparse aperture that results from sharing the onboard resources like high gain APAA, PA, processors etc with other electronic equipment. The sparse aperture, if not filled coherently leads to artefacts thus making the image useless. They adopted the Auto Regressive (AR) approach to estimate the parameters from the available data and then used those coefficients to fill the gaps. [103]

Exploring the research being conducted in the other branches of science and engineering, within

the purview of parametric modelling, it may also be noted that Linear Predictive Coding (LPC) is widely used in communication systems and in Voice over Internet Protocols (VoIP) to regenerate missing data frames.

Also, the System Identification (SID) techniques were explored as well. In SID techniques, the available data are analyzed and processed according to certain set procedures to infer a suitable data-based mathematical model that is then used for prediction. With this approach, there are different off-shoots such as AR, State Space Models, etc. Similar to the previous parametric techniques, SID also estimates the model representative parameters (such as state matrices and vectors for state space models) that are then used to predict or regenerate the data in the missing regions.

5.2.2 Adapted Methodology for Algorithm Selection

It was identified while discussing different signal processing stages that the gaps in the synthesized data eventually produce artefacts and the most suitable stage to apply any filling scheme is at the raw data because once the compression starts—due to the matched filtering operation, the gaps are filled thus any corrections at later stages would be very difficult.

While selecting a suitable model, a fundamental limitation needs to be kept in mind that due to design features of ICW SAR technique, there are 100 % periodic gaps in the synthesized data. Any selected model should be iterative such that it yields minimum prediction error. Furthermore, the selected model should not need any *a priori* knowledge such as model order, initial states (or observability/controllability matrices for the state space systems models) etc. The model should derive all such *a priori* knowledge from the available dataset, without any user involvement/decision making.

Keeping these aspects in mind, different parametric models were explored, especially the possibility of adapting the research potentials and advancement taking place in the field of automation and control system engineering, where similar problems are considered as SID.

The initial SID implementations produced encouraging results once these were applied to the simulated point targets (under a no clutter scenario). Therefore, this approach was selected to demonstrate that sparse aperture filling is possible and thereby the concept of ICW SAR is achievable.

Within SID, state space modelling techniques are widely used. Within state space modelling techniques, the Numerical Algorithm for Sub-space State Space System Identification (N4SID) developed by [106] for a closed loop scenario, is a popular choice among the researchers in SID community. The reasons to focus on state space and N4SID models for further research and im-

plementation are:

- These are batch data processing techniques, thus by using a reasonably large batch (say 1000 samples), these would infer the data representative model. These techniques are independent of any *a priori* information and provide a unique and stable solution.
- A state space formulation provides flexibility as these may be used as a standalone technique, or may be combined with other approaches to achieve a higher degree of accuracy.
- Once model building is done as a standalone—employing N4SID algorithms only—then these are always convergent (non-iterative) and yield a unique solution. Over period of time, a continuous research has shown that these may be used in a non-convergent (iterative) manner to obtain higher accuracy (reduced prediction error). During this research, the results are combined with other techniques (such as Prediction Error Model (PEM)), where different input selection parameters are changed, the model is estimated, the results are evaluated in relation to the available observations, iterated again, until minimum error is achieved etc.)) to provide more flexibility and accuracy.
- These arguments are further strengthened as a lot of research activity is currently taking place in SID and control system engineering that may, in the future, be exploited to our advantage by adapting part of it to suite our requirements.

Selected Model. Having identified that state space SID models are appropriate in this scenario, the N4SID is further selected as the core of the gap filling approach.

Before getting into the particulars of this algorithm, it is pertinent to set at relevant background about system identification, what the parameters of a model are and how these may be estimated by N4SID.

5.2.3 Fundamentals of System Identification

To keep the system identification model building simple, coherent and focused [107] is the main reference. The existing tools have been suitably tailored/modified to meet our requirements. During subsequent discussions, if any other reference is used, it will be mentioned.

A system is an object in which variables of different kinds interact and produce observable signals. System outputs are of main interest as these are further used for subsequent systems or within the same system (as feedback). User defined external signals to the system are called inputs. Besides these there are disturbances as well that have direct bearing on the outputs. These disturbances may be classified as directly measurable and un-measurable. Un-measurable disturbances may be observed from their influence on the outputs. Figure 5 - 14 represents a simple system.

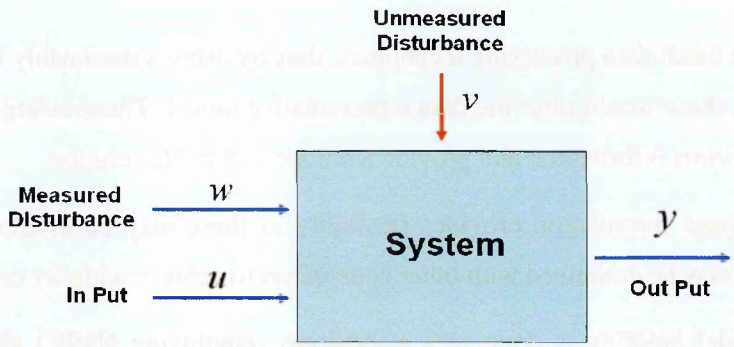

Figure 5 - 14: A simple system with variables

It would be an ideal situation if a detailed mathematical model along with corresponding observations is available. There may be an analytical or numerical solution for that mathematical model. But finding an exact solution of analytical models is a difficult process. Similarly the observations taken under noisy environment may not be truly representative of the system. Once the mathematical model and observations are combined in another model such as a Kalman Filter, an optimal solution may be achieved. But in most experimental work or natural processes the mathematical model may not be available or non-existing, but may be required for further use with prediction, control etc. Therefore it becomes imperative to estimate a representative mathematical model from the available data only. This leads to a separate field in the science and engineering called SID that may be defined as "SID deals with the problem of building mathematical models of dynamic systems based on the observed data from the system".

The mathematical models of the dynamic systems are described as differential (continuous time) or difference (discrete time) equations. They describe the dynamic behaviour of the system as a function of time [106]. For a given system, the relationship between the input $u(t)$ and output $y(t)$ at any time 't' may be represented by difference equation as :

$$x(t+1) = Ax(t) + Bu(t) + Ke(t) \qquad \ldots\ldots\ldots\ldots\ldots \qquad (5 - 9)$$

$$y(t) = Cx(t) + Du(t) + e(t) \qquad \ldots\ldots\ldots\ldots\ldots \qquad (5 - 10)$$

In this model, vectors $u(t) \in \square^{m}$ and $y(t) \in \square^{\ell}$ are the measurements recorded at time instant 't' of respectively the 'm' inputs and 'ℓ' outputs of the process; the vector $x(t) \in \square^{n}$ is the state vector of the process at discrete time instant 't' , containing numerical values of 'n' states where 'n' is the order of the system; $A \in \square^{n \times n}$ is the system matrix that describes the dynamics of the system; $B \in \square^{n \times m}$ is the input matrix that represents the linear transformation by which the inputs influence the next state, $C \in \square^{\ell \times n}$ is the output matrix which describes how the internal state is

transferred to the outside world in the measurements $y(t) \in \square^{\ell}$, $D \in \square^{\ell \times m}$ is the direct feed through matrix; K is the Kalman gain or the factor to minimize the error and $e(t)$ is the error or residual.

The Eqs. 5 - 9 and 5 - 10 represent a dynamic system that is also known as Deterministic SID model [106]. However, in the ICW scenario, only the output '$y(t)$' from the SAR is available, and no input '$u(t)$' is present, thus these equations may be simplified as: [106]

$$x(t+1) = Ax(t) + Ke(t) \qquad \text{State Transition Equation} \qquad (5\text{ -}11)$$

$$y(t) = Cx(t) + e(t) \qquad \text{Observation Equation} \qquad (5\text{ - }12)$$

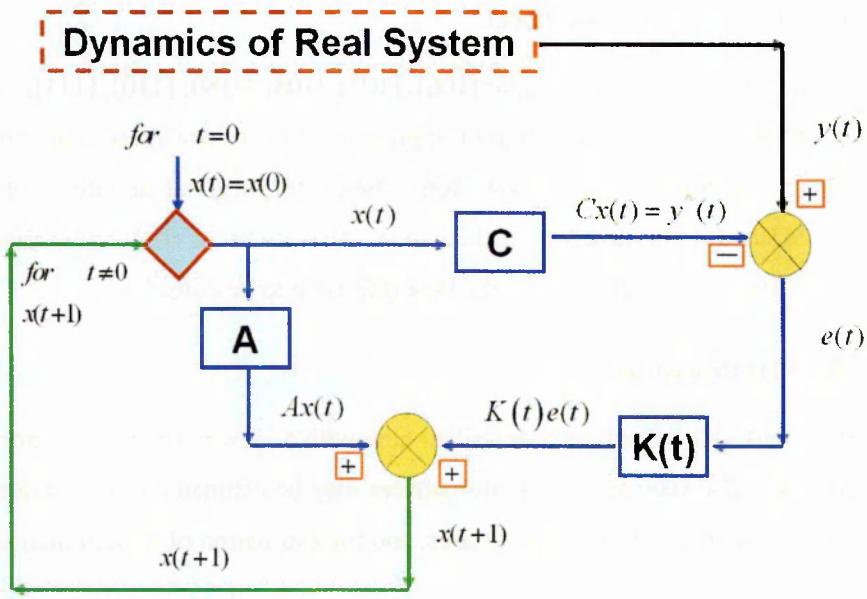

Figure 5 - 15: Stochastic state space flow diagram

The dynamic system represented by Eqs. 5 - 11 and 5 - 12 is also known as Stochastic SID model. [106] This model may be further explained with the help of the functional block diagram shown in Figure 5 - 15.

We can suppose that there is a hidden real dynamic system (a SAR in this case) for which we do not have the mathematical model, but which has provided output $y(t)$, sampled at constant sampling intervals (considered 1 in this case). Now it is required to estimate and build the mathematical model that would be reasonably representative of the hidden dynamical system. For an estimated initial condition (or state) 'x(0)' at t=0, the estimated value of $y(t)$ would be: $\hat{y}(t) = Cx(t)$. This is an estimated value, which once compared with the actual value of $y(t)$ gives a difference or error, $e(t)$. The aim is to keep this error to a minimum. For this purpose, the error is

multiplied by the Kalman gain 'K' and fed back.

To estimate the next state, according to Eq. 5 - 11, the same $x(t)$ would also be fed to the feedback loop through the state matrix 'A' and added to the product of K and $e(t)$. This would then calculate the next state, $x(t+1)$ that is then fed through the C matrix to estimate the next value of $\hat{y}(t)$. This is then compared to the actual value of $y(t)$ to derive the error, $e(t)$, and the process is repeated.

The fundamental question which still remains unanswered is how to estimate A, C, K and the state vector $x(t)$. These matrices and vectors define the parameters of the model. Since these are estimated in different sub-spaces, these are given the name of Sub Space State Space models, and in view of the fact that the data are manipulated using numerical methods, the technique overall is called N4SID. This is a batch data processing technique that is directly applied to a selected segment of the data to infer the model.

Different researchers (for example [106], [107], [108], [109], [110], [111], [112] and many others) have adopted or suggested different approaches to estimate these matrices and vectors, but for simplicity the approach given by [106]—being the original architects of this method—is followed. Also, for the detailed mathematical derivations of the widely practiced stochastic SID models, [106] is considered to be the best reference to be consulted.

5.2.4 SID Procedure

A simplified SID procedure is described here with a view to draw necessary inferences for further discussions. The state space system matrices may be estimated in two stages as: the estimation of a sequence of (Kalman filter like) states, and the estimation of system matrices.

- The data are arranged according to a special type of matrix known as a block Hankel matrix. If it is assumed that the system evolves according to Eqs. 5 – 11 and 5 – 12 then at any given time, the expected value of $y(t)$ conditional on the past observations is the product of an extended observability matrix and the state vector at that time, conditional on the past observations.
- By taking the orthogonal projection (QR decomposition) of the block Hankel matrix, it is possible to show that these projections are equal to that extended observability matrix and the non-steady state Kalman filter sequence. It means that by these numerical manipulations, the state sequence may be retrieved directly if the extended observability matrix is known.
- To find the extended observability matrix:
    - The decomposed matrix is first multiplied by two weighting matrices. These weighting matrices are obtained from different algorithms such as the Principal Component Algorithm (PCA), Un-weighted PCA (UPC) or Canonical Variate Algorithm (CVA). Within

these algorithms, these matrices are obtaining from the covariance matrices of the past/available data.

- By deciding which algorithm would be used to obtain the weighting matrices, the product of weighting matrices and the decomposed matrix (i.e., the lower left triangular matrix R of the QR decomposition), is then further decomposed using singular value decomposition (SVD). This decomposition in turn is used to find out the order of the system by inspecting the singular values in the 'S' matrix. It also yields that the row space of this decomposition is indeed the row space of the Kalman filter states and the column space is the column space of the extended observability matrix.

- The procedure adapted up to this point helps in extracting the Kalman filter states and the extended observability matrix. Knowing these, then it is easy to recursively estimate the state space system matrices, for which detailed procedures are given by [106].

Having a look at these steps which are taken to find the state space system matrices, it is convenient to say that N4SID algorithms:

- Do not need any *a priori* knowledge about the system dynamics, initial states, order of the system or observability/controllability matrices, rather these are derived during the identification process.
- Yields numerically stable solutions.
- For a given set of conditions such as which type of weighting algorithm to be used, how the data needs to be arranged in the block Hankel matrix (how many rows, as number of the columns are calculated from this information automatically), the order of the system etc. the algorithm yields a unique solution that is always convergent (non-iterative) and with no non-linear optimization part involved, thus these do not suffer from sensitivities to the initial states. [108]

5.2.5 Evaluating Model Performance

In order to improve the model accuracy (i.e., minimum prediction error), researchers such as [107] have suggested techniques to make the convergent (non-iterative) N4SID a non-convergent (iterative) algorithm.

Note the "prediction error" in this sense is a measure of how well the estimated model fits the available data. It is assumed that if the estimated model is fitting the observed data well, then it is also likely that it is predicting the missing data well.

As discussed previously, overall the performance of the estimated model is dictated by the set of conditions such as the order of the model (i.e., the number of rows/columns in the state space ma-

trices); the number of past/future samples considered, the selection of the algorithm to estimate the weighting matrices, etc. These variables eventually provide a solution in the form of a model-estimation through N4SID. However, as the performance is conditional on these sets of variables, selecting different ones may give better results (reduced model prediction error). Thus, a process of iteration, where these variables are changed one after the other and the model performance evaluated in terms of least overall error, is undertaken. By iterating the estimation process, the error is recorded each time and that model (estimated system matrices) is selected that yields minimum prediction error. The selected model is then used for estimating the data in the missing regions.

5.2.6 Overall Algorithm

These factors have been incorporated in the N4SID based sparse aperture filling algorithm. Different blocks of the algorithm are shown in Figure 5 - 16.

N4SID works on real numbered column vector only, whereas the RADARSAT-1 has both I and Q channels (in the complex number format). In order to proceed further with the SID procedures, as a first step, these I and Q channels are separated and processed in parallel and then towards the end, these gap filled data vectors are recombined in the same complex format as is used in the signal processor.

As stated, the N4SID does not look at the gaps, it is only there to infer the data representative stochastic state space model (A, C, K and $x(t)$). For a single iteration, under the same conditions, it would yield a unique solution i.e., the values of these matrices and the order would be same. So by running the N4SID on the available data (gaps are there but these gaps are transparent to the algorithm), it infers a model. The stepwise implementation follows:

- As gaps appear along the rows, so at one time, select only one column of the raw data matrix. Replace the gaps with Not a Number (NaN) so that it remains transparent to the N4SID. During subsequent discussions, it would be referred to as a data vector.
- Let the N4SID run for the first time. As a result it infers a model.
- Evaluate this model by feeding available data values (i.e., Y(t)= [y(1) to y(20), and then y(41) to y(60), ...and so on up till end of the data vector]). As a result, another estimated data vector would be generated like: [$\hat{Y}(t)$=[$\hat{y}(1)$ to $\hat{y}(20)$, and then $\hat{y}(41)$ to $\hat{y}(60)$, ..., and so on up till end of the Y(t)].
- Find the root mean square error (RMSE) between the available (actual) data vector Y(t) and the estimated data vector $\hat{Y}(t)$.
- Save the estimated model (i.e., the matrices) and the error against first iteration.

- Now change the input parameters, say change the order of the model to be estimated. And let N4SID run for the 2nd time. It would infer another model (model matrices with different values). Estimate the data vector as done for the first iteration and save the model and the RMSE against the 2nd iteration.
- Repeat this procedure by changing different conditions such as the order of the matrix, method to find out the weighting matrices, the number of rows in the block Hankel matrix etc, and obtain the corresponding model and the RMSE.
- After a few (say 10) iterations, if the RMSE values are analysed with a view to select the one that has minimum value, it means that model produces the closest representative model for the data. Select that model to be used for predicting in the missing regions for that selected column of the sparse aperture matrix (only I channel).

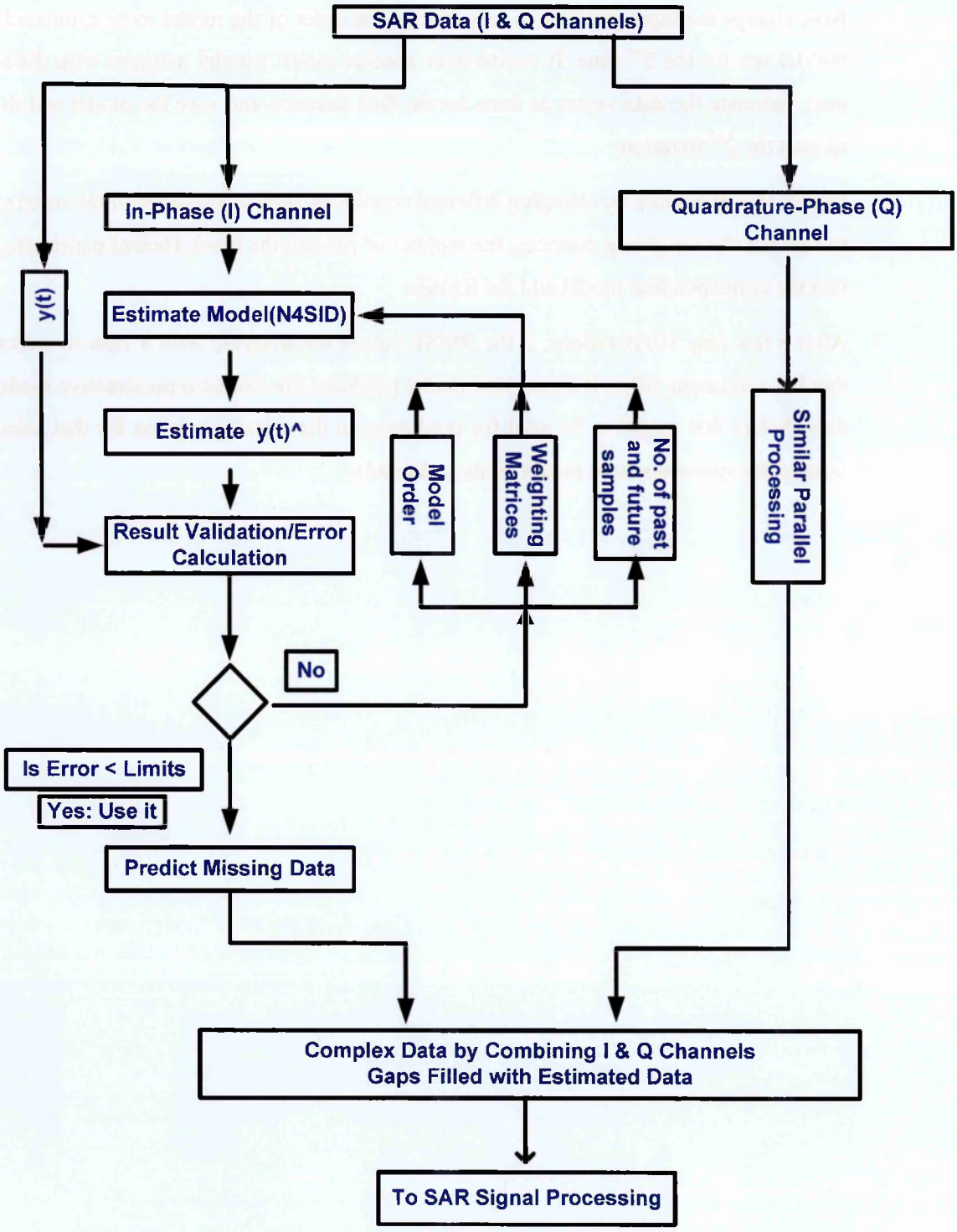

Figure 5 - 16: Complete Sparse Aperture Filling Algorithm

- What happens once the model is selected but there are no Y(t) in the missing regions such as: Y(t) = [y(21) to y(40), y(61) to y(80), ……., an so on up till end of the row].
- For this case, since all the required matrices are there, the states are propagated and the data will be estimated recursively by using Eqs. 5 – 6 and 5 – 7. As an example;

At time instance t = 20: $\Rightarrow \quad y(20) = Cx(20) + e(20)$

The next state would be: $\Rightarrow \quad x(21) = Ax(20) + Ke(20)$

At time t = 21, y(21) = 0 because of the gap, thus:

$0 = Cx(21) + e(21)$

$\Rightarrow \quad -Cx(21) = e(21)$ which is also equivalent to: $\hat{y}(21) = -Cx(21)$

the next state would be: $x(22) = Ax(21) + K[-Cx(21)]$

similarly $\hat{y}(22) = -Cx(22) + e(22)$

the data would be estimated in the missing regions accordingly. During these recursions, the role of K as an error reducing factor is very important.

- The same procedure is adopted in parallel to the Q – channel of the data that was separated at the start and data is predicted in the missing regions.
- At the end, both gap filled I – and Q – channels are combined to complete the gap filling on one column of the data.
- The process continues for rest of the rows of the raw data matrix, repeating the process on each row.
- The process ensures that the original available data are not disturbed and carried forward to the gap filled matrix.

5.3 Application of the Sparse Aperture Filling Algorithm to RADARSAT–1 Dataset

The N4SID based gap filling algorithm was applied to a simulated dataset which was obtained from a model that was representing different point targets, without any statistical distribution. It was a simple model that was assumed to be in a noise free environment. The initial gap filling results were encouraging, thus were accordingly published in [113].

Now the same algorithm is applied to the RADARSAT-1 test dataset. The gap filling is performed at each column of the raw data. The performance is analysed at the two stages. As the gap filling is carried out in the raw data, so firstly it is discussed at a single column level in comparison to continuous and the interrupted apertures. The gap filled raw data matrix is then passed on to the signal processor for range and azimuth compression. Secondly it is discussed at the SLC amplitude, image as well as at a single column level.

Figure 5 - 17 has been plotted to show the performance of the gap filling algorithm at the raw data. It shows only the real part of the signal of one range cell (column) across all the range lines (rows) of the raw data matrix. The estimated data (red) has been plotted over the continuous aperture data (blue) so that it can be readily compared to the expected continuous aperture values. The available data points of the interrupted aperture (black dotted) are also marked for convenience.

The results show that the algorithm (red) tries to catch up the required signal (blue) in the missing regions but due to large gaps (100 %), the rapidly changing and highly excursive nature of the original signal, the overall performance is not encouraging.

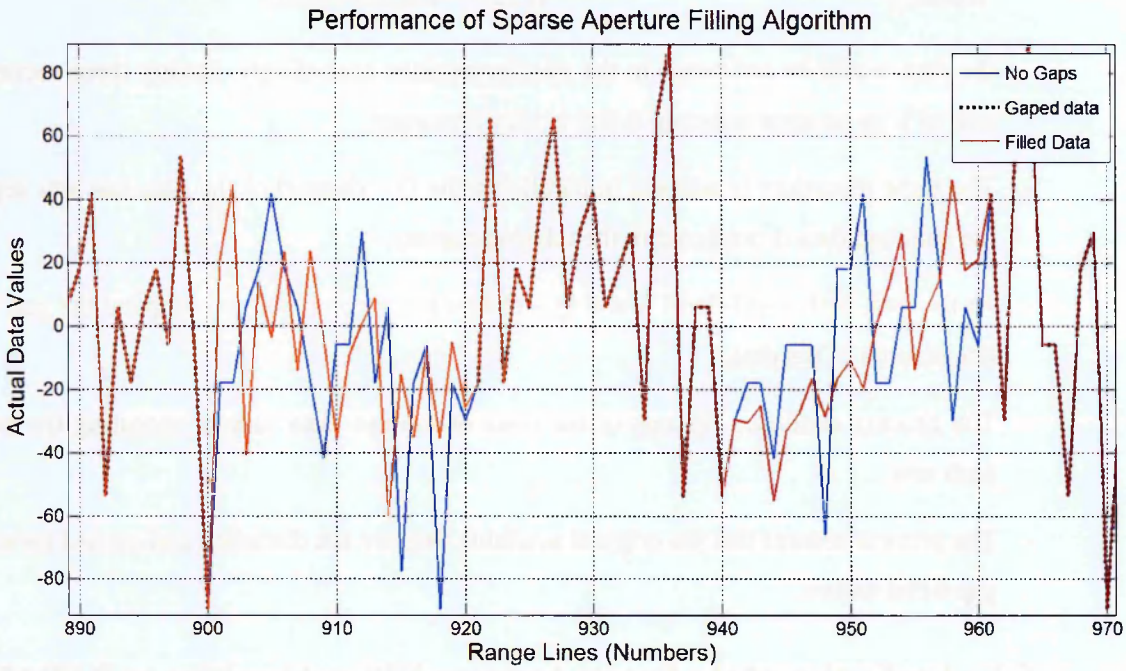

Figure 5 - 17: Sparse aperture filled by N4SID algorithm

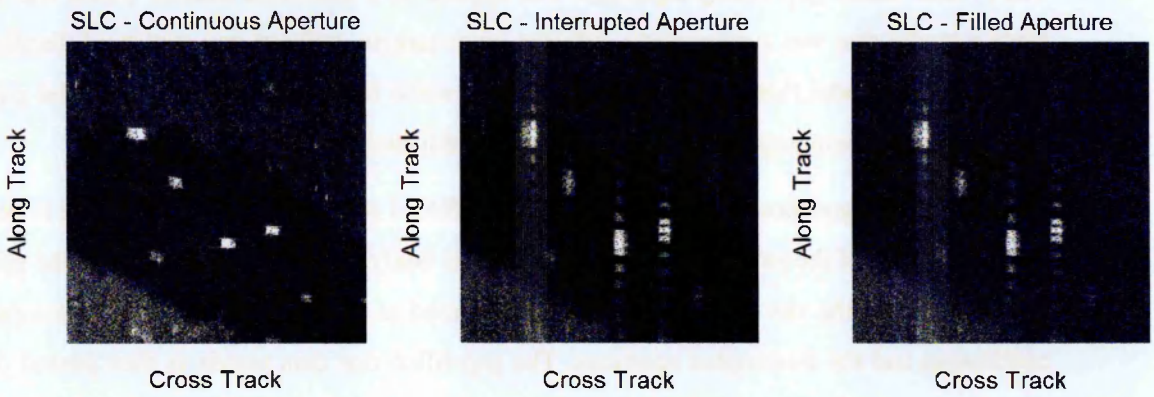

(a) **(b)** **(c)**

Figure 5 - 18: Comparison of SLC amplitude images for continuous, interrupted and gap filled apertures

To analyse the performance of gap filling algorithm at the SLC level, the complete gap filled raw data matrix is now passed on to the signal processor to perform the range and azimuth compression. As a result, the SLC amplitude image is shown in the part (c) of Figure 5 - 18. In order to draw close comparison to the SLC amplitude images of continuous and interrupted apertures of the same area, these are also plotted in parts (a) and (b) of the Figure 5 - 18, respectively.

Comparatively looking at these images, it appears that the major impact of the gaps i.e., appearance of the artefacts in the interrupted aperture image shown in part (b) are still visible in the gap filled image in the part (c). The main reason of presence of these artefacts is due to the unsatisfactory performance of gap filling algorithm at the raw data stage, which propagates through the signal processing stages.

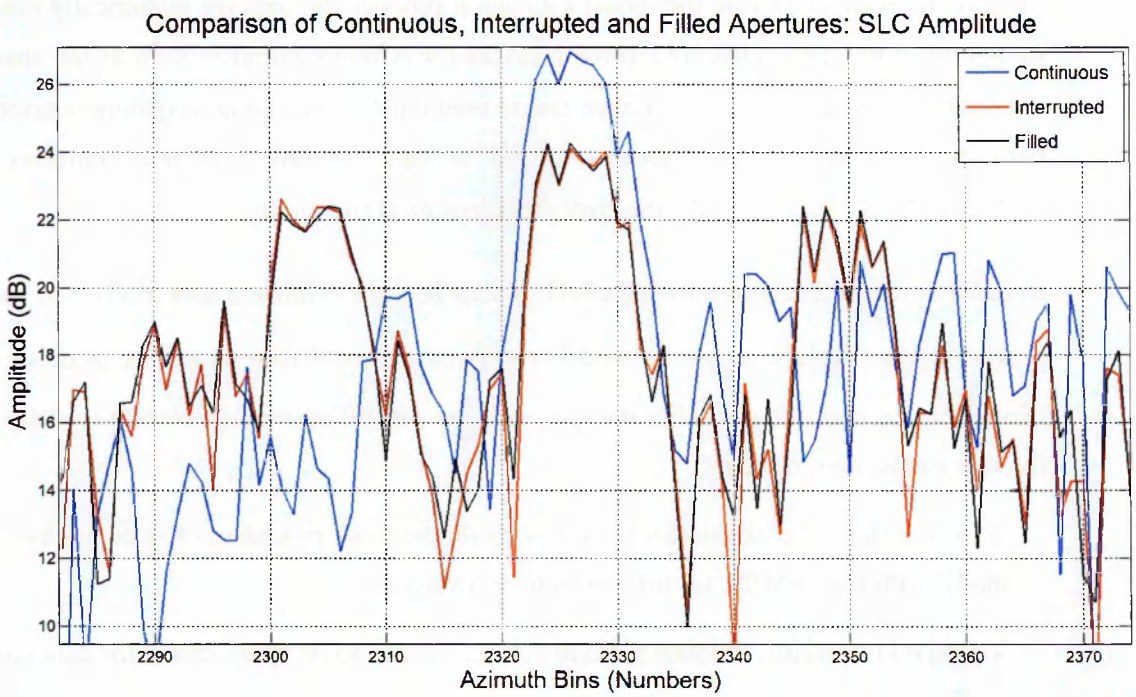

Figure 5 - 19: SLC amplitude of one range bin (column) across all the azimuth bins (rows) to compare the continuous, interrupted and sparse aperture filled apertures

To draw the insight comparison of the continuous, interrupted and the sparse aperture filled SLC amplitude data, the magnitude plot of one range bin across all the azimuth bins is shown in Figure 5 - 19. The SLC amplitude of the same range bin for the continuous aperture (blue) shows presence of a strong scatterer with a magnitude of ~ 27 dB. Due to the sparse aperture, the artefacts

appear in the processed image and as a result reduce the magnitude of the same object to ~ 24 dB. By applying the gap filling algorithm, the magnitude of this object should have been increased but there is only a marginal improvement and the effect of artefacts remains visible.

While analysing the performance of the gap filling algorithm, it appears that the Kaman filter gain '*K*' is not reducing the error during the gap filling stage. As stated earlier, N4SID is a batch processing algorithms. Thus once it is applied to a reasonably long data vector, say with 1000 samples, it yields data representative state space model in the form of *A*, *C*, *x(t)* and *K* during the estimation process.

For the missing data regions where $Y(t)$ is not available, this inferred model is used to predict the data values by recursively propagating forward the states which, as a result, yield the estimated $\hat{Y}(t)$ for the gaps. The model is indeed derived considering periodically 20 samples spread over the entire batch of the data vector. The role of available data, after inferring the model, as such finishes, whereas in reality, it has significant role even during the data estimation process for the missing regions. During the model estimation process, the data are numerically manipulated to determine the data-based covariance matrices for different purposes such as the state covariance matrix, the data output covariance matrix used during calculating weighting matrices etc. As here in this case, the gaps are 100% and as data estimation process continues say for $\hat{y}(21), \hat{y}(22), \hat{y}(23), \ldots\ldots, \hat{y}(40)$, the error e(t) keeps on accumulating.

In order to reduce the accumulating effect, if somehow the estimated data $\hat{Y}(t)$ is fed back to the available data $Y(t)$ and again the model is inferred, it would then mean that model is stepwise taking into account the error. For this purpose, the gap filling through N4SID is made adaptive through following procedure:

- As a first step, infer the model by following the previous procedure of selecting the estimated model with least RMSE, for the available data values:

  Y(t)= [y(1) to y(20), and then y(41) to y(60), ...and so on up till end of the data vector].

- Estimate only the first missing values along the data vector as $\hat{y}(21), \ldots\ldots \hat{y}(41), \ldots\ldots, \hat{y}(61)$ and so on up end of the periodic gaps.

- Now feedback/merge these first values with the available data vector, which would look like:

$$Y(t)=\left[\underbrace{y(1),\ldots\ldots,y(20)}_{\text{Already Available}},\ \underbrace{\hat{y}(21)}_{\text{fedback}},\ \underbrace{\text{NaN, NaN, }\ldots\ldots\text{,y(40)}}_{\text{missing}},\ \underbrace{y(41),\ldots\ldots,y(60)}_{\text{Already Available}},\ \underbrace{\hat{y}(61)}_{\text{fedback}},\ \underbrace{\text{NaN, NaN, }\ldots\ldots\text{,y(80)}}_{\text{missing}},\ \ldots\ldots,\right]$$

Now infer the model for this available data that indeed carries original 20 available samples +

one sample estimated. This inferred model would be different from that which was achieved for 20 samples.

- Again estimate the data for the missing regions, feedback the first estimated data i.e., $\hat{y}(22)$, ..., $\hat{y}(42)$, ..., $\hat{y}(62)$,....., to the input data Y(t).
- This means that each time the available data to estimate the model is incrementally increasing. Follow the procedure till all the gaps are filled.

This adaptive N4SID gap filling procedure is applied to a single column of the same dataset used previously. The results are shown in Figure 5 - 20. It shows that this modification marginally reduces the RMSE for the first few iterations and then again the error starts increasing. The figure shows that feeding back up to 4 data samples, the error was reducing but after that it gradually again rises, thus giving overall similar results to those achieved previously.

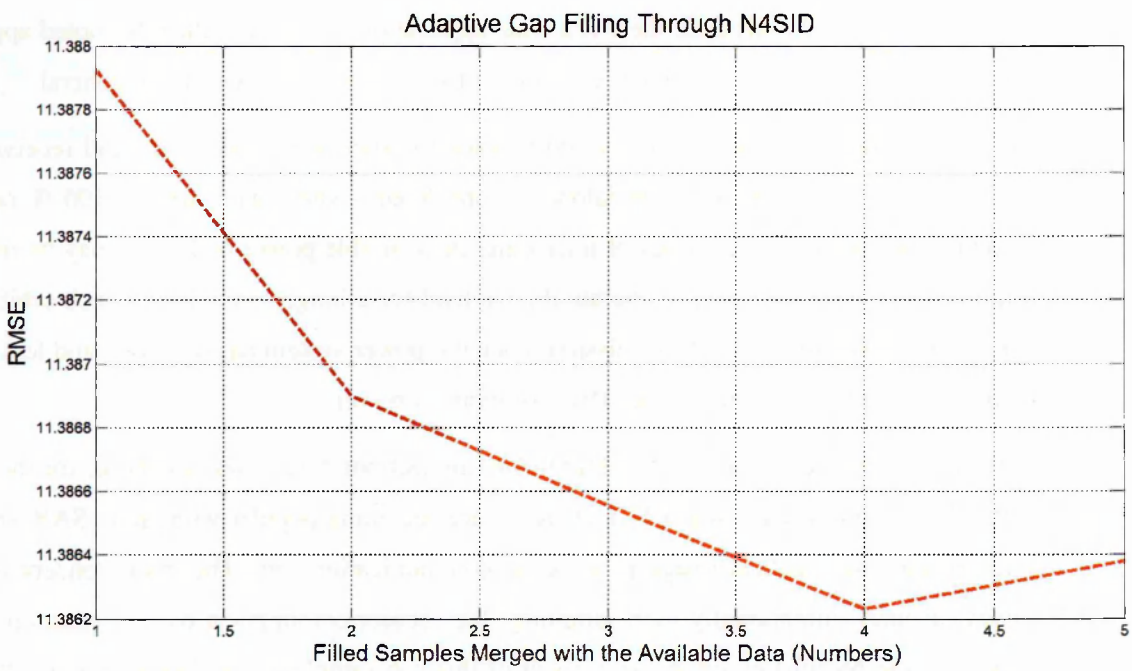

Figure 5 - 20: The performance of adaptive gap filling through N4SID

5.3.1 Performance Analysis of the Gap Filling Algorithm and the Way Forward

Adapting this gap filling methodology was inspired by its initial performance on the simulated data. Now comparing the simulated data with the available RADARSAT-1 data, it appears that simulated data was lacking many aspects. The point targets were not showing the very excursive nature of real SAR data. It was also not taking into account the multiplicative nature of the speckle effects which essentially appear in the real SAR data due to the coherent nature of the

electromagnetic radiation.

The main reason of unsatisfactory performance of the algorithm is due to the nature of the input real SAR data which is rapidly changing, highly excursive with levels ~ ± 80 to ± 120 and periodic wide gaps – 100 %. In addition, the signal processing algorithms require coherent data. During model estimation process, the I and Q channels were separated from each other. The gap filling was done separately on each channel. The error in the gap filled one channel indeed adds up during the signal processing stages. The technique of adaptive N4SID shows marginal improvements in reducing the RMSE for the initial few iterations but then the error increases.

The SID model was inferred as a single input and single output (SISO) model by feeding only a single column of the matrix across all the rows. The system performance may improve if multiple input multiple output (MIMO) modelling approach is exploited. For a MIMO system, several columns may be considered simultaneously instead of one by one.

Although the results achieved by applying the gap filling algorithm do not yield satisfactory performance on the real SAR data, there is a wide application potential of the interrupted approach to this research in particular and to the other areas of science and engineering, in general.

The ICW design as a whole requires 100 % gaps for alternative transmitter and receiver operations. But if interruption, as a standalone is considered—where gaps are not 100 % rather few percent—then within the confines of microsatellite available power budget, it may be beneficial: at the beginning of a mission to operate the payload for a longer time during each orbit with the same power; and at the end of the mission when the power system has degraded and less power is available, it could help mitigate the effects of reduced power.

Few sparse aperture scenarios were highlighted in sections 5.2.1. Besides those, for the last few years, the compressed sensing (CS) techniques are becoming popular with radar, SAR, image and video processing, medical image processing, communications etc. The main concept of CS revolves around intentionally sub-sampling the sensor/communication information by not respecting the Nyquist criterion. As a result of this sub-sampling, the data acquired suffers from similar problems as faced here with ICW SAR concept. Currently a lot of research is going on in the CS field. Recently (May 2012) 1st international conference on CS applied to radars was held in Germany [114]. Participants presented different approaches to solve the sparsity problems. Despite all these ongoing efforts, up till now (to the best of author's knowledge), these techniques could not be demonstrated in a practically available sensor (optical, radar or a SAR). However, the potentials of research can never be denied and in future, there may be success in practically developing a sensor which is designed on the principles of ICW SAR/CS.

5.4 Summary and Conclusions

This chapter dealt with the major key issue of the appearance of image artefacts with the ICW SAR design. ICW SAR design provides an engineering solution to the main problem faced by the CW SAR design if it is considered for implementation from a microsatellite of ~ 150 kg category, but this design suffers from signal processing problems due to periodically cutting off the transmitter which results in synthesizing a sparse aperture.

This problem was analysed in the light of RADARSAT-1 data by introducing gaps which are expected from ICW SAR operation. Stepwise signal processing and comparison with continuous and interrupted apertures provided insight into the associated processing problems. Having identified the nature of problem, the gap filling approach that was adapted for simulated SAR data was applied to a RADARSAT-1 test dataset. Due to the rapidly changing and highly excursive nature of the real SAR data under the scenario where 100 % periodic gaps are experienced, the performance of gap filling algorithm was found to be unsatisfactory.

To ascertain the fidelity of the ICW SAR technique, artefact-free SAR imagery, which is necessarily required to measure the backscattering properties of distributed targets, should be obtained. In the absence of a suitable gap filling algorithm to demonstrate the reduction of artefacts in the processed image, for time being, this concept is set aside from the suitable SAR design options for microsatellite implementation.

6 DETAILED DESIGN ASPECTS OF ECMP SAR

The ICW SAR concept is based on utilizing a minimum antenna size (i.e., 3.66 m which is 26 % smaller than the 5 m antenna needed for the ECMP SAR) and provides larger swath (58 km which is ~ 23 % wider than achieved from the extended mode pulsed SAR at 30^0 inclination), but it introduces 100 % periodic gaps in the synthesized aperture that gives birth to signal processing problems. In the absence of suitable gap filling techniques which provide fidelity to demonstrate the practical applicability of ICW SAR technique, it is therefore proposed to focus on the ECMP SAR technique to use it from the 150 kg microsatellite platform.

The proposed system architecture (i.e., merging the ECMP SAR payload and the SSTL-150 bus) needs detailed technical analysis so that any minor changes, if required, may be incorporated in the bus, and to find out the limitations and the potentials of the mission. Besides other issues, the most pronounced technological challenge remains: how to design and fit a light-weight, compact (that yields reduced stowed volume during launch), durable (maintains its shape in the micro-gravity and true thermal space environment) antenna within given mass, volume and cost constraints?

The ECMP SAR concept for a low cost and light-weight microsatellite based SAR design is build upon using a 5 m reflector antenna with a single SSPA, to acquire a dual polarized (HH and HV) imagery through a strip map mode of operation. From the implementation point of view, this chapter focuses on technical aspects related to: power subsystem; antenna design configurations; the ambiguities, flexibilities and limitations; imaging time and the data handling and transmission; attitude determination, knowledge, control and position knowledge; estimated mass and cost budgets; detailed block diagram; image quality; and, the applicability of ECMP SAR to other frequency bands.

6.1 Power Subsystems

6.1.1 The Solar Cells/Panels

The available power capacity onboard SSTL-150 bus is strongly dependent on the efficiency of the solar cells (a solar cell's energy conversion efficiency is the percentage of incident light ener-

gy that actually ends up as electric power). As these cells are becoming more and more efficient, so is this power generation capacity increasing. Last time the SSTL-150 bus was used with Rapideye missions and single junction GaAs solar cells that were only 18 % efficient were employed. Thus, at a 600 km, sun synchronous orbit could only provide ~ 80 – 100 W average power per orbit. The later versions of SSTL buses are employing triple junction GaAs/Ge or ultra triple junction (UTJ) cells, which are ~ 25 – 28.5 % efficient (at 25^0 C) [115].

Figure 6 – 1 shows the SSTL-150 platform's body reference frame. It also shows the body mounted solar panels. The standard bus comes with total area of 1.8137 m^2. Representative performance parameters of these types of cells are 275 Wm^{-2} with an aerial mass density of 4.6 kgm^{-2} [100]. Had 1.8137 m^2 been a single panel with a sun tracking capability, it would have produced average power of ~ 200 W per orbit given 600 km altitude, 97.70^0 inclination, period of 96.69 minutes and maximum eclipse of 34.49 minutes. Indeed, the sun angle for these given orbital parameters continuously changes, and power production through solar cells is strongly dependent on the incident angle of the solar radiations, thus on average the total power production is ~ 170 W per orbit. [9]

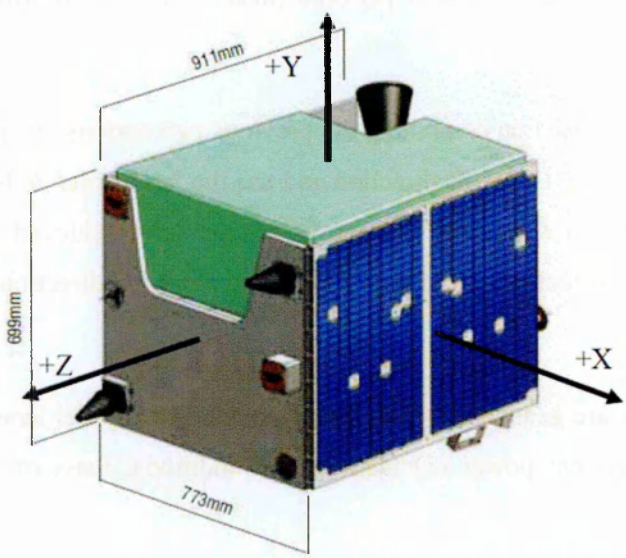

+ X-panel	0.911 m×0.699 m
- X-panel	0.911 m×0.699 m
- Z-panel	0.773 m×0.699 m
Total:	1.8137 m^2

Figure 6 - 1: Body reference frame of SSTL-150 platform

Source: Adapted from **[90]**

In order to increase the average power produced per orbit, there are three options:

Option 1: These buses can be provided with additional deployable panels along +Y or +Z direction. If a standard sized deployable panel along +Y direction is used, then the average power per orbit is ~ 217 W and if along the +Z direction, then an average power of 234 W can be pro-

duced. [9] The mass of body mounted solar panels of 1.8137 m^2 is already counted in the 103 kg bus mass but if deployable panels are used then an additional 3 - 4 kg needs to be included in the overall mass budget of the bus.

Option 2: Given this research focuses on future technologies (few years), and as there are technological advancements taking place in solar cells—especially improving their efficiency for the given size of the cells, it would be pertinent to take into account the capabilities of state of the art technologies instead of what was available in 2008.

As has been reported by [116] Boeing – Spectrolab has developed a solar cell that can convert almost 41 percent of the sunlight that strikes it into electricity. Furthermore, the researchers at Lawrence Berkeley National Laboratories have developed a new type of semiconductor, zinc-manganese-tellurium, combined with a few atoms of oxygen, that can convert around 45 percent of sunlight into electricity. The initial cost of these cells is high. As claimed by [117] (on 19th Apr 2011) a solar cell efficiency of 43.5 % has been achieved and these cells are already being used in the space. These claims have been tested and independently verified by United States' National Renewable Energy Laboratory. Thus by using these cells (43.5 %), the standard body mounted solar panels of 1.8137 m^2 would yield ~ 264 W per orbit (instead of ~ 170 W with 28 % efficient cells [9]).

Option 3: This option is based on combining the previous two options i.e., use standard deployable solar panels either along +Y or +Z direction and use the latest solar cells that yield 43.5 % efficiency. If this were the case then the average power per orbit achieved from deploying standard solar panel along +Y direction would be ~ 337 W and along +Z direction 363 W, respectively.

Here, option 3, where 363 W are generated by deploying an additional panel along the +Z direction, is considered for subsequent power calculations. An additional mass of 4 kg would be counted in the mass budget.

This is the raw power that would be available at the beginning of life (BOL). It is assumed that the solar array degrades at 0.5 – 2.75 % per year. [100] Taking the worst case scenario (2.75 % degradation / year), ~ 13.75 % degradation is estimated over a 5 years mission life. Thus the power available by the end of life (EOL) would be ~ 313 W.

6.1.2 Power Conditioning and Onboard Batteries

The raw power needs to be conditioned according to the onboard requirements of different subsystems. An important component in the power system is the battery charge regulator (BCR). Its function is to regulate the charging/discharging of the batteries through solar panels/load accord-

ingly. As a standard, 6 BCRs are configured on one module. Each BCR supports 80 W, thus in total, 480 W may be regulated through one module. One module weighs 2.25 kg (already included in the mass of SSTL-150 bus). These modules are considered to be ~ 90 % efficient. [115] Given this efficiency, the raw power of ~ 313 W would yield a conditioned power of ~ 280 W per orbit.

The battery provides local energy storage and is an important component of the spacecraft power system. The battery can supply power in addition to that from the solar array to cope with high peak power demands (during SAR imaging), or those periods when the total system power demand exceeds the instantaneous power production capability of the solar arrays. The battery also provides the only source of power during eclipse. [94]

The satellite battery design is highly dependent on the satellite's mission which in return determines the orbit from where the satellite needs to operate. The orbit determines the charge/discharge (mainly how many eclipses per year) characteristics of the battery. Since a battery can only be re-charged a finite number of times, it often determines the mission lifetime.

An important factor in determining the battery's lifetime is the Depth of Discharge (DOD), which is simply the percentage of total battery capacity removed during a discharge period. In general higher percentages imply a shorter cycle life. [94]

For the ECMP design, the battery should satisfy the requirements of: expected lifetime of ~ 5 years, a large number of charge/discharge cycles (>5,000/year or 25,000 for 5 year), DOD 10 – 40 %, the ability to withstand temperature variations (– 20 to +50^0C), and the ability to withstand vacuum and high vibration levels so as to be able to survive the launch.

Indeed, the SSTL-150 bus is equipped with 15 Ah (ampere hour) capacity Li-ion cells. These cells have specific energy density of 70 – 150 Whkg^{-1} (watt hours per kg) and are 96 % energy efficient. At 20 % DOD these are expected to last for 15 – 18 years. [115]

As the bus operates at 28 V DC, 100 % fully charged, 15 Ah capacity battery means it can store a charge of up to 420 W. For sustaining a long lifetime, if a 40 % DOD is assumed, then it means 168 W should be drawn while remaining within safe limits. This capacity, in light of the adopted solar panel approach, looks low, thus additional cells need to be added to make it 21.5 Ah capacity. If this is the case, then 40 % DOD would be able to support 240 W during one orbit. The utilization of this capacity depends which part of the orbit is being used for imaging. As a worst case scenario, if imaging is carried out during an eclipse period, then the batteries have to sustain the combined power demand of housekeeping and the payload power drainage. The housekeeping power is consumed for navigation and control, data handling, telemetry, data transmission etc.

and is ~20 Wh that would be ~ 33 W per orbit. For an entire eclipse period of 35.49 minutes, the housekeeping needs are ~12 W. Although imaging can not be done through an entire eclipse period batteries can only be charged once the satellite comes out of the eclipse. Thus this housekeeping power required during eclipse period has to be set aside. If this is the case, then the power left for the SAR payload during eclipse period would be 228 W.

Already installed 2 batteries provide 15 Ah capacity and weigh ~ 6 kg (70 $Whkg^{-1}$). Incorporating another battery of 7.5 Ah capacity would add 3 kg extra that needs to be catered for while calculating the mass budget. All the power subsystems onboard SSTL buses are designed for a mission lifetime of 7 years in LEO. [115]

6.2 Antenna Design

For the proposed microsatellite SAR mission, the antenna design plays a critical role. It not only provides an interface between RF power source (SSPA) and the space for transmission and reception of the electromagnetic energy but also contributes significantly to reducing the mission cost/mass. Thus, for the proposed antenna design (in addition to satisfying the electrical parameters) it would have the following constraints:

- how to achieve compact stowage volume with an extremely light-weight structure?
- ease of construction and maintenance during launch and subsequent deployment in space.

It was established in chapter 4 that for ECMP SAR, a 5 m parabolic reflector antenna is required. Within this design, the choice is between:

- Newtonian (single parabolic reflector – used with TecSAR) or Cassegrain (dual reflector – planned to be used with MAPSAR) configurations, from the perspective of how to illuminate the main reflector.
- And either deployable or inflatable, from the perspective of its effects on the net stowage volume during launch and how to deploy it in the space after launch.

For carrying out the necessary comparison, a couple of assumptions are considered here:

- Although the Cassegrain configuration yields slightly higher far field gain than achieved from the Newtonian configuration [41], it is assumed that both would yield the same far field gain. Also, both would result into similar far field radiation patterns for the given aperture size.
- The main reflector's surface inaccuracy limits are assumed to be $\pm 1/8$ of the operating wavelength. The far field antenna gain distributions shown in Figure 4 - 19 were simulated according to this inaccuracy limit.

In general, reflector antennas in the context of radar applications are considered suitable for developing low cost systems that need very high gain (mainly a function of the aperture size) and limited scanning capability. These are built in a wide variety of shapes and sizes with a corresponding variety of feeds to illuminate the surfaces, to suite a particular application. For the proposed design, the Newtonian or Cassegrain configurations are of interest, thus these are shown in Figure 6 - 2.

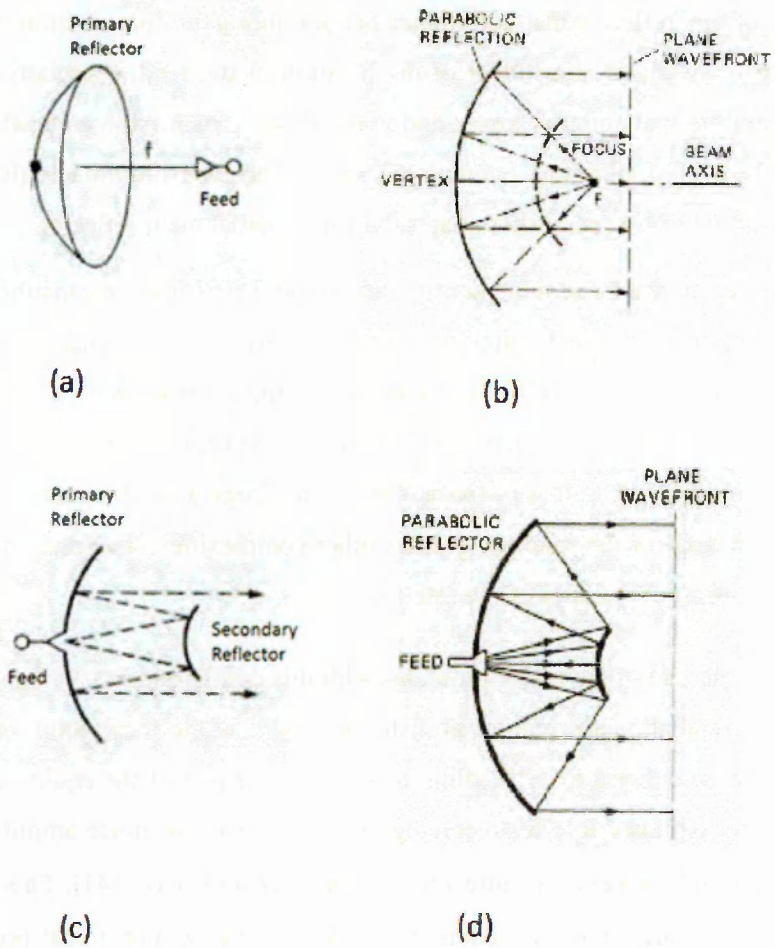

Figure 6 - 3: Newtonian and Cassegrain reflector illumination configurations

Source: Adapted from [41]

Figure 6 – 2 (a) shows the basic geometry of the Newtonian configuration. The paraboloid collimates electromagnetic radiation from the feed which is kept at a focus point. It can be shown by considering the geometrical optics that a spherical wave emerges from the focal point and is transformed after reflection into a plane wave front as shown by the rays model in Figure 6 – 2 (b). [41]

In general, the aperture efficiency of this configuration is considered medium to high as compared

with the Cassegrain configuration. The relationship of the focal length, the depth of paraboloid and the diameter of the paraboloid was established in Eq. 4 - 4. By varying the focal length, the far field sidelobe performance can be adjusted according to the requirements.

Similarly Figure 6 – 2 (c) and (d) show the basic geometry and ray model of the Cassegrain antenna, in comparison to that of the Newtonian design. The basic concept of this antenna configuration was derived from optical telescopes. In this configuration, two reflectors are used. The primary/parabolic reflector is the same as that of the Newtonian design, and it is the size and shape of this reflector that determines net aperture gain. Introduction of a secondary reflector facilitates convenient adjustment of the location of the feed, especially closer to the RF PA, thus reducing the transmission losses and mass of the transmission channel. The virtual focal point in both these configurations remains the same. The feed illuminates the hyperboloidal secondary reflector, which in return illuminates the paraboloidal main reflector.

In the case of the Newtonian configuration, the 0.6 *f/D* ratio means the feed needs to be kept at a focal length of 3 m. At L-band, for such a long focal length, a narrow beam from the feed horn is required to reduce the spill-over losses. To get this narrow beam, a larger horn would be required. During launch phase, this feed assembly has to be kept closer to the main body of the payload to conserve space. Once it is in space, then such a large and heavy feed assembly at 3 m away from the main body of the satellite, besides other complexities, would act like a gravity boom thus affecting the aerodynamics of the satellite.

In addition, one of the major problems with this configuration is getting the RF power to the feed. With a conventional prime-focus dish, the feed is at the focal point, out in front of the parabolic reflector, so either a lossy feedline is necessary or part of the equipment is placed near the feed. The latter is reasonable for receiving systems, since low-noise amplifiers (LNA) are quite compact, but high-power transmitters tend to be large and heavy [41]. This problem gets worse if dual (or quad) polarizations are required as a design feature. For a dual polarization, at least 2 cables are required, one each for H and V polarized receiver channels. These cables introduce transmission losses and add mass.

A dish antenna with multiple reflectors, like the Cassegrain antenna, looks like an obvious solution to these problems. In this case, there is no need to deploy the feed away from the RF PA. It can be kept at the vertex and there would be no need for any RF cables, only a small waveguide is required to connect the power from the PA to the feed. If this is to be the case, then the major concern remains how to mitigate the blocking/shadowing effects of the secondary reflector on the radiations from the reflector.

For reflector antennas having (diameter to wavelength) D/λ ratio in the range of 10 – 15, the Newtonian configuration is considered suitable as it yields less shadowing effects as compared to the Cassegrain configuration. For the larger values of D/λ ratio, the Cassegrain configuration is considered better. In our case this ratio is 21.27, thus Cassegrain configuration is recommended. This is the reason MAPSAR with the 5 m width and 7.5 m length reflector antenna is using the Cassegrain design.

As described earlier, the aperture efficiency for a Newtonian reflector is maximized by balancing the feed taper (focal length adjustment) and minimizing the transmission losses etc. but is typically 55 – 65 %. However, dual reflector systems are considered comparatively more efficient as transmission losses are low which enable aperture efficiencies in excess of 70 %. [41]

The last decade has seen enhanced interest in using large reflector antennas not only for spaceborne radar applications but also for communication satellites. The major technology drivers remain the low cost, light-weight, large apertures that yield high gain, compact stowage volume during launch phases etc. To this effect, most successful missions have been the Thuraya communication satellites using AstroMesh Deployable Reflector antennas of 9 m and 12 m. These antennas were developed by the Northrop Grumman Space Technology group. They have developed these mesh antennas of varying sizes. Among others, the 6 m diameter antenna for L-band is of our interest. This reflector weighs only 14.5 kg and its stowage dimensions are $0.60 \times 0.66 \times 1.54$ m. [52] This is designed for a Newtonian configuration with offset feed. Although it falls within the envisaged ~ 25 kg mass for the antenna we are looking for, is commercially available off the shelf and is a developed and space qualified product; however it poses the following challenges to our overall design:

- Its stowed volume once added to that of the bus volume (1.54 m stowed height of the antenna + ~ 1 m height of the bus, in total ~ 2.54 m height) would require a dedicated launch.
- The already discussed issues pertaining to feed location for the Newtonian design in a microsatellite would remain there.

Against this backdrop, an inflatable technology provides a viable solution. The concept of using this technology—with the Newtonian configuration—was discussed in section 2.6.2.2. If it is slightly modified by taking out the deployable feed and replacing it with what is being used with MAPSAR antenna i.e., a Cassegrain feed arrangement, this would look like as shown in Figure 6 – 3. In this figure, the left portion shows the configuration during launch phase. The Cassegrain part is shown separately on the top—as it needs to replace Newtonian middle part. Once launched and the satellite is in space, the antenna can be inflated to look as shown in the right portion of the

figure.

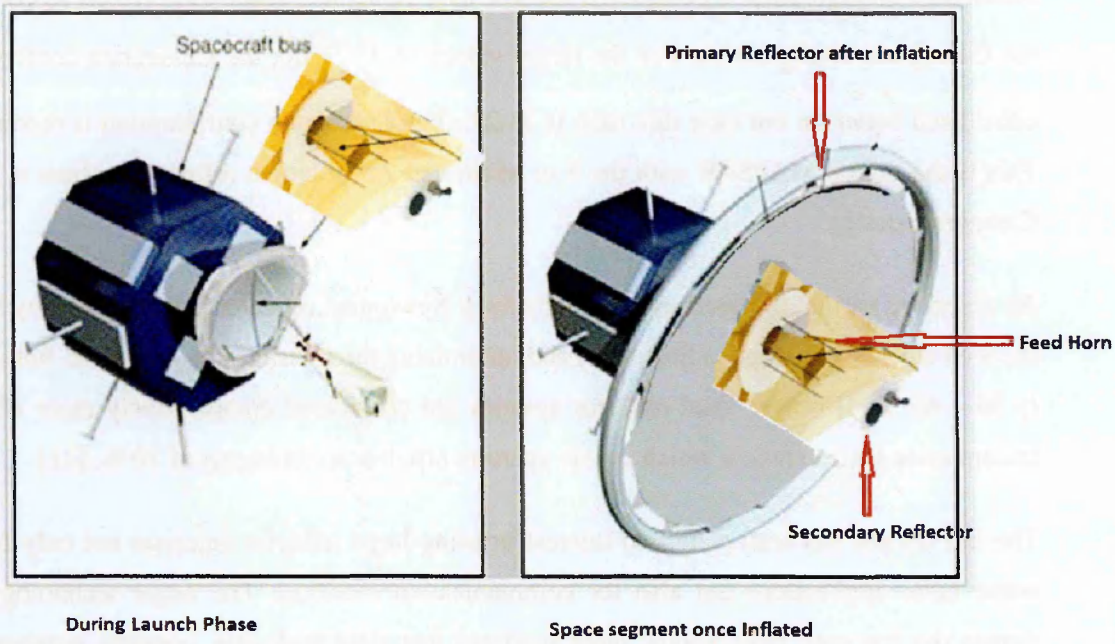

Figure 6 - 4: Combination of inflatable concept and the Cassegrain configuration

This modification results in keeping the feed at the antenna vertex and only a small secondary reflector would need to be deployed, once the satellite will be in the space. During the launch phase, this secondary reflector may also be kept closer to the bus if it is designed using a telescopic mast. This configuration would yield compact volume, almost same as that of the bus itself. The primary reflector remains un-inflated during the launch phase thus ensuring the reduced stowage volume as shown in the figure.

As was discussed in section 2.7 an inflatable technology demonstrator (with 14 m diameter antenna) was tested in space. [55] Now an improved version of the same design has been adapted for a Ku-band, 35 m diameter inflatable reflector antenna. [54] This technology is comparatively very low cost (e.g. design and development cost for 14 m antenna was USD 1 M only [55]). For the ECMP SAR mass calculations, an inference may be directly drawn from the L-band, 6 m AstroMesh antenna that weighs 14.5 kg. This weight is only for the deployable reflector that includes the support structures and the mesh. If a similar mesh is used, then it may be possible to replace the mechanical support structure by inflatable structures, while remaining within ~ 15 kg mass budget. As the feed is kept at the vertex, thus there is no need to have strong feed holding/support structures; it would be only the light-weight secondary reflector and its supports that need to be deployed in space. Keeping these aspects in mind, it may be confidently estimated that the feed, secondary reflector, the inflatable structures and the mesh, all should weigh ~ 25 kg (similar to the mass of 21 kg, 4.5 m deployable antenna being used with TecSAR-2, that has 8

feed arrays with at least 8 coaxial cables and is based on Newtonian configuration).

6.3 Ambiguities, Limitations and Flexibilities

6.3.1 Range Ambiguity

In order to define and analyse the range ambiguity and its effects, let us make a distinction at the outset about two different aspects of this phenomenon, which are: the SAR operational aspects and the radiometric aspects of the SAR image formation.

The operational aspects take into account the factors to ensure that at any instance of time, there should be only one pulse impinging in the BW_{3dB} swath, otherwise it is difficult to make the distinction between the returns from different pulses.

The radiometric aspects of the SAR image formation deals with the effects which appear as the ground objects duplication on image along range direction. These are caused by overlapping return signals from different pulses which come back to radar on the same time. The contributing factors are the high level of antenna range pattern sidelobes, low backscattering level in main lobe, and high backscattering level in one of the sidelobes. It is difficult for the SAR processor to correct these effects. [118]

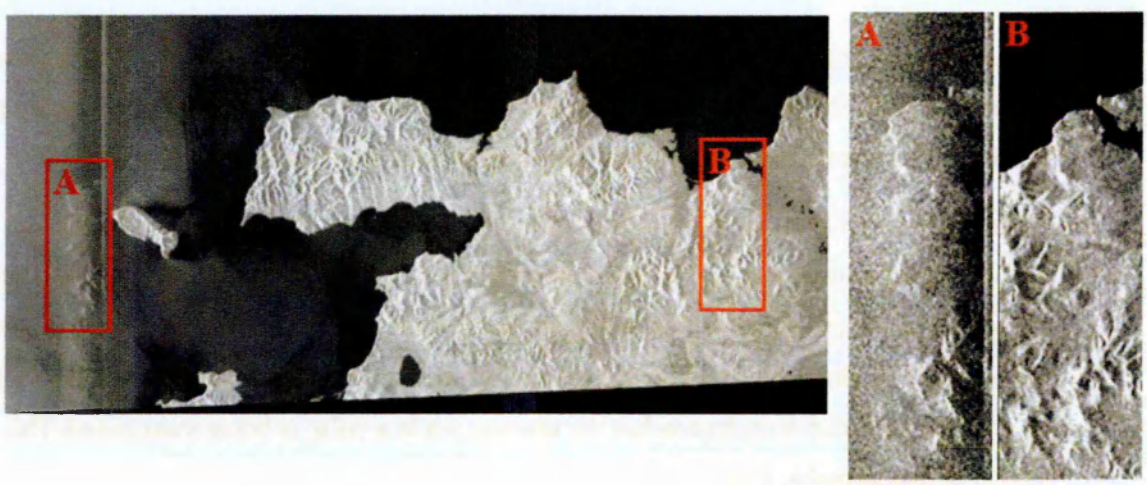

Figure 6 - 5: RADARSAT-1 image showing the Range ambiguity

Source: adapted from [118]

The image shown in Figure 6 - 5 was acquired by RADARSAT-1, Orbit 66267, Survey mode SWA (W1+W2+W3_S7). Range ambiguity signal (A) appears in beam W1 on the sea surface. In reality this signal comes through sidelobe from mountain area (B) in beam W3. Bright strip in left part of image designate the nadir ambiguity.

During the subsequent discussions and the analysis, first the operational range ambiguity would be dealt with followed by radiometric aspects.

From the operational point of view, calculating the range and azimuth ambiguities for the space-borne SAR mission is a complicated process but for the ECMP SAR, additional complexities are added due to the need to maximally extend the chirp so that peak RF power remains within safe limits of the single SSPA. In order to address the range and azimuth ambiguities, the minimum diameter of the parabolic antenna was calculated according to:

$$\text{Eq. } 4-3 \Rightarrow \qquad D_{\min}^2 = \frac{16\lambda v_s}{\pi c}\left[\frac{h}{\cos\beta}\right]\tan\beta$$

This shows that the minimum antenna area requirement remains a function of:

- Operating wavelength – that is fixed in this case as only L-band is being used.
- The mean altitude of the satellite – also fixed here at ~ 600 km.
- Satellite velocity – linked to the set orbital parameters, but it varies according to Earth tangential speeds at different latitudes. For the purpose of short imaging intervals of ~ 2 minutes, it is usually considered almost constant.
- The incidence angle – was considered 30^0 at that time but actually it needs to be varied from 20 – 50^0 to satisfy the user requirements.

The selected minimum diameter of the antenna yields a band of usable PRFs. With a view to plan my ECMP SAR, the minimum PRF limit had to be further lowered so that the necessary time slot in the PRI is created for this extension. This necessitated an oversized 5 m antenna.

Besides this consideration, another limitation on the choice of PRF is imposed by the fact that due to the large distance involved between an orbiting SAR and the Earth, many pulses and many echoes are in the propagation path at any instant of time. Since it is a pulsed system that works on the principle of alternatively switching on and off the transmitter and the receiver, the PRF should be selected such that no echo reaches the antenna while a pulse is being transmitted. This leads to a band of unacceptable PRFs.

For the ECMP SAR, choosing a usable band of PRF becomes complicated because of the desire to maximally extend the chirp (~ 40 %) within the given bounds of set PRI, so that peak RF power fed at the input of the antenna is kept within safe limits for the single SSPA and the onboard power system. Therefore before proceeding further, let us define the safety limits for the SSPA and the batteries.

By operating the satellite batteries within the safety limits of 10 – 40 % DOD, a longer life may be achieved. The batteries onboard SSTL–150 bus if operated at 20 % DOD are expected to last

for 15 – 18 years. [115] By increasing the DOD limit to 40 %, these are expected to serve for 7.5 – 9 years. This research aims at proposing a design for a mission life of 5 years. By keeping a safety limit at 40 % DOD, batteries should last for more than 5 years mission life. This implies that at 28 V, 3 batteries each with 7.5 Ah capacity can be used to draw 3 A of current, to yield a net 252 W of DC power.

These power limits are for the worst case scenario when the SAR is operated during eclipse. The situation improves (i.e., DOD limit reduces) once it is operated during sun-light hours. At that time, to reduce the burden from the batteries, the DC power generated by the solar panels and going to the batteries for charging them may be diverted to the payload to lessen the burden from the batteries.

As mentioned previously, the single GaN based SSPA developed by [49] for radar-specific applications can support up to 204 W RF output at 60 % PAE. To achieve optimized performance and longer life, if it is operated at ~ 75 % of the maximum capacity, it would yield ~ 150 W RF power, while drawing ~ 250 W DC power from the power system.

Certain aspects related to calculating the usable PRFs are:

- While calculating the usable PRF, there appear to be different possibilities under one set of variables e.g. at one given incidence angle, the receive window time (the time to image the swath in slant range) i.e., $T_{R,W} = \frac{2\left(R_{S,F} - R_{S,N}\right)}{c}$ remains fixed for a given 3 dB beamwidth of the antenna pattern. Now either the chirp width τ', P_t or P_{av} can be kept constant and then the usable PRF is calculated. From the hardware perspective, it is convenient to keep τ' and P_t constant and vary the average power – which is to be drawn directly from the batteries or a combination of batteries and the solar panels (during sun-light hours).
- In addition, the usable PRF varies according to the number of pulses or echoes that are simultaneously allowed in the transmission path. Varying this number one after the other, different usable PRFs may be calculated.
- One set of these variables may not be applicable to the complete range of incidence angles from 20 – 50^0. Therefore, this range is subdivided into groups of 5^0 each.
- For 20^0 going higher in the number of pulses, needs higher PRF, keeping τ' and P_t constant, the required average power increases, as the duty cycle is increasing.

Procedure

Let us take the example of incidence angle of 20^0.

- Given the antenna radiation pattern of Figure 4 - 19 the 3 dB beamwidth is 3.1^0. This yields a near slant range of 632 km and far slant range of 645 km. By incorporating the effects of curvature of Earth, the achievable ground swath would be 37.5 km.
- The two way travelling time for the pulse at the near slant range $\frac{2R_{S,N}}{c}$ is 4.21 ms .
- Along the slant range, the receive window time/imaging time may be calculated from the two way difference between near and the far slant ranges, given by: $T_{R,W} = \frac{2\left(R_{S,F} - R_{S,N}\right)}{c} = 83\ \mu s$
- For the ECMP SAR, as was previously calculated that in order to keep the peak RF power low, the chirp should be extended to $120\ \mu s$. To keep a safety margin of $12\ \mu s$, the total minimum time/PRI should be : $120 + 83 + 12 = 215 \mu s$ (which is equivalent to PRF= 4650 Hz). Under this situation, this may be considered as the upper bound of the PRF. The lower bound should be at least 1.1 times the minimum PRF (2950 Hz).
- If 4650 Hz PRF is considered, then there would be 19.6 pulses simultaneously present in the transmission channel. It implies the returns from the near edge of the swath would be interfering once pulse number 20th is being transmitted. In order to find the best unambiguous frequency, the 'n' (i.e., the number of pulses/echoes simultaneously present in the transmission channel) should be a whole number.
- This may be achieved through a simple procedure by dividing the 2 way travelling time of the near slant range with appropriate whole numbers e.g. if n=19 $\Rightarrow$ $4.2166 \times 10^{-3} / 19 = 221.92\ \mu s = 4506\ Hz$. It means that a PRI of $222\ \mu s$ or the PRF is exactly set at $4506\ Hz$, then there would be 19 pulses travelling in the transmission channel without any overlap at the time of transmission or reception.
- The same process by lowering the value of 'n' should continue until the lower limit of PRF is reached, for a give incidence angle.
- Given the incidence angle of 20^0, means there can be 5 best PRFs that corresponds to $n = 15 - 19$, as shown in Table 6 – 1. A similar procedure is followed at other incidence angles.
- As the incidence angle increases, the slant range swath increases, which in return needs large $T_{R,W}$, that eventually occupies larger portion of the PRI. This factor leads to reduced choice of a suitable PRF at 35^0 and beyond.

Analysis

By using the highlighted set of parameters for the given incidence angles presented in Table 6 - 1, the SNR distribution over the slant ranges have been calculated at these angles and shown in Figure 6 – 5. SNR distributions for 20 – 40^0 are plotted with an increment of 5^0 (except for 37.5^0). While obtaining these plots, it is ensured that: the angular variations in σ^0 as given in Table 4 - 3 are used; and the ground range resolution is calculated by incorporating the curvature of the Earth effects.

As evident in almost all the plots shown in Figure 6 – 5 that the effects of the nadir returns are far below the main lobe returns, thus these may conveniently be ignored.

By increasing the incidence angle up to 40^0, the saturation point reaches with respect to finding a suitable PRF and also supporting the required peak RF power is considered, because:

- The slant range swath becomes so wide that it occupies ~ 78 % of the PRI and space to extend the chirp is restricted.
- Even at this angle, although a suitable PRF is available, by considering a mean value of $\sigma^0_{HH} = -17.5$ dB for this incidence, the achieved $\mathrm{SNR}_{\mathrm{HH}} = 8.17$ dB. This is under the worst case scenario of imaging during an eclipse period once 150 W RF power is generated while remaining within safety limits of 40 % DOD of the batteries. To obtain higher values of SNR, higher RF power is required, that will drive the PA and the batteries out of the safety limits.

Incidence angle	$R_{S,N}$ **(km)**	$R_{S,F}$ **(km)**	**No of Pulses**	**PRF (Hz)**	$T_{R,W}$ (μs)	P_t **(W)**	τ' (μs) **and duty cycle**	P_{av} **(W)**	**Ground Swath (km)**
20^0	632	645	15	3557	83	60	120 (42 %)	25	37.5
20^0	632	645	16	3794	83	60	120 (45 %)	27	37.5
20^0	632	645	17	4031	83	60	120 (48 %)	29	37.5
20^0	**632**	**645**	**18**	**4268**	**83**	**60**	**120 (51 %)**	**31**	**37.5**
20^0	632	645	19	4506	83	60	120 (54 %)	33	37.5
25^0	654	670	15	3440	111	60	120 (41 %)	25	41
25^0	**654**	**670**	**16**	**3669**	**111**	**60**	**120 (44 %)**	**26**	**41**
25^0	654	670	17	3900	111	60	120 (46 %)	28	41
30^0	**682**	**704**	**16**	**3517**	**144**	**80**	**120 (42 %)**	**34**	**45**

30^0	682	704	17	3736	144	80	120 (44 %)	36	45
35^0	**719**	**746**	**16**	**3337**	**185**	**100**	**100 (33 %)**	**33**	**52**
37.5^0	**741**	**773**	**17**	**3440**	**210**	**150**	**65 (22 %)**	**34**	**57**
40^0	**766**	**801**	**17**	**3328**	**237**	**150**	**60 (20 %)**	**30**	**62**

Table 6 - 1: The best PRFs at different incidence angles

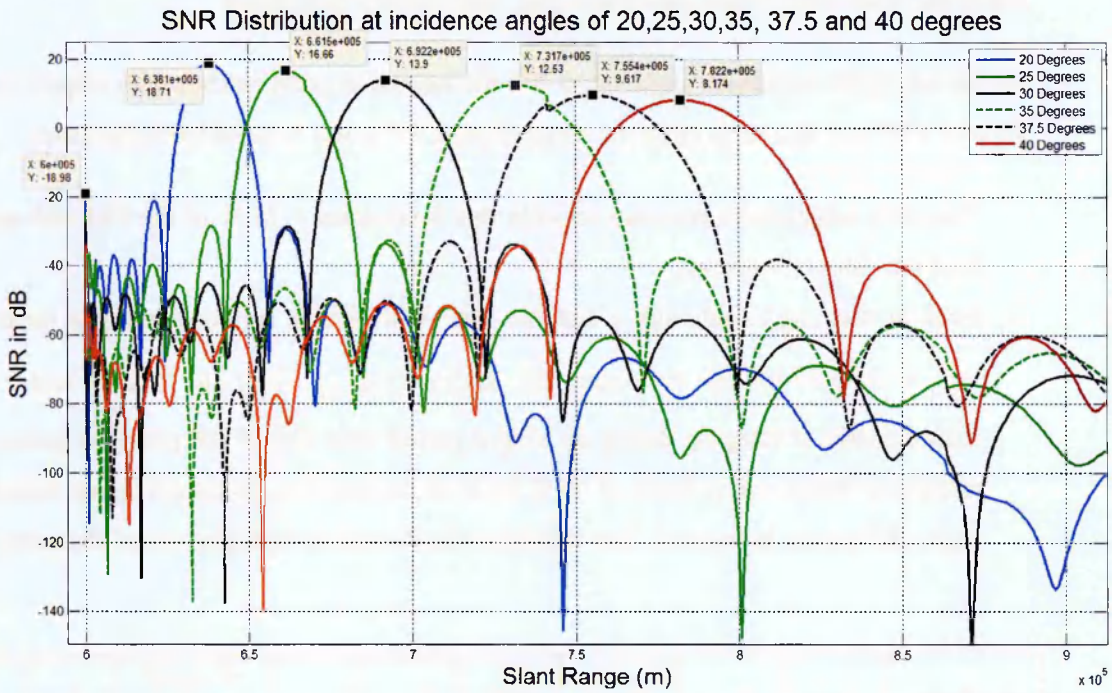

Figure 6 - 6: Comparison of SNR distributions according to variations in the incidence angles

Figure 6 – 5 shows the complete distributions from the nadir to the farthest slant range, whereas Figure 6 – 6 is a zoomed in part of this figure. It is plotted to highlight the SNR in the positive regions. It shows that as the incidence angle increases, the SNR decreases. Hence it may be commented that the proposed design would be limited to the incidence of 40^0 once:

- the capabilities of the onboard power system are fully exploited within safety limits of 40 % DOD
- the selected SSPA is operated at ~ 75 % of the maximum capacity
- and the 5 m parabolic reflector antenna are considered.

As it was discussed in chapter 4, a 6 dB dynamic range between mean values of σ^0_{HH} and σ^0_{VH} should be considered. This condition may not be satisfied at 40^0 incidence as achieved SNR_{HH} is only 8.17 dB, thus reducing the dynamic range to 2.17 dB only.

The situation slightly improves at 37.5^0 once a $\mathrm{SNR}_{\mathrm{HH}} = 9.6$ dB is achieved for $\sigma^0_{HH} = -17.5$ dB by using 150 W RF power. It provides an opportunity to detect $\sigma^0_{VH} = -21$ dB with a positive SNR at the near and far edges of 3 dB beam width.

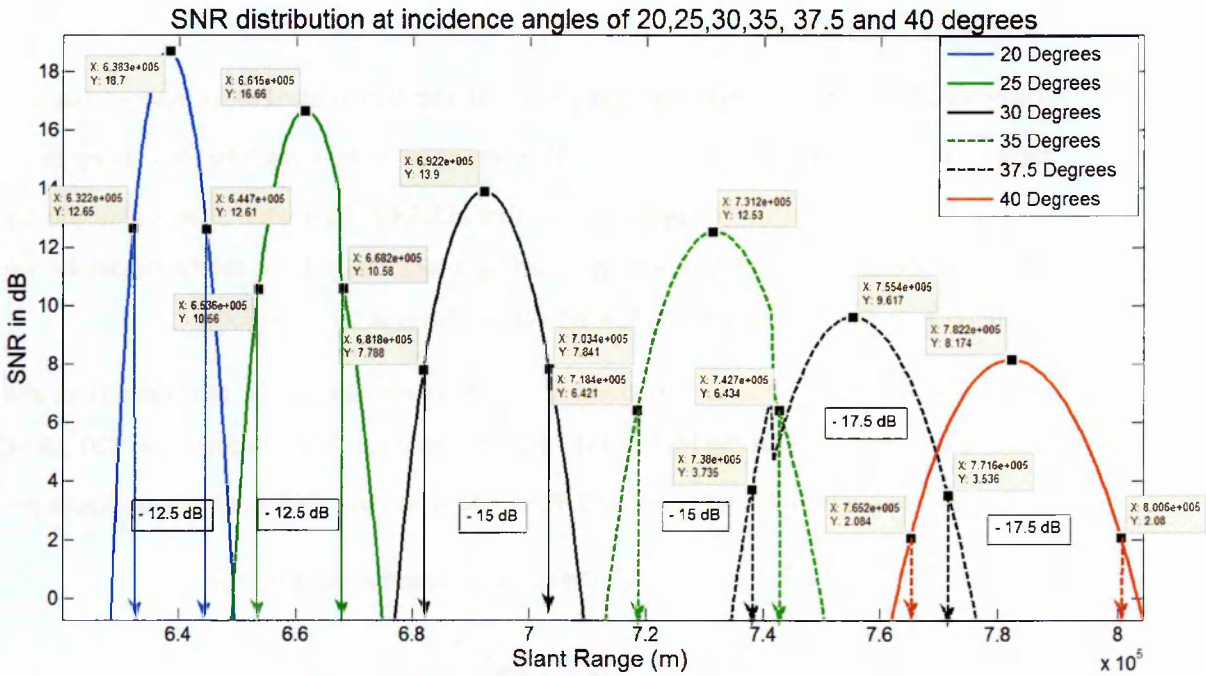

Figure 6 - 7: Zoomed in part of Figure 6 – 5 highlighting the usable portion of the SNR

35^0 incidence angle provides 6.5 dB dynamic range, with 100 W RF power for $\sigma^0_{HH} = -15$ dB. Under the assumption of a worst case scenario where 40 % DOD is assumed during the eclipse, the DC power can support up to 150 W RF power. If 150 W peak RF power is used, then a $SNR_{HH} = 14.28$ dB is achieved. It means $\sigma^0_{VH} = -23.28$ dB is detectable at the edges of the 3 dB beamwidth.

While looking at the plot of 37.5^0, a prominent notch is observed. It can also be seen in other plots where it is not prominent. While calculating the SNR plots, standard backscattering profiles from distributed targets are used as a reference value for the σ^0. These profiles are incident angle dependent as shown in Figure 4 – 13. A detailed description already entered in Table 4 - 3 where it was discussed that mean values for small increments of 5^0 are used. Once these values jump from one group of angles to the next, it becomes prominent and thus reflected in the SNR plot. For this particular case, it jumps from 26 – 30^0 (– 15 dB) to 30 – 35^0 (– 17.5 dB). These jumps cause these notches in the corresponding plots.

After selecting the suitable PRFs and analysing their impact on the corresponding SNR plots, let us consider other contributing factors which affect the radiometric aspects of the SAR image. These are the high level of antenna range pattern sidelobes, low backscattering level in main lobe,

and high backscattering level in one of the sidelobes.

The antenna range pattern sidelobes were discussed for the 5 m antenna in section 4.2.4 and the discussions which followed Figure 4 – 18 through 4.21. Due to low antenna gain distribution at the nadir incident angles, the effect of nadir returns, as observed in Figure 6 – 5 and 6 – 6 can conveniently be ignored.

To proceed further, let us take the example of 30^0 incident angle. Let us assume that a distributed target with a mean value of $\sigma^0 = -$ 15 dB is observed at the main lobe. If a strong target appears with a very high value of σ^0 appears in the first sidelobe, then what effects it would have on the main lobe detection. In other words, how strong a target may be at the first sidelobe what would cause reflections at the target with low reflectivity level at the main lobe.

The response of the SNR to variations in the σ^0 is non-linear due to range effect and antenna gain. If it is assumed that the PRF = 3517 Hz, the chirp can be extended up to 120 μs (42 % duty cycle) and with a peak RF power of 150 W, would return the SNR as shown in Figure 6 – 5.

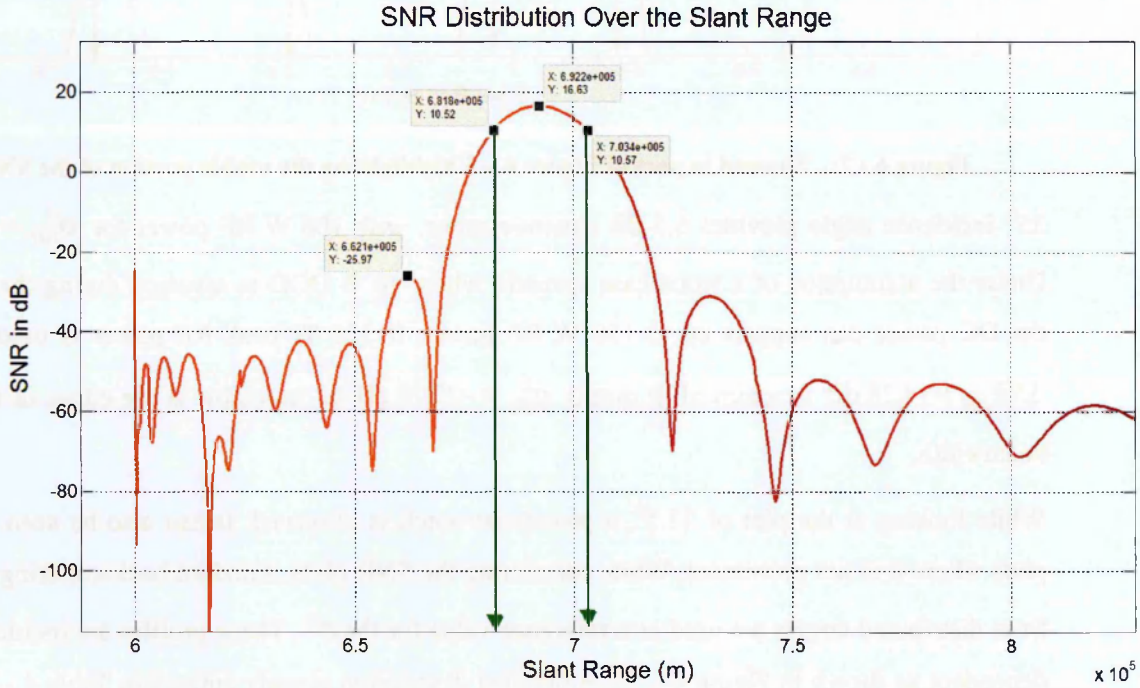

Figure 6 - 8: Range ambiguity to signal ratio at 30^0 incident angle

As can be seen that the BW_{3d} swath is achieved once the SNR drops by 6 dB. Now what should be the σ^0 value of a target at first sidelobe which should cause the returns to be stronger than the returns from the $\sigma^0 = -$ 15 dB at the edges of swath. Since it is a non-linear relationship, thus by iterating different values in the SNR equation, it is found to be ~ 24 dB. The reference range for the ALOS is 9 – 26 dB for the single/dual polarizations. Thus, this range ambiguity level is con-

sidered sufficient for the ECMP SAR design at 30^0. This value is incident angle dependent and varies as incident angle is changed.

6.3.2 Azimuth Ambiguity

Similar to the range ambiguity, the azimuth ambiguity can also be classified relating to the SAR operational aspects and the radiometric aspects of the SAR image formation.

While dealing with the SAR operational aspects relating to the azimuth ambiguity, one has to take into account those factors which ensure that the estimated Doppler bandwidth is adequately sampled during synthesis process. This can be ensured by selecting the PRF which over-samples the estimated Doppler bandwidth by at least a factor of 1.1. The selected PRFs shown in the Table 6 – 1 consistently ensure this over-sampling as lowest selected PRF is 3328 Hz which is over-sampling the minimum PRF 2890 Hz by a factor of 1.15. If Doppler bandwidth is not adequately sampled then another phenomena known as "Ghosting" is observed in the SAR image. Ghosting can not be corrected by the SAR processor.

Azimuth ambiguity effects pertaining to the radiometric aspects of the SAR image appear as the ground objects duplicating on image along azimuth direction. It is caused by overlapping the return signals from one pulse but with multiply Doppler frequencies. The contributing factors for the azimuth ambiguity are the high level of antenna azimuth pattern sidelobes, low backscattering level in main lobe, and high backscattering level in one of the sidelobes. SAR processor does not correct this effect. [118]

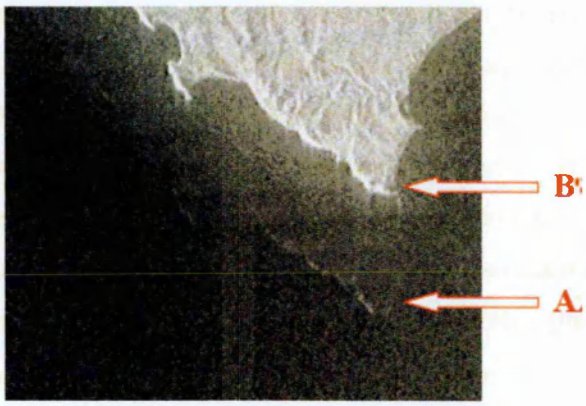

Figure 6 - 9: RADARSAT-1 image showing the azimuth ambiguity

Source: adapted from [118]

To quote an example, the image acquired by RADARSAT-1 SAR during orbit 66267 while in the Survey mode SWA using Beam S7 is considered here. The Azimuth ambiguity signal (A) appears on sea surface with low backscattering level. In reality this signal duplicates azimuth sidelobe

from land area (B) with high backscattering level.

To quantify other contributing factor in the context of 5 m antenna radiation pattern and its SNR response along the azimuth direction, only one range cell across all the azimuth bins is taken at one time, at 30^0 incident angle. The same parameters which are used to generate Figure 6 – 7 are utilized here to obtain this plot.

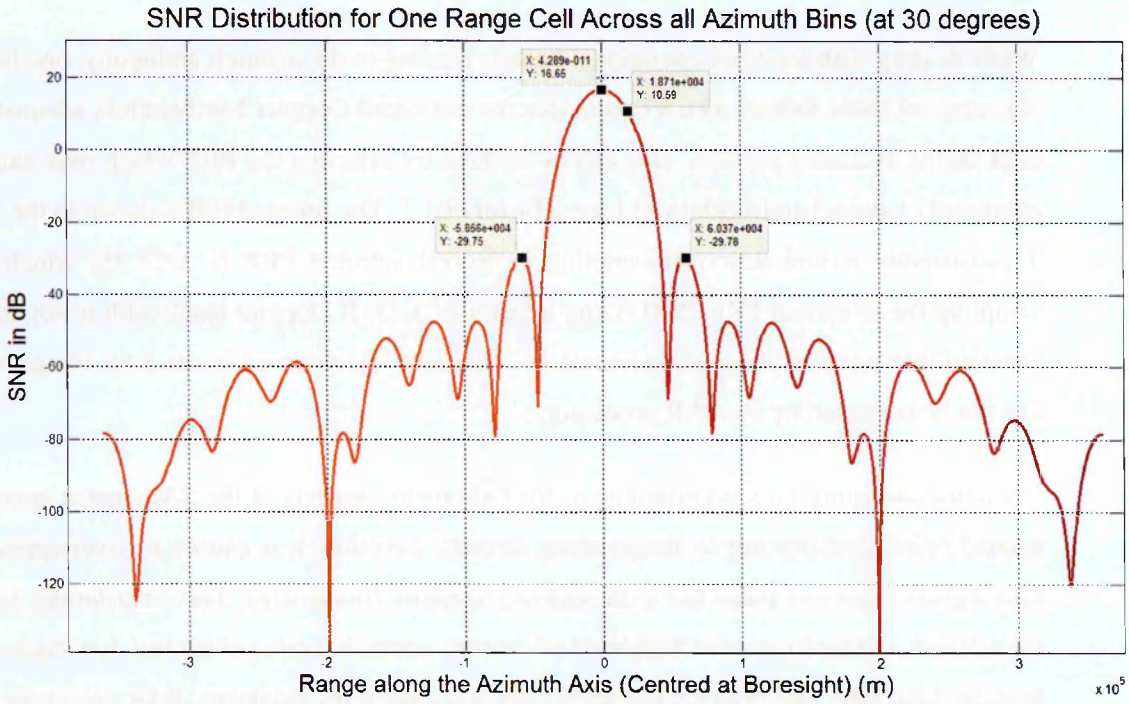

Figure 6 - 10: Azimuth ambiguity to signal ratio

The horizontal axis shows the distance along the azimuth direction with respect to the antenna bore sight considered perpendicular to the velocity vector. Since only one range cell across all the azimuth bins is considered, thus range is considered constant, which returns a symmetrical SNR plot. At the centre of the beam, a target of – 15 dB backscattering level is used. The SNR equation is iterated to find out how strong a target can be at the first sidelobe, which would cause the reflections within azimuth $BW_{3\ dB}$ swath. For the azimuth direction, this is a linear relation (opposite to the range direction where it is non-linear) as the effect of range on the SNR is considered constant. It is found out that if $\sigma^0 = 25$ dB , it would be strong enough to interfere and introduce reflections in the main lobe image. The reference value for the ALOS had been 21 dB for the single/dual polarizations. As advocated by [91], a value of > 20 dB is always desirable.

6.4 Estimated Power Budget and Imaging Time

Under the worst case scenario of operating the SAR during eclipse, if it is assumed that the batteries were fully charged once the satellite entered the eclipse, then within the safety limits of ~ 40

% DOD, 250 W DC power would be available. During eclipse, only 12 W are required but to be on the safer side, 50 W are reserved for this purpose. Thus 200 W are available for SAR operation.

As mentioned in Table 6 – 1, the mean average RF power needed from incidence angles of 20 – 40^0 is ~30 W. With 60 % efficient SSPA, the DC power required is 50 W.

Thus, under these conditions, the 200 W per orbit ($\cong$ 130 Wh) available DC power can support SAR operation for ~ 2.5 minutes/orbit.

Given this capability, how much is the area that can be imaged during one year?

- At 30^0 incidence angle, the ground swath = 45 km
- The satellite velocity, $v_s = 7.56$ km / s
- In 2.5 minutes/orbit, the area to be imaged = $7.56 \times 60 \times 2.5 \times 45 = 51{,}030$ km^2
- With 14.85 orbits/day, the area imaged per year ~ 276×10^6 km^2
- Approximate global forest covered area = 72×10^6 km^2
- If it is required to image the global forests once a year, then the SAR needs operational time for ~ 40 seconds/orbit out of 2.5 minutes/orbit imaging time.
- Rest of the time may be utilized for other applications such as disaster monitoring and relief efforts.

6.5 Estimated Data Rates and Data Downlink Bandwidth/Speed

Since it is a pulsed system (although in extended chirp mode), thus would, like most of the other spaceborne SAR missions, suffer from the limited onboard data storage and subsequent downlink data transfer problems. The single channel (HH Polarized) anticipated data rate would be:

$$\text{Data Rate} = 2 \times B \times N \times \frac{T_{RW}}{PRI} \quad \ldots\ldots \qquad (6 - 1) \qquad [119]$$

where:

B = System Bandwidth = 9.6 MHz. This is the bandwidth required for range resolution of 30 m at the near edge of the range swath once 30^0 incidence angle is considered (while calculating this value, the effects of the curvature of Earth were taken into account and local incidence angle was used). To ensure adequate and safe sampling, It is preferred to over sample it, thus instead of 9.6 MHz, 10 MHz is considered here.

The appearing of the number 2 means that the required bandwidth is being sampled respecting the Nyquist criteria.

N= number of bits per sample (also called the quantization rate), 8 bits ADC is considered.

T_{RW} = Swath width time (the time required to image the swath in slant range) = 144 μs

PRI= Pulse Repetition Interval/Inter Pulse Period = 284 μs

Thus, Eq. 6-1 $\Rightarrow$ $\text{Data Rate} = 2\times10\times10^{6}\times8\times\frac{144\times10^{-6}}{284\times10^{-6}} = 81.13 \text{ Mbps}$

Most of the SAR systems use compression techniques to reduce this data rate. If 6 most significant bits (MSB) out of 8 are taken, then the data rate would be 60 Mbps.

Note: As the data produced would be in the complex numbers format that would be coming from separate I and Q channels before these are stored. 60 Mbps data rate encompasses both these channels.

Since the design focuses on HH and HV polarizations, thus to cater for the second channel, the same amount of data would also be generated, consequently the total estimated data rate would be 120 Mbps.

The baseline capabilities as discussed in chapter 3 show that SSTL-150 bus carries 16 GB solid state data storage dual redundant modules. The data generated at 120 Mbps, means that data may be stored up to 2.22 minutes of SAR operation under strip map imaging mode, at 30^0 incidence.

The SSTL-150 and SSTL-300 buses inherit similar onboard processors, RAM, the data buses, the control area networks, micro controllers etc. Recent literature shows the SSTL-300 bus being used with the NovaSAR-S payload would carry 32 GB solid state data storage dual redundant modules [26]. Using a higher capacity data storage module does not involve hardware changes if it has same pin configurations. Thus a similar module with 32 GB capacity may be used with this proposed design. If this is to be the case, then the data produced by operating SAR for 4.44 minutes may be stored.

SSTL-150 bus has data downlink equipment that supports 105 Mbps. The DMC satellites operating from similar orbits remain in the line of sight of the ground stations for ~ 8 – 10 minutes, while maintaining the required data downlink budget. 120 Mbps data produced for 2.5 minutes would be ~ 18 GB of the data that would need ~ 2.85 minutes data downloading time to a ground station.

Table 6 - 2 has been prepared with a view to estimating the data rates generated by varying the incidence angles from 20 – 40^0 and shows the effects of these data rates on onboard storage and data downlink. The worst case scenario appears to be at 40^0 because it has the largest swath that produces significantly higher data rates of 190 Mbps (for both HH and HV channels). The onboard memory can store up to 2.8 minutes of the data generated at this rate. This data storage

capacity is higher than the 2.5 minutes of SAR operation that can be supported from the onboard power system while remaining within safe limits. However for this particular case, the data has to be downloaded before carrying out any further SAR imaging in the next orbit. This situation is relaxed for the $\leq 30^0$ inclinations because data can be generated for 2.5 minutes of imaging operations but these can be stored for longer periods – thus providing the flexibility for the data to be carried to the next orbits for the downlink transmissions.

Incidence Angle	**Ground Swath (km)**	$T_{R,W}$ (μs)	**PRF (Hz)**	**Estimated Dual Channel Data Rates (6 MSB) – (Mbps)**	**32 GB can Store Data of how many minutes of SAR operation**	**Time Required to Downloading data for 2.5 minutes of SAR Operation through 105 Mbps link (minutes)**
20^0	37.5	83	4268	85	6.27	2.02
25^0	41	111	3669	98	5.45	2.33
30^0	45	144	3517	122	4.38	2.9
35^0	52	185	3337	148	3.6	3.5
37.5^0	57	210	3440	173	3.07	4.11
40^0	62	237	3328	190	2.8	4.52

Table 6 - 2: Estimated data rates from 20 – 40^0 incidence angles

When to download the data to a particular ground station depends upon the location of the satellite in the orbit and the location of the ground station. If it is assumed that the ground station is located closer to the equator in Africa, then the satellite/ground stations would be visible to each other only twice a day. Thus data downloading would really be a problem but not the unique one. The DMC satellites suffer from similar problems but as a standard procedure, the ground stations of the member countries allow each other to use the resources once these are free. The data are downloaded to these ground stations of the member countries and through internet, are transferred to the concerned home ground station that collects and stores the respective data. Adapting this distributed data downlink technique provides a suitable solution for the proposed SAR design.

Another option, although comparatively expensive, may be to relay this data through geostationary communication satellites, to the designated ground station. Most of the SAR missions (such as ALOS, TerraSAR-X and TandemSAR–X etc.) resort to this arrangement due to large data rates that are produced during imaging operation.

6.6 Effects of Attitude Determination and Control on Antenna Pointing

Aerial platforms fly in a dense atmosphere thus encounter severe disturbances. These disturbances are introduced due to gusts of wind, the continuous vibrations introduced due to the engines, comparatively less accurate navigational and attitude control instruments etc. These disturbances degrade the image quality, if not accurately measured and corrected in the motion compensation stage of the signal processing. Space provides a micro-gravity environment that is conducive for very stable platforms. Most of the modern day microsatellite buses are equipped with highly sensitive and accurate sensors that provide required stability and attitude control during imaging.

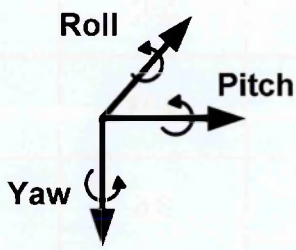

Roll	About the azimuth (along track) direction (the same direction as the platform velocity).
Pitch	About the range (cross track) direction (perpendicular to the orbit plane)
Yaw	About the radius vector (nadir pointing) direction (perpendicular to the roll and pitch)

Figure 6 - 11: Attitude pointing and its orientation with respect to scene

Although satellites provide very stable platforms, SAR imaging from space altitudes experiences long travelling times, as compared to operations from the counterpart aerial platforms. During imaging, simultaneous illumination of the same spot on the ground is necessary, thus antenna pointing is considered an important aspect of the mission design. [120]

Antenna pointing accuracy is directly linked to the satellite's orientation (attitude). Any disturbance can cause platform misalignments, which correspond to antenna footprint errors on the ground. Usually, satellite attitudes are described by means of rotations around three orthogonal axis, i.e., in terms of roll (R), pitch (P) and yaw (Y) – as shown in Figure 6 - 11. [120]

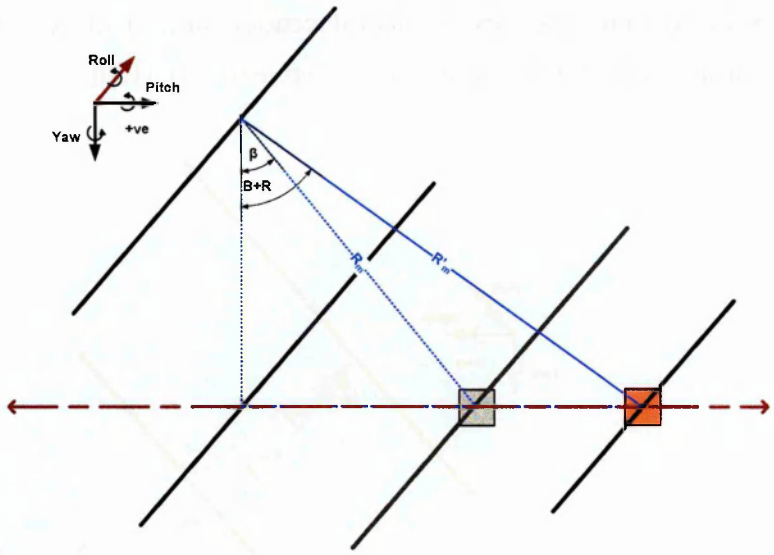

Figure 6 - 12: Affect of change in the Roll (R) on the incidence angle and corresponding change in the scene centre along range direction

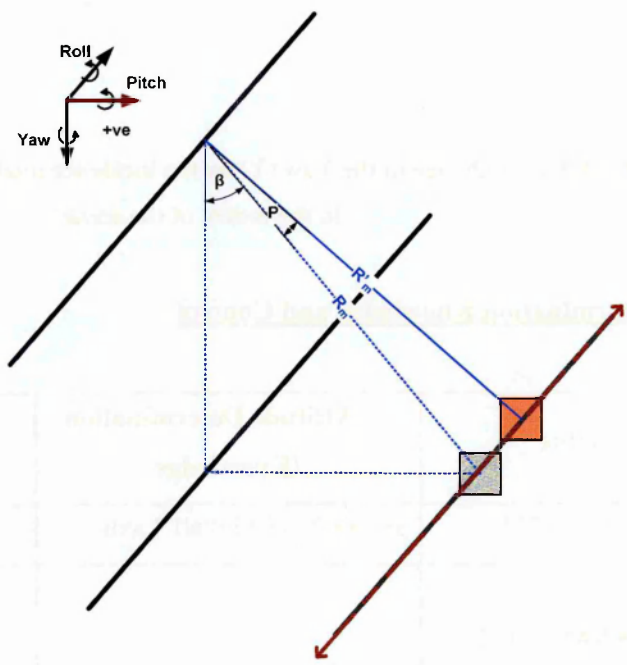

Figure 6 - 13: Affect of change in the pitch (P) on the incidence angle and corresponding change in the scene centre along the azimuth direction

Roll is a rotation about the flight path (azimuth direction) causing a footprint displacement in the range direction (across track) as represented in Figure 6 - 12, while a pitch error is a rotation about the axis that is parallel to the range direction, causing a footprint displacement in the azimuth direction (Figure 6 - 13). Yaw is a rotation about the altitude (height) axis, which affects the

footprint in both the range and azimuth directions, since it rotates with respect to the ground plane, causing a change to the squint angle (Figure 6 - 14). [120]

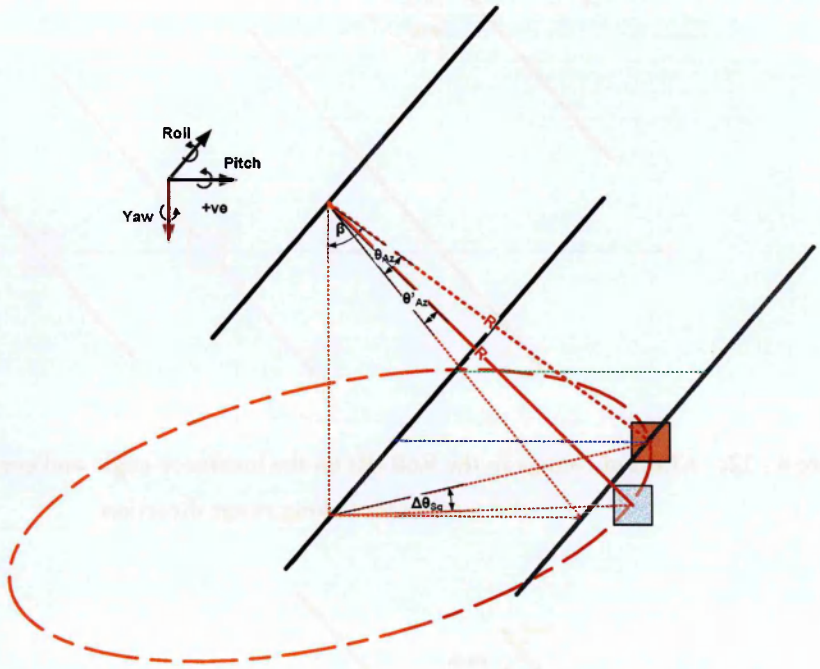

Figure 6 - 14: Affect of change in the Yaw (Y) on the incidence angle and the corresponding change in the centre of the scene

Attitude Determination/Knowledge and Control

Satellite	Attitude Determination /Knowledge	Attitude Control
ALOS-1 [121]	$\pm 0.0003^0$ (3 SD) all 3 axis	R, P, Y: ± 0.095°(3 SD)
RADARSAT-1 [122]	–	R: –0.255° to 0.180°, P: –0.895° to 1.005°, Y: –0.313° to 0.128°
RADARSAT-2 [123]	R, P, Y: ± 0.02°(3 SD)	R, P, Y: ± 0.05°(3 SD)
TerraSAR-X [124]	R, P, Y: ± 0.01°	R, P, Y: ± 0.01°(1 SD)
SSTL-150 Bus [90]	$\pm 0.00694^0$ (1 SD) all 3 axis	$\pm 0.01^0$ (1 SD) all 3 axis

Table 6 - 3: Radar satellites' attitude determination and control accuracies

Table 6 - 3 shows the attitude determination and control accuracies of different radar satellites. The attitude determination/knowledge and the control capabilities of SSTL-150 bus are very close and comparable to most of these large sized SAR missions especially L-band ALOS. In order to quantify the SSTL-150 bus capabilities in a meaningful analysis, let us consider the worst case scenario of 40^0 inclination.

- This inclinations yields a slant range at the centre of the ground swath, $R_{S,C} = 783.244$ km.
- If it is desired to maintain the antenna pointing at 40^0, but due to $\pm\ 0.01^0$ inaccuracy in the attitude control (say along the roll), the antenna pointing would be corrected within (40 ± 0.01^0). This results in a slant range that may be 783.129 km or 783.359 km (that is an error of ±115 m, or this may be interpreted as the misalignment of the scene by 115 m).
- Given the SSTL-150 bus attitude knowledge of $\pm\ 0.00694^0$, this misalignment may be measured/known within $40 \pm 0.01 \pm 0.00694^0$ (i.e., 40.01694^0, 40.00306, 39.99694, 39.98306^0) and would have corresponding slant ranges of 783.438 km, 783.279 km, 783.209 km, 783.050 km. The likely geometry is shown in the figure below.

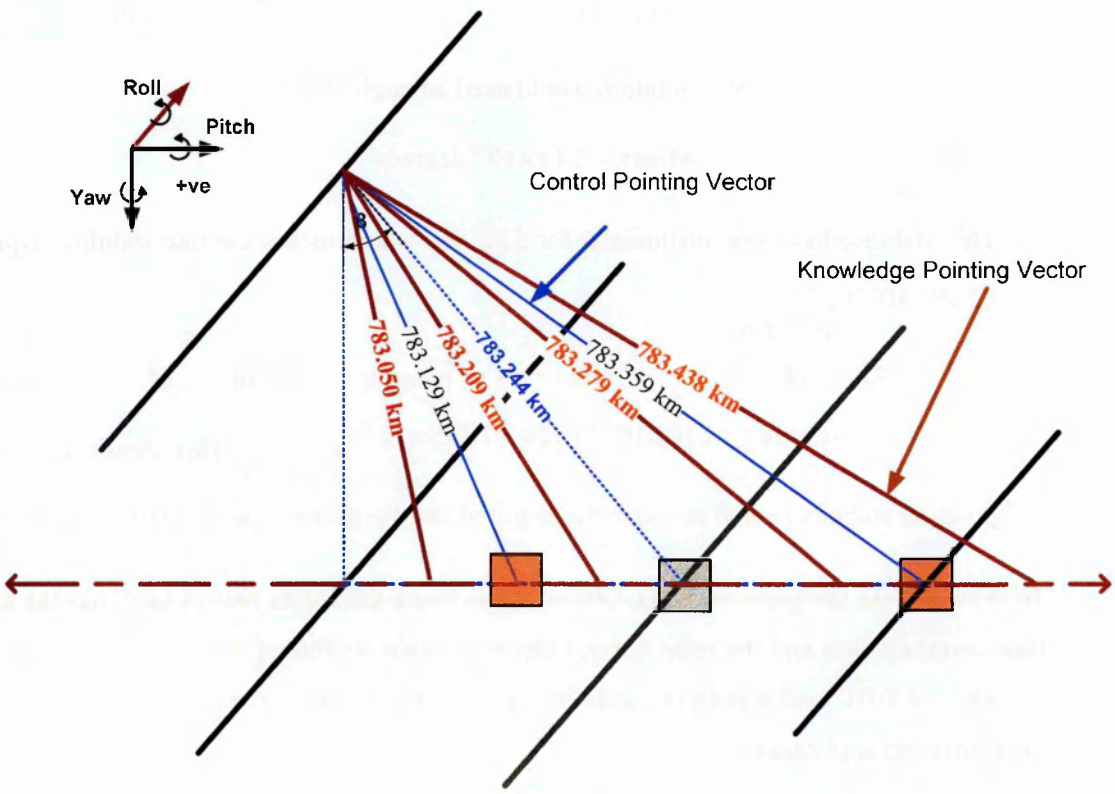

Figure 6 - 15: Representation of the desired pointing, the control pointing and the pointing knowledge vectors at 40^0 inclination.

This shows that due to the inaccuracies of the control system and the pointing vector knowledge,

there would be variations of 35 m to 194 m between what is the desired directional vector (40^0), what can be achieved from the control directional vector (40 ± 0.01^0) and what can be known pointing direction ($40 \pm 0.01 \pm 0.00694^0$).

Extending this argument means that the antenna footprint would have ground range and azimuth swaths of ~ 62 km×62 km, and a 35 m to 194 m misalignment is expected.

If the standalone affect of this misalignment on the image quality is visualized, it apparently looks devastating, but actually it has to be seen how randomly it is occurring and what are its effects on the pulse to pulse operation. Thus it needs to be analysed in light of the platform stability.

Platform Stability

The platform pointing stability is analysed with respect to its affects on the time lapse of 2 way transmission of a pulse. For determining the stability requirements, let us consider the worst case scenario of 40^0 inclination:

- The two way transmission time would be: $t_d = \frac{2 \times R_{S,C}}{c} = 5.22$ ms
- The 30 m ground range resolution would need an angle stability =

  $$\frac{30}{R_{S,C}} = 3.83 \times 10^{-5} \text{ radians} = 2.19 \times 10^{-3} \text{degrees}$$

  This stability has to be maintained for 5.22 ms, which means the rate stability required is = $(2.19 \times 10^{-3})^0 / 5.22$ ms
- The SSTL-150 bus provides a pointing stability of 1.5 arcsec/sec, $\Rightarrow$ 1.5 arcsec/s = $(4.16 \times 10^{-4})^0$/s = $(2.175 \times 10^{-6})^0 / 5.22$ ms This shows that the rate of pointing stability is well suited to the required rate for pulse to pulse stability requirements.

To draw a close comparison, SSTL-300 which is being used with NovaSAR-S has the same attitude determination and the orbit control electronic suite as that of SSTL-150 bus, and a control accuracy of 0.01^0 and a pointing stability of 2 arcsec/sec are considered sufficient for most of their intended applications.

As stated in chapter 3 while discussing the intended applications that proposed design should match the capabilities of the ALOS in order to acquire similar imagery. The ALOS had the attitude control of R, P, Y: ± 0.095° (3 SD), which is very close to what SSTL-100 bus is offering ~ ± 0.01° [121]. As mentioned in Table 6 – 3, the attitude determination/knowledge and attitude control offered by SSTL-150 bus are better than RADARSAT-1 & 2 and are comparable to Ter-

raSAR-X and ALOS.

6.7 Effects of Position Knowledge on the Intended Applications

While dealing with different intended applications in chapter 3, it was discussed that long term measurement of geological phenomenon is necessary to identify the potential hazards that may lead to geological hazards such as earthquakes, landslides, volcanic activities etc. For this purpose, the temporal separation in the repeat-pass interferometry of days, months, or even years, can be useful, and the L-band SAR provides a viable solution. [82]

In this type of application, it is assumed that the target has changed position at a relatively slow pace. For this purpose, if two acquisitions are made at two different times from the same position, with the same viewing geometry, such that there is no across track baseline, then the phase of the interferogram depends only on the change in the topography between the acquisition times. [62]

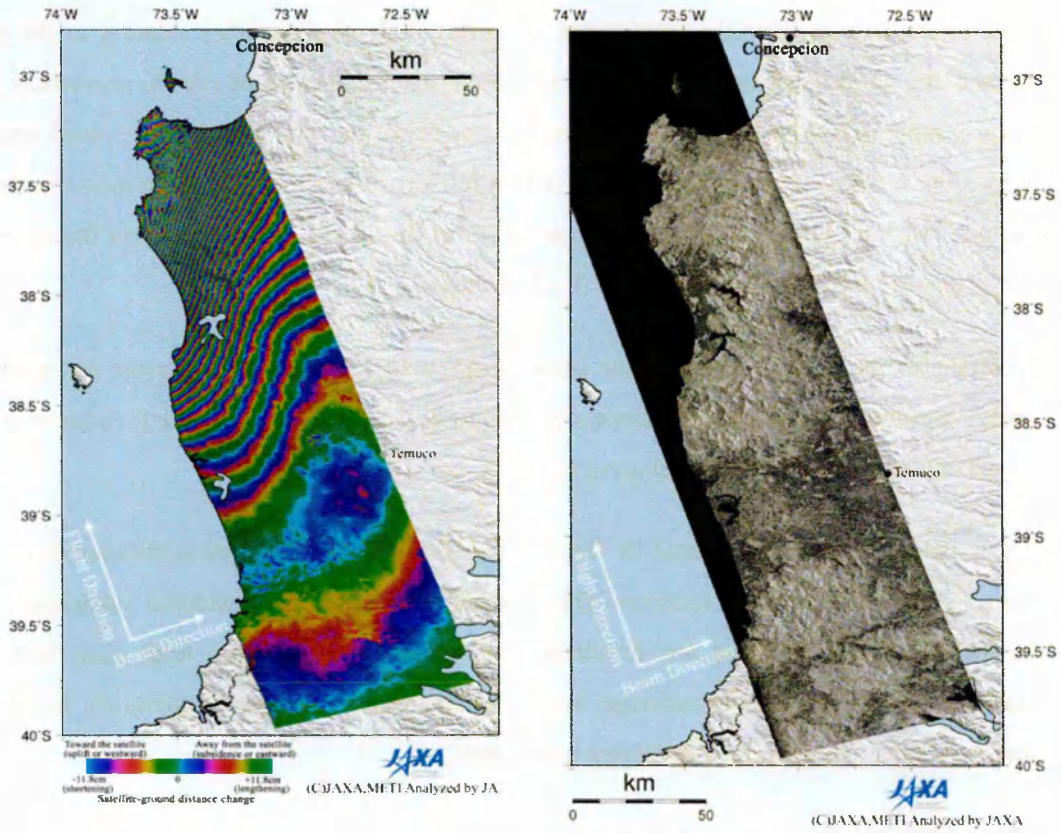

Figure 6 - 16: ALOS interferogram showing deformation map (left) and amplitude image (right)

Source: adapted from [82]

To quote an example, the ALOS imagery is shown in Figure 6 - 16. On February 27, 2010, a magnitude 8.8 earthquake occurred off the coast of middle Chile, in the South America. By using

ALOS, an emergency observation was taken to determine the state of damage caused by the earthquake. During this process, the differential interferometric SAR (DInSAR) analysis was used to detect crustal deformation associated with the earthquake using the data previously acquired on January 15, 2010. [82]

The left figure is an interferogram generated from PALSAR data acquired before and after the earthquake using the DInSAR technique. A colour pattern illustrates changes of satellite-ground distance for the period. The right figure is a amplitude image acquired after the earthquake indicating an observation field of 250 km from south to north. In the interferogram, there are 28 cycles of colour fringes. It is interpreted that ground movement towards the satellite around north-western coastal area relative to the south-eastern inland area are about 3m. Considering a mechanism of this earthquake, the colour pattern indicates an uplift or westward displacement. The colour changes from red, blue, green, yellow and back to red indicate an shortening of the satellite-ground distance, and one colour cycle = 11.8cm. [82]

This example highlights the importance of differential interferometry relating to the geological hazard detection. Although it is related to post-disaster detection of crustal movement but nonetheless same technique is used for the pre-disaster detection. The pre-disaster crustal detection is a very slow moving phenomenon, where only a few centimetres crustal movements in the tectonic plates/fault lines are expected over a year or so, as discussed in chapter 3 and the corresponding requirements mentioned in the Tables 3 – 2 through 3 – 4.

In order for the SAR to re-image the same hazard area – temporally separated but with the same viewing geometry and from the same very location, the SAR platform needs to know its position in space to comparable detection accuracies.

The position knowledge offered by the SSTL-150 bus is ± 10 m that is measured by using sun sensors and on board GPS receiver. This position knowledge is considered sufficient for the polarimetric images as those are simultaneously acquired – and need high short term platform stability not the position knowledge, but for interferometric image acquisitions, highly accurate and very sensitive position knowledge is required.

Other SAR missions such as ALOS, RADARSAT-2and TerraSAR-X/TandemSAR-X etc. that are capable of providing interferometric images, utilize an attitude and orbit control electronics (AOCE) suite that is based on highly sensitive integrated multi-sensors. For example, ALOS had AOCE that contained star trackers, inertial reference unit and a dual frequency carrier phase tracking of the GPS receiver. In addition, to precisely know the satellite position and to calibrate the dual frequency GPS receiver, the laser ranging techniques were used and the satellite was fit-

ted with a laser corner-cube reflector. As an integrated result of all these sensors and the laser ranging, provided ± 1 m position knowledge. This AOCE suite not only incurs heavy cost but also weighs 39.8 kg. [121] SSTL-150 platform is limited to supporting a ~ 50 kg payload, thus this type of AOCE suite may not be suitable for the allocated mass budget of the payload.

After analysing the associated engineering problems relating to the position knowledge resolution concerning the interferometric capabilities of the ECMP design, let us analyse the interferometry processing stages with a view to find out a possible solution to obtain interferometric imagery. Obtaining an interferogram involves following stages: [82]

- Acquiring SLC images. Synthesizing (SLC) radar images (two or more) from the raw SAR data. One image is considered as master and the others as slaves.
- Co-registration of master and slave images. This involves point by point registration of the two images to be combined by approximate re-sampling. The geometrical difference between the images must be modelled very precisely, at the pixel level, which implies that the matching between corresponding pixels must be almost perfect. Only the properly matched portion contributes to the coherent combination; the remainder behaves like noise. The experimental results show that interferometric coherence varies as a function of the relative shift between the two images [82]. It is observed that a registration error of 0.4 pixels causes coherence to drop by 10% whereas an error of 0.8 pixels reduces coherence by half.

  Because of these requirements, it will then be necessary to stretch one of the images so that it can be registered on the other. This stretching operation must preserve the phase content of the deformed image. Otherwise, bias would be introduced in the interferometric measurements.
- Calculating the phase differences. By using the co-registered master and slave images, the phase difference map is prepared which carries the required information. In order to reduce the noise/error, more images (slaves) may be used instead of a single slave. [82]

  As claimed by [82] that it is possible to correct the geometric effects by using more images but there are complexities too, which may introduce the errors.
- Finishing task. It includes fine adjustment to the orbit and projecting the product into the desired map geometry. As a sequel to the above mentioned procedure, the raw phase differences between two images needs to be refined by properly modelling the orbit. This orbital modelling helps in reducing the errors introduced in the interferogram. This may be accomplished by throwing away the error fringes and preserving the ones which are error free.

Now if we combine the above two aspects—i.e., the position knowledge resolution and the interferometric processing—can it be possible to reduce the errors introduced by the poor position knowledge. The co-registration process also involves stretching the slave images to match the

master image, but there is a limit to this stretching. If stretched more than the limits, errors would be introduced. As stated above that by obtaining more slave images and then coherently processing these with a view to reduce these errors, may be helpful. But these aspects need further research.

Because of these reasons, the ECMP SAR employed on the SSTL-150 bus may or may not be providing interferometric imagery necessarily required for pre-disaster detection of tectonic plates. Nevertheless, SAR imagery may be acquired for carrying out amplitude/intensity based image comparisons of the temporarily separated images of the same area—as discussed for the forest change detection (Figure 3 – 4) or post-earthquake analysis (Figure 6 – 15) . This type of change detection based on amplitude/intensity images would benefit the relief efforts in the post disaster situation especially under inclement weather when optical sensors may not provide required timely imagery.

6.8 ECMP SAR Functional Diagram

Figure 6 - 17 represents the block functional diagram of the proposed HH and HV polarimetric SAR payload. In the case of CW design, the echo is received before the transmitting signal ends, thus it remains a convenient solution to mix the copy of the transmitted signal with that of the echo signal and obtain the difference. This difference is known as the beat frequency which carries all the range and azimuth information about the scene. For the ECMP SAR design under investigation, the transmission pulse does not remain present for the entire duration of the PRI and as the pulse finishes, the antenna is switched to the receiver, thus once the echo starts receiving, the transmitted pulse has already ended. For this type of situation, the receiver has to be based on a heterodyne scheme where:

- the incoming signal is first down converted to an intermediate frequency (f_i) before extracting the base band. or
- the baseband signal is directly extracted from the carrier frequency (f_c) without getting it first down converted to f_i.

Both these heterodyne techniques have their pros and cons but step wise down conversion is considered beneficial as it ensures high fidelity of the baseband signal, thus this approach is considered for adaptation with the proposed design.

<u>The Transmitter</u>

The design benefits from a monostatic configuration which provides well synchronized transmitter and receiver operations by employing a single master oscillator (MO). All the other higher frequencies, timing and synchronization signals are generated from this MO. This facilitates in

maintaining a high degree of coherency essential for the extraction of quadrature components.

The MO is a highly stable crystal controlled oscillator. The output of the MO is up converted to operating frequency f_c (1.28 GHz) by using Local Oscillator (LO) in the transmitter block. The output is fed to the chirp generator to generate the chirped signals of a required duty cycle and bandwidth. The output of the chirp generator is fed to the single GaN based SSPA that amplifies this RF to required output levels – which were discussed in the previous sections.

At the time of transmission of the signal, under the worst case scenario, the maximum RF power is 150 W (~ 22 dB). Since it would only be this signal that needs to be isolated from the receiver, thus a low cost and light-weight T/R switch which is capable of providing maximum of 30 dB isolation, is sufficient for this purpose. A single pole double throw (SPDT) switch would be required to isolate the single transmitter signal from two horizontally and vertically polarized receiver signals.

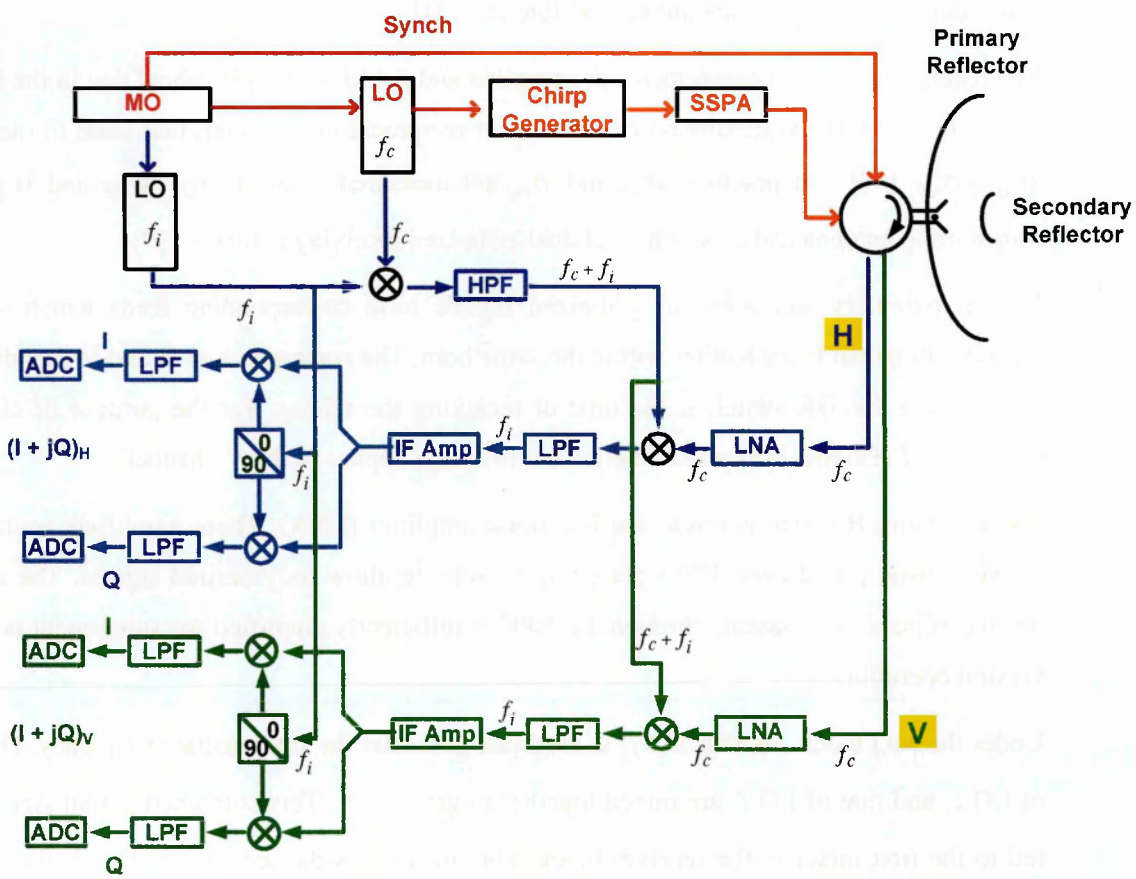

Figure 6 - 17: Block functional diagram of horizontally and vertically Polarized SAR

This high powered RF signal is fed to the Cassegrain antenna through the T/R switch. As previously discussed, the horn is kept at the vertex of the antenna. This configuration helps in reducing

the RF cables to minimum lengths since the PA is practically almost attached to the horn itself. The output of the horn is directed towards the secondary reflector which reflects these RF signals towards the primary reflector. The operation of switching the T/R switch on and off to transmit and receive directions is synchronized from the onboard signals taken from the MO. This switching on and off is controlled by the onboard micro-controllers/micro-processors.

Horizontally and Vertically Polarized Receiver Channels

To make a distinction from that of the transmitter, the boundaries of horizontally polarized and vertically polarized receivers are marked blue and green, respectively.

The function of the receiver is to amplify, filter, down convert, and digitize the echoes of the radar transmission in a manner that provides the maximum discrimination between desired echo signals and undesired interference signals. The interference commonly comprises not only the noise generated in the receiver itself but also the energy received from galactic sources, different communication systems onboard the satellite etc. [41]

The results of ground measurements as compiled and published by [59] show that in the backscattering direction, the scattering process is almost reciprocal in character, that leads to the equality $\sigma_{VH} = \sigma_{HV}$ [59] . In practice, σ_{HH} and σ_{VH} are measured as a pair by using and H-polarized transmitting antenna and a two channel dual-polarized receiving antenna. [59]

Both horizontally and vertically polarized signals have corresponding feeds which would be placed orthogonal to each other within the same horn. The corresponding H and V signals are taken out from the T/R switch at the time of receiving the echoes. For the purpose of clarity, the treatment of H signal is explained below but the same applies to the V channel.

The incoming H signal is fed to the low noise amplifier (LNA). These amplifiers actually have tuneable band pass filters (BPF) placed at the inlet to allow only desired signals. The incoming desired signals after passing through the BPF is sufficiently amplified for subsequent down conversion operations.

Under the MO block, another LO f_i is used that generates the intermediate frequency. The output of LO f_i and that of LO f_c are mixed together to get $f_c + f_i$. This combined output signal is then fed to the first mixer in the receiver block. This mixer gets the second input from the incoming echo that would be centred at f_c, and the frequency spread is the bandwidth, B. The purpose of this first mixer is to down convert the echo operating at f_c to f_i. The output is passed through LPF, tuned to allow only $f_i + B$. This signal is then amplified by the IF amplifier and fed to splitter to get two similar outputs.

In order to get the quadrature output (I and Q channels), the output of LO f_i is orthogonally phase shifted. There are two mixers, each for down converting I and Q channels. The I channel's mixer gets the one input from the splitter and the second input from the 90^0 phase shifted output of LO f_i. The output of this mixer is passed through the LPF and then digitized. Similarly the Q channel mixer gets one input from the splitter and the second input directly form the LO f_i. The output of this mixer is also passed through LPF and then digitized. The digitized data may be stored separately as I and Q channel data or they may be combined to gather to yield complex number format as $(I + jQ)_H$.

Similar treatment is given to the vertically polarized echo channel in the receiver. The output of V-channel would be $(I + jQ)_V$. During imaging, this data would be stored in the onboard solid state memory modules and would be subsequently transmitted to the ground stations.

6.9 Estimated Space Segment Mass Budget

It has been discussed at length in section 6.2 about the benefits of using Cassegrain configured inflatable reflector antenna. It was also estimated, by taking inferences from other similar antennas, that how it would be possible to accommodate the mass within ~ 25 kg.

Estimated Payload Mass	
Sensor electronics for transmitter/receiver, considering GaN based, dual redundant SSPA.	~ 30 kg
Cassegrain Antenna comprising: – Inflatable technology components – Primary reflector – Secondary reflector with small telescopic deployable mechanism. – Feed horn at the antenna vertex.	~ 25 kg
Estimated Bus Mass	
Standard SSTL-150 Bus	103 kg
Additional deployable standard solar panel	4 kg
Additional battery	3 kg
Total Estimated (payload and platform) mass	~ 165 kg

Table 6 - 4: Estimated Mass Budget

For estimating the mass of the onboard sensor electronics, the inference may be drawn from that of the NovaSAR-S electronics that weighs ~ 30 kg. For the ECMP design, due to low isolation requirements, only a SPDT T/R switch is essentially required instead of heavy duplexers. In addition, the light-weight (~ 2 kg), dual redundant, GaN based SSPA are used instead of TWTA which are expensive and heavy (~ 6 kg each). Using a single SSPA instead of a TWTA has significant proportionate effects on the mass of the sensor electronic suite.

The bus mass estimation is based on the standard SSTL-150 bus with additional solar panel and a battery. The combined estimated mass budget is shown in Table 6 - 4.

6.10 Price Comparison of ECMP Design vis-à-vis NovaSAR-S

To envisage the cost of the different propositions this research intends to bring out on the overall mission, a price comparison with a nearest contender, NovaSAR-S, is carried out. Although it is very difficult to exactly compare two missions that have different capabilities and operate in two different frequency bands, yet if the net cost each mission offers vs. the potentials and limitations of each mission, are also kept in mind, then the proposed design offers a suitable low cost alternative choice. The inspiration to compare the price with NovaSAR-S is based on the fact that both utilize the SSTL buses and both are in private/public domain, with almost similar mission objectives.

	NovaSAR-S (Pound Sterling in Millions)	**Proposed ECMP Design (Pound Sterling in Millions)**
Platform	SSTL–300 : 9.5	SSTL–150: 6.5
SAR Payload	Total payload allocations: 11.5 Antenna (APAA) ~ 60 % of payload cost : 6.9 Backend Sensor Electronics: 4.1	Total payload estimated cost: 5 Antenna (5 m inflatable reflector): 1 Design and development + Backend sensor electronics + SSPA : 4.1
Launch	Dedicated (Russian): 16	Shared (~ 1/3): 5
Insurance: **Launch** **Payload**	 ~ 5 (Full) ~ 2 (Full)	 ~ 1.6 (Shared) ~ 2 (Full)
Total	~ £ 44 M	~ £ 20.1 M

Table 6 - 5: Estimated price comparison between NovaSAR-S and the proposed ECMP SAR

The comparison presented in Table 6 - 5 shows that individual estimated price of the proposed design is approximately less than half the price of NovaSAR-S and is comparable to second generation DMC optical payloads such as Nigeriasat-2 (~ £ 20 M). The major cost saving

contributors are the use of a light-weight bus, reflector antenna and the shared launch.

The launch costs are variable and difficult to estimate. Similarly associated launch insurance cost varies for each launcher. These estimates are widely accepted in the space industry [8]. While calculating this price comparison, the Russian launcher is assumed to have the lowest launching costs. For the European or American launchers, this cost increases to ~ £ 21 M [8]. For the 5 m diameter inflatable antenna, the inference is drawn from the 14 m diameter inflatable antenna that was used as the technology demonstrator from space in 1996 and its price was USD 1 M [55]. Considering the inflation and also the reduced size (5 m instead of 14 m), ~ £ 1 M is estimated for ECMP antenna design and development.

The individual price difference is significant and best fits for building a constellation such as DMC to get much enhanced potentials and capabilities. From the constellation point of view, the low unitary cost and less capable mission means increased chances of putting more satellites together – that provide greater flexibility, increased accessibility, higher degree of redundancy, distributed load on the resources etc. These characteristics are difficult to achieve from a single, expensive but more capable sensor. For example, within the same price budget as NovaSAR-S mission, there can be at least two proposed ECMP SAR missions, which means half the revisit time (~ 25 days), flexibility of operation, distributed load on the resources (such as data downloading links etc.) and so on.

Rapideye is a constellation of 5 identical optical satellites which were built upon the SSTL-150 bus. Because of the compact stowage volume, all 5 satellites were injected into the space by using a single Russian rocket in 2008 [6]. Since proposed ECMP SAR design also aims to reduce the stowage volume by using inflatable technology for the antenna, this means the volume can be kept similar to that of the bus itself, then it would be possible to launch multiple SAR satellites by using a single rocket. If this is the case, then the launch cost may further be reduced and a constellation of 5 identical satellites may be injected into the space with a total cost of ~ £ 85 M. The revisit time may reduce to ~ 10 days or less, if operated from the same orbital plane. But if operated from the different planes (such as SAR-Lupe that uses 3 planes [3]), then the revisit time may further be reduced to ~ 3 – 5 days.

6.11 Spatial and Radiometric Elements of Image Quality

After going through various aspects of the SAR design in the light of SSTL-150 bus, the final design needs to be analysed from the image quality perspective. Broadly speaking it is subdivided into spatial and radiometric image quality parameters. These are indeed interlinked to each other and combined effect is taken into account while dealing with the image quality.

6.11.1 Spatial Elements of Image Quality and Multilooking

As regards the range resolution, it remains the function of bandwidth 'B' which was calculated at the near edge of the BW3 dB swath in the slant range direction. From the applications, it was deduced that a 30 m by 30 m (range, azimuth) spatial resolution should serve most of the intended applications. To have a ground range resolution of 30 m after taking into account the curvature of earth effects, requires a system bandwidth of 9.6 MHz. This bandwidth is slightly over sampled by the ADC to $B' = 10$ MHz. This over sampling indeed results as ~ 29 m range resolution. This is a single look range resolution.

The theoretical value of a single look azimuth resolution is considered to be half of the antenna length in azimuth direction (after incorporating the curvature of earth effects). It is thus calculated as:

$$\frac{D}{2} \times \frac{R_e}{R_e + h} = 2.28 \text{ m}. \text{ [75]}$$

Although a single look intensity image yields high spatial resolution but radiometric resolution is poor and the speckle effects are prominent. The speckle in the SAR images is a scattering phenomenon which complicates the image interpretation and reduces the accuracy of image segmentation and classification. [70]

Multilook processing is a procedure commonly adapted to reduce the speckle effects. Spatial filtering (averaging) can affect the inherent scattering characteristics in polarimetric SAR data [70]. Multilook processing is broadly catagorized into two catagories: incoherent and coherent [70]. The term coherent means the phase information is preserved while incoherent means the sample intensity/amplitude are preserved and phase information is discarded.

Incoherent Multilooking: it is implemented by averaging the neighbouring pixels—either in range, azimuth or both—of the intensity/amplitude SLC images. For a signle channel polarimetric SAR system such as Radarsat-1, the scene information is contained in the intensity (or amplitude) and the phase is uniformally distributed which conveys no useful information. Incoherently averaging the neighbouring pixels reduces the speckle effects by trading off the spatial resoultion (worsening it) with the radiometirc resolution (improving it). [91]

Incoherent multilooking (or the spatial averaging) has the advantages such as: (1) simple to apply, (2) speckle noise reduction in homogeneous areas is effective, and (3) the mean value is preserved. However, the major deficiency of these filters is the degradation of spatial resolution due to indiscriminately averaging the pixels from inhomogeneous areas. From the image processing point of view, the multilook image would blur the edges and smear the bright point targets and linear features, such as roads and buildings. Other techniques such as wavelet transform, neural networks etc., are employed to address these problems of spatial averaging filters—particularly in the inhomogeneous areas. [70]

Nonetheless, the phase information—considering the fact that it does not carry any information in the context of a single polarimetric SAR—in the case of incoherent multilooking, is lost.

Coherent Multilooking (Multilook Complex): for the polarimetric SAR, the 1 – look data can be represented by a scattering matrix and the phase information of each polarimetric channel is very important—thus, needs to be preserved for further polarimetric image processing. To form multilook data, the scattering matrix can not be averaged, because, the average of complex values does not reduce the speckle noise effect, and, as such the phase can not be averaged. [70]

The standard technique of multilooking the polarimetric (coherent) sinle look image is to convert the scattering matrix into a covariance or coherency matrix and then sample average is taken[70]. Let us review the coherent multilook procedure using the covariance matrix. For the ECMP SAR design, there are only HH and HV polarimetric channels, thus the scattering matrix would be reduced to:

$$S = \begin{bmatrix} S_{HH} \\ S_{VH} \end{bmatrix} \quad \ldots\ldots \quad (6-2) \quad [70]$$

Let

$$k = [S_{HH}\ S_{VH}]^T \quad \ldots\ldots \quad (6-3) \quad [70]$$

and the covariance matrix:

$$C = k \times k^{*T} = \begin{bmatrix} |S_{HH}|^2 & S_{HH}S_{VH}^* \\ S_{HH}^*S_{VH} & |S_{VH}|^2 \end{bmatrix} \ldots (6-4) \quad [70]$$

where $[\ ]^T$ is the transpose of the matrix and $[\ ]^*$ is the complex conjugate. SAR data are multilook processed for speckle reduction by averaging several neighbouring 1-look pixels.

$$Z = \frac{1}{N}\sum_{i=1}^{N} C(i) = \begin{bmatrix} \langle |S_{HH}|^2 \rangle & \langle S_{HH}S_{VH}^* \rangle \\ \langle S_{HH}^*S_{VH} \rangle & \langle |S_{VH}|^2 \rangle \end{bmatrix} \quad \ldots\ldots \quad (6-5) \quad [70]$$

where C(i) is the 1-look covariance matrix of the ith pixe and N is the number of looks. The resulting multilooked matrix Z is a Harmitian matrix. The diagonal terms of Z are intensities where as off-diagioanl terms contain the phase information.

For the proposed ECMP SAR, inorder to obtain almost same sized azimuth resolution as that of the range resoultion (~ 29 m), N=14. The coherent multilooked Z matrix will contain, at each pixel, a 4 by 4 matrix similar to shown above. By adapting this procedure, the phase information is maintained.

6.11.2 Radiometric Elements of Image Quality

In the preceding sections, various baseline capabilities of the SSTL-150 bus were evaluated with a view to realizing their influence on the design aspects of the SAR payload. This evaluation helped in suggesting necessary changes in selecting highly efficient solar cells, additional battery and enhanced solid state data storage etc. With these suggested changes in mind, let us analyse the design to exploit these potentials to broaden the scope of the applications.

At this stage, in order to evaluate the image quality of the proposed ECMP SAR design, let us keep all the other parameters the same as mentioned in the Table 6 – 1 except the RF power. Previously it was being varied for each case according to the variations in the incidence angles; now fix it to 150 W – which is permissible while remaining within the safety limits of the onboard power subsystem and the SSPA. The SNR obtained at different incidence angles indicates different detection potentials of the proposed design. The results so achieved are presented in the Table 6 – 6.

6.11.2.1 Noise Equivalent Sigma Zero

A simple way of characterizing imaging radar is to determine the surface backscatter cross section which gives a SNR equal to 1. This is called noise equivalent backscatter cross section 'σ_n' or noise equivalent sigma zero (NESZ) [18].This is a key element of the image quality. It is visually tied to the more or less black nature of the darkest areas of the image. it is estimated over a surface which is assumed not to backscatter any energy towards the radar such as airport strips, calm water, shadowed areas etc [91]. It is calculated by $\text{NESZ}=\frac{\sigma^0}{SNR}$ .... (6 – 6) [91]

	20^0	**25^0**	**30^0**	**35^0**	**40^0**
σ^0 (dB) Used	– 12.5	– 12.5	– 15	– 15	– 17.5
SNR Achieved (dB)	22.7	20.66	16.63	14.3	8.2
σ_n (dB) – NESZ	– 35.2	– 33.16	– 31.33	– 29.3	– 25.7

Table 6 - 6: NESZ variations with respect to incidence angle

The angular dependency of σ^0 was already discussed in chapter 4. The 1st row of the Table 6 - 6 shows the values of σ^0 that are used at different incidence angles. The 2nd row represents the achievable SNR with peak RF power of 150 W at all the incidence angles. The 3rd row represents

the σ_n values.

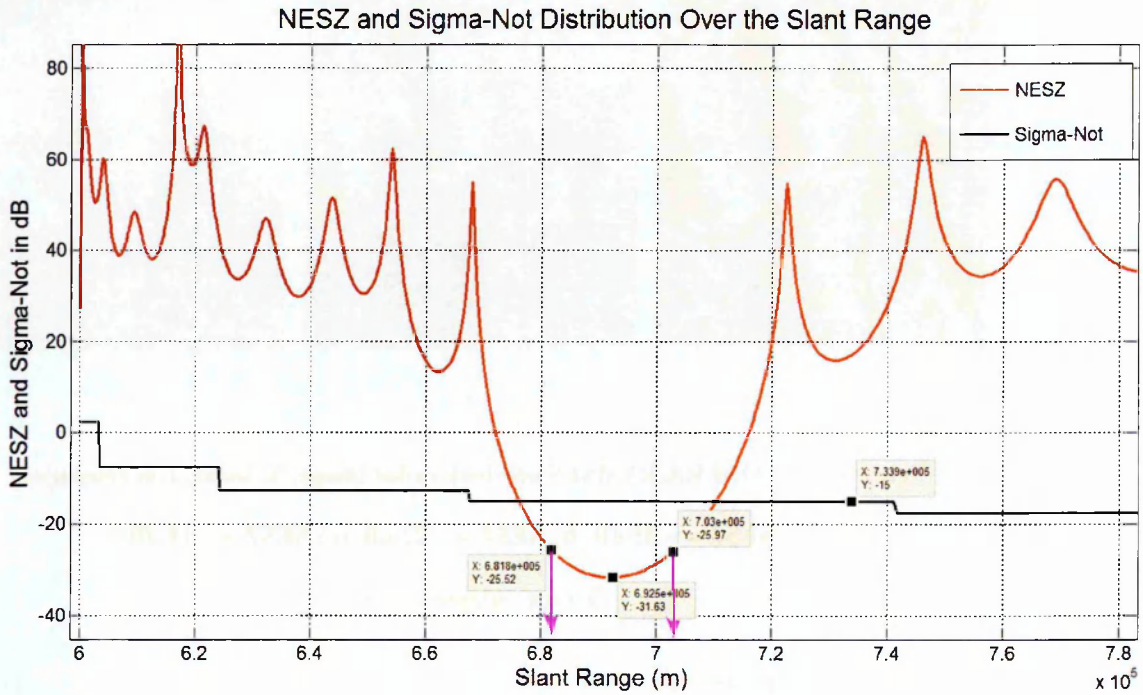

Figure 6 - 18: The NESZ and the σ^0 distribution over the Slant Range at 30^0 incident angle

Figure 6 - 18 shows the NESZ distribution along the slant range at 30^0. The angular dependent values of σ^0 are also over plotted in black. The slant range swath is marked at the points where the NESZ values are increased by 6 dB from – 31.63 dB. The slant range swath is 22 km which is equivalent to ~ 45 km on the ground range.

The NESZ values which can be achieved from the ECMP SAR design can best be related to the SAR image shown in Figure 6 – 18 (a) through (c). These are the urban radar images (X-band, single look, 1 m) with varying image noise levels. This example, with a value typical for an air-borne acquisition (a), NESZ = – 35 dB shows a huge contrast between the brightest zones (buildings) and their shadows. For the (b) NESZ = – 22 dB and the (c) shows that NESZ increases to a value of approximately –18 dB. For the last case, it would be difficult to work directly on a single-look image, hence prior multi-look filtering is desirable. [91]

It is pertinent to mention that the NESZ values presented in the Table 6 – 6 are closely comparable to the FDB ALOS values which are ~ – 27 to – 30 dB at 41^0 incident angle. This discussion may be summarized on this note that the applications oriented design approach adopted at the start of the research, indeed yields wider application potentials than anticipated earlier, comparable to what FDB ALOS offered.

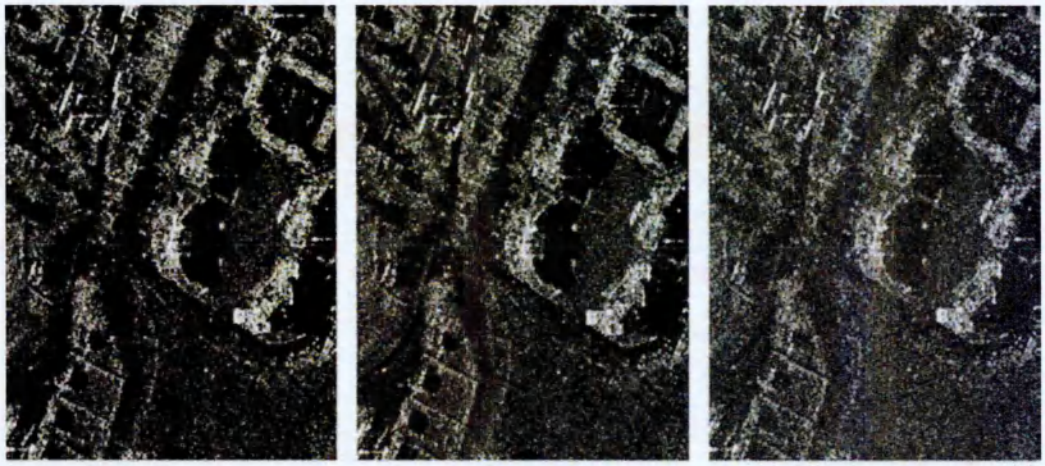

(a) (b) (c)

Figure 6 - 19: ONERA/RAMSES one-look radar image, X- band, 1-m resolution,

(a) NESZ = – 35 dB (b) NESZ = – 22 dB (c) NESZ = – 18 dB

Source: adapted from [91]

6.11.2.2 Radiometric Resolution

"It is the expected spread of variation in each estimate of scene reflectivity as observed in an image" [62]. Smaller radiometric resolution is 'better'. Radiometric resolution for a given radar may be improved by averaging (multilooking), but at the cost of spatial resolution. [62]

It characterizes the radiometric stability of a stationary part of an image (with constant σ^0 and NESZ). It depends upon the speckle intensity i.e., number of looks "N" and the level of image noise. It is defined by:

$$\gamma = 10\log_{10}\left(1+\frac{1+\frac{1}{SNR}}{\sqrt{N}}\right) \quad \ldots\ldots \quad (6-7) \qquad [91]$$

A single look (N=1) SLC image, for which speckle noise is maximum, has a radiometric resolution larger than 3 dB. As the value of N increases, the spatial resolution worsens while radiometric resolution improves (i.e., value reduces, as lower value is better). [91]

By using the angular dependent SNR value presented in Table 6 – 6 and the Eq. 6 – 7, the radiometric resolution is calculated for coherently multilooking for N = 14. The results so achieved are presented in Table 6 – 7.

This table shows that as the number of looks increase, the radiometric resolution improves. For N=14, the radiometric resolution ~ 1 dB. It is pertinent to mention that this value matches radiometric accuracy of FBD ALOS (the radiometric specifications presented in Table 3 – 1).

	20^0	25^0	30^0	35^0	40^0
SNR Achieved (dB)	22.7	20.66	16.63	14.3	8.2
Radiometric resolution 'γ' for a Single Look => N=1	3.02	3.028	3.057	3.09	3.327
Radiometric resolution 'γ' for Coherent multilook => N=14	0.973	0.976	0.988	1.001	1.098

Table 6 - 7: Radiometric Resolution for a single look and 14 x multilooks

6.12 Applicability of ECMP SAR Design to other Frequency Bands

The ECMP SAR concept and the detailed design analysis presented in this thesis had been applications oriented and L-band specific. However, it is important to ascertain the applicability of ECMP SAR design at higher frequency bands.

The ECMP SAR concept/design was evolved around availability of a suitable high power and high efficiency SSPA. The central idea of the research had been to operate the SAR at low instantaneous RF power levels—which could be directly supported by a single SSPA.

As was discussed in chapter 2 GaN based SSPAs are very efficient (PAE) at low frequency bands and a single amplifier can provide RF output of 204 W with ~ 60 % efficiency, at L-band [49]. Similarly, as claimed by [46] at S-band, space hardened, 150 W, GaN based, 53.8 % efficient SSPA is also available.

If an ECMP design is to be built at S-band, then this 150 W PA can be used. At S-band, almost the same antenna gain can be achieved with ~ 2.9 m diameter parabolic antenna, as was achieved from a 5 m diameter antenna at L-band. With this SSPA and reduced sized antenna, the ECMP advantages may be accrued by using SSTL-150 bus. It would yield ~ 30 km ground swath at 30^0 incidence.

Going higher in the frequency bands such as C- and X-bands, the RF output power from a single SSPA with high efficiency is difficult to achieved, but these high frequency bands provide an added advantage of high antenna gain with reduced sized antenna. At X-band, a 3 m diameter parabolic antenna can provide ~ 50 dB gain. This gain is enough to compensate the low power output from a single SSPA (e.g. ~ 20 W RF outputs at X-band are common). But using a large antenna to compensate the low RF output power of a single SSPA has associated problems of reduced ground swaths. To increase the ground swath, multi-feed with multiple RF PAs are needed, (such as used with TecSAR) which makes the design complicated.

To summarize this discussion, it may be ascertained that ECMP provides best results at L-band with ~ 45 km ground swath from a single beam, but can provide a suitable design at S-band with comparatively reduced swath (~ 30 km) from a single beam. For the C- and X-bands, the design is possible with a single SSPA but the achievable ground swath will be reduced significantly.

6.13 Summary and Conclusions

This chapter dealt with a number of key issues that encompass the ECMP SAR design in the framework of the selected SSTL-150 bus. Initially the onboard power subsystem is analysed with a view to enhancing the power generation capabilities in the light of latest developments taking place in the field of solar cells – particularly making them more efficient. By adapting to state of the art solar cells which are offering 43.5 % efficiencies against those 28 % efficient cells currently onboard this bus, the available power generation capacity can be increased significantly. Furthermore, by using standard deployable solar panels which are otherwise being used with a lighter SSTL-100 bus, the power generation capacity can further be increased. This enhanced capacity is then analysed with respect to the requirements especially during eclipse and it was worked out that the design would need to use extra battery to enhance the current 15 Ah capacity to 21.5 Ah capaciy so that under an adverse case scenario, the power could be guaranteed for the SAR operation.

As previously identified the major cost cutting approach is to build the overall design with a significantly reduced stowage volume that helps in injecting multiple payloads through a single rocket launch. The reflector antenna configuration plays an important role, thus available options are analysed and a dual reflector – Cassegrain configuration with inflatable technology is considered most suitable for this purpose.

Keeping the available power, the capabilities/constraints of a single SSPA and the antenna beam pattern in mind, the best PRFs are worked out to address the ambiguities. Overall analysis of these factors leads to limit the maximum incidence angle, due to unavailability of suitable PRF and the safety limits of the onboard power subsystem and the SSPA. These constraints then lead to calculating the available imaging time per orbit and how much area of the Earth can be imaged per year.

The sensor viewing geometry and operating parameters help to estimate the data rates. Realizing the available data storage resources, it appears to be insufficient for the available imaging time, thus it is suggested to upgrade the data storage from 16 GB to 32 GB. Another associated problem is data downlink rate. Although the data downlink rate is sufficient in relation to the time the satellite remains visible to a ground station, the satellite has to revisit that ground station once per every orbit – which is very difficult to achieve. As a low cost solution, the data downlink through DMC member countries is suggested with an option of hiring geostationary communication

bandwidth to relay the data, as an alternative but costly approach.

In order to maintain the simultaneous illumination of the same spot on the ground during SAR imaging, the antenna pointing is considered an important aspect of the mission design. The available resources onboard the selected platform are analysed with a view to evaluating their effects on the stability. Besides this, the platform's position knowledge capability is also discussed in light of its effects on the intended applications particularly those which necessarily require temporally separated interferometric images. The limitation of the platform on this account is realized and also the interferometric processing stages discussed with a view to lessen the effects of poor position knowledge resolution. It has been found out that the errors may be reduced by taking more than two observations of the same area for developing the interferogram. But this aspect, in the light of poor position knowledge resolution needs further dedicated research.

As the bus needs additional resources, particularly for power generation and storage, which does not involve major changes in the bus design, these additional components would contribute to the overall mass budget, which is estimated keeping these aspects in mind. It also includes the broad mass distribution of the payload subsystems.

Keeping various cost effects related to the overall mission design, development, integration, launch, insurance etc. the price comparison is carried out in response to that of NovaSAR-S.

Overall, the proposed design provides a low cost, light-weight, microsatellite based dual (HH and HV) polarized SAR solution with moderate resolution, swath, revisit and NESZ etc., – which make it an attractive option for building a constellation to enhance its temporal response that offers greater operational flexibility, at a comparable price to that of the optical microsatellite sensors.

6.13.1 Comparison of FBD ALOS and ECMP SAR

After passing through different stages of the options and finally proposing ECMP SAR design with SSTL-150 bus, it is pertinent to draw a close comparison with that of the FDB ALOS. This comparison provides a closer view of the specifications of the FBD ALOS—which was taken as a reference at the start of the thesis, and now what the proposed design is offering. This comparison is presented in Table 6 – 8.

	FBD ALOS	**Proposed ECMP**
Sensor/Platform Parameters		
Frequency	1270 MHz / 23.6 cm	1280 MHz
Bandwidth	14 MHz (dual, quad-pol., ScanSAR)	9.6 MHz

Transmission power	2 kW (peak power)	150 W (extended chirp mode with ~ 20 – 50% duty cycle)
Polarizations	Dual pol. (HH+HV or VV+VH)	Dual Polarized: HH & HV
Incidence Angle	Strip map: 9.9 – 50.8 deg.	Strip map: 20 – 40^0
Ground resolution Rg (1 look) x Az (2 looks)	~ 9 m x 10 m (single polarization at 41.5°) ~ 19 m x 10 m (dual pololarization at 41.5°)	~ 2.28 m x 30 m (azimuth, range for 1 look) ~ 30 m x 30 m (14 x1 multilok)
Swath	Swath width 70 km (single/dual polarization at 41.5°)	37 – 62 km (20 – 40^0 incident angle dependent)
Data rates	240 Mbps (single/dual/quad-pol)	85 – 190 Mbps (20 – 40^0 incident angle dependent)
Orbit Inclination	98.16 deg. Sun Synchronous (SS)	97.79 deg, SS
Revisit	46 days	54 days
Platform's Attitude, Orbit and Control System (AOCS)		
Attitude determination/ knowledge	±0.0003^0 (3 SD) all 3 axis	±0.00694^0 (1 SD) all 3 axis
Attitude Control	R, P, Y: ± 0.095°(3 SD)	± 0.01^0 (1 SD) all 3 axis
Position Knowledge	± 1m	± 10 m
Pointing Control	30 arcsec (3 SD)	36 arcsec (3 SD)
Pointing stability (Jitter)	1.2 arcsec/sec (3 SD)	1.5 arcsec/sec (3 SD)
Radiometric Specifications		
Noise Equivalent Sigma Zero (NESZ)	-27 ~ -30 dB (dual polarization. At 41.5°)	– 35.2 dB (20^0) – 33.16 (25^0) – 31.33 (30^0) – 29.3 (35^0) – 25.7 (40^0)
Ambiguities – Range	9 - 26 dB (single/dual polarization at 41.5°)	~ 24 dB at (30^0)
Ambiguities – Azimuth	21 dB (quad-polarization At 21.5 ° - 41.5°)	~ 25 dB at (30^0)
Radiometric accuracy	< 1 dB relative	0.973 to 1.098 dB (20 – 40^0 incident angle depended)

Table 6 - 8: Comparison of ALOS and proposed ECMP SAR Spatial, Radiometric and Platform Specifications

From the sensor and platforms point of view, the proposed design is closely matching the capabilities/specifications of FBD ALOS except for:

- Spatial resolution (ECMP SAR design offers 30 m (at 30^0) whereas ALOS had 10 m (at 41.5^0) range resolution. As a matter of fact, the ECMP SAR range resolution can be improved by increasing the bandwidth to match with that of the ALOS).

- The incident angle (proposed design is limited to 40^0 only because of power and PRF constraints).
- Revisits (it got 54 days as compared to 46 days offered by ALOS).

From the AOCS point of view, rest of the specifications are almost matching except position knowledge that is poor in the case of SSTL-150 bus. The impact of position knowledge on the differential interferometry has been discussed at length in section 6.7.

From the radiometric specifications point of view, the range and azimuth ambiguity values are matching to those of the ALOS (rather better by few dB because of antenna size (particularly in the range direction) and respective sidelobe gain of the radiation pattern). The radiometric resolution, which is, indeed incident angle dependent, is also comparable to these specifications.

6.13.2 Applications to be Served by ECMP SAR

After arriving at this proposed ECMP SAR design, it is pertinent to look back at different applications which can be served with these specifications.

6.13.2.1 Forestry Related

Forest resource monitoring that includes the routine mapping of deforestation, clear-cuts, fire (scars) and flooding. This also includes the subsequent assessment of the affected areas which were either clear cut or fire burn and how those are now re-growing.

This forest assessment should not be misunderstood with forest resource assessment applications which include the inversion of dendrometric or structural parameters at the stand level such as biomass measurements, forest species, and stand structural organization, tree classification etc.

6.13.2.2 Disaster Monitoring Related

For the flooding, L-ban with HH polarization is a good choice as discussed in the light of L-band, ALOS, HH polarized example quoted in chapter 3. It will be better to get this type of imagery with 40^0 incident angle which provides ~ 60 km swath. Since design does not offer ScanSAR capability, thus operating a single ECMP SAR is limited to 54 days revisit time. As it is a very low budget design, thus by putting more satellites in a constellation should reduce this time significantly.

Oil spill detection and Hurricane detection is also possible but due to unavailability of ScanSAR capability, it needs to have more satellites in the constellation.

6.13.2.3 Geological Hazard Detection and Post Disaster Operation

Geological hazard detection or pre-disaster phase—in which the periodic movements of the tec-

tonic plates are recorded and through modelling the geological hazard risk assessment is carried out—is principally related to the repeat pass differential interferometry. For this capability to have it with the sensor, the platform should have a very good position knowledge (~ ± 1 m). The SSTL-150 bus is limited to ± 10 m. Because of this poor position knowledge, there are likely to be more errors introduced while co-registering master and slave images. As has been discussed previously that the effect of these errors can be reduced by taking more images of the same area and then averaging them through additional differential interferometric stages. To ascertain the possibility of providing this differential interferometric capability, it needs specific research on the subject. Thus from the point of view of pre-disaster detection point of view, this may/may not be achieved.

Nevertheless, SAR imagery may be acquired for carrying out amplitude/intensity based image comparisons of the temporarily separated images of the same area—as discussed for the forest change detection (Figure 3 – 4) or post-earthquake analysis (Figure 6 – 15) . This type of change detection based on amplitude/intensity images would benefit the relief efforts in the post disaster situation especially under inclement weather when optical sensors may not provide required timely imagery.

6.13.3 Potential Applications

Keeping in view the detection capabilities (mainly the NESZ at varying incident angles) that are offered by the proposed design, there may be other applications which can also be served besides mentioned above. These may include:

- Crops mapping
- Aquaculture mapping
- Monitoring of land subsidence
- Rice mapping
- Snow and ice mapping
- Hydrology and water resource management
- Land use monitoring and land cover classification
- Surveying of archaeological sites – as L-band offers deep penetration of the incident waves, can particularly be helpful.

7 CONCLUSIONS AND FUTURE WORK

This chapter summarizes the work presented in this thesis and highlights the key contributions of the current research. In order to improve the applicability of the ECMP SAR technique, several suggestions are proposed for further research.

7.1 Summary and Major Conclusions

The research presented in this thesis aimed at providing a SAR system design that should overall reduce the size and cost of the current/planned spaceborne SAR missions by a factor of two. Being an active sensor, SAR is a power hungry payload thus it has been conventionally employed on large spacecraft. As the relevant technology developed so were the design concepts refined which reduced the SAR missions from mega-satellite to a mini-satellite in the category of ~ 500 kg. The current lightest weight operational mission is TecSAR which is 300 kg but it is very expensive (~ £ 127 M). This unitary cost is significantly high for building a SAR based constellation or complementing the existing optical payload based small satellite constellations such as DMC and Rapideye with SAR payloads.

In order to exploit the potentials of an affordable mini-satellite based SAR mission, the SSTL planned NovaSAR-S mission which would weigh ~ 400 kg at a cost of ~ £ 50 M. This cost vis-à-vis counterpart optical mission's cost of ~ £ 20 M in this weight category, is more than double.

To achieve the desired aim, the research identified certain mass and cost cutting approaches to devise the design. The salient aspects of these are:

- Injecting the satellite into space consumes almost half of the mission cost (in the weight category of ~ 500 kg and the price range of ~ £ 50 M)—if it is a dedicated launch. The deciding factor to determine a dedicated or a shared launch is not solely the space segment's mass rather a combination of mass and the stowage volume during the launch. Thus building the overall design which yields a compact stowage volume—to facilitate a shared launch—is as necessary as reducing the mass. The shared launch costs ~ 1/3 of the dedicated cost.
- To build the payload around already designed, tested and space qualified platforms rather

building the platform around the payload.

- The spaceborne SAR antenna design and the PA play significant role in reducing the mass, cost and volume of a mission. By exploiting the latest technological developments in the antenna and PA fields, a novel combination of using a passive reflector antenna with a single SSPA was identified as the main area of potential research, as up till now, none of the spaceborne SAR missions have used this combination.
- By weighing the pros and cons of application-driven or performance-driven design philosophies, it was decided to follow the narrow range of application-driven approach to achieve a light-weight and low cost mission.

By focusing on a narrow application-driven approach, the intended applications were analysed with a view to derive the sensor parameters (mainly the L-band, 10 – 50 m spatial resolution, ~ 50 km swath, HH and HV polarization etc.). The available SSTL buses offer baseline capabilities and also impose limitations on the payload. Consequently the SAR payload design had to address these—often conflicting—applications-driven sensor requirements and the platform capabilities and the limitations. The intended single platform-based SAR design had to address these requirements and limitations, and had to be bounded around this framework.

Nowadays the SAR designs follow either pulsed or the CW configurations. The pulsed system yields the major benefit in the form of a mono-static operation by sharing a common antenna. But it needs to operate at high instantaneous power levels which necessitate a compatible power supply chain which results in increasing the design complexity, weight and cost of the system. Once this technique was analysed for microsatellite implementation, it necessitated major changes in the power sub-system. In case of the CW SAR technique, the payload and the bus operate at low instantaneous power levels which enable the use of a single SSPA instead of a heavy and expensive TWTA. But the CW design needs to use two satellites, one each for transmitter and receiver, to achieve adequate antenna isolation. This analysis showed that none of these techniques in the original form ideally fitted the constraints imposed by the design environment explained above. Further analysis suggested two variants of these basic techniques that could provide engineering design solution from a single microsatellite platform.

The first showed that a CW SAR can be implemented in a mono-static way, sharing a single antenna, from a single platform, if it is operated in an interrupted mode. But these interruptions introduce gaps in the synthetic aperture. Processing this synthesized gapped data results in artefacts in the reconstructed images. To fill in the gaps in the interrupted aperture, statistical estimation techniques such as N4SID were adopted. These techniques initially showed satisfactory results on the simulated data. To establish the efficacy of the gap filling algorithm, it was

applied to the RADARSAT-1 dataset. Due to rapidly changing and highly excursive nature of the real SAR data, and the 100 % periodic gaps, the gap filling algorithm could not suppress the artefacts to the adequate levels. If it could have been demonstrated that it is possible to statistically fill the gaps, which in return result in suppressing the artefacts in the processed image, then it would have helped in validating the practicability of the ICW SAR concept. Nevertheless, similar research in the context of CS is taking place in other fields of science and engineering and the potentials of research can never be denied and in future, there may be success in practically developing a suitable technique which addresses these types of problems. From the perspective of this research the concept of ICW technique was—for time being—set aside.

The second technique—which is the selected/recommended one—is a variant of the pulsed technique, and is based on the ECMP concept. It fits into the bounds of multidimensional framework of the intended design approach, by utilizing a 5 m parabolic reflector antenna at L-band. This antenna in return provides the opportunity to lower the minimum PRF limit i.e., a larger PRI, to extend the chirp so that peak RF power fed to the input of the antenna is reduced to the levels which could be directly supported by a single SSPA while remaining within safety limits of the onboard power sub system of SSTL-150 bus. The major advantage achieved from the ECMP vis-à-vis ICW technique is in the form of a continuous synthesized aperture which yields an artefact free processed image.

For the ECMP SAR design, the major challenge remains as how to design and develop a 5 m reflector antenna while remaining within the confines of the SSTL-150 bus payload restrictions of ~ 50 kg. To address this problem a detailed analysis, based on drawing the inferences from the other successful antenna developments and demonstrations, was carried out. It showed the possibility of developing a 5 m parabolic Cassegrain reflector with inflatable technology while remaining within ~ 25 kg mass budget, at an affordable cost. A Cassegrain configuration facilitates in keeping the feed at the vertex, thus getting rid of strong support structures to deploy and keeping the horn at ~ 3 m away from the antenna vertex. It provides suitable engineering solution to many problems inherent in the Newtonian configuration. A Cassegrain configuration in combination with inflatable technology would ensure achieving compact stowage volume during launch phase, thus saving considerable proportionate cost if other deployable techniques are used.

SSPA in comparison with electron beam PA offers many advantages such as extremely low cost, low power losses, comparable PAE, light-weight and compact volume etc. Therefore for the L-band use, the GaN based SSPA which offers ~ 200 W RF power output with 60 % PAE (similar to the one developed by [49] for the radars) was selected to draw necessary inferences and make different calculations.

The applications-driven design approach was adopted at the start of this research. It was assumed

that focusing on a narrow range of applications would help in keeping the design simple and light-weight. After going through different design stages and finally selecting/recommending the ECMP SAR design approach, the NESZ values achieved while remaining within the safety limits of the onboard power subsystem and the SSPA has been worked out and presented in chapter 6. The achievable σ_n values suggest wider application potentials from the proposed ECMP SAR design than—initially anticipated.

While analysing the generic aspects of the ECMP SAR approach, it can be concluded that from the engineering design point of view and considering the availability of a highly efficient (~ 53%, 150 W (RF) SSPA at the S-band, a ground swath of ~ 30 km can be achieved. At C- and X-bands, an ECMP SAR can be designed but the single beam ground swath would be reduced considerably, and to compensate this reduced swath, a multi-feed with multiple PAs would be required. Nevertheless, a single beam ECMP SAR design at L to X-bands can be accommodated on a SSTL-150 bus by using a reflector antenna fed from a single SSPA.

7.2 Future Work

Although the proposed concept of ECMP SAR fulfils the desired aim and objectives of using SAR on a single microsatellite (~150 kg), yet there are many facets of this research that need to be explored through dedicated future research.

The concept of ECMP SAR revolves around using a 5 m parabolic Cassegrain reflector antenna with inflatable technology at L-band. As was previously mentioned that inflatable technology is becoming popular with the space mission where a very large antennas such as 35 m diameter at Ku-band are required. This technology has a promising future especially in the micro-gravity environment of the space which provides an air free atmosphere – conducive to large scale structure/antennas to operate with minimal support structures. This technology has already been demonstrated in space with 14 m antenna. The low cost SAR mission that has emerged as an outcome of this research would need to have this type of the antenna technology in hand, if it has to be demonstrated to the outside world. It may act as a jump off point to start the research here at SSC on the inflatable technology. To gain experience and grasp the inflatable technology, the project may be initiated at the scaled versions of the desired antenna size. This inflatable technology can be used with other applications such as communication satellites.

As the solar cells find vast applications, a lot of research and development is taking place to increase the efficiency of individual cells. A few sources were identified during this research; it would be pertinent to explore these potentials and adapt these high efficiency cells into future SSTL buses/missions.

The proposed design has identified that there are wider detection potentials than what were ini-

tially anticipated. In order to exploit these benefits, it may be considered as an area of future research to explore the suitable applications which could be served with these achievable σ_n values.

As identified in the chapter 6 that the platform's position knowledge resolution (10 m) is not adequate as compared to ALOS (1 m). It will have implications once temporarily separated images are acquired for interferometric processing. The effect can be compensated by taking more than two observations of the same area for developing the interferogram. But this aspect, in the light of poor position knowledge resolution needs further dedicated research.

The feed (horn)—irrespective whether used with Newtonian or Cassegrain configurations—plays very important role in the reflector antennas. The size of the feed at L-band is found to be considerably large. The size can be reduced and made more efficient to lower the feed losses, through dedicated research in future.

The proposed ECMP SAR concept is based on using a single SSPA (which is a low cost product ~ $ 10,000 utmost), the backend sensor electronics is also presumably not very expensive as it involves crystal controlled oscillators, modulators and demodulators, 8 bit ADC and microcontroller/processor. Nowadays, these parts often come as fully configured modules/cards which are commercially available off the shelf products. In this backdrop, it is possible to initiate a low cost ECMP SAR/inverse SAR project at L-band by integrating these modules and components. The large size parabolic dish antennas and assemblies are also available in the SSC/university. It provides a good opportunity, as a first step, to design an ECMP inverse SAR, which should initially focus on detecting the international space station—for the proof of concept and as a technology demonstrator. This basic design then can be improved upon, for extension to space or to the aerial platforms, in future.

References

[1] [CCRS-2008]. Canada Centre for Remote Sensing: Fundamentals of Remote Sensing. [Online]. http://www.nrcan.gc.ca/sites/www.nrcan.gc.ca.earth-sciences/files/pdf/resource/tutor/fundam/pdf/fundamentals_e.pdf , [Accessed: 01/08/2011]

[2] D. Hodgson, L. Boland, W. Sun, "Operational Earth Observation - Continuity of the Disaster Monitoring Constellation," in *Proceeding of International Astronautical Congress (IAC),* Valencia, Spain., 2006, pp. IAC-06-B5.1.02.

[3] [SAR-Lupe:2006], "EO Portal: Sharing the Earth Observation Resources , SAR-Lupe Constellation," https://directory.eoportal.org/get_announce.php?an_id=8343, [Accessed on 29/06/2011],.

[4] [COSMO-Skymed-2007]. EO Portal: COSMO-SkyMed (Constellation of 4 SAR Satellites). [Online]. https://directory.eoportal.org/get_announce.php?an_id=8990 [Accessed on: 04/03/2012]

[5] [COSMO-Skymed-2012]. (5th Oct, 2007) Mission Cost of COSMO-Skymed. [Online]. http://www.deagel.com/C3ISTAR-Satellites/COSMO-SkyMed_a000256001.aspx, [Accessed on: 23/02/2012]

[6] [RapidEye-2008]. (2008, Aug.) Near Earth LLC. [Online]. http://www.nearearthllc.com/analysis/presentations/vol4.9.5.pdf

[7] R. L. Nathansohn, U. Naftaly, "Overview of the TecSAR Satellite- Hardware and Mosaic Mode," *IEEE: Geoscience and Remote Sensing Letters*, vol. 5, no. 3, pp. 423 - 426, Aug. 2008.

[8] Philip Whitikar, SSTL Project Manager for NovaSAR-S, 8th Feb 2012, Personel Liason Meeting.

[9] Tippawan Wanwiwake, A Microsatellite Based Synthetic Aperture Radar, 2011, PhD Thesis, SSC, University of Surrey, Guildford, UK.

[10] J.J. van der Sanden, "Applications Potential of RADARSAT-2: A Preview," Report prepared by Canada Centre for Remote Sensing in collaboration with Canadian Ice Service for Canadian Space Agency, http://www.scs.gmu.edu/~rgomez/Nov10_17_hyper/applications%20potential%20of%20RADARSAT2.pdf, Apr 2001,[Accessed: 06/08/2011].

[11] Jürgen Puls Reinhard Schröder, "The MAPSAR Mission: Objectives, Design and Status ," in *EUSAR-2006*, http://elib.dlr.de/43957/1/EUSAR_2006_MAPSAR_paper.pdf [Accessed on: 18/07/2011], pp. INPE, p. 4481-4488.

[12] Ian G. Cumming, Frank H. Wong, *"Digital Processing of Synthetic Aperture Radar Data"*. London: Artech House, 2005, ISBN: 1-58053-058-3.

[13] David Schneider. IEEE Spectrum: Radio Eye in the Sky. [Online]. http://spectrum.ieee.org/computing/hardware/winner-radio-eye-in-the-sky IEEE Spectrum, Jan 2009

issue, [Accessed: 20/07/2011]

[14] Evan C. Zaugg, Derek L. Hudson, David G. Long, "The BYU Micro SAR: A Small, Student-Built SAR for UAV Operation," in *IEEE International Conference on Geoscience and Remote Sensing Symposium, 2006. IGARSS 2006. 31 July - 4 Aug*, Denver, 411-414.

[15] [SSTL-2011]. SSTL's Light Weight SAR Mission: NovaSAR-S. [Online]. http://www.sstl.co.uk/Downloads/Datasheets/1767-SSTL-SAR-Datasheet, [Accessed: 03/07/11]

[16] Björn A. Dietrich,....., Thomas Neff, "The MAPSAR Mission: Objectives, Design and Status," Anais XII Simpósio Brasileiro de Sensoriamento Remoto, Goiânia, Brasil, 16-21 abril 2005, INPE, p. 4481-4488.

[17] Christian Wolff. (2011, Aug) Radar Basic Principles. [Online]. http://www.radartutorial.eu/01.basics/rb05.en.html

[18] Charles Elachi, *Spaceborne Radar Remote Sensing: Applications and Techniques.*: IEEE Press, 1988.

[19] Y. Osawa,...., H.Wakabayashi. (2006) A SAR System on the ALOS. [Online]. http://www.isprs.org/proceedings/XXXI/congress/part1/193_XXXI-part1.pdf [Accessed on 29/06/2011]

[20] [JERS-1/LSAR-1992]. FAS: Federation of American Scientists. [Online]. http://www.fas.org/spp/guide/japan/earth/jers1.htm, [Accessed on 29/06/2011]

[21] Rolando L. Jordan, Yunjin Kim. (2006, Apr.) Spaceborne SAR Antennas for Earth Science. [Online]. http://descanso.jpl.nasa.gov/Monograph/series8/Descanso8_06.pdf [Accessed on: 22/12/2011]

[22] [Envisat-2002]. EO Portal: Sharing Earth Observation Resources - Envisat (Environmental Satellite). [Online]. http://www.eoportal.org/directory/pres_ENVISATEnvironmentalSatellite.html, [Accessed on 13/07/2011]

[23] [ERS1-1991]. EO Portal: Sharing the Earth Observation Resources: ERS - 1. [Online]. http://www.eoportal.org/directory/pres_ERS1EUROPEANREMOTESENSINGSATELLITE1.html, [Accessed on 13/07/2011]

[24] [ERS2-1995]. EO Portal: Sharing Earth Observation Resources - ERS-2. [Online]. https://directory.eoportal.org/get_announce.php?an_id=4630 [Accessed on 13/07/2011]

[25] [Radarsat_1-1995]. CSA (Canadian Space Agency): Radarsat-1 Components and Specifications. [Online]. http://www.asc-csa.gc.ca/eng/satellites/radarsat1/components.asp [Accessed 13/07/2011]

[26] [Radarsat_2-2007]. CSA (Canadian Space Agency) : Radarsat 2 Overview. [Online]. http://www.asc-csa.gc.ca/eng/satellites/radarsat2/inf_over.asp, [Accessed 13/07/2011]

[27] [TerraSARX-2007]. EO Portal: Sharing the Earth Observation Resources: TerraSAR-X. [Online]. https://directory.eoportal.org/get_announce.php?an_id=7357, [Accessed on: 04/03/2012]

[28] [Spaceflight-2009]. (18th Apr 2009) RISAT-2. [Online]. http://spaceflightnow.com/news/n0904/17milsat, [Accessed on 29/06/2011]

[29] W. Wiesbeck, "SDRS: Software Defined Radar Sensors," in *Geo-science and Remote Sensing Symposium, held on: 09 - 13 Jul 2001 at Sydney, Australia, published in IEEE IGARSS 2001 Proceedings*, pp. 3259 - 3261, vol.7.

[30] Y. Sharay U.Naftaly, "TecSAR: design considerations and programme status," *IEE Proceedings on Radar, Sonar and Navigation*, vol. 153, no. 2, pp. 117 - 121 , April 2006.

[31] [TecSAR-2006]. EO Portal: TecSAR (SAR Technology Demonstration Satellite). [Online]. https://directory.eoportal.org/get_announce.php?an_id=12614. [Accessed on: 23/07/2011]

[32] [Atlasaerospace-2009], "India launches TecSAR-2, [online] http://www.atlasaerospace.net/eng/newsi-r.htm?id=4398, [Accessed on 29/06/2011]," 2009.

[33] [ARRL-1974], *The ARRL (American Radio Relay League, Inc) Antenna Book*. Newington, Connecticut,: Published by ARRL, 1974.

[34] Dan Thisdall. ([Accessed: 23/3/11]) Flightglobal-2011. [Online]. http://www.flightglobal.com/articles/2011/03/07/353931/surrey-satellite-takes-the-small-route-to-the-high-ground.html

[35] [Spider-2011]. United Nations Platform for Space-based Information for Disaster Management and Emergency Response. [Online]. http://www.un-spider.org/news-en/4966/2011-03-15t111800/microsatellites-emergency-monitoring-and-response. [Accessed: 23/3/11]

[36] D. Hall, L. Gomes, P. Whittaker, M. Cohen, "An Affordable Small Satellite SAR Mission," Berlin, Germany, conference proceedings, IAA-B8-0203, 2011.

[37] Gordon Petrie, "Current & Future Spaceborne SAR Systems," VIII International Scientific & Technical Conference "From Imagery to Map: Digital Photogrammetric Technologies", September 15-18, 2008 – Proceedings, Croatia, 2008.

[38] [Imsar-2010]. Manufacturers of Nano SAR. [Online]. http://www.imsar.com/products. [Accessed: 06/08/2010]

[39] Alex Margulis, Evan C. Zaugg, Matthew C. Edwards, "The SlimSAR: A Compact, Flexible, High-Performance, Polarimetric, Multi-Band SAR for Operation on a Small UAS," Aehken, Germany, Conference Proceedings of EUSAR-2010,.

[40] Bassem R. Mahafza, Atef Z. Elsherbeni, *"MATLAB simulations for radar systems design"*.: Chapman & Hall / CRC CRC Press LLC, ISBN: 1-58488-392-8, 2004.

[41] Merrill I. Skolnik, *"Radar Handbook"*, 3rd ed.: McGraw-Hill Professional, ISBN 0071485473, 2008.

[42] P. Hoogeboom, M.P.G. Otten, J.J.M. de Wit, "Feasibility Study of an FM CW SAR System," 1999, [Accessed: 20/07/2011].

[43] Mathew Edwards, David G. Long, "MicroASAR: A Small, Robust LFM CW SAR For Operation on UAVs and Small Aircraft,".

[44] Evan C. Zaugg, "New Advances in LFM-CW SAR: Theoretical Developments and Practical Applications," in *Conference Proceedings of EUSAR-2010*.

[45] Stepan Lucyszyn, "Power Added Efficiency Errors in RF Power Amplifiers," *International Journal of Electronics*, vol. 82, no. 3, pp. 303-312, 1997.

[46] K. Seina, A. Tsuchika, J. Kanaya K. Nakade, "Development of 150 W S-band GaN Solid State Power Amplifier for Satellite Use," in *Asia-Pacific Microwave Conference Proceedings (APMC), 7-10 Dec, 2010*, Yokohama, Japan, pp. 127-130.

[47] Helmut Vogt, Andreas Peters, Ernst Bosch Peter Ehret, "L-Band TWTAs for Navigation Satellites," *IEEE Transactions on Electronic Devices*, vol. 52, no. 5, May 2005.

[48] M. Ludwig, N. Le Gallou1, "50W L-Band and 25W Ku-Band SSPA for European Space programs," 2005.

[49] [Aethercomm-2010]. Gallium Nitride (GaN) Microwave Transistor Technology for Radar Applications. [Online]. http://www.aethercomm.com/articles/9.pdf, [Accessed: 23/07/2010]

[50] F. Deborgies, ""Microwave Technologies for Satellite Systems: an ESA perspective"," in *Gallium Arsenide applications symposium. GAAS, 6-10 October 2003*, Munich.

[51] [Techspace-2011]. Northrop Grumman's Astro Aerospace Delivers Deployable Reflector to Astrium for Alphasat I-XL Spacecraft. [Online]. http://www.spacemart.com/reports/Northrop_Grumman_Astro_Aerospace_Delivers_Deployable_Reflector_to_Astrium_for_Alphasat_IXL_Spacecraft_999.html, [Accessed: 23/07/2010]

[52] [Astroaerospace-2011]. AstroMesh Deployable Reflector. [Online]. http://www.as.northropgrumman.com/products/aa_thuraya/assets/DS-409-AstroMeshReflector.pdf, [Accessed: 23/07/2011]

[53] [ICLDover-2011]. ICL Dover: Inflatable and Deployable Antennas. [Online]. http://www.ilcdover.com/Inflatable-and-Deployable-Antennas/, [Accessed: 01/04/2011]

[54] Houfei Fang, and Ubaldo O. Quijano, John K. H. Lin, "Concept Study of a 35-m Spherical Reflector System for NEXRAD in Space Application ," Newport, Rhode, 1 - 4 May 2006.

[55] Rebekah L.Tanimoto, Gregory L. Davis. (2008, Aug) JPL.NASA: Mechanical Development of Antenna Systems for Space Missions. [Online]. http://descanso.jpl.nasa.gov/Monograph/series8/Descanso8_08.pdf, [Accessed on: 25/02/2012]

[56] [Envisat Cost Effects - 2002]. ESA: Observing the Earth - Envisat in a nutshell. [Online]. http://www.esa.int/esaEO/ESA1K3V9EYC_index_0.html, [Accessed on: 24/02/2012]

[57] [SSTL-300]. SSTL-300 Satellite Platforms. [Online]. http://rsdo.gsfc.nasa.gov/images/catalog2010/SSTL300.pdf , [Accessed On: 26/11/2011]

[58] [T/R Modules-2010]. (2010, Nov.) Microwave Components and Sub-systems : T/R Modules. [Online]. http://www.microwaves101.com/encyclopedia/transmitreceivemodules.cfm, [Accessed on: 26/02/2012]

[59] Fawwaz T. Ulaby, M. Craig Dobson, *"Handbook of Radar Scattering Statistics for Terrain"*. London, Newyork: Artech House, 1989, ISBN: 0-89006-336-2.

[60] R.T. Lord, M.R. Inggs. (2000) Applications of Satellite Imaging Radar, Department of Electrical

Engineering, University of Cape Town, South Africa,. [Online]. http://rrsg.uct.ac.za/applications/applications.html, [Accessed: 01/08/2011]

[61] [ALOS-2011]. ([Accessed: 01/08/2011]) Observation results of flooding in Thailand. [Online]. http://www.eorc.jaxa.jp/ALOS/en/img_up/pi-sar_thailand_110924-27.htm

[62] [ESA-2000], "Synthetic Aperture Radar Land Applications Tutorial," http://www.tiger.esa.int/training/SAR_LA1_th.pdf, 2000, [Accessed: 02/08/2011].

[63] C. Elachi, L. Jordan, T. Bicknell, "Spaceborne synthetic-aperture imaging radars: Applications, techniques, and technology," *Proceedings of IEEE*, vol. 70, no. 10, pp. 1174 - 1209, Oct 1982.

[64] Diane L. Evans, Mahta Moghaddam, "LightSAR Science Requirements and Mission Enhancements: Report of the LightSAR Science Working Group," NASA and JPL (California Institute of Technology), Mar, 1998, [online]: http://southport.jpl.nasa.gov/lightsar/lsscireq.pdf, [Accessed: 02/08/2011].

[65] [IUCN-2000]. IUCN (International Union for Conservation of Nature) - Forest cover and distribution. [Online]. http://www.iucn.org/about/work/programmes/forest/fp_resources/fp_resources_forest_cover.cfm, [Accessed: 02/08/2011]

[66] [Britannica-2000]. Britannica Online: Distribution of the world's forests. [Online]. http://www.britannica.com/EBchecked/media/56196/Interactive-map-showing-the-geographic-distribution-of-the-worlds-forests, [Accessed: 02/08/2011]

[67] Eric Pottier Jong-Sen Lee, *Polarimetric Radar Imaging from Basics to Applications*. ISBN: 13: 978-1-4200-5497-2: CRC Press, Boca Raton, London, New York, 2009.

[68] Anders Krantz, ""Mapping of Clear Cuts in Swedish Forest using Satellite Images Acquired by the Radar Sensor ALOS"," SLU, ISRN SLU-SRG-AR-265-SE, 2009.

[69] [NOAA-2012]. (2012) NOAA-AVHHR. [Online]. http://www.class.ngdc.noaa.gov/data_available/avhrr/index.htm

[70] A. Calle, A. Romo, J. Sanz J.L. Casanova. Forst Fire Detection and Monitoring by means of an Integrated MODIS-MSG System. [Online]. http://www.iki.rssi.ru/earth/articles/sec9_12.pdf

[71] (2006, [Accessed on:24/09/2012]) Polarimetric Observation by PALSAR. [Online]. http://www.eorc.jaxa.jp/ALOS/en/img_up/pal_polarization.htm

[72] [JPL-1999]. (2012, 24 Sep) LightSAR-Monitoring Floods, Jet Propulsion Laboratory (JPL). [Online]. http://southport.jpl.nasa.gov/lightsar/floods.htm

[73] D. C., Speck, R., Devereux, B. Mason, "Flood Detection in Urban Areas Using TerraSAR-X," *IEEE Transactions on Geoscience and Remote Sensing,* vol. 48, no. 2, pp. 882-894, 2010.

[74] Masanobu Shimada and Manabu Watanabe Ake Rosenqvist, "ALOS PALSAR:Technical outline and mission concepts," in *4th International Symposium on Retrieval of Bio- and Geophysical Parameters from SAR Data for Land ApplicationsInnsbruck,* , , Austria, November 16-19, 2004.

[75] Chris Oliver, Shaun Quegan, *"Understanding Synthetic Aperture Radar Images"*. Religh: SciTech

Publishing, Inc., 2004, ISBN: 1-891121-31-6.

[76] NOAA SAR Manual, "SAR and Mesoscale Storm Systems," in *http://www.sarusersmanual.com/ManualPDF/NOAASARManual_CH15_pg331-340.pdf*, 2003, pp. 331-340.

[77] Hui Shen, W. Perrie, and Yijun He, "On SAR hurricane wind speed ambiguities," in *IEEE International Geoscience and Remote Sensing Symposium, IGARSS 2007.*, Barcelona, 23-28 July 2007 , pp. 2531 - 2534.

[78] I. Chunchuzov, B. Ramsay P.W. Vachon, "Detection and Characterazion of Polar Mesoscale Cyclones in Radarsat1 images of the Labrador Sea," in *Canadian Journal of Remote Sensing,* , 2000, pp. Vol. 26, No.3, pp.213 - 230.

[79] E.Uhlhorn P. Dodge, "Wind fields from SAR: Could they improve our understanding of storm dynamics," Laurel, MD, USA., The Symposium Record of Emerging Coastal and Marine Applications of Wide Swath SAR John Hopkins APL Technical Digest, Jan-Mar, 2000, Vol.21, No.1, pp.86-93, 2000.

[80] Carlo Colesanti, Janusz Wasowski, "Investigating landslides with space-borne Synthetic Aperture Radar (SAR) interferometery," *Engineering Geology*, vol. 88, no. 3-4, pp. 173-199, 15 Dec 2006.

[81] V. Singhroy, Hiroshi Ohkura, Nancy Glenn, "Earth Observation for Landslide Assessment," Canadian Centre for Remote Sensing, Ottawa, Report Prepared by: CEOS (Committee for Earth Observation) Land Hazard Team ftp://ftp2.cits.rncan.gc.ca/pub/geott/ess_pubs/219/219939/13245.pdf, 2002.

[82] A. Friedrich, A.Hajnsek c. Minet, "Requirements for an L-band SAR-mission for global monitoring of tectonic activities ," in *Second Workshop on Use of Remote Sensing Techniques for Monitoring Volcanoes and Seismogenic Areas, 2008. USEReST 2008.* , 2008, pp. 1-3.

[83] Timothy H. Dixon, "SAR Interferometry and Surface Change Detection," Report of a Workshop Held in Boulder, Colorado : February 3-4, 1994, Prepared by JPL , [online]: http://southport.jpl.nasa.gov/scienceapps/dixon/, Jul 1995.

[84] [CEOS-2000], "The Use of Earth Observation Satellites for Hazard Support: Assessments and Scenarios," ESA, CEOS (Committee on Earth Observation Satellites), Final Report by CEOS Disaster Management Suppot Group , [Online]: http://ceos.esrin.esa.it/plenary16/papers/plenary16_doc14_dmsg_final/final_report/DMSG_final.html, 2000.

[85] P.J. Mouginis-Mark M.E. Mackay, "The Effect of Varying Acquisition Parameters on the Interpertetation of SIR-C data: The Virunga Volcanic Chain," Vol 59, pp. 321-336, 1997.

[86] [CEOS-2000a], "Earthquake Hazards CEOS Disaster Management Support Project," NOAA, http://ceos.esrin.esa.it/plenary16/papers/plenary16_doc14_dmsg_final/final_report/DMSG_final.html 2000.

[87] C.C. Schmullius D.L. Evans, "SAR Frequency and Polarization Requirements for Applocations in Ecology, Geology, Hydrology and Oceanography: a tabular status quo after SIR-C/X-SAR,"

International Journal of Remote Sensing, vol.18 No. 13 pp.2713-2722, 1997.

[88] Arthur P. Cracknell, Herbert J. Kramer, "An overview of small satellites in remote sensing," *International Journal of Remote Sensing*, vol. 29, no. 15, pp. 4285-4237, Aug 2008.

[89] [SSTL-100]. SSTL Small Satellite Platforms. [Online]. http://rsdo.gsfc.nasa.gov/images/catalog2010/SSTL100.pdf, [Accessed: 02/04/11]

[90] [SSTL-150]. SSTL Small Satellite Platforms. [Online]. http://rsdo.gsfc.nasa.gov/images/catalog2010/SSTL150.pdf, [Accessed: 02/04/11]

[91] Jean-Claude Souyris Didier Massonnet, *Imaging with Synthetic Aperture Radar*, 1st ed. Switzerland: EPFL Press distributed by CRC press, ISBN: 978-2-940222-15-5, 2008.

[92] Jean-Philippe Merliot Sophie Ramongassie and., "P-Band SAR Satelltie for Biomass Mission," in *IGARSS - 2012* , Munich, 2012.

[93] Roger J. Sullivan, *Radar Foundations for Imaging and Advanced Concepts*. ISBN: 9781891121227: SciTech Publishing, 2004.

[94] B.D. Marron, "Alternatives for Military Space Radar," CBO: Congressional Budget Office., [online]: http://www.cbo.gov/ftpdocs/76xx/doc7691/01-03-SpaceRadar.pdf, [Accessessed on: 05/12/2011] 1st Jan, 2007.

[95] Ian Encke, David Hall, Yvonne Munro, Ian Hønstvet, "AstroSAR -LITE – A Radar System for the Tropics," in *Anais XIII Simpósio Brasileiro de Sensoriamento Remoto*, Florianópolis, Brasil, , INPE, 21-26 Apr 2007, pp. 4907-4913.

[96] J. R. Wiley J. Larson & Wertz, *Space Mission Analysis and Design.*: Kluwer Academic Publishers, 2004.

[97] Robert A. Nelson. (2010) "Antennas: The Interface with Space". [Online]. http://www.aticourses.com/antennas_tutorial.htm, [Accessed on: 13/12/2011]

[98] Eric Johnston. (20 June 2008) Determining the focal length of a parabolic dish (axi-symmetric, circular). [Online]. http://www.satsig.net/focal-length-parabolic-dish.htm, [Accessed on: 13/12/2011]

[99] Tippawan Wanwiwake, Craig Underwood, "A Bi/Multi-Static Microsatellite SAR Constellation," in *Published as a book chapter: "Small Satellite Missions for Earth Observation - New Developments and Trends"*, ISBN 978-3-642-03500-5, Ed.: Publishers Springers, Germany, 2010.

[100] [Solar-2008]. SSTL Sub-systems data sheets: Space Solar Panel and Solar Cell Assymbly. [Online]. http://www.sstl.co.uk/Downloads/Datasheets/Subsys-datasheets/Solar-Panels-ST0035172-v005-01, [Accessed on: 09/03/2012]

[101] Masoud Salehi John G. Proakis, *Communication System Engineering*. ISBN 0-13-300625-5 : Printice-Hall International, Inc, 1994.

[102] M.R. Kosek H. C. Stank.intz, "Sparse Aperture Fill for SAR using Super-SVA," *IEEE*, pp. http://ieeexplore.ieee.org/stamp/stamp.jsp?arnumber=00510659, 1996.

[103] Don Akamine, Russell Lefevre, Joseph Salzman, "Interrupted Synthetic Aperture Radar," *IEEE*

AESS System Magazine, vol. 17, no. 5, pp. 33-39, May 2002.

[104] Jean E. Piou, Joseph T. Mayhan, Kevin M. Cuomo, "Ultrawide-Band Coherent Processing," *IEEE Transactions on Antennas and Propagation*, vol. 47, no. 6, June 1999.

[105] M. Fiani-Nouvel, L. Bosser, "Reconstruction of sparse bandwidth by regularization method in SAR imagery," *IEEE Conference on Radars, held on 24-27 April 2006*, vol. 10.1109/RADAR.2006.1631822, pp. 8-24.

[106] Bart De Moor, Peter Van Overschee, *Subspace Identification for Linear Systems; Theory-Implementation-Applications*. Boston/London/Dordrecht: Kluwer Academic Publishers, ISBN 0-7923-9717-7, 1996.

[107] Lennart Ljung, *System Identification: Theory for the Users*. NJ: Prentice Hall, ISBN 0-13-656695-2, 1999.

[108] Bart De Moor, Peter Van Overschee, "N4SID: Subspace Algorithms for the Identification of Combined Deterministic-Stochastic Systems," *Automatica, Special Issue on Statistical Processing and Control*, pp. ESAT/SISTA-34-I, 1994.

[109] Joe Qin, Lenart Ljung, Weilu Lin, "“On Consistency of Closed-Loop Subspace Identification with Innovation Estimation," in *43rd IEEE Conference on Decision and Control*, Nassau, Dec 14-17, 2004, p. 2195.

[110] Cesareo H. Iglesias Segismundo Izquierdo Millan, "State Space Modelling of Co- integrated Systems using Subspace Algorithms," in *International Conference on Modelling and Simulations-ICMS'04*, Valladolid, Spain, Sep 22-24,2004.

[111] Lennart Ljung Dietmar Bauer, "Some Facts about the Choice of the Weighting Matrices in Larimore Type of Subspace Algorithms," *Automatica*, vol. 38, no. 5, pp. 763-773, Sep 2008.

[112] Richard H. Jones, "Fitting Autoregressions," *Journal of American Statistical Association*, vol. 70, no. 351 , pp. 590-59, Sep 1975.

[113] Naveed Ahmed, Craig I. Underwood, "Switched CW SAR – A Novel and Low Cost SAR Solution for Microsatellites," in *8th IAA Symposium on Small Satellites for Earth Observation*, Berlin, Germany, April 4 - 8, 2011.

[114] [CoSeRA-2012]. 1st International Workshop on Compressed Sensing Applited to Radars. [Online]. http://workshops.fhr.fraunhofer.de/cosera/index.html

[115] [SSTL-2008]. SSTL: Small Satellite Power System: Scalable power conditioning and switching. [Online]. http://www.sstl.co.uk/Downloads/Datasheets/Subsys-datasheets/Datasheet-Powersystem-contact-sheet--November-2008. [Accessed on: 08/03/2012]

[116] [Michael-2006]. CNET News: Solar cell breaks efficiency record. [Online]. http://news.cnet.com/Solar-cell-breaks-efficiency-record/2100-11395_3-6141527.html. [Accessed on: 09/03/2012]

[117] [Nicolus-2011]. (2011, Apr) Clean Technica.com : Solar Junction Breaks Solar World Record with 43.5% Efficiency. [Online]. http://cleantechnica.com/2011/04/19/solar-junction-breaks-

concentrated-solar-world-record-with-43-5-efficiency/, [Accessed on: 07/03/2012]

[118] Igor Elizavetin, "Radiometric Artefacts on SAR images," in *10th international scientific and technical conference: From Imagery to Map: Digital Photogrammertric Techniques*, Gaeta, Italy, Sep 2010, pp. http://www.racurs.ru/download/conf/Italy2010/Presentations/Elizavetin.pdf [Accessed on: 29/09/2012].

[119] Christopher R.Jackson, Samuel W. McCandless, "Principles of Synthetic Aperture Radar," Chapter-1 of SAR Marine User's Manual, http://www.sarusersmanual.com/ManualPDF/NOAASARManual_CH01_pg001-024.pdf, 2003.

[120] C. B. Liang, X. D.Wang, W. Q. Ding, "Time and Phase Synchronisation Via Direct-path Signal for Bistatic Synthetic Aperture Radar Systems," *IET Radar, Sonar & Navigation*, vol. 2, no. 1, pp. 1-11, 2008.

[121] [ALOS-Attitude]. ESA-Earthnet online: ALOS Design. [Online]. https://earth.esa.int/web/guest/missions/3rd-party-missions/historical-missions/alos/design [Accessed on:1/4/2012]

[122] S. K.Srivastava,P. L. Dantec, S.Cote, "RADARSAT-1 Radiometric Performance Maintained in Extended Mission," in *CEOS SAR Workshop*, Germany, 2004.

[123] [Radarsat2-Bus]. (2008) RADARSAT-2 Status/Bus. [Online]. http://www.radarsat2.info/about/construction/bus.asp.

[124] B. Kazeminejad, M. Kirschner, R. Kahle. (2008) First In-orbit Experience of TERRASAR-X Flight Dynamics Operations, German Space Operations Center (DLR/GSOC). [Online]. http://www.weblab.dlr.de/rbrt/pdf/ISSFD_07017.pdf.

[125] Philipp Hartlz Richard Bamlery, "Synthetic aperture radar interferometric back ground," German Aerospace Center (DLR), Institute of Navigation, University of Stuttgart, Germany, http://www.iop.org/EJ/article/0266-5611/14/4/001/ip84r1.pdf?request-id=506b6250-6f05-406a-8ab2-d11e8cb9d4d6, 1998.

[126] Mehrdad Soumekh, *"Synthetic Aperture Radar Signal Processing with Matlab Algorithms"*. ISBN 0-471-29706-2: Wiley Interscience, 1999.

[127] Azlindawaty Mohd Khuzi, Gobi Ventharatnam, Chung Boon Kuan, Chuah Hean Teik, Chan Yee Kit, "The Design and Development of Airborne Synthetic Aperture Radar," *IEEE*, pp. http://ieeexplore.ieee.org/iel5/6913/18661/00861615.pdf?arnumber=861615, Faculty of Engineering, Multimedia University Jalan Multimedia, Cyberjaya, Malaysia 2000.

[128] John F. Shaeffer, Michael T. Tuley Eugene F. Knott, *Radar Cross Section.*: Book-mart Press,Inc, North Bergen, N.J, ISBN : 0-89006-174-2, 1985.

[129] Evan C. Zaugg, "New Advances in LFM-CW SAR: Theoretical Developments and Practical Applications," Conference Proceedings of EUSAR-2010,.

[130] Noud Maas, Roland Bolt, Laura Anitori Matern Otten, "Light Weight Digital Array SAR," IEEE International Symposium on Phased Array Systems and Technology (ARRAY), 2010, Issue

Date:12-15 Oct 2010, 2010.

[131] Brian Eggleston Allen Katz, "UHF GaN SSPA for Space Applications," Digital Object Identifier: 10.1109/RWS.2010.5434222 , 2010.

[132] Alex da Silva Curiel, "Small Satellites in Constellation-Constraints," http://www.deos.tudelft.nl/gamble/docs/GAMBLE_toulouse_dasilvacuriel.pdf, GAMBLE WORKSHOP 2003.

[133] Randolph L. Mosesb M¨ujdat C¸etina, "SAR Imaging from Partial-Aperture Data with Frequency-Band Omissions," *Laboratory for Information and Decision Systems, Massachusetts Institute of Technology, USA*, 2003.

[134] Spaceflight-2009, "RISAT-2," http://spaceflightnow.com/news/n0904/17milsat, [Accessed on 29/06/2011], 2009.

[135] [NovaSAR-2011]. SSTL. [Online]. http://www.sstl.co.uk/Downloads/Datasheets/1767-SSTL-SAR-Datasheet, [Accessed on 30/06/11]

[136] [Artimis-2010]. SAR Solution Providers. [Online]. http://www.artemisinc.net/Products , [Accessed: 15/07/2010]

[137] J.J.M.de Wit, Adriano Meta, Peter Hoogeboom. (2005) FM-CW Based Miniature SAR Systems for Small UAVs. [Online]. http://www.dtic.mil/cgi-bin/GetTRDoc?AD=ADA471972, [Accessed: 20/07/2011]

[138] Bill Sweetman. Radar Revolution: GaN Transistors for Future Radars, [20/06/2011]. [Online]. http://www.aviationweek.com/aw/blogs/defense/index.jsp?plckController=Blog&plckBlogPage=BlogViewPost&newspaperUserId=27ec4a53-dcc8-42d0-bd3a-01329aef79a7&plckPostId=Blog%3a27ec4a53-dcc8-42d0-bd3a-01329aef79a7Post%3a6d9b59dd-cd0e-40fc-ac16-8ac29d40910d&plc

[139] [CCRS-2008a], "Advanced Radar Polarimetry Tutorial," Canadian Centre for Remote Sensing, 2008, [Accessed: 27/08/2011].

[140] A.Beaudoin, …., T.L.Toan, "Relating Forest Biomass to SAR data," *IEEE Transactions on Geoscience and Remote Sensing,* vol. 30, no. 2, pp. 403 - 411, Mar 1992.

[141] M.C. Dobson, …. F.T. Ulaby, "Dependence of Radar Backscatter on Coniferous Forest Biomass," *IEEE Transactions on Geoscience and Remote Sensing*, vol. 30, no. 2, pp. 412 - 415, Mar 1992.

[142] Morten Bakke, Subspace Identification using Closed Loop Data, Jun 2009, MSc thesis, Norwegian University of Science and Technology, Department of Engineering Cybernatics.

Appendix A: SAR Fundamentals

Geometry and Basic Principles of Synthesising Aperture

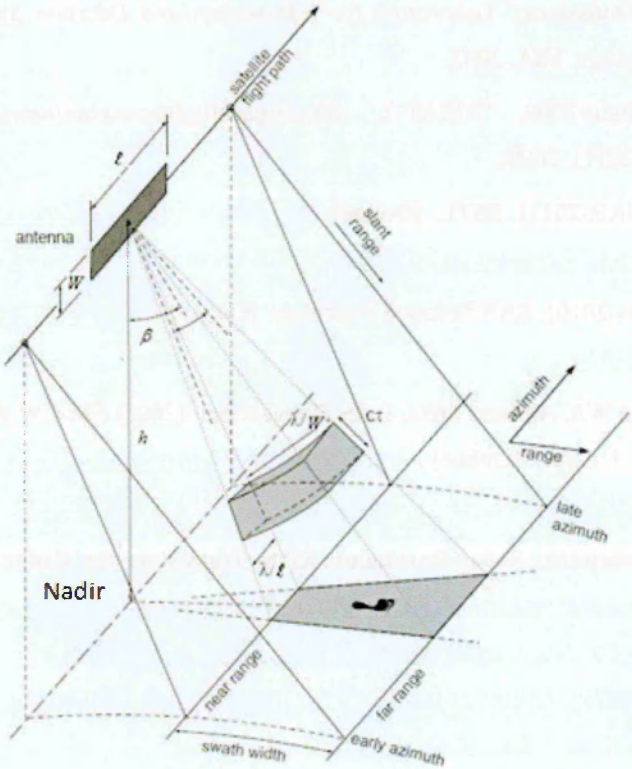

Figure A - 1: The radar geometry and the beam footprint

Source: Adapted from [125]

Figure A - 1 pictorially shows the geometry and the beam footprint of spaceborne radar. It is assumed that the satellite carrying the payload follows a flight path (known as the azimuth direction) that is aligned with the relative platform velocity vector. It can be considered as a vector parallel to the net sensor motion. The direction orthogonal to the azimuth is called range direction. [12]

In most of the spaceborne SAR missions, a rectangular antenna is used, as shown in Figure A - 1. This rectangular antenna has two dimensions: the length (ℓ) along the azimuth direction and the width (W) that is perpendicular to the (ℓ).

This antenna, once energised with the RF power, generates a far field radiation pattern/beam that

can be viewed as a cone, and the footprint viewed as the intersection of the cone with the ground. The beam has two dimensions: its angular width in the azimuth and in the range. In each direction, the half power beamwidth, 'BW_{3dB}' is defined by the angle subtended by the beam edges, in which the beam edge is defined when the radiation strength is 3 dB below the maximum. [12]

In azimuth, with a uniformly driven, rectangular aperture, the beamwidth is approximately the wavelength (λ) divided by the antenna length (ℓ) and is given by:

The azimuth angle: $\theta_a = \frac{\lambda}{\ell}$ (radians) ..... (A: 1)

Similarly in the range direction, the antenna beamwidth subtends an angle, called range angle, given by: $\theta_r = \frac{\lambda}{W}$ (radians) ..... (A: 2)

In this figure, 'h' is the altitude of the satellite measured from the mean sea level on the Earth, and the 'Nadir' is a point on the Earth's surface directly below the sensor. For a spherical Earth model, the vector from the sensor to the Earth's centre intersects the Earth surface at the nadir.

With respect to the nadir, the incidence angle 'β' may be defined as the angle between the nadir vector and another vector that originates at the sensor's centre and terminates at the centre of the swath in the range direction.

The incidence angle 'β' and the range angle 'θ_r' determine the near, far and centre slant ranges denoted by $R_{S,N}$, $R_{S,F}$ and $R_{S,C}$ respectively, as following: [40]

$$R_{S,N} = h / \cos(\beta - \theta_r/2) \quad \text{.....} \quad \text{(A: 3)}$$

$$R_{S,F} = h / \cos(\beta + \theta_r/2) \quad \text{.....} \quad \text{(A: 4)}$$

and

$$R_{S,C} = h / \cos\beta \quad \text{.....} \quad \text{(A: 5)}$$

The azimuth resolution ΔA at slant range '$R_{S,C}$' to the target for a real aperture radar (RAR) is calculated by: [126]

$$\Delta A = R_{S,C} \times \theta_a = \frac{R_{S,C} \times \lambda}{\ell} \quad \text{.....} \quad \text{(A: 6)}$$

Let us consider an airborne X-band radar that has $\lambda = 3$ cm and $\ell = 1$ m and $R_{S,C} = 15$ km,

$$\Rightarrow \quad \Delta A = 450 \text{ m}$$

This is in fact a very poor azimuth resolution due to small antenna length; it would get worst for the spaceborne cases where much longer slant ranges are involved.

In order to improve upon the azimuth resolution, the antenna length needs to be increased signifi-

cantly. But there is a physical limitation beyond which it cannot be increased. This limitation can be turned into an advantage to obtain the fine azimuth resolution resulting from a wide beamwidth by the radar that has the capability of precisely measuring the phase and Doppler. For the radar that has a beam directed orthogonal to its direction of the movement, the large beamwidth will cause an object on the ground to be illuminated and traversed by the radar beam for an extended period of time. During this time, the radar collects phase and Doppler measurements that, through signal processing, allow for an aperture to be constructed or synthesized, equivalent to the distance the physical antenna moves while the location remains in the beam. This is the basic concept behind SAR. [119]

In 1951 it was observed by Carl Wiley, of the Goodyear Aircraft Corporation, that "a one to one correspondence exists between the azimuth coordinate of a reflecting object and the instantaneous Doppler shift of the signal reflected to the radar by that object. He concluded that the frequency analysis of the reflected signals could enable fine azimuth resolution than that permitted by the azimuth width of the physical beam itself, which governed the performance of the RAR designs of that era" [119].

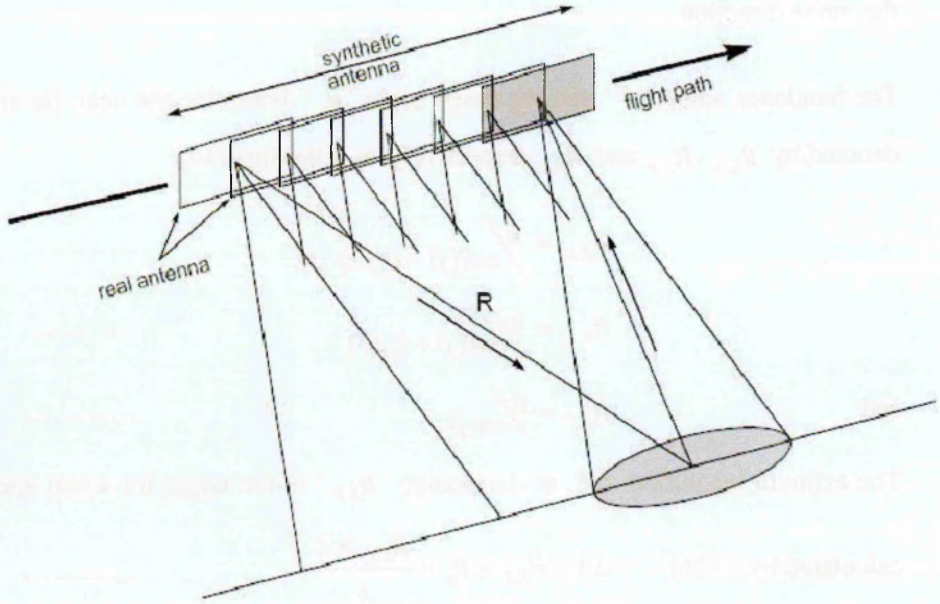

Figure A - 2: Concept of synthesizing a long antenna

Source: Adapted from [125]

Figure A - 2 pictorially depicts the above mentioned concept such that electromagnetic pulses at discrete intervals of time are transmitted which are reflected from the Earth surface. Now in be-

tween transmission of these pulses, the platform carrying the SAR is also moving forward, due to this forward movement, the Doppler shift is introduced, that is recorded in the receiver and once processed over observation time, yields a fine azimuth resolution. Now in this case the forward movement of the platform is virtually incorporated to "synthesize" a long antenna. This antenna synthesis once coupled with efficient signal processing techniques makes it possible to achieve fine azimuth resolution. Thus it may be said that SAR is a signal processing technique to improve the azimuth resolution beyond the limitations of physical antenna aperture [127].

The received signal would be recorded as a voltage (function of time) thus represents one dimension only. But if it is arranged according to the operation of the SAR, in a matrix format, it would result representing two dimensions i.e., range and azimuth as required for developing the map like image. For detailed explanation let us consider the scenario for an airborne SAR payload as represented in Figure A - 3.

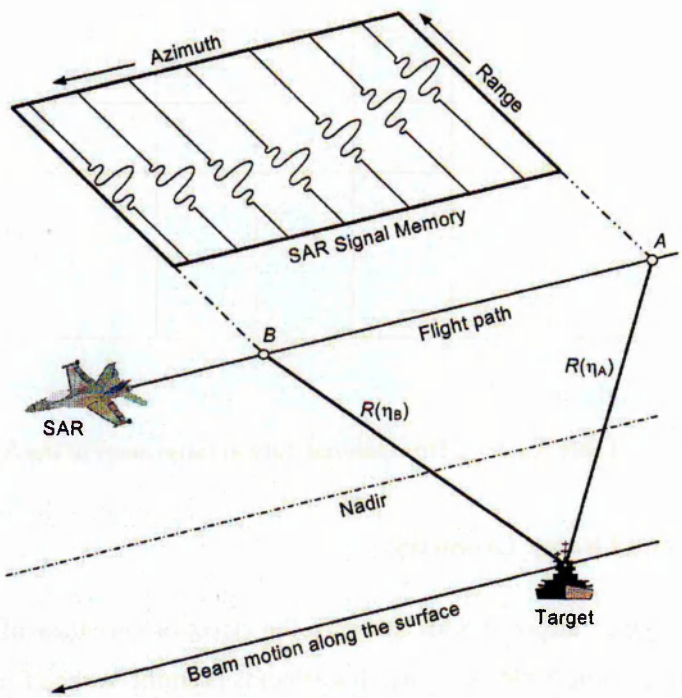

Figure A - 3: How the received SAR data are placed in a two dimensional signal memory

Source: Adapted from [12]

For simplicity, let us assume that the radar beamwidth is finite in azimuth and range directions. When the sensor is at point 'A', the target is just entering the radar beam. At this instance of time, chirp number 1 is transmitted. It lit up the entire scene. Its echo would be received, down converted to baseband, digitized and recorded in line number (column) 1, as shown in Table A – 1. The platform then moves half of the antenna length in azimuth direction and transmits the next

chirp and its returns are recorded in the range line number 2 and so on (until the target leaves the antenna beamwidth in opposite direction). This is how the complete scene/target would be observed and recorded by the SAR. At the end, the matrix so achieved would look like shown in the Table A -1.

Azimuth

RANGE SAMPLES	1	2	3	4	5	....	....	....

Table A - 1: 2 Dimensional data arrangement in the SAR memory

Satellite Ground Range Geometry

For the short range airborne SAR systems, the effect of curvature of the Earth is negligible. But for the satellite borne SAR missions, this effect is prominent, therefore, needs to be accounted for while dealing with different ranges/resolutions.

If we consider a locally circular Earth and the radar beam operating orthogonal to the azimuth direction, then the relationship between slant range 'R_s' and ground range 'R_g' is illustrated in Figure A - 4. Let the line joining the radar and the Earth's centre intersects the Earth at point 'E'. Ground range is the arc length along the Earth's surface from 'E' to the target. It is marked by 'R_g' in the figure, and 'γ'is the angle subtended by this arc at the centre of the Earth. 'R_e' is the local radius of the Earth, taken at the scene centre. Let 'h' be the altitude of the platform with respect to point 'E', 'β' is the off nadir angle/incidence angle and 'θ_i' is the local incidence an-

gle (i.e., the angle between the normal of the backscattering element and the incoming radiation). [12]

For the locally circular Earth approximation, the geometric variables in the figure are related by the law of sines and cosines. [12], [75]

$$\frac{R_e}{\sin\beta} = \frac{R_e + h}{\sin\theta_i} = \frac{R_S}{\sin\gamma} \qquad \text{.....} \qquad \text{(A: 7)}$$

and with the approximation of 'γ' to be small,

$$R_g = R_e\,\gamma \qquad \text{.....} \qquad \text{(A: 8)}$$

The local incidence angle 'θ_i' is larger than the off-nadir angle/incidence angle 'β' by 'γ'. The difference is negligible in the airborne case, but is few degrees in the satellite case. Thus

$$\gamma = \theta_i - \beta \qquad \text{.....} \qquad \text{(A: 9)}$$

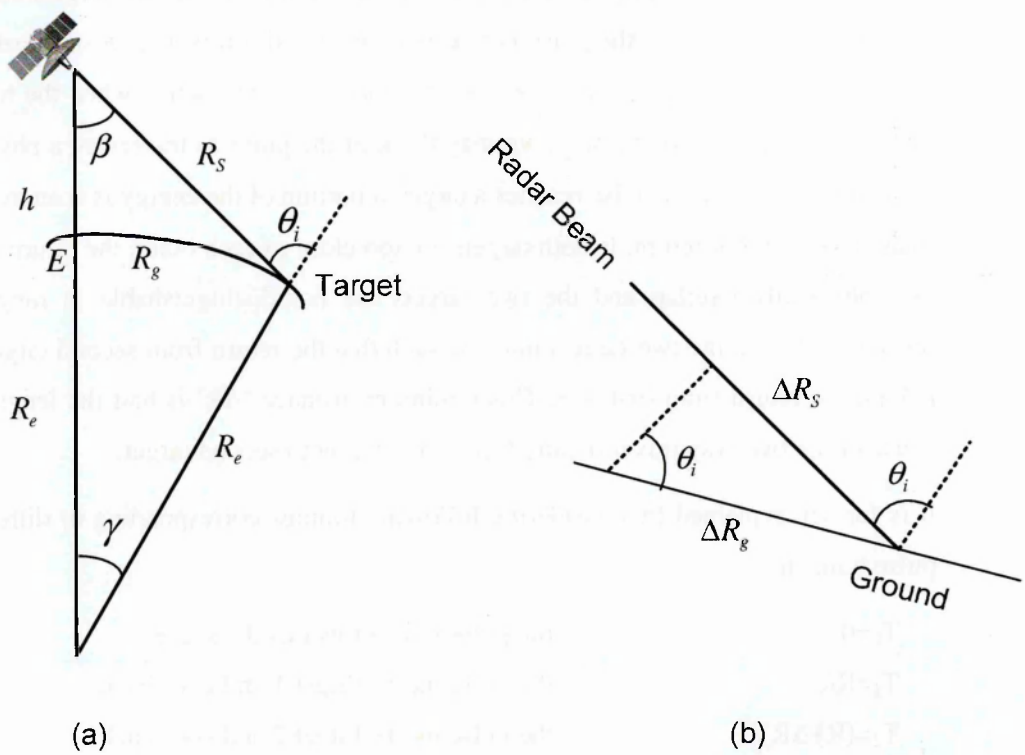

Figure A - 4: Satellite cross-track geometry, illustrating the effects of curvature of Earth.

Source: Adapted from [12], [75]

For a radar, the slant range resolution ΔR_s is given by : [75]

$$\Delta R_s = c/2B \qquad \ldots\ldots\ldots\ldots \qquad \text{(A: 10)}$$

where the 'B' is the bandwidth of the chirp being used. The rationale for derivation of this equation would be discussed in the next sections.

This relationship shows that the slant range resolution remains constant across the range swaths. But the local incidence angle affects the ground range resolution 'ΔR_g' according to the relationship:

$$\Delta R_g = \Delta R_s / \sin\theta_i \qquad \ldots\ldots\ldots\ldots \qquad \text{(A: 11)}$$

this shows that the 'ΔR_g' varies non-linearly across the swath.

Why a Narrow Pulse or a Chirp is Needed for Fine Range Resolution

In order to derive the range resolution expression for the radar to distinguish between two neighbouring targets that are separated by a distance 'ΔR' in range direction as shown in Figure A - 5, let a single pulse of length τ seconds is transmitted toward these two targets so that it encounters them sequentially. Since the pulse is τ seconds long and it travels at a speed of light, the leading edge of the pulse would have travelled a distance of '$c \times \tau$'metres when the trailing edge of the pulse is transmitted. In this way, we may think of the pulse as traversing a physical distance of '$c \times \tau$'metres. When the pulse reaches a target, a portion of the energy is scattered back toward the radar as an echo or return. If both targets are too close to each other, the returns from the two targets physically overlap and the two targets are not distinguishable in range. The minimum distance between the two targets must be such that the return from second target follows directly behind the return from first one. This minimum distance 'ΔR' is half the length of the pulse because of the two-way travel required from first target to second target.

It is further explained by considering following timings corresponding to different stages as the pulse transmits:

$T_0=0$	the pulse is sent towards the scene
$T_1=R/c$	the pulse meets Target 1 and goes back
$T_2=(R+\Delta R)/c$	the pulse meets Target 2 and goes back
$T_3=2T_1=2R/c$	the pulse from Target 1 reaches the radar
$T_4=2T_2=2(R+\Delta R)/c$	the pulse from Target 2 reaches the radar

In order to distinguish between T_3 and T_4, it depends on how long the pulse is i.e., 'τ'.

$$T_4 - T_3 = 2\Delta R/c < \tau \qquad \text{or} \qquad \Delta R = c\tau/2$$

is the shortest separation that can be measured (below this value the pulses would be merged). Since SAR works in the slant range direction, thus we would call this as slant range resolution:

$$\Delta R_S = c\tau/2 \qquad \ldots\ldots\ldots\ldots \qquad \text{(A: 12)}$$

An important concern is the resolution of the time measurement 'τ', as it determines the slant range resolution. It is an established relationship in the radar theory that this time resolution is inversely proportional to the bandwidth 'B' of the transmitted signal. For an ideal case where the constant of proportionality is taken as 1, then $\tau = 1/B$. [75]

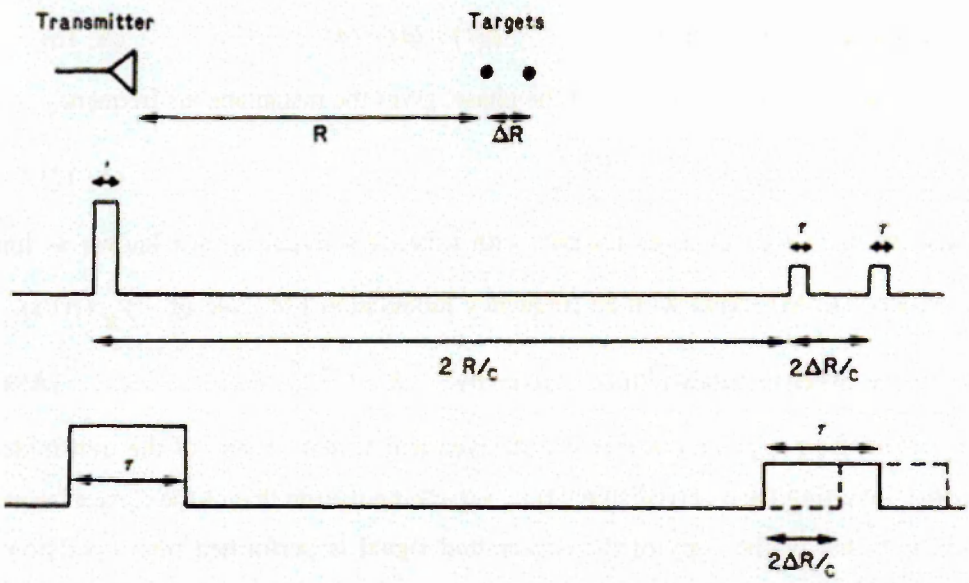

Figure A - 5: Sketch explaining the echo return from two neighbouring point targets

$$\Delta R_S = c\tau/2 = c/2B \qquad \ldots\ldots\ldots\ldots \qquad \text{(A: 13)}$$

Thus, in order to get a fine slant range resolution (i.e., small ΔR_s), a narrow pulse 'τ'or a pulse with wide bandwidth is needed.The energy (E) of a received pulse is given by:

$$E = P\tau \qquad \ldots\ldots\ldots\ldots \qquad \text{(A: 14)} \qquad [18]$$

where 'P' is the instantaneous peak power. This energy determines the capability of a sensor to detect a target. So it can be increased by either increasing 'P' or 'τ'. 'P' can not be increased beyond certain limits due to technical constraints. If 'τ' is increased then 'B' will reduce that will yield poor range resolution. Thus in order to have a high detection capability (large E) and a fine slant range resolution (large B), a signal is required that should have large τ and large B. This may not be possible as both these requirements are conflicting with each other. To meet these conflicting conditions, a chirp signal is used. [18]

As an example, the ERS-1 satellite had the pulse duration of 37.1 μs. For a simple pulse, it would yield a slant range resolution of 5.565 km. The means by which this long pulse is compressed to provide a fine resolution of few meters makes use of the form of the transmitted pulse i.e., the chirp. [75]

In many SAR systems, most commonly used transmitted waveform $p(t)$ is of the form:

$$p(t) = \exp\{i(\omega_0 t - \alpha t^2)\} \text{ for } |t| \le \tau'/2 \quad \text{.....} \quad \text{(A: 15)} \quad [75]$$

where the ω_0 is the carrier frequency of the radar (radians/s), and τ' is the chirp length. The phase (radians) of the signal is: $\phi(t) = \omega_0 t - \alpha t^2$ ..... (A: 16) [75]

and by taking the time derivative of the phase, gives the instantaneous frequency f_i (Hz) as:

$$f_i(t) = (\omega_0 - 2\alpha t)/2\pi \quad \text{.....} \quad \text{(A: 17)} \quad [75]$$

Since the frequency changes linearly with time, this signal is thus known as linear frequency modulated (LFM) signal with an frequency modulation FM rate of α/π (Hz/s). Thus the total frequency sweep or bandwidth B, is given by: $B = \alpha\tau'/\pi$ (Hz)..... (A: 18)

The return from a point scatterer is a delayed and scaled version of the transmitted pulse. After down converting the received signal (i.e., separating it from that of the carrier frequency), correlation with that of the copy of the transmitted signal is performed (that operation is also called matched filtering). After matched filtering, it produces a response whose shape is given by:

$$h_r(t) = \int_{-\tau'/2}^{\tau'/2} \exp(i\alpha s^2) exp\{-i\alpha(s+t)^2\} rect\left(\frac{s+t}{\tau'}\right) ds \quad \text{.....} \quad \text{(A: 19)} \quad [75]$$

$$= (\tau' - |t|)\,\text{sinc}\left\{\frac{\alpha}{\pi}(\tau' - |t|)\right\} \text{rect}(t/\tau') \quad \text{.....} \quad \text{(A: 20)} \quad [75]$$

where $\text{rect}(t) = \begin{cases} 1 \text{ for } |t| \le 1/2 \\ 0 \text{ for } |t| > 1/2 \end{cases}$ and $\text{sinc} = \dfrac{\sin \pi t}{\pi t}$

Since $h_r(t)$ is obtained by correlating the $\exp(-i\alpha s^2)$ with itself, it is often referred to as the autocorrelation function (ACF). [75]

The first positive zero of this signal (and others of related type) is often taken as a measure of the time resolution τ. This is controlled by the sinc function and occurs when $\alpha(\tau' - |t|) = \pi$ that has the solution: $t = \tau = \dfrac{\tau'}{2}\left[1 - \sqrt{1 - \dfrac{4}{\alpha\tau'}}\right]$ ..... (A: 21) [75]

and for a large $\alpha\tau'$ product, a good approximation yields: $\tau \square \frac{1}{B}$ ..... (A: 22)

The ratio of the resolution after processing to the original pulse length is known as the compression ratio, given by: $\frac{\tau'}{\tau} \square \tau' \times B$ ..... (A: 23)

that means the compression ratio is equal to time bandwidth product. As an example, the ERS-1 had a compression ratio of 575 (= 27.6 dB) with a chirp length, τ'=37.1 µs, that would be equal to a time resolution τ =64.5 ns. [75]

For a large time bandwidth product, the match filter response $h_r(t)$ may be written to a good approximation as: $h_r(t) = \tau' \text{ sinc } \left(\alpha\tau' t/\pi\right) = \tau' \text{ sinc } (Bt)$ ..... (A: 24) [75]

this expression is often referred to as the ideal form of the SAR point spread function.

SAR and the Azimuth Dimension

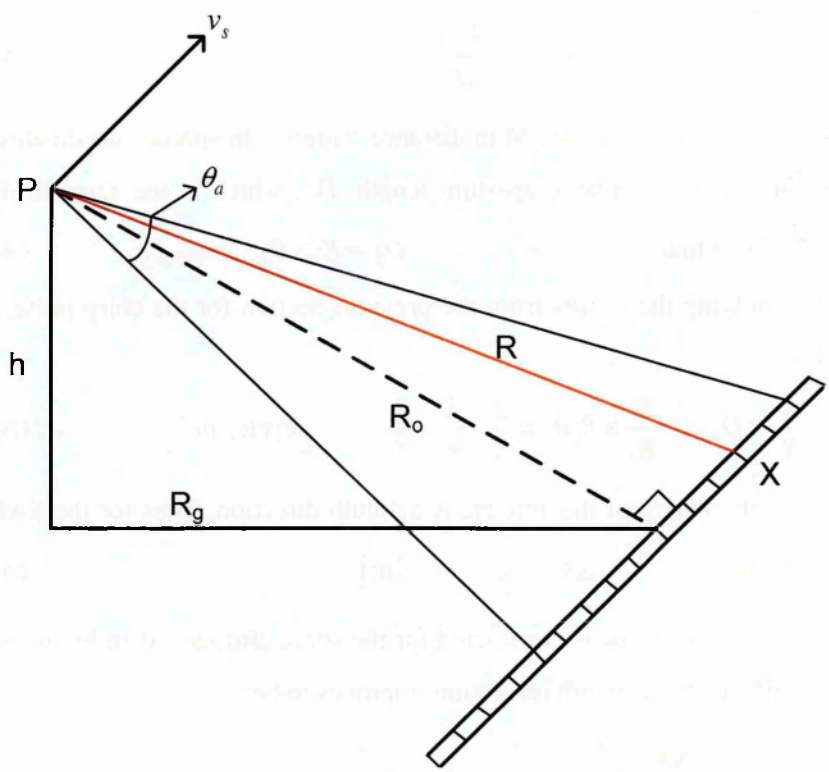

Figure A - 6: The flat- Earth geometry of an airborne SAR

The SAR is famous for its handling of the returns which after processing, yield very fine azimuth resolution, that is otherwise difficult to achieve through RAR. Figure A - 6 represents the flat-Earth geometry of an airborne SAR. After the range processing, a strip of range (bin) is shown in

the figure. It is assumed that the effects of the range curvature are ignored, thus for the simplicity purpose, a straight strip is considered. For the RAR, the azimuth resolution would be $\Delta A = R_o \times \theta_a$ where R_o is the slant range at the position of the closest approach and θ_a is the antenna's beam-width in azimuth direction. If a coordinate system is assumed that has the x-axis along the velocity vector of the platform and its origin is at a point X on this strip that is defined by R_o. A point scatterer X is considered on this strip as shown in the figure. If the azimuth coordinate is x, then the geometry satisfies: $R^2 = R_o^{\,2} + x^2$ ..... (A: 25) [75]

For a narrow beam, X is only illuminated when $x << R_0$

then $$R = R_o + \frac{x^2}{2R_o}$$ ..... (A: 26) [75]

The corresponding two way phase delay at the carrier frequency would be:

$$\phi(x) = -\frac{4\pi R_o}{\lambda} - \frac{2\pi x^2}{\lambda R_o}$$ ..... (A: 27) [75]

This would have an associated rate of change of phase with distance given by:

$$\frac{\phi(x)}{dx} = -\frac{4\pi x}{\lambda R_o}$$ ..... (A: 28) [75]

which is equivalent to linear FM in distance variable. In spatial coordinates, the equivalent of the pulse length is the synthetic aperture length D_S, which is the azimuth distance illuminated at range R_o, such that $D_S = R_o \times \theta_a$ ..... (A: 29) [75]

Now by applying the results from the previous section for the chirp pulse, the spatial bandwidth would be :

$$\frac{1}{2\pi} \times \frac{4\pi}{\lambda R_o} \times D_S = \frac{2}{\lambda R_o} \times R_o \theta_a = \frac{2}{\lambda} \times \frac{\lambda}{\ell} = \frac{2}{\ell} \quad \left[\text{cycles m}^{-1}\right]$$ ..... (A: 30) [75]

where ℓ is the length of the antenna is azimuth direction. Thus for the SAR, the azimuth resolution would be: $\Delta A = \ell/2$ [m] ..... (A: 31) [75]

Similarly, once the same is considered for the space altitudes, then by incorporating the curvature of Earth effects, the azimuth resolution improves to be:

$$\Delta A = \frac{\mathrm{R_e}}{\mathrm{R_e} + h} \times \frac{\ell}{2} \quad [\mathrm{m}]$$ ..... (A: 32) [75]

This result shows that the SAR azimuth resolution is half the antenna length in azimuth direction and is independent of slant range and wavelength.

Eq. A: 27 gives the associated rate of change of phase in terms of distance. Now once motion of the platform v_s is to be incorporated, then it is often desirable to interpret it in terms of time,

by changing $x = v_s \times t$ so that:

$$\phi(t) = -\frac{4\pi R_o}{\lambda} - \frac{2\pi v_s^2 t^2}{\lambda R_o} \quad \text{[radians]} \quad \ldots\ldots\ldots \quad \text{(A: 33)} \quad [75]$$

and rate of change of phase with respect to time:

$$f_d = \frac{1}{2\pi}\frac{d\phi(t)}{dt} = -\frac{2v_s^2 t}{\lambda R_o} \quad \text{[Hz]} \quad \ldots\ldots\ldots \quad \text{(A: 34)} \quad [75]$$

and similar to the range chirp bandwidth (Eq.A:17), the azimuth bandwidth may also be calculated as:

since the azimuth FM rate $\left(\frac{\alpha_{az}}{\pi}\right) = \frac{2v_s^2}{\lambda R_o}$ $\left[\text{Hz s}^{-1}\right]$;

and the azimuth synthesis time = $\frac{D_s}{v_s} = \frac{R_o \lambda}{v_s \ell}$ $[s]$; (this is equivalent to τ' in range direction); thus the azimuth bandwidth = Azimuth FM rate ×azimuth synthesis time.

$$\Rightarrow \quad \left(\frac{\alpha_{az}}{\pi}\right) \times \frac{D_s}{v_s} = \frac{2v_s^2}{\lambda R_o} \times \frac{R_o \lambda}{v_s \ell} = \frac{2v_s}{\ell} \quad \text{[Hz]} \quad \ldots\ldots \quad \text{(A: 35)}$$

This bandwidth governs the sampling requirements; that is, it defines the lower limit of PRF. However the two-way signal drops down from the centre of the main lobe towards the edges by 6 dB, and the azimuth spectrum rolls off slowly. An over-sampling factor of 1.1 to 1.4 is often used to reduce the azimuth ambiguity power; that is, the PRF is set to the over sampling factor multiplied by azimuth bandwidth. [12]

Similar to the ideal form of the SAR point spread function in range (Eq. A: 24), the equivalent ideal compressed signal (azimuth point spread function) in time coordinates is given by:

$$h_s(t) = \frac{R_o \theta_a}{v_s} \operatorname{sinc}\left(\frac{2v_s t}{\ell}\right) \quad \ldots\ldots \quad \text{(A: 36)} \quad [75]$$

Eqs. A: 24 and A: 36 are equivalent in a sense that the chirp length τ' in range direction and bandwidth 'B' have equivalence of azimuth synthesis time $\frac{R_o \theta_a}{v_s}$ and azimuth bandwidth $\frac{2v_s}{\ell}$ respectively.

The sinc function is characterized by main lobe and high sidelobes. These sidelobes are reduced by using suitable weighting functions. Application of these functions on one hand reduces the sidelobes but on other hand widen the main lobe. The first zero crossing of the main lobe is considered as the resolution of the system. The definition of the resolution needs to incorporate the effects of weighting function used.

Choice of Pulse Repetition Frequency (PRF)

SAR uses a series of pulses to synthesize the aperture. These pulses are repeated according to a set frequency called PRF. The selection of a suitable PRF is governed by a set of parameters that are discussed as following:

- **Nyquist Sampling Rate (Azimuth Ambiguity)**

In order to meet the Nyquist criteria of sampling, PRF should be higher than the azimuth bandwidth $= \frac{2v_s}{\ell}$ (Eq. A: 35) i.e., a pulse should be send every time the platform moves forward half the antenna length in the azimuth direction. Therefore the minimum PRF: $PRF_{\min} \geq \frac{2v_s}{\ell}$

Here in this equation, v_s refers to the platform velocity.

For the case once the SAR is operating from the aircraft, the slant rang to the target is short, thus effects of the curvature of Earth may be ignored. The difference between the platform velocity v_s and the ground velocity v_g (with which the electromagnetic wave front interacts with the ground) is negligible. But this difference becomes significant once space altitudes are considered, thus the effects of curvature of Earth need to be taken into account.

The ground velocity v_g is related to the spacecraft velocity v_s, by $v_g \approx \left[\frac{\mathrm{Re}}{\mathrm{Re}+h}\right] v_s$. In order to accurately estimate the Doppler, the effective/relative velocity v_e is used, that is related to satellite and ground velocities as: $v_e = \sqrt{v_s v_g}$ . ..... [12]

Therefore, the minimum PRF should be: $PRF_{\min} = \frac{2v_e}{\ell}$ ..... (A: 37)

This equation sets the minimum estimated PRF but in practice, an azimuth over-sampling factor which is usually 1.1 – 1.4 times the minimum PRF should be taken into account. [12]

- **Range Swath (Range Ambiguity)**

It is also desired that at any instance of time there should be only one pulse/chirp impinging in the range swath. If there are more than one pulses/chirps impinging in the same area then it will be difficult to distinguish between the echoes coming from different pulses. [12]

Thus in the slant range the time required by a pulse to impinge on the surface and reflect back is:

$$\frac{2\left(R_{S,F}-R_{S,N}\right)}{c}$$

Therefore the maximum PRF should be less than this time such that:

$$PRF_{\max} \leq \frac{c}{2\left(R_{S,F}-R_{S,N}\right)} \qquad \ldots\ldots\ldots\ldots\ldots\ldots \qquad \text{(A: 38)}$$

- **Nadir Return**

As was previously discussed that the ground range resolution changes non-linearly across the swath, having largest values at the nadir and smallest at the farthest edge of the antenna beam width. The returns from the ground below the sensor may be strong enough to interfere with those from the main beam. Predominantly, the strength of these returns is dictated by the fact that which part of the antenna beam pattern in range direction impinges at the nadir. This aspect is also, in return coupled with the SAR incidence angle.

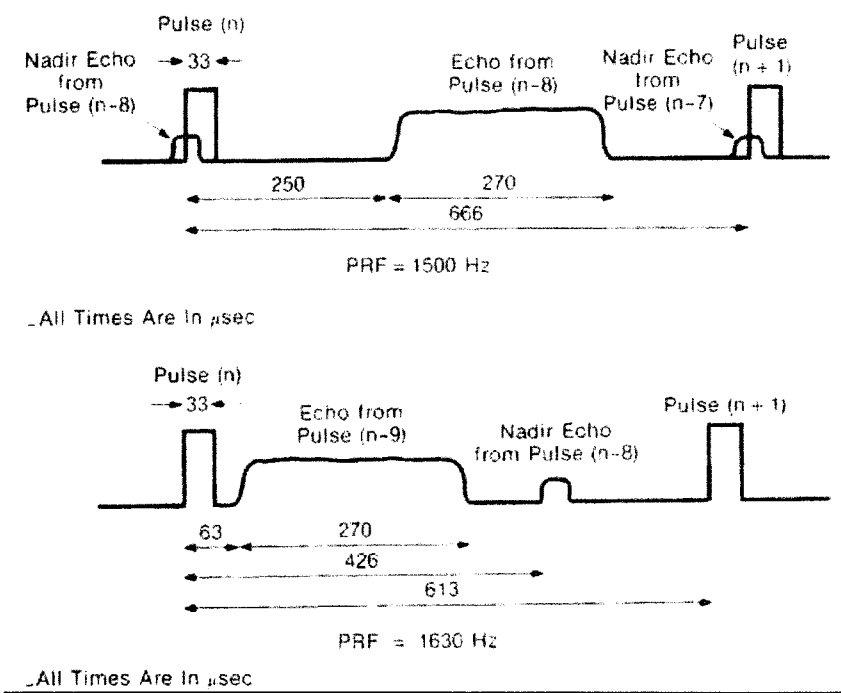

Figure A - 7: Seasat SAR timing diagram

Source: Adapted from [18]

In order to mitigate these effects, the PRF may be tuned in such a way that nadir returns are adjusted at a time that does not interfere with the returns from the main lobe. This aspect is highlighted in the Figure A - 7, which shows the Seasat SAR timing. For this sensor, if the PRF

would had been set at 1500 Hz, the nadir returns were interfering with the time of transmission of the pulse. So by changing PRF to 1630 Hz, its receiving timing was so adjusted that it was neither interfering with the time of sending the pulse nor once the echo was being received.

Minimum Antenna Area

Eqs. A: 37 and A: 38 set the lower and upper limits on the usable PRF band so that the azimuth and range ambiguities could be avoided. Eq. A: 38 may also be written in terms of incidence angle as:

$$PRF_{\max} \leq \frac{c \times W \times \cos^2 \beta}{2\lambda h \times \sin \beta} \text{ [Hz] } \ldots\ldots\ldots\ldots \quad \text{(A: 39)} \quad [18]$$

Combining Eqs. A: 37 and A: 39, $\Rightarrow \quad \frac{c \times W \times \cos^2 \beta}{2\lambda h \times \sin \beta} \leq PRF \geq \frac{2v_s}{\ell}$

$$\Rightarrow \quad \text{Minimum Antenna Area} = W\ell \geq \frac{4\lambda h v_s \sin \beta}{c \times \cos^2 \beta} \text{ [m}^2\text{]} \quad \ldots\ldots \text{ (A: 40)} \quad [18]$$

This equation determines the minimum size of the rectangular antenna for SAR. It needs appropriate modifications if other types of the antennas are to be used. But nonetheless it yields a significantly large sized antenna for the satellite platforms mainly because of large values of 'h' and 'v_s'.

Radar Equation for SAR

- **Radar Equation for a Point Target**

The radar equation connects the power aperture product of the transmitter with that of intercepted power aperture product of the receiver, the location of the scattering target relative to the transmitting and receiving antennas and the target scattering properties. For a monostatic radar, wherein the transmitting and receiving antennas are co-located, or same antenna is used for both transmission and reception, the power received by the antenna, as a result of backscattering from a point target – whose location is defined by (ψ_a, ψ_r) i.e., the small angles (within antenna 3 dB beam widths (θ_a, θ_r)) in azimuth and range directions, respectively, is given by:

$$P_R(\psi_a, \psi_r) = \frac{P_t \times G^2(\psi_a, \psi_r) \times \lambda^2}{(4\pi)^3 \times R_S^4} \times \sigma \quad \text{[W]} \quad \ldots\ldots\ldots \quad \text{(A: 41)} \quad [59]$$

where:

P_t = Peak RF power (which is fed at the input of the antenna), (W).

G = Gain of the antenna if same antennas is shared between the transmitter and the receiver. If radar is used from monostatic/multi-static locations where separate antennas are used, then their respective gains to be used here.

λ= Wavelength of the radar centre frequency (m).

R_S = The slant range to the target (m).

σ = The radar cross section (RCS) of the target (considered a point target in this case).

"The above equation pertains to a target whose physical dimensions are such that the solid angle it subtends is much smaller than the solid angle of the radar beam. Such a target will be referred to as a point target even though it may have a complex geometry and non-uniform scattering properties". [59]

The radar cross section σ, characterizes the scattering strength in the back scattering direction in the form of an area. In general, σ of a given target is related to its shape and dielectric constant, the viewing geometry, the wavelength λ and the polarization directions of the incident and scattered waves.

The σ may be defined in terms of the ratio of the scattered power density S_p^s measured at a distance R_S from the scatterer to the power density S_q^i of an incident plane wave. [59] Thus,

$$\sigma_{pq} = \lim_{R_S \to \infty} \left(4\pi R_S^2 \frac{S_p^s}{S_q^i} \right) \quad \text{.....} \quad \text{(A: 42)} \quad [59]$$

where the limit as $R_S \to \infty$ that the observation point is in the far-field region. The subscripts q and p denote the polarizations of incident and scattered waves, respectively.

- **Radar Equation from a Distributed Target**

The radar equation given by A: 41 for a point target may be extended to the distributed target by integrating the backscattered power over the illuminated area A. [59] By illuminated area, means the area of the ground that is lit by half power beamwidth of the antenna main lobes in both range and azimuth directions. Thus:

$$P_{Rp}(\beta) = \iint_A \frac{P_{tq} \times G^2(\psi_a, \psi_r) \times \lambda^2}{(4\pi)^3 \times R_S^4} \times \sigma_{pq}^0 dA \ \text{[W]} \quad \text{.....} \quad \text{(A: 43)} \quad [59]$$

where β is the incidence angle as previously defined. The polarization indices p and q are included in the above expression to show the connection between the q-polarized transmitted power, the p-polarized received power, and the pq-polarized backscattering cross section per unit area σ^0_{pq}, which is defined as the backscattering cross section of a distributed target of horizontal area A, normalized with respect to A. Thus,

$$\sigma^0_{pq} = \sigma_{pq} / A \qquad \text{.....} \qquad \text{(A: 44)} \qquad [59]$$

Often, σ^0 is referred to as the backscattering coefficient, for short.

When Earth's surface is used as a reference plane, traditionally the orthogonal pair of linear polarizations known as horizontal and vertical, to describe the direction of the electric field, are used. The Eq. A: 42 may be written in the form of HH and HV-polarized backscattering coefficient as:

$$\sigma_{HH} = \lim_{R_S \to \infty} \left(4\pi R_S^2 \frac{\left|E_H^s\right|^2}{\left|E_H^i\right|^2} \right) \qquad \text{.....} \qquad \text{(A: 45)}$$

and

$$\sigma_{VH} = \lim_{R_S \to \infty} \left(4\pi R_S^2 \frac{\left|E_V^s\right|^2}{\left|E_H^i\right|^2} \right) \qquad \text{.....} \qquad \text{(A: 46)}$$

where the relationship $S_q = \left|E_q\right|^2 / \eta$ is used that has the quantity η that describes the intrinsic impedance of the medium, which in this case is considered as air (=1). [59]

In backscattering direction, the scattering process is reciprocal in character, that leads to the equality $\sigma_{VH} = \sigma_{HV}$. [59]

In practice, σ_{HH} and σ_{VH} are measured as a pair by using H-polarized transmitting antenna and a two channel dual-polarized receiving antenna.

- **Radar Equation for a Narrow Beam Scatterometer**

If the distributed target has uniform properties across the area illuminated by the antenna beam, and if the beam is sufficiently narrow, such that $\sigma^0(\theta_i)$, where θ_i is the local incidence angle,

may be regarded as constant over the angular extent of the narrow beam then Eq. A: 43 may be written as:

$$P_{Rp}(\beta) = \frac{P_{tq} \times \lambda^2}{(4\pi)^3} \times \sigma^0_{pq}(\theta_i) \iint_A \frac{G^2(\psi_a, \psi_r)}{R_S^4} \times dA \quad \text{[W]} \quad \text{..... (A: 47)} \qquad [59]$$

$$P_{Rp}(\beta) = \frac{P_{tq} \times \lambda^2}{(4\pi)^3} \times \sigma^0_{pq}(\theta_i).I \quad \text{[W]}$$

where $I = \iint_A \frac{G^2(\psi_a, \psi_r)}{R_S^4} \times dA$ is called the illumination integral, which may be resolved with the help of additional approximations such as; $R_S \approx R_0$ where R_o is the slant range at the position of the closest approach, thus it may be considered as constant and can be taken outside of the integral; and the antenna pattern is replaced with an equivalent pattern of the gain G (i.e., considered constant within very narrow limits). These approximations then lead to:

$$P_{Rp}(\beta) = \left[\frac{P_{tq} \times \lambda^2 \times G^2 \times A}{(4\pi)^3 \times R_0^4} \right] \times \sigma^0_{pq}(\theta_i) \quad \text{[W]} \quad \text{..... (A: 48)} \qquad [59]$$

where 'A' is the area illuminated by the equivalent beam of the antenna.

- **Radar Equation for the SAR**

The assumptions made in deriving the Eq. A: 46 are well suited to the imaging radar (real aperture radar) and the SAR because the dimensions of the illuminated ground cell are very small relative to the distanced R_S ($\approx R_0$) between the radar and the cell.

Now while dealing with the illuminated area 'A' in the context of the SAR, it would be considered as the small facet or the elemental area over which the phase is coherent (effectively constant). However, for the non-uniform distributed targets, different facets contribute independent phases, the observed electric field is dominated by interference effects, giving rise to the phenomenon known as speckle. For these distributed targets, the quantity of interest is the average value of σ^0 within a pixel or 'A'. [75] Therefore, the:

$$A = \Delta R_g \times \Delta A$$

where ΔR_g is the SAR's ground range resolution (that is local incidence angle dependent and var-

ies non-linearly across the swath) and the ΔA is the SAR's azimuth resolution. As had been discussed previously that $\Delta A = \frac{\ell}{2}$ thus we would use, $A = \Delta R_g \times \frac{\ell}{2}$ ..... (A: 49)

Furthermore, developing the SAR equation need to incorporate additional aspects such as:

- Antenna Synthesis Factor: to improve upon the azimuth resolution that is achieved from a real aperture radar, the SAR synthesises a long aperture by coherently integrating 'n' number of pulses during the azimuth synthesis time. This factor is given by: $\frac{f_r R_S \lambda}{v_s \ell}$, where f_r = The pulse repetition frequency.
- Compression Ratio: To improve upon the SNR, pulse compression technique is used where instead of using a very narrow and high powered pulse, a chirp signal is transmitted. The compression ratio expression given in Eq. B: 23 may also be incorporated here as: $\frac{\tau'}{\tau}$, where τ' is the chirp length and τ is the time resolution needed to achieve desired slant range resolution. Introducing this factor to the radar equation, significantly improves the SNR that mostly exceeds 20 dB. For example, the ERS-1 had a compression ratio of 575 (27.6 dB) and Seasat SAR had 634 (28 dB). [75] , [18]

$$P_{Rp}(\beta) = \underbrace{\left[\frac{P_{tq} \times \lambda^2 \times G^2}{(4\pi)^3 \times R_0^4}\right] \times \sigma_{pq}^0(\theta_i)}_{\text{Single Pulse}} \times \underbrace{\Delta R_g \times \frac{\ell}{2}}_{\text{Resolution Cell/ facet/elemental area}} \times \underbrace{\frac{f_r \times R_0 \times \lambda}{v_s \times \ell}}_{\text{Antenna Synthesis Factor}} \times \underbrace{\frac{\tau'}{\tau}}_{\text{Compression Ratio}} \quad [\text{W}] \quad \text{...(A: 50)}$$

By simplifying this expression and replacing $R_0 \approx R_S$, the receive power expression for the HH and HV polarizations, respectively would be:

$$P_{RH}(\beta) = \left[\frac{P_t \times G^2 \times \lambda^3 \times \Delta R_g \times f_r \times \tau'}{(4\pi)^3 \times R_S^3 \times 2 \times v_s \times \tau}\right] \times \sigma_{HH}^0(\theta_i) \quad [\text{W}] \quad \text{.....} \quad \text{(A: 51)}$$

and $$P_{RV}(\beta) = \left[\frac{P_t \times G^2 \times \lambda^3 \times \Delta R_g \times f_r \times \tau'}{(4\pi)^3 \times R_S^3 \times 2 \times v_s \times \tau}\right] \times \sigma_{VH}^0(\theta_i) \quad [\text{W}] \text{.....} \quad \text{(A: 52)}$$

these resultant receive powers have angular dependencies on gain of the antenna, the ground range resolution, the slant range and the back scattering coefficient. While calculating the respective receive powers, these need to be accounted for at small incremental steps of the incidence angles.

The above discussion may be summarized on the note that the power received due to backscatter-

ing from an illuminated area that subtends a small solid angle as viewed from the radar is directly proportional to the backscattering coefficient σ^0, regardless of the specific type of the radar used. These equations may be written in a compact form as:

$$P_{RH}(\beta) = k \times \sigma^0_{HH}(\theta_i) \qquad \ldots\ldots \qquad \text{(A: 53)} \qquad [59]$$

where k may be regarded as a system constant representing the quantity inside the square brackets of Eqs. B: 48 or B: 49. If required, then other polarization indices may be used accordingly.

This received signal power needs to compete with the inherent noise power (P_N) of the SAR system, that is given by:

$$P_N = K \times T_{sys} \times B \times NF \times L_{oss} \qquad \ldots\ldots \qquad \text{(A: 54)} \qquad [128]$$

where,

K= Boltzmann's constant = 1.6 x 10^{-23} $WK^{-1}Hz^{-1}$(= 1.38 x 10^{-23} JK^{-1})

T_{sys} = Radar operating temperature, K.

B = System bandwidth.

NF= Receiver noise figure. The ideal receiver does not add any noise to the signal to be amplified, and the input to output signal to noise ratios remains same. But actually receivers do add some noise of their own, hence this term is included in the noise power. It determines how much the receiver degrades the input signal to noise ratio.

$Loss$= Lumped losses (scanning, beam shape, collapsing, integration, cable etc.) in the system.

Often, the combined effect of received signal power and the noise power is expressed in terms of SNR given by:

$$(SNR)_p = P_{Rp} / P_N \qquad \ldots\ldots \qquad \text{(A: 55)}$$

By taking into account the approximation derived in Eq. A: 23, a simplified SNR expression for n coherently integrated pulses can be written as:

$$(SNR)_n = \left[\frac{(P_t \times f_r \times \tau') \times G^2 \times \lambda^3 \times \sigma^0 \times \Delta R_g}{(4\pi)^3 \times R_S^3 \times 2 \times v_s \times K \times T_{sys} \times NF \times Loss} \right] \qquad \ldots\ldots \qquad \text{(A: 56)}$$

While using this equation, the relevant polarization dependent σ^0_{pq} should be used. The role of the term $P_t \times f_r \times \tau'$ is important as it sets the average RF power fed to the input of the antenna.

Appendix B: Statistical Distribution Tables and Histograms of σ^0 at L-Band

Introduction

The SAR images have different average tones, exhibit different textures and present large pixel to pixel intensity variations [59]. Tone refers to the relative brightness of objects in an image. Generally, tone is the fundamental element for distinguishing between different targets or features. Variations in tone also allow the elements of shape, texture and pattern of objects to be distinguished [1]. "The average tone of an image is the average value of the image intensity for all pixels contained in that image. This average tone is proportional to average received power which, in return, is directly proportional to the backscattering coefficient σ^0 of the imaged target. In other words, σ^0 of a statistically homogeneous distributed target is, by definition, proportional to the mean value of the random variable process characterizing the intensity variations in the radar image" [59].

Texture refers to the arrangements and frequency of tonal variations in particular area of an image. A target with a rough surface and irregular structures, such as forest canopy, results in a rough textured appearance. Texture is one of the most important elements for distinguishing features in radar imagery [1]. Statistically speaking, texture is the low spatial-frequency intensity variations of the image. For the image of a "backscattering coefficient for a distributed target", the texture becomes the spatial variation of σ^0 from one region of the image to another [59].

Another significantly important aspect of the SAR images is due to the random variations due to phase-interference effects—known as speckle, and these are characteristic feature of a scattering pattern for any distributed target [59]. Speckle is introduced due to coherent nature of electromagnetic radiations used for SAR operation.

Therefore, in a radar image, there are three types of intensity variations that may be observed: tonal variations between one distributed target (such as a sea) to another (such as ships), textural variations from one region of a distributed target to another, and random fading variations at the

pixel to pixel scale. These variations are governed by different processes and are characterized by different PDFs. [59]

After World War II, an exhaustive research and field experiments were conducted to measure σ^0 variations for different types of terrain, trees, vegetation cover, snow etc. Subsequently that information was collected, processed and publicly released by [59].

To remain focused on the intended applications during this research, only statistical distribution tables (SDT), the plots of σ^0 variations as function of incidence angle and histograms relating to the trees, shrubs and short vegetation are included here. The purpose of this appendix is to highlight different aspects of the sensor- and target-specific variations on the σ^0 at L-band so that these values – which were acquired as a result of field experiments by [59], could be used as a reference in the thesis.

- **SDT and Histogram of σ^0 for Trees at L-band**

	HH Polarization		HV Polarization	
Incidence Angle	**Mean (dB)**	**SD (dB)**	**Mean (dB)**	**SD (dB)**
20^0	– 12.6	4.0	– 16.7	4.3
30^0	**– 14.6**	**4.6**	**– 18.7**	**4.1**
35^0	**– 16.9**	**2.7**	**– 22.2**	**1.6**
40^0	– 14	2.7	– 20.7	3.1
50^0	– 11.4	1.0	– 19.2	1.3
60^0	– 16.5	5.2	– 18.6	4.5

Table B - 1: SDT for HH and HV Polarizations at L-band for Trees

Table B - 1 shows the field measurements of σ^0 variations as function of incidence angle, for both HH and HV polarizations. At 30^0 the mean values are – 14.6 dB (SD = 4.6) and – 18.7 (SD=4.1) for HH and HV polarizations, respectively. The worst case scenario over this incidence angle range of 20 – 60^0 is observed at 35^0 that is – 16.9 (SD=2.7) and – 22.3 (SD=1.6) for HH and HV polarizations, respectively. The available histogram of the data at 35^0 is shown in Figure B - 1.

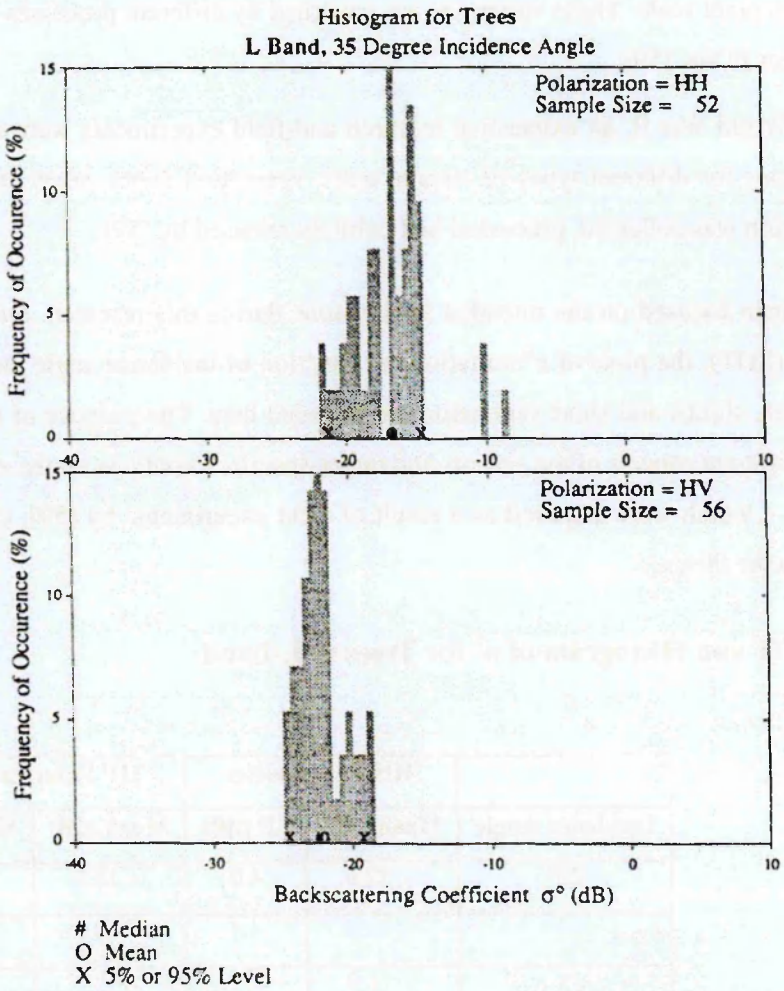

Figure B - 1: Histogram of σ^0 for the Trees at 35^0 Incidence Angle

- **SDT, Histogram and Angular Distribution of σ^0 for Shrubs at L-band**

Table B - 2 shows the data collected from the field measurements of σ^0 variations as function of incidence angle, for both HH and HV polarizations, respectively. At 30^0 the mean values are – 15 dB (SD = 6.5) and –25.4 dB (SD=5.5).

In addition, the angular plots showing the dependence of σ^0on the incidence angle has also been included. The corresponding curves show the variations in the mean values of σ^0 within a ±5% occurrence level. These plots are not simply graphic display of the information in the statistical distribution tables; they represent the product of smoothing functions applied to the source data as a function of angle. These plots are shown in. More so Figure B - 3 represents the sample histogram for an incidence angle of 40^0.

	HH Polarization		HV Polarization	
Angle	Mean (dB)	SD (dB)	Mean (dB)	SD (dB)
20^0	– 12.5	6.7	– 24.8	5.7
30^0	**– 15.0**	**6.5**	**– 23.4**	**5.5**
35^0	–10.5	4.9	– 22.3	3.3
40^0	– 19.4	5.7	– 28.3	4.4
45^0	– 14.3	4.0	– 24.9	2.9
50^0	– 14.5	4.9	– 24.6	3.4
60^0	– 23.8	4.5	– 30.9	3.5

Table B - 2: SDT for HH and HV Polarizations at L-band for Shrubs

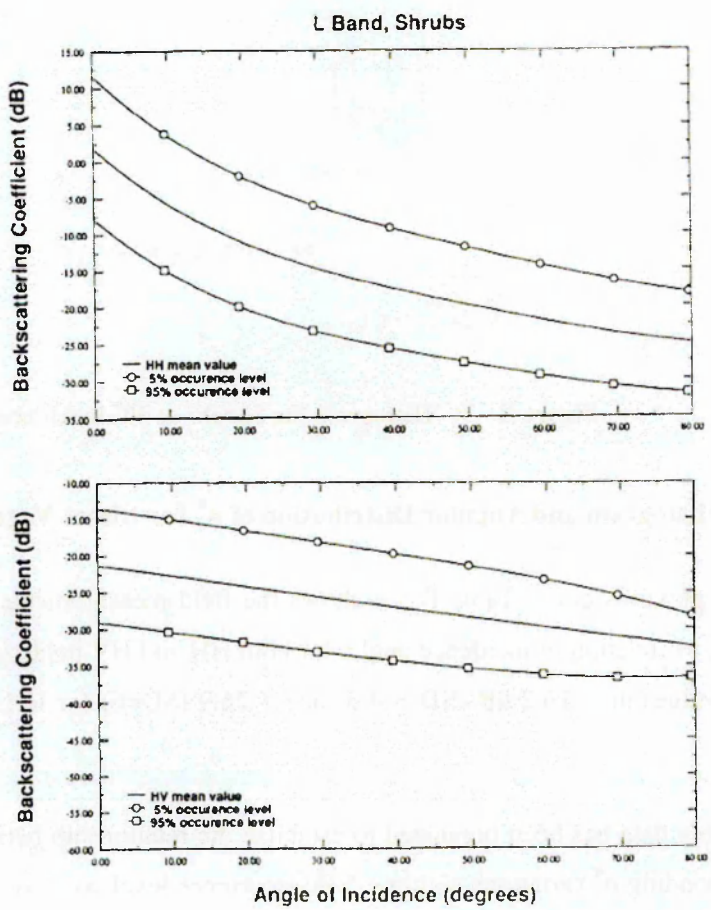

Figure B - 2: Relationship between Incidence Angle and $\sigma^0$for Shrubs

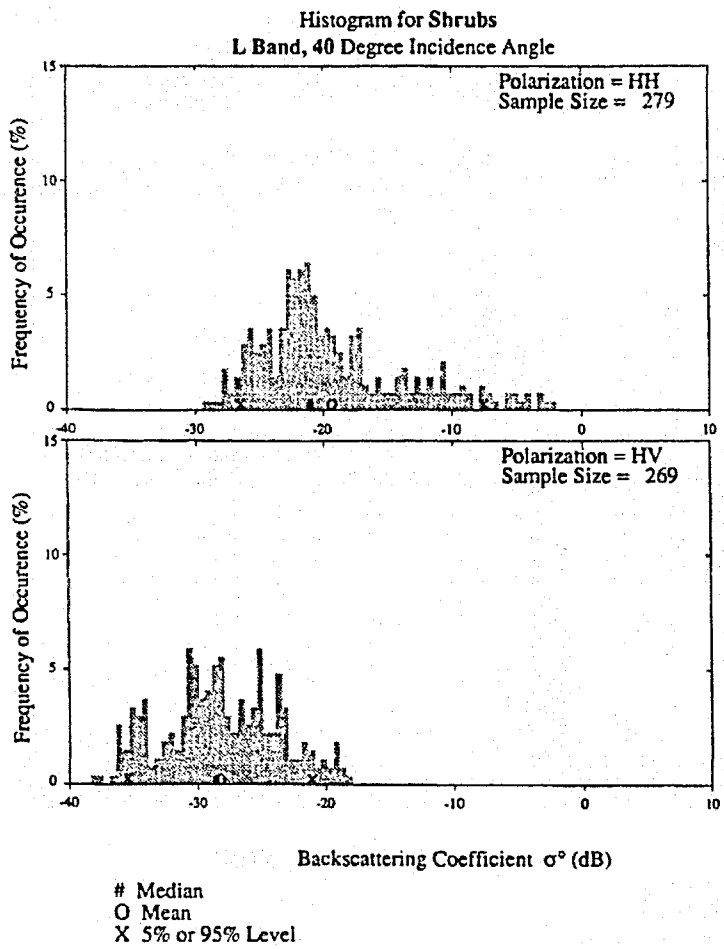

Figure B - 3: Histogram for Shrubs at 40^0 Incidence Angle

- **SDT, Histogram and Angular Distribution of σ^0 for Short Vegetation at L-band**

Similar to previous cases, Table B - 3 shows the field measurements of σ^0 variations for short vegetation, as function of incidence angle, for both HH and HV polarizations, respectively. At 30^0 the mean values are –16.2 dB (SD = 4.6) and – 26.9 (SD=6) for HH and HV polarizations, respectively.

The available data has been organized to establish the relationship between incidence angles and the corresponding σ^0 variations within ± 5 % occurrence level, as shown in Figure B - 4. More so, the sample histogram for 40^0 is also shown in Figure B - 5.

	HH Polarization		HV Polarization	
Angle	**Mean (dB)**	**SD (dB)**	**Mean (dB)**	**SD (dB)**
20^0	– 13.4	6.5	– 26.1	5.9
30^0	**– 16.2**	**6.6**	**– 24.9**	**6.0**
35^0	– 13.1	7.3	– 23.8	5.2
40^0	– 19.9	5.9	– 29.7	4.9
45^0	– 16.7	6.7	– 26.2	4.5
50^0	– 16.6	7.5	– 26.9	6.4
60^0	– 23.9	4.9	– 32.3	4.2

Table B - 3: SDT for HH and HV Polarizations at L-band for Short Vegetation

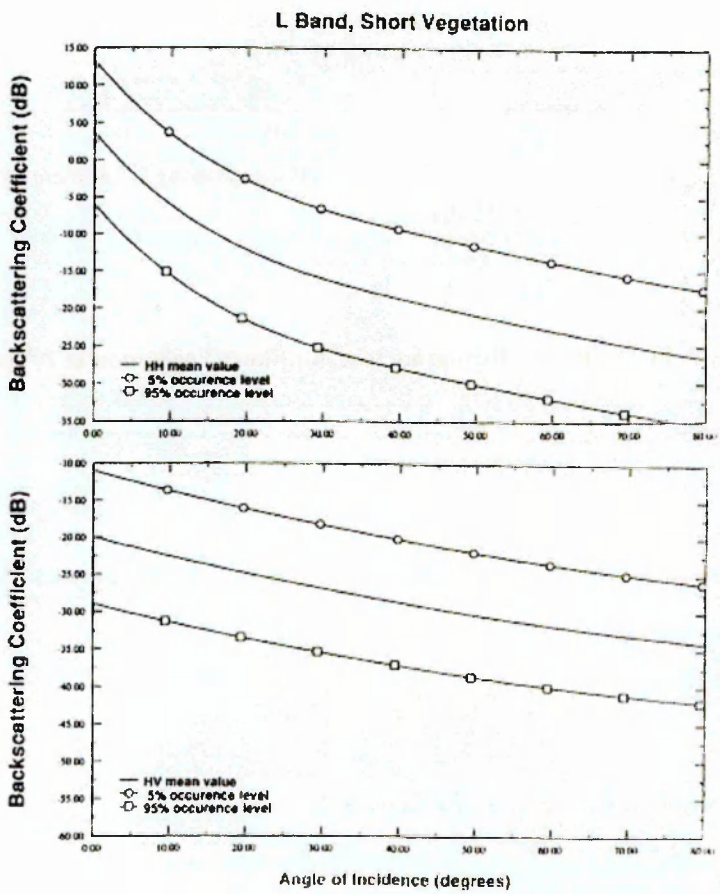

Figure B - 4: Relationship between Incidence Angle and σ^0 for Short Vegetation

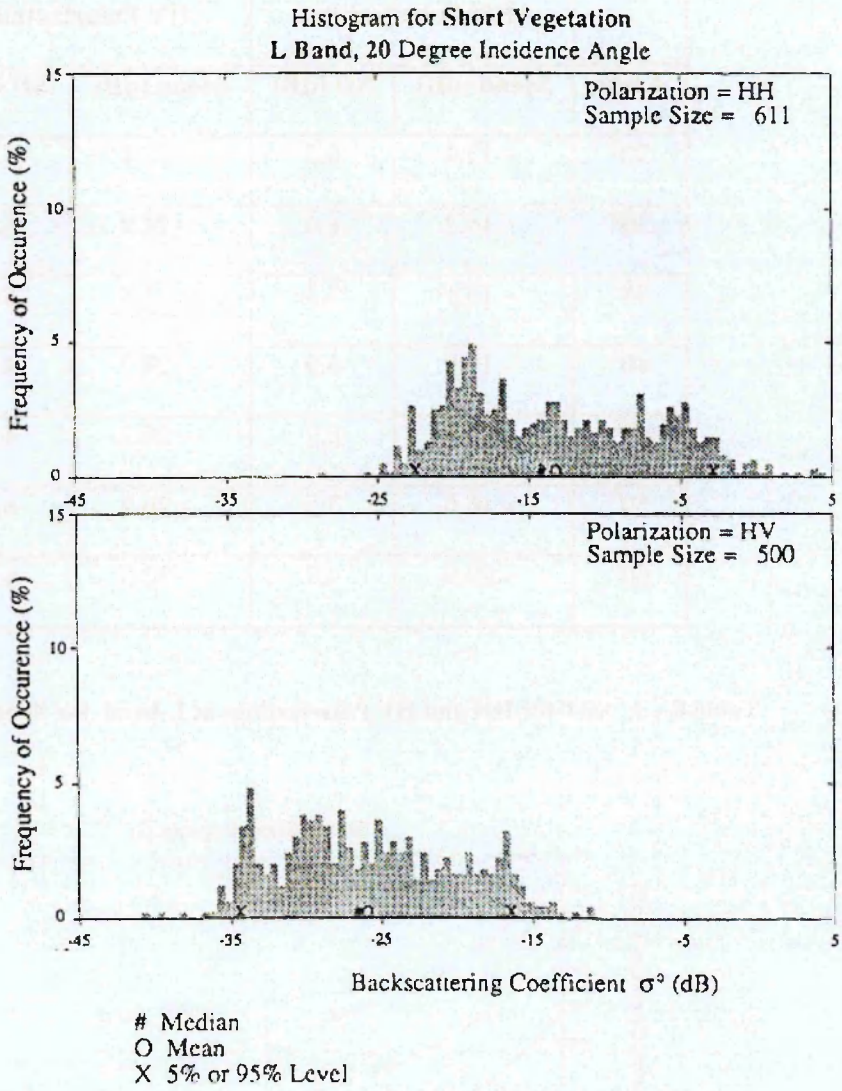

Figure B - 5: Histogram of σ^0 for Short Vegetation at 20^0 Incidence Angle

Appendix C: Radiometric Artefacts on SAR Images

What are SAR Image Artefacts?

"Most important for the final identification of objects and processes on SAR images are their brightness properties. These properties mainly depend on the radar signal backscattering level and characterize such object's features as electricity resistance and surface roughness. The brightness properties of radar images are formed by so called radar channel. This channel could be regarded as consisting of blocks of radar equipment, channel of radio waves propagation – atmosphere and ionosphere, backscattering surface, and ground processing facilities which form images as special information products. Each of these components brings it own contribution into final brightness budget and partially influence on objects visibility. It is evidence, that common user want mainly to have deal with brightness contribution derived from signal backscattered from ground surface. Therefore, contributions from other parts of radar channel could be regarded as noise components which interfere with useful signal. As the processing practice shows the responses from ground objects could be overlapped on radar images by atmosphere variations or artefacts formed by applied processing algorithm, so the common user can not distinguish their brightness contributions. Therefore, the detailed analysis of artefacts and errors involved into images on any acquisition and processing stages could be quite interesting from point of view of SAR image processing." [118]

Sources of Radiometric Artefacts

Following are the commonly know radiometric artefacts inherent to spaceborne SAR images: [91], [118]

- range ambiguity;
- azimuth ambiguity;
- nadir ambiguity;
- objects ghosting due the local Doppler frequency estimation errors;
- objects displacement due the absolute Doppler frequency estimation errors;
- insufficient range antenna pattern compensation;
- data loss;
- changing of range time delay code;
- scalloping;

- automatic gain control effects;
- analog-digital converter saturation effects;
- banding;
- ScanSAR beams stitching;
- atmosphere effects;
- processing effects;
- radar viewing nature effects.

A detailed explanation has been given with the help of many spaceborne SAR images by [118]. Further discussion on each factor is considered out of the scope of this research. In the context of this thesis, the appearance of image artefacts is due to gaps in the synthesized data, therefore, where so ever word "artefact" appears in the text it is considered as due to these gaps.